Theory of Transfer Processes in Molecular Nano-Hybrid Systems:

A Stochastic Schrödinger Equation Approach for Large-Scale Open Quantum System Dynamics

D I S S E R T A T I O N

zur Erlangung des akademischen Grades doctor rerum naturalium

im Fach Physik mit der Spezialisierung
Theoretische Physik

eingereicht an der
Mathematisch-Naturwissenschaftlichen Fakultät
der
Humboldt-Universität zu Berlin

von
Thomas Plehn M. Sc.

Präsidentin der Humboldt-Universität zu Berlin:
Prof. Dr.-Ing. Dr. Sabine Kunst

Dekan der Mathematisch-Naturwissenschaftlichen Fakultät:
Prof. Dr. Elmar Kulke

Gutachter:
1. Dr. habil. Volkhard May
2. Prof. Dr. Andreas Knorr
3. Prof. Dr. Alessandro Troisi

Tag der mündlichen Prüfung: 28.2.2020

Abstract

Understanding the electronic processes in hybrid nano–systems based on molecular and semiconductor elements opens new possibilities for optoelectronic devices. The precise comprehension of the relevant synergies between both material classes is the highest goal. Therefore, it requires for models which are both nanoscopic and atomistic – and so for adapted computational methods. In particular, "standard" methods for computing open quantum system dynamics become very inefficient and cumbersome with increasing system size. In this regard, it is a key challenge of this thesis, to establish a new stochastic Schrödinger equation technique. It bypasses the computational limits of the quantum master equation and enables dissipative simulations of imposing dimensionality. Its enormous potential is demonstrated in studies on excitation energy transfer and charge separation processes in two of such nanoscale hybrid systems: i) *para*-sexiphenyl molecules deposited on a flat ZnO surface (6P/ZnO), and ii) a tubular dye aggregate of C8S3 cyanines coupled to a CdSe nanocrystal (TDA/NC). Both systems are promising candidates for novel optoelectronic materials.

After optical excitation, the 6P/ZnO system exhibits exciton transfer from the 6P part to the ZnO. Close to the interface, Frenkel excitons may further initiate charge separation where electrons enter the ZnO and holes remain in the 6P part. Both mechanisms are studied here using finite atomistic interface models. Laser–pulse induced ultrafast wave packet dynamics including more than 125000 interface states are simulated. Subsequently, slower dissipative hole motion in a layer of 2553 6P molecules is studied starting from scenarios of ultrafast charge separation with immediate electron trapping at the ZnO surface. For this purpose, the own stochastic Schrödinger equation simulation technique is applied.

The study on the TDA/NC interface is based on a gigantic equilibrated nuclear structure of the aggregate including 4140 dyes. A generalized Frenkel exciton model is employed and different polarization effects in the TDA are considered. Thanks to the stochastic Schrödinger equation approach, energy relaxation in the exciton band of the TDA is simulated in outstanding quality and extend. Then, Wannier–Mott excitons of the NC are added and incoherent rates for exciton transfer from the TDA to the NC are computed. Different spatial configurations are studied and it is discussed why the Förster model possesses no validity here.

Altogether, the presented dynamics are pioneering in complexity and spatial extent. Simulations of non–Markovian dynamics are successfully executed to realistic systems including up to 4140 molecules and lasting for several picoseconds. Using the 6P/ZnO interface, the importance of an explicit laser–pulse treatment for understanding ultrafast charge separation kinetics at hybrid interfaces is illustrated. The involvement of charge transfer excitons is clarified in detail. Charge separation slightly outweighs the exciton transfer. Nevertheless, critical features must be named that make free charge carrier generation at that interface difficult. Also the existing picture of the TDA/NC system is complemented. The present exciton model is considerably more realistic than others presented in literature. It allows directly monitoring the predicted unidirectional energy relaxation from the outer to the inner wall of the TDA. Concerning the transfer to the NC, it is shown that the excitonic coupling generally stays below 1 meV. Even in direct proximity, the anticipated hybrid excitons between TDA and NC fail to appear.

Auszug

Das Verstehen der elektronischen Prozesse in Nano-Hybridsystemen, bestehend aus Molekülen und Halbleiterstrukturen, eröffnet neue Möglichkeiten für optoelektronische Bauteile. Das Begreifen der Synergien zwischen beiden Materialklassen ist das höchste Ziel. Dafür benötigt es nanoskopische und gleichzeitig atomare Modelle – und somit angepasste Rechenmethoden. Insbesondere "Standard"-Ansätze für die Dynamik offener Quantensysteme werden mit zunehmender Systemgröße jedoch sehr ineffizient und mühsam. Somit ist es eine zentrale Herausforderung dieser Arbeit, eine neue Methode, basierend auf einer stochastischen Schrödinger-Gleichung, zu etablieren. Diese umgeht die numerischen Limits der Quanten-Mastergleichung und ermöglicht Simulationen von imposanter Größe. Ihr enormes Potenzial wird hier in Studien zu Anregungsenergietransfer und Ladungsseparation an zwei Nano–Hybridsystemen demonstriert: I) *para*–sexiphenyl Moleküle auf einer flachen ZnO Oberfläche (6P/ZnO), und II) ein tubuläres C8S3 Farbstoffaggregat gekoppelt an einen CdSe Nanokristall (TFA/NK). Beide Systeme sind vielversprechende Kandidaten für neue optoelektronische Materialien.

Im 6P/ZnO System findet nach optischer Anregung Energietransfer vom 6P Anteil zum ZnO statt. Direkt an der Grenzfläche können Frenkel-Exzitonen zusätzlich Ladungsseparation initiieren, wobei Elektronen ins ZnO transferiert werden und Löcher im 6P Anteil verbleiben. Beide Mechanismen werden hier mit endlichen atomaren Modellen untersucht. laserpulsinduzierte ultraschnelle Wellenfunktionsdynamiken mit über 125000 Zuständen werden simuliert. Anschließend wird die langsamere dissipative Lochkinetik in einer Schicht aus 2553 6P Molekülen, ausgehend von ultraschneller Ladungsseparation mit sofortiger Immobilisierung des Elektrons an der ZnO Oberfläche, studiert. Dazu wird die eigene Simulationstechnik der stochastischen Schrödinger-Gleichung verwendet.

Die Studie an der TFA/NK Grenzfläche basiert auf einer gigantischen equilibrierten Aggregatstruktur aus 4140 Molekülen. Ein generalisiertes Frenkel-Exzitonenmodell wird benutzt, und Polarisationseffekte im TFA werden bedacht. Der Ansatz der stochastischen Schrödinger Gleichung ermöglicht bemerkenswerte Einblicke in die Aggregat-interne Exzitonenrelaxation. Danach werden Wannier-Mott-Exzitonen des NK hinzugefügt und inkohärente Raten des Exzitonentransfers zum NK berechnet. Unterschiedliche räumliche Konfigurationen werden untersucht und es wird diskutiert, warum das Förster-Modell hier keine Gültigkeit besitzt.

Die Studien besitzen Pioniercharakter in Hinblick auf Komplexität und Größe. Nicht-Markov'sche Dynamiken von der Dauer mehrerer Pikosekunden werden in realistischen Systemen mit bis zu 4140 Molekülen simuliert. An der 6P/ZnO Grenzfläche wird die Bedeutung der expliziten Laserpulsbehandlung für das Verständnis der ultraschnellen Ladungsseparation an Hybridgrenzflächen gezeigt. Auch das Auftreten von Ladungstransfer-Exzitonen wird im Detail erläutert. Die Ladungsseparation überwiegt leicht im Vergleich zum Exzitonentransfer. Trotzdem müssen kritische Eigenschaften genannt werden, welche die Generation freier Ladungsträger erschweren. Ebenso wird das bislang existierende Bild des TFA/NK Systems erweitert. Das präsentierte Exzitonenmodell ist wesentlich realistischer als alle zuvor verwendeten. Der vorhergesagte unidirektionale Energietransfer von der äußeren zur inneren Wand des TFAs wird direkt abgebildet. Weiterhin wird gezeigt, dass die exzitonische Kopplung zwischen dem TFA und dem NK im Allgemeinen weniger als 1 meV beträgt. Selbst in nächster Nähe positioniert gibt es keine Hinweise auf die vorhergesagten Hybridexzitonen zwischen TFA und NK.

Contents

List of Publications

- J. Megow, Th. Plehn, R. Steffen, B. Röder and V. May, *Photoinduced Excitation Energy Transfer in Hexapyropheophorbide a*, Chem. Phys. Lett. B, **585**, 178–183 (2013)
- Th. Plehn, J. Megow and V. May, *Concerted charge and energy transfer processes in a highly flexible fullerene-dye system: a mixed quantum-classical study*, Phys. Chem. Chem. Phys., **16**, 12949–12958 (2014)
- Th. Plehn, D. Ziemann, J. Megow and V. May, *Frenkel to Wannier–Mott Exciton Transition: Calculation of FRET Rates for a Tubular Dye Aggregate coupled to a CdSe Nanocrystal*, J. Phys. Chem. B, **119**, 7467–7472 (2015)
- Th. Plehn and V. May, *Charge and Energy Migration in Molecular Clusters: A Stochastic Schrödinger Equation Approach*, J. Chem. Phys., **146**, 034107 (2017)
- Th. Plehn, D. Ziemann and V. May, *Atomistic Simulations of Charge Separation at a Nanohybrid Interface: Relevance of Photoinduced Initial State Preparation*, J. Phys. Chem. Lett., **9**, 209–215 (2018)
- Th. Plehn and V. May, *Charge Migration Kinetics at a Nanoscale ZnO/Molecule Interface Structure: A stochastic Schrödinger Equation Approach*, Chem. Phys., **515**, 187–192 (2018)
- Th. Plehn, D. Ziemann and V. May, *Charge Separation at an Organic/Inorganic Nanohybrid Interface: Atomistic Simulations of a para–Sexiphenyl ZnO System*, Phys. Chem. Chem. Phys., **20**, 26870–26884 (2018)
- Th. Plehn, D. Ziemann and V. May, *Simulations of Frenkel to Wannier–Mott Exciton Transitions in a Nanohybrid System*, J. Phys. Chem. C, **122**, 27925–27934 (2018)
- D. Ziemann, Th. Plehn and V. May *Excitation Energy Transfer Dynamics in Nano–Hybrid Systems*, http://www.lumipedia.org/ on "Förster Resonance Energy Transfer and Beyond"
- L. Wang, Th. Plehn, and V. May, *Ultrafast Exciton Dynamics in 1D and 2D Para-Sexiphenyl Clusters*, J. Chem. Phys., (submitted)

1. Introduction

Archaeological finds bear witness to simple hand axes and flint stone tools produced about 1 million years ago. Since then, the history of mankind is a history of technological developments. Early fruits of this co–evolution were the massive cultural changes in the Neolithic era (e.g., sedentism and commerce), which became only possible due to practicing agriculture and stock farming. Other prominent examples are the social movements in the early 18th century, which went hand in hand with the groundbreaking inventions of the industrial revolution. Since the late 20th century, nanotechnology has started to rise to a leading interdisciplinary driving force and has become indispensable in today's society. Standardized production processes for combining molecules and other tiny elements smaller than 100 nm to functionalized modules are the outcome of continuous achievements in this field. On the one hand, the fabrication of smaller and smaller nanostructures for microelectronic devices is in the focus. By composing different nanostructures to *hybrid* materials, on the other hand, it is the intention to induce synergy effects leading to novel interesting physical and chemical properties. Hybrid nanostructures and their innovative functionalities are hoped to guarantee further technological development. This hope has already triggered plenty of different research activities for more than a decade.

In particular, hybrid materials consisting of chromophore dye molecules and semiconductor nanostructures (e.g., quantum dots or nanocrystals) are intensively studied for targeted applications in the field of optoelectronics [1] ranging from photovoltaics [2, 3, 4] and artificial light harvesting [5, 6, 7, 8] through light emitting nanomaterials [9, 10, 11] to optical switches [12] and photodetectors [13, 14]. The main technological interests are thereby novel concepts beyond the conventional inorganic solar cells or the vague organic hetero bulk junctions [15]. Other high goals are the efficiency enhancement and general improvement of already existing organic/inorganic materials with light emitting functionality [1, 10]. Concrete plans for device production concerning the latter LED technology are already existing today (see, e.g., Refs. [16, 17, 18, 19, 20]). In general, due to the abundance of different opportunities, the research community is looking optimistically into the future also with substantial improvements in photovoltaics expected. The high expectations of the molecule/semiconductor structures are related to the idea to combine "the best of the two worlds". In fact, the specific features of both material classes in principle match perfectly [21, 1, 22, 23]. For instance, the remarkable stability and charge carrier mobility of all semiconductors [24, 25] or the narrow and tunable emission band of quantum dots and nanocrystals [22, 4] can be composed favorably with the very high oscillator strength and exciton binding energy of molecular complexes [26, 27] as well as their extremely precise chemical functionalities [1, 28]. Indeed, the repertoire of carbon chemistry holds an incredible stack of possible substances with differences in optical properties, size, aggregation behavior,

functional anchor groups or even concerning sustainable factorization and recyclability [29].

Spectroscopic studies tremendously benefit from simple fabrication routines for creating molecule/semiconductor structures. The span of the inspected hybrid systems ranges thereby from very basic structures [30, 31, 7] with only one type of molecule and a single kind of semiconductor component (e.g., complexed in solution) to very sophisticated architectures consisting of several functional modules designed in more complex compositions [8, 26, 11, 28]. The latter type of hybrid superstructures are often assembled in form of rigid macroscopic units or multilayers on smooth surfaces [24, 5, 6, 3, 15, 14] where the trend is clearly towards device fabrication [17, 1, 13, 2, 3, 10].

In marked contrast to that, theoretical approaches and computer simulations show great difficulties modeling the two material classes together on a nanoscale [25, 22, 29]. Both classes rely on different theoretical ansatzes and contain own established assumptions and approximations. These must now be complied in one interface model [1, 23]. It is another critical issue that many of the interesting structural and electronic properties appear only on the nanoscale. On this scale, however, vast numbers of electronic states are relevant and reliable electronic structure computations become extremely time–consuming unless some simplifying assumptions are made. Due to these conceptual difficulties, so far, the majority of electronic system studies are devoted to only small and simple hybrid structures (see details below). One prominent simplifying assumption is the introduction of system periodicities concerning crystalline semiconductor slices and regular molecular layers [32, 33, 34, 35, 36, 37, 38]. By concentrating on a small unit cell, electronic structure calculations then simplify significantly and it becomes possible to realize interface simulations with ab–initio parameterization. Contrarily, atomistic models and time–domain simulations of finite large–scale nanostructures are very rare. For instance, the optoelectronic properties of molecule/nanocrystal complexes can only be adequately described when considering the finite systems as a whole. Also concerning regular hybrid interface architectures, the introduction of a unit cell means often that important wide–ranging processes cannot be simulated properly. At this point, more effort must be generally invested into developing atomistic models in order to systematically promote further theoretical understanding of the "merging" of the optoelectronic properties.

The present thesis contributes greatly to that need. Two realistic hybrid nano–interface systems are studied. The first system describes *para*–sexiphenyl molecules assembled on a ZnO surface. The second system consists of a gigantic tubular dye aggregate coupled to a spherical CdSe nanocrystal. Both kinds of compositions are promising candidates for novel optoelectronic applications and have been subject of many experimental investigations (see details below). The particular focus of this work lies on time–domain simulations of the occuring optoelectronic processes. Thereby, exciton transfer mechanisms, phenomena of photoinduced charge separation, dissipative exciton motion and charge carrier migration are discussed. These processes take place on very different time–scales. Moreover, the large–scale character of both systems plays a central role. In this work, it is a main concern to present finite system studies which are both of realistic size and in atomistic resolution. Therefore, it describes the key

challenge to introduce combinations of atomistic models to ensure the required precission. Moreover, novel simulation techniques which guarantee efficient computational performances in large–scale applications must be worked out. The discussed insights into the kinetics bring forward the understanding of both specific interfaces in many ways. Moreover, the executed large–scale studies on dissipation witness a significant progress achieved in the field of open system dynamics.

The remaining of this chapter serves as a compact introduction to fundamental aspects of all parts of the thesis. The different topics are presented in line with the global structure of the work. It begins with a debate on the basic principles of the quantum state diffusion. The method of the stochastic Schrödinger equation is introduced as a promising simulation technique. Then, the mechanisms of excitation energy transfer, photoinduced charge separation and charge carrier migration at the *para*–sexiphenyl/ZnO interface system are generally discussed. A likewise background is given on the exciton relaxation and energy transfer in the tubular dye aggregate/CdSe nanocrystal system. Finally, a rough outline of the thesis is provided.

Stochastic Schrödinger equation methodology

Atomistic simulations of charge separation processes are a critical topic. In general, systems of enormous size must be considered in order to achieve realistic impressions on those kinetics. Moreover, corresponding simulations generally involve two independent degrees of freedom (the one of the electron and the one of the hole charge). Accordingly, a vast number of different interface states inflates electronic system models. The same is valid concerning the description of electron–hole pair excitations in a semiconductor component. In finite interface models on charge separation and other excitation energy transfer processes, hence drastically increasing numbers of relevant electronic states must be anticipated when turning to nanoscale sizes. This describes a great task and special approaches and numerical algorithms are required. Thereby, many numerically optimized algorithms for solving exciton equations (i.e., eigenvalue problems) of gigantic dimensionality can be found in literature [39, 40]. Similarly, very efficient mathematical methods exist to solve the time–dependent Schrödinger equation [41, 42, 43]. These methods are of fundamental interest and therefore well–established. In harsh contrast to that, it is a special task of this work to develop an efficient simulation technique for dissipative time–dependent phenomena, which is particularly suited for application to large–scale systems.

Dissipative phenomena appear generally when electronic system dynamics are coupled to molecular vibrations [44, 45]. Related simulations require a very large number of vibrational modes and simulations are typically executed in terms of open system dynamics (i.e., by solving the quantum master equation [44]). Thereby, it is the idea to introduce a sub space, which is only span by the electronic system states. The vibrational harmonic oscillator modes are collectively described in terms of a bath with a certain spectral density. However, concerning large–scale systems, solving the quantum master equation is extremely inefficent. As visualized on the left-hand side of Fig. 1.1, the very unfavorable scaling behavior of its computational costs, when increasing the number of incorporated electronic states N, is responsible for that. In principle, solving the quantum master equation means propagating directly the reduced density matrix

Figure 1.1.: Flow chart of the quantum state diffusion (QSD) method versus the quantum master equation (QME) ansatz for open system dynamics. The scaling behavior of the computational costs of both methods is indicated in powers of the system size, N. The QME propagates directly the reduced density matrix in Liouville space which generally scales $\propto N^4$. The QSD works on Hilbert space vectors and scales $\propto N^2$, however M different stochastic state trajectories are required.

which is of size N^2. Accordingly, its propagation operation in Liouville space generally scales $\propto N^4$ (see, e.g., the Redfield tensor [44]). This scaling behavior describes a significant numerical limitation which must be circumvented.

Therefore, here the (by far less popular) quantum state diffusion methodology [46] is consulted. The basic functionality of this approach is illustrated on the right–hand side of Fig. 1.1. Contrarily to the master equation ansatz, the quantum state diffusion describes a sampling method based on an ensemble of stochastic state trajectories which obey a stochastic Schrödinger equation. Such equation is the centerpiece of the here implemented open system dynamics. In practice, it means that individual vectors of dimensionality N are propagated in Hilbert space of the electronic system. Motivated by existing works [47, 48, 49, 50, 51], in this thesis a novel numerical procedure is conceived based on a simple strategy. Its implementation allows propagating the stochastic state vectors with N^2–scaling behavior. Accordingly, a computational benefit can be expected whenever the number of required trajectories M (to obtain converged results) stays below N^2 (see again Fig. 1.1). The straightforward parallelization of sampling M trajectories further opens opportunities for enormous improvements of the computational performance. Such a technique for efficient open system dynamics in application to truly large–scale systems is of unique relevance and also concerning other research areas a highly welcome method. In this work, its potential is demonstrated in two concrete system studies with $N = 2553$ and $N = 4140$. These numbers appear huge in reference to comparable simulation works in literature [51, 52]. Moreover, by taking into account non–Markovian effects the offered technique is advantegous to usually

chosen less sophisticated models on this system scale [53, 54, 55] (see also Sec. 4.2).

Para–sexiphenyl molecules deposited on ZnO surfaces

The first concrete studies in this work concentrate on large–scale interface structures generated by aggregation of *para*–sexiphenyl molecules on top of flat ZnO surfaces. Although ZnO has been a well–known and appreciated solid state material for industrial fabrication of a diversity of products for long [56, 57], it has experienced a revival via new processing techniques in nanotechnology [58, 59, 24, 60, 61] (see also Sec. 5.1). In particular, solar cell and LED industries appreciate the diversity of different nanoscale forms (e.g., quantum dots, nanocrystals or surface patterns), which can be designed and generated easily, as well as the favorably tunable band gap of doped ZnO materials [58, 24, 61]. Also in combination with molecular films, ZnO surfaces have been already extensively investigated in experiments during the last few years. Until date, a plenty of different types of molecules or mixed molecular films have been deposited and examined on ZnO [24, 15, 62]. Existing studies thereby include morphological [63, 64, 65] and spectroscopic measurements [66, 67, 68] – also in concert with electronic structure calculations [69, 35, 70, 62, 38]. One particular focus lies on aggregation layers of *para*–sexiphenyl (6P) molecules. The simple chemical structure of 6P is illustrated in Fig. 1.2a. The aggregation behavior and growth mechanism of 6P on the three popular ZnO surfaces (indicated in Fig. 1.2b) is well–understood from molecular modeling [71] and microscopy imaging techniques [65, 68]. Assisted by continuous aggregation, the 6P molecules are subject to self–assembly forming regular 3d herringbone lattices [71]. As shown in Fig. 1.2c and d, the 6Ps are thereby either observed in up–right standing position or found flat lying on ZnO substrate. In particular, these self–assembly features promise very simple, uniform and cheap device fabrication.

The level alignment of the particular 6P/ZnO (0001) interface is given in Fig. 1.2e (measured by Blumstengel et al. [68]). The 6P HOMO/LUMO gap amounts 3.5 eV, which is 0.2 eV larger than the determined band gap of the ZnO. Accordingly, resonant energy transfer is possible from excited 6Ps to electron–hole pair excitations in the opponent ZnO part. This process is sketched in Fig. 1.3a. (To be correct, concerning the intermolecular excitonic coupling, molecular excitations are actually not the primary photexcitations in the aggregate part. Instead, a certainly broadened Frenkel exciton band is created.) In principle, also the reverse process is possible starting from electron–hole pair excitations with somewhat higher energy. Nevertheless, this process is assumed to be less efficient regarding relaxation processes and shall not be further treated in the framework of this thesis. In order to guarantee functionality in the sense of a solar cell, the excitation (bound Frenkel exciton) must dissociate into extractable charge carriers to both sides of the 6P/ZnO interface. This relies elementary on mechanisms of charge separation. As illustrated in Fig. 1.3b, after optical excitation of Frenkel excitons and possible intermolecular excitation energy transfer, an electron is injected from an excited 6P at the surface into the conduction band (CB) of the ZnO (i.e., by means of an electron transfer reaction across the interface). The formerly excited 6P remains positively charged and defines a molecular localized hole. According to the level alignment (see again Fig. 1.2e), the latter is bound to the 6P aggregate. In awareness of the mutual Coulomb interaction, the hole and electron

Figure 1.2.: The *para*–sexiphenyl/ZnO interface. Panel a: Chemical structure of the *para*–sexiphenyl (6P) molecule. Panel b: Wurtzite crystal structure and the three prominent ZnO surfaces. Panel c and d: Schematic view on the two observed characteristic aggregation types of 6P on flat ZnO substrate. Panel e: Measured energy level scheme of the 6P/ZnO (0001) interface [68], including valence and conduction band (VB and CB) of the ZnO and each the highest occupied and lowest unoccupied molecular orbital (HOMO and LUMO) of three 6Ps.

Figure 1.3.: Transfer processes at the *para*–sexiphenyl (6P)/ZnO interface (for more details on the energy levels, see Fig. 1.2). Valence and conduction band (VB and CB) of the ZnO are shown against the highest occupied and lowest unoccupied molecular orbitals of each two (panel a and c) or three (panel b) 6Ps. Panel a: Optical excitation of the 6P molecules (step 1) and excitation energy transfer to electron–hole pair excitations in the ZnO (step 2). Panel b: Optical excitation (step 1), intermolecular excitation energy transfer to the interface region (step 2), charge separation via electron transfer across the interface into the CB of the ZnO (step 3) and subsequent hole migration between the 6Ps (step 4). Panel c: Optical excitation of a charge transfer exciton.

are finally subject to migration processes. This situation describes a charge–separated interface state. Besides excited states at the interface and the latter charge–separated states, one often concerns a third type of so–called charge–transfer excitons. These are detected in spectroscopic measurements [15, 72] and define charge–separated states which can be directly optically excited (see also Ref. [73]). As illustrated in Fig. 1.3c, the optical excitation of charge–transfer excitons opens the opportunity to much faster charge carrier generation.

In the sense of photovoltaics, the processes leading to charge separation (see Fig. 1.3b and c) play an elementary role. The energy transfer process from the 6P aggregate to the ZnO (see Fig. 1.3a), however, is unwanted because it minimizes the yield of charge carrier generation. This makes a comparative examination of both types of processes very interesting. In this work, the transition of excitation energy and the photoinduced charge separation are confronted in terms of two sub studies (visualized in Fig. 1.4a and b). Both studies are based on similar finite interface designs. Despite the model character of the constructed interface system, representative insight on the occuring processes can be expected. It might be either interpreted as a finite outtake of a macroscopic interface architectures or related directly to a ZnO nanoparticle structure. Afterwards, a third study is devoted to charge carrier migration at the interface which happens once the charge separation process is completed. Thereby, main attention is focused on the important question whether the charges are able to overcome their common Coulomb attraction or not. For this purpose, a second type of 6P/ZnO interface is introduced (see Fig. 1.5)

Excitation energy transfer at the *para*–sexiphenyl/ZnO nano–interface

Meanwhile an overwhelming amount of different experimental studies and measurements on excitation energy transfer between molecular and semiconductor nanostructures has been piled up. It witnesses the tremendous interest in this topic (see, e.g., Refs. [12, 24, 5, 13, 2, 6, 30, 4, 67, 15, 74]). As the "door–opener" to tailored optoelectronic features, detailed understanding of the excitonic coupling across the hybrid interfaces is of general relevance and extremely important. Nevertheless, theoretical studies and time–domain simulation works have not been stimulated in such "abundance". Moreover, the much fewer number of available computational studies concentrated either on periodic hybrid interfaces [75, 1, 35, 36, 38] or on rather tiny finite hybrid systems [76, 77]. The formation of hybrid states with interesting "mixed" excitonic features was postulated thereby already early by Agranovich and Bassani et al. [78, 79, 75] by means of analytical interface models of periodic organic/inorganic quantum well structures. Concerning small sizes, nowadays, it is possible to determine the electronic properties of finite hybrid complexes using ordinary DFT approaches. In such way, the excitonic couplings between a porphyrin sensitizer and a nanocrystal was determined by Prezhdo et al. [76]. Different more involving ab–initio ansatzes were presented by Tamura and Burghardt et al. [77] (in application to a very tiny finite CdSe/rhodamine system). More recent works of Knorr and Richter et al. [35, 38] report on excitonic coupling and excitation energy transfer between a periodic molecular film of ladder–type quarterphenyl molecules and a plane ZnO surface (with the focus on an effective mass model to treat the electron–hole pairs in the ZnO). The excitonic properties of a regular monolayer of pentacene on a TiO_2 surface were also recently investigated by employing a DFT/Bethe–Salpeter equation ansatz [36]. Altogether, the total number of computational studies is rather small and concrete knowledge is still limited.

The present study begins with an elaborate and very illustrative explanation of the nature of the excitonic interaction across the 6P/ZnO interface. The considered model system (see Fig. 1.4a) is much more expanding than any of the periodic cells studied so far. In turn, it is essentially too large for an uniform ab–initio modeling. Instead, here the computational approach is inspired by Ref. [80]. There, excitonic couplings were determined between a CdSe nanocrystal (of about half of the size of the present ZnO cluster) and a single chromophore molecule using a combination of semi–empirical and ab–initio methodologies. A likewise diabatization ansatz is introduced here. Accordingly, the interface is fragmented into smaller substructures and full system (diabatic) states are constructed as direct products of several site states with zero wave function overlap [44]. Frenkel exciton and electron–hole pair excitations are computed residing on the 6P aggregate and the ZnO cluster, respectively. The price for the diabatization ansatz is paid with an enormous number of required excitonic couplings between the latter two types of excitations. The very common but less accurate point–dipole approximation (Förster–type coupling) is avoided and all coupling terms are determined in atomistic resolution of both system components.

The second part of the exciton study concentrates on the translation of initially populated Frenkel excitons into electron–hole pair excitations of the ZnO. Thereby, a debate is given on whether the Frenkel exciton decay obeys the simple picture of an

Figure 1.4.: The studied processes in the two designed *para*–sexiphenyl (6P)/ZnO model systems. Panel a: Excitation energy transfer (EET) from Frenkel excitons (FX) in a stack of 20 6P molecules to electron–hole pair (EHP) excitations in the hemispherical ZnO cluster (with 5 nm diameter). Panel b: Photoinduced charge separation (CS) processes (direct excitation of charge transfer states is not sketched).

exponential loss of population or appears with more complex characteristics. To answer this question is important as it enlightens the complexity of the transfer process and thus declares the need for more sophisticated time–domain simulation approaches. For this purpose, transfer rates according to Fermi's golden rule are computed using the excitonic couplings determined beforehand. In direct comparison, coherent wave packet dynamics are simulated. If the rate model obeys any restriction, it becomes clear in this manner. Moreover, different initially populated Frenkel excitons in the 6P aggregate are probed in order to detect possible dependences on the energetic alignment of exciton donor and acceptor states. The observed characteristic times of the exciton decay are finally confronted with the time–scales of the mechanism of charge separation across the interface.

Photoinduced charge separation at the *para*–sexiphenyl/ZnO nano–interface

The procession of charge separation is of primary importance. Concerning bulk hetero junctions, likewise processes were already studied a lot. Intensive organic/organic interface simulation works can be found from many groups focusing on only few hundred femtoseconds or ranging up to many picoseconds (see particularly Troisi et al. [81, 82] and Burghardt et al. [83, 84]). In turn, the general basics of modeling charge separa-

tion at interfaces are well–understood. Popular simulation methods are thereby, e.g., different incoherent transfer rate ansatzes [85, 86, 87], the multi configurational time–dependent Hartree method for coherent exciton–phonon dynamics [83, 84], the time–dependent density functional theory [88] or different kinetic Monte–Carlo approaches [89]. As explained above, however, the combination of molecular and semiconductor models leads to conceptual difficulties. In harsh contrast, therefore, much fewer works can be found on time–domain simulations of charge separation at organic/inorganic hybrid systems. The most of these studies have been made possible by means of the method of nonadiabatic molecular dynamics. Indeed, it has become a popular instrument since the pioneering simulation work of Prezhdo et al. in 2002 on stimulated charge injection from an covalently attached isonicotinic acid molecule into a TiO_2 surface (by using a tiny periodic simulation cell) [90]. Since then, several other ab–initio nonadiabatic molecular dynamics simulations on more involving molecule/semiconductor systems have followed [32, 76, 33, 91, 37]. Nevertheless, the investigated systems or simulation cells have remained rather small. At this place, also the illustrative works of Lu et al. should be stated [92, 34]. In close relation and based on the same method, they presented time–domain simulations of charge separation across a periodic P3HT/ZnO interface and directly drew comparison against data from simulations of the prominent P3HT/PCBM bulk hetero junction [93]. Thereby, the problematic issue of the characteristic ZnO surface states was debated (see, e.g., also Refs. [94, 66] and references therein). These latter surface states are accused to prevent efficient electron injection into the ZnO bulk zone and shall be also an issue in the framework of this thesis.

Whenever concerning interface charge separation processes, special attention must be paid to the charge transfer coupling across the interface. Its terms mediate the important electron injection from the surface–attached 6P molecule into all possible ZnO conduction band states (step 3 in Fig. 1.3b). Due to the "merging" of organic and inorganic electronic systems at the interface, straightforward ab–initio computations become very costly, extremely inefficient and simply inappropriate for non–periodic systems beyond very small size. In this work, therefore an own parametrization scheme is employed. It makes possible to obtain estimate values based on an approximate ab–initio modeling. The conceived approach is basically inspired by the partitioning scheme established by Troisi et al. [95, 96]. However, here it is furthermore the idea to directly identify an initial electron acceptor state based on a phenomenological picture of the injection process. This describes a dramatic simplification, because the critical ab–initio calculation of the molecule/ZnO junction part is circumvented. Instead, in the present ansatz, the complete parametrization of the injection processes is achieved based on two separate electronic structure calculations (one of the 6P and one of the ZnO cluster). The presented ansatz is very intuitive, simple and can be straightly applied to other systems.

In total more than 125000 electronic interface states are computed in order to investigate the charge separation in the 6P/ZnO model system (see again Fig. 1.4b). Besides, it is assumed that the influence of molecular vibrations is negligible and that the entire interface kinetics can be simulated in terms of coherent wave packet dynamics. This assumption allies with the present focus on laser–pulse induced processes on the femtosecond time–scale. (On this time–scale, also interactions of the injected electrons with

ZnO lattice phonons should be of minor importance.) Again, the convenient diabatic state ansatz (based on fragmentation of the system) is employed. Here, it turns out to be very helpfully in order to uncover the detailed spatio–temporal evolution of the excited aggregate states and their complex interplay with the charge–separated states. Thanks to the localized state picture, on one side, initial intermolecular excitation energy transfer to the interface can be properly monitored. If observed, this would cleary indicate on an indirect charge separation process according to Fig. 1.3b (i.e., cascade–like exciton migration and subsequent electron transfer to the ZnO part). On the other side, also the direct optical excitation of charge–transfer excitons [73] can be properly distinguished (see Fig. 1.3c). To answer the question about which of the two types of charge separation mechanisms is the dominant one describes a formidable task. In this work, it is addressed as a key point – namely, in dependence on the laser–pulse energy.

Another typical issue is the "robustness" of the charge separation dynamics with respect to small variations within the model system. Such investigations are of general importance as well. Here, a study on the influence of energetic disorder in the system shall be an adequate instrument. It helps to identify possibly very specific and resonant passages of charge separation. Further, it provides a first impression on the dynamics under condition that vibronic interactions are additionally taken into consideration.

Great effort is finally undertaken to clarify the role of an explicitly simulated laser–pulse excitation. In fact, simulations of short–time dynamics generally request careful considerations of initial conditions [32]. This is particularly the case whenever photoinduced dynamics shall be simulated by simplified excited state ansatzes. Concerning highly complex system, it is to be expected that slightly different initial conditions result in essentially varying dynamics. Here, an elaborate discussion is devoted to that critical issue. The concrete influence of replacing the laser–pulse excitation by different initial excited state ansatzes is inspected. The offered discussion is of high relevance since rather arbitrary initial conditions are still used very commonly (see, e.g., Refs. [92, 84, 34]).

Dissipative charge carrier migration at the 6P/ZnO interface

Efficient solar cell devices are formally characterized by high yields of extractable charge carriers [97]. These are generated to both sides of the interface and finalize the process of charge separation on the picosecond up to nanosecond timescale. Concerning organic/organic interfaces, a long series of theoretical works has helped again to unravel the underlying key mechanisms (see, e.g., Refs. [73, 97, 81, 83, 85, 98, 99, 100]). Nevertheless, details on the dissociation of charge–separated states into free charge carriers at organic/inorganic interfaces are widely unknown until today. One reason is surely the requirement of such studies for extended (and not periodic) system structures. Related large–scale simulations of electron and hole motion are extremely computationally demanding when turning to time–scales of several picoseconds and especially when including vibronic effects.

A third sub study of this work is devoted to enlighten the reason for the so far respectively low efficiency of charge carrier generation at existing ZnO photovoltaic hybrid devices [72]. Major issues shall be made out with the wish to mark the beginning of important improvements. Therefore, the second even larger 6P/ZnO interface model

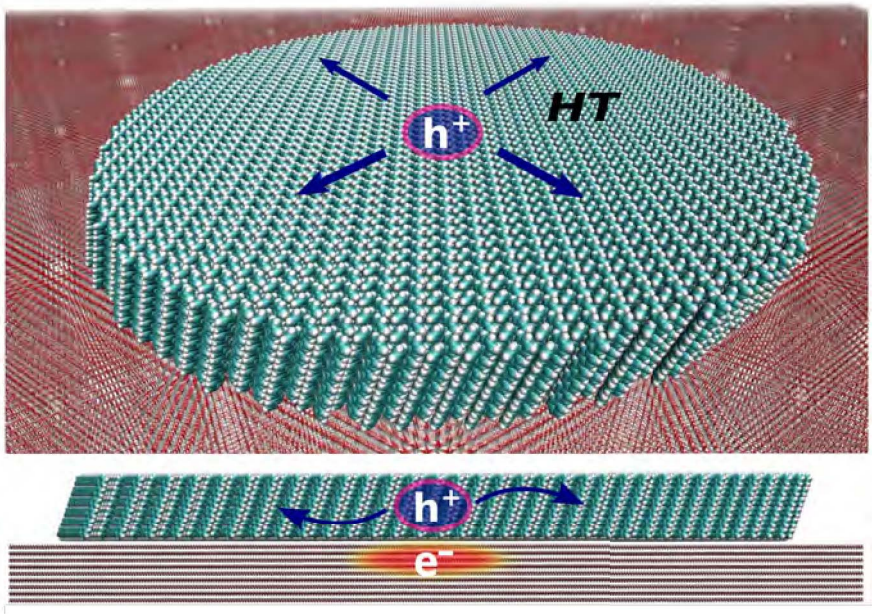

Figure 1.5.: The studied hole transfer (HT) mechanism in a realistic film of a number of 2553 *para*–sexiphenyl (6P) molecules assembled on a flat surface of a macroscopic ZnO substrate (inclined 3d and side view). The investigation concentrates on charge separation which lead to immediate immobilization of the electron at the ZnO surface region (see red shading in the side view). A possible initial electron and hole positioning is illustrated. The arrows indicate the motion of the hole within the 6P aggregate.

sketched in Fig. 1.5 is conceived. It is directly related to the realistic structure shown in Fig. 1.2c (see also Refs. [64, 65, 68]) and describes 2553 upright–standing 6Ps assembled on a macroscopic ZnO slab in a layer–like herringbone lattice. The simulated charge carrier kinetics take place on the picosecond time–scale.

It is a well–known phenomenon at ZnO surfaces (see, e.g., Ref. [94, 66, 34]), that injected electrons may move very fastly to so–called trapped surface states. Here, particular focus is on such scenarios of an electron immobilization close to the interface region right after a very fast charge separation process. For simulations on the picosecond scale, accordingly the "trapped" electron state can be directly prepared and it remains to study the much slower hole migration.

The gigantic ZnO slab describes a significant computational obstacle. Besides the direct Coulomb attraction to the trapped electron, indeed also the entire surrounding of the localized hole participate to a site–dependent potential energy correction. A single–particle ansatz of the complete ZnO slab is clearly impossible. Instead, a special hole transfer model is developed as part of this thesis. It incorporates the influence of the gigantic surrounding interface structure in terms of a polarizable continuum. This results in a very elegant expression of a screened electron–hole interaction and allows modeling such vast interface structure in a very realistic way.

In general, the motion of the hole in the 6P layer is manipulated strongly by its

Coulomb–attraction to the immobilized electron. This effect characterizes fundamentally the dissipative dynamics of the hole, i.e., its motion under the impact of vibronic interactions. The here executed simulations involve the vast number of 2553 hole states and reach up to several picoseconds. This is only made possible in application of the own developed stochastic Schrödinger equation technique. Likewise simulations at organic/inorganic interfaces on this scale have never been documented before. Here, the question about the influence of vibronic effects on the generation of free charge carriers is elaborately discussed in direct confrontation with corresponding pure–coherent hole motion. In particular, dynamics starting from different electron trapping scenarios are analyzed. By that, former observations from measurements at different polymer/ZnO interfaces [72] are supplemented with detailed theoretical findings.

Gigantic tubular dye aggregate decorated with a CdSe nanocrystal

The second type of hybrid system studied in this thesis is depicted in Fig. 1.6a. It describes a double–walled tubular dye aggregate (TDA) consisting of C8S3 cyanine molecules and a closely positioned CdSe nanocrystal (NC). Both bodies are coupled via excitonic interaction. In fact, two types of interesting exciton transfer processes were measured in likewise TDA/NC system: i) after optical excitation in the high–energy range fast exciton relaxation takes place within the TDA and ii) excitation energy is transfered from the TDA to the NC on essentially longer time–scale. Here, it is the intention to introduce an exciton model based on a realistic nuclear structure and to investigate both processes theoretically. Open system studies of pioneering extent are presented. Dissipative dynamics on the exciton relaxation from the outer to the inner wall of the TDA are provided for the first time. Further, the exciton transfer from the TDA and the NC is quantified in terms of transfer rates based on Fermi's golden rule. Thanks to a strict atomistic modeling, both sub studies deliver novel insights on the excitonic processes in remarkable spatial resolution.

In principle, the TDA represents two loosely bound rolls of J–aggregate. These form an inner and an outer wall (see Fig. 1.6a or Fig. 1.7a). Molecular J–aggregate have been lying in the focus of extensive research for more than 80 years [101, 102]. They consist of specific types of dye molecules which conglomerate to regular aggregates by means of self–assembly in aqueous solution (for details see Sec. 8.1). Once assembled, they commonly show remarkable optoelectronic features like, e.g., vast exciton delocalization, large oscillator strength and an very sharp fluorescence peak [103, 104]. Their particular type of aggregation, however, is very sensitive to chemical alternations of the side–chains of the dyes. In this sense, simple chemical modifications of the residuals opens a broad scope of possible aggregate morphologies with different excitonic properties [102]. For instance, customized sizes and morphologies like flat 2d, tube–like or other 3d structures can be manufactured rather straightforwardly [105, 106, 107, 108, 109, 110] and, going one step further, also the excitonic properties can be selectively tailored. In this way, e.g., the wave length of the aggregate fluourescence can be tuned appealing. Altogether, J–aggregates are highly interesting materials for nanotechnological device fabrication in the fields of optoelectronics [102]. In this context, it is not surprising that J–aggregates appear nowadays also in many hybrid systems. Especially phenomena of excitation energy transfer between J–aggregates and semiconductor components are a

Figure 1.6.: The tubular dye aggregate/nanocrystal (TDA/NC) system. Panel a: Exemplary TDA/NC interface achitecture with several NCs and possible excitation energy transfer processes after optical excitation. Panel b: View into the constructed double–walled TDA. The outtake offers a magnified view of a single C8S3 cyanine molecule (in the outer wall). Panel c: Crystal structure of the created CdSe NC.

hot topic. For more than 10 years, a plenty of different hybrid structures consisting of either planar films or tubular J–aggregates and semiconductor quantum dots have been investigated (see, e.g., Refs. [111, 112, 13, 8, 11, 26]) and first commercial production of photodetector devices is prognosed to commence in the near future (for details, see Sec. 8.1).

Exciton relaxation in the tubular dye aggregate

The tubular type of aggregation is maybe the most special type of all. According to their "quasi 1d" structure and being stable enough to last for very long, tubular aggregates are considered as nanoscopic "conduit cables" for directional energy transport. Indeed, remarkable transmitting properties and exciton diffusion length of more than 1 μm were already reported [113, 109]. The tubes are moreover attributed with a large oscillator strength. Altogether, this has been inspirational to create novel artificial light harvesting systems in combination with nanostructured semiconductor component. Also the here treated TDA has attracted great attention during the last two decades. In particular, an ongoing series of spectroscopic and microscopic studies [114, 115, 116, 117, 8], but also many theoretical works have been released [105, 118, 119, 120, 121, 107, 122]. Today, the excitonic processes within the TDA are widely understood (see Fig. 1.7).

So, it is generally clarified that excitons on the inner (blue coloring) and the outer wall (red coloring) can be selectively addressed via energetically different photoexcitation [119, 107, 122]. For instance, optical excitation in the high–energy region essentially populates excitons residing on the outer wall of the TDA (see process 1 in Fig. 1.7a and b). According to pump–probe measurements, the subsequent exciton relaxation process takes place within only few picoseconds (see process 2 in Fig. 1.7b). Interestingly, it is accompanied by unidirectional excitation energy transfer from the outer to the inner wall (see process 2 in Fig. 1.7a). Although many aspects have been already uncovered until date, the relaxation process is still not fully understood and describes currently an active field of research [123, 124, 26, 125]. The present work contributes greatly to these recent studies by presenting pioneering time–domain simulations.

The study begins with the 64 nm long TDA fragment illustrated in Fig. 1.6a and b. It consists of 4140 dye molecules. The gigantic nuclear structure foots on formerly executed molecular dynamics simulations and describes an extremely realistic view on the TDA. Based on it, a generalized Frenkel exciton model [122] is introduced and intermolecular excitonic couplings are determined in atomic resolution. The present ansatz distinguishes significantly from the standard Frenkel exciton model and the simple dipole–dipole interaction applied in earlier theoretical works [118, 119, 121]. The here introduced generalized exciton picture explicitly takes into consideration dispersive interaction effects. Usually, dispersion results only in a rather collective shift of the computed exciton band. Concerning the TDA, however, this is not the case [122]. In fact, dyes in the inner and the outer wall "feel" a very destinct polarizable surrounding and dispersion has a particular impact on the shape of the exciton spectrum.

The entire excitonic system of the TDA is here treated as an open system in interaction with a bath of intramolecular vibrational modes. It includes the huge number of 4140 excitons. The own stochastic Schrödinger equation technique is employed. Again, its workability and power is demonstrated impressively. Different high–energy exciton wave packets are prepared and dissipative dynamics of the relaxation process are documented. In marked contrast to the here executed studies, earlier time–domain simulations were restricted to exciton relaxation within the inner tube, i.e., the actually interesting translation of excitation energy between the walls remained undetected. Moreover, these studies rely on more simple approaches (e.g., Pauli Master equation [119]) and (though disorder attributed) analytic model system [118, 119]. The here applied description is substantially more sophisticated. For the first time, the exciton relaxation is discussed in molecular resolution. The continuous energy dissipation is documented precisely by monitoring the internal energy of the excitonic system. The computed relaxation kinetics to a thermal distribution of the exciton population are compared with available spectroscopic data [119, 124, 26, 125].

Excitation energy transfer from the tubular dye aggregate to the nanocrystal

During the last years, TDAs have been further considered as auspicious and versatile components in nanostructured hybrid materials for optoelectronics. For efficient light harvesting and subsequent directive energy funneling, for instance, designs of rope–like bundles of several TDAs contacted with quantum dots are conceivable [116, 126]. Indeed, single TDA decorated with tiny nanocrystals were already spectroscopically

Figure 1.7.: Transfer processes in the tubular dye aggregate (TDA)/nanocrystal (NC) systems. Panel a: Initial excitation of the TDA (step 1), Frenkel exciton (FX) relaxation in the TDA from the outer to the inner wall (step 2), and exciton transition from the FXs in the TDA to Wannier–Mott excitons (WXs) in the NC. Panel b: Energy level diagram of the excitonic system. Levels on the left and right hand side represent the FX band of the TDA and the WX band of the NC, respectively. Process steps 1 to 3 are indicated (orange arrows: exciton relaxation due to vibronic effects, on the ps–scale; blue arrows: subsequent exciton transfer from a thermal distribution to the NC, on the ns–scale).

studied [8]. Thereby, clear message was given on efficient excitation energy transfer from the quantum dots to the outer wall of the TDA. The efficiency of the reverse process is less high due to the fast exciton relaxation within the TDA to the inner wall (which is "more remote" to the quantum dots). In the last part of this thesis, the slower process of excitation energy transfer from the TDA to a CdSe NC is simulated (step 3 in Fig. 1.7a and b). According to the measurements, it takes place on the nanosecond time–scale. On that scale, the TDA–internal relaxation processes are already completed and a thermal distribution of Frenkel exciton population can be assumed.

The former constructed Frenkel exciton model is then merged with a model for Wannier–Mott excitons of the NC shown in Fig. 1.6c. The latter are computed as Coulomb correlated electron–hole pair excitations. As a key challenge, again thousands of excitonic coupling matrix elements between both nanostructures are computed in atomistic resolution. After the former concrete time–domain simulations on the picosecond time–scale, at this place, incoherent rates according to Fermi's golden rule describe the more adequate way to quantify the exciton transfer. Concerning the expected nanosecond time–scale, energy transfer is initialized from a thermal distribution of Frenkel exciton populations. Transfer rates for different spatial configuration of the NC with respect to the TDA are computed. Their inverse values can be confronted

with the earlier measured transfer times. Diverse interesting insights on the sensitivity of the transfer with respect to the spatial TDA/NC set–up are collected. The achieved results are important for future device fabrication.

The study is completed with a discussion on the validity of the Förster rate model of energy transfer [127]. Therefore, the simulated distance dependence is directly compared with the prominent $1/R^6$–dependence (with donor–acceptor distance R) of Förster's point–dipole approximation. Although its original purpose was in the field of energy transfer between well–separated molecules, the convenient dipole–dipole modeling is nowadays also commonly applied to tubular aggregate/NC systems [26] and many other nanoscopic composite systems [12, 128, 5, 30, 7, 129, 27]. Contrarily to the assumptions of Förster, modern systems are rather characterized by vast extended exciton delocalizations and close distances. According to that, it is highly interesting and very important to figure out whether its application is justified or results in seriously misleading impressions [130, 131].

Outline of the thesis

The organization of the thesis is summarized as follows. In Chap. 2, an overview on the utilized methodologies for computing molecules and semiconductor nanostructures is given. The specificities of large–scale hybrid systems are worked out and the different interface Hamiltonians are fundamentally discussed. The basics of open and closed quantum system dynamics are recaptured in Chap. 3. The relevant regimes of transfer phenomena are introduced. Chap. 4 is devoted to the methodology of quantum state diffusion. A general introduction of the approach is offered. Afterwards a detailed discussion on the own developed stochastic Schrödinger technique is presented. The chapter closes with explaining the strategy to simulate large–scale open system dynamics. Time–domain simulations of the excitation energy transfer and photoinduced charge separation kinetics at the *para*–sexiphenyl/ZnO model interface are discussed in Chap. 5 and 6, respectively. Afterwards in Chap. 7, the simulation works on dissipative hole migration in the film of upright–standing *para*–sexiphenyl molecules on ZnO are presented. Therefore, the stochastic Schrödinger equation approach is utilized. Its performance in application to the large–scale system is impressively demonstrated. The gigantic tubular dye aggregate with the closely positioned nanocrystal is studied in Chap. 8. Simulation results on Frenkel exciton relaxation in the aggregate are discussed. For a second time, the own stochastic Schrödinger equation technique is instrumented. Finally, the hybrid system is completed by adding the nanocrystal. Transfer rates for exciton transition from the tubular aggregate to the nanocrystal are computed. A summary and an outlook of the thesis is given in Chap. 9.

Several Appendixes supplement this work. Detailed information on the own developed interface charge transfer model, the applied generalized Frenkel exciton model as well as the conceived interface polarizable continuum model are given in the Appendixes A, B and C, respectively. Furthermore, the background on the atomic centered partial charges is enlightened in Appendix D and several mathematical proofs and computational details on the executed electronic structure calculations and time–domain simulations are provided in the Appendixes F and G, respectively.

2. Modeling of Electronic Nanosystems

This chapter introduces the theoretical background for modeling composite electronic structure systems. The particular focus lies on the development and discussion of hybrid organic/inorganic interface system. In Sec. 2.1, the description starts concerning single molecular structures. The Hamiltonian and Schrödinger equation of the molecular electronic system are formulated in Secs. 2.1.1 and 2.1.2, respectively. Sec. 2.1.3 is then devoted to the practical computation of the molecular ground state. The INDO and DFT approaches are briefly explained. Both are applied throughout this work. In Sec. 2.1.4, the CI method and the TD–DFT are introduced. Both allow computing the excited electronic structures. In particular, the first excited singlet state is of interest regarding later excitonic studies. Finally, the modeling of the cationic ($+1e$ totally charged) ground state is described in Sec. 2.1.5.

Sec. 2.2 is organized similarly but concerning semiconductor nanostructures instead. Here, only TB–based methodologies are of practical value. An empirical TB and a DFTB scheme is described in Sec. 2.2.1. Both are utilized in this work to achieve the ground state of two semiconductor structures and the related quasi–bands of single–particle states. Afterwards, Sec. 2.2.2 continues with developing electronic excited states. Semiconductor nanostructures produce a manifold energetically very dense Wannier–Mott excitons, i.e., correlated electron–hole pair excitations. In Sec. 2.2.2, anionic ($-1e$ totally charged) states are introduced, which represent the semiconductor structures under condition that an excess electron populates one of the conduction band–like states.

In Sec. 2.3 the focus is on composite systems. It starts with the general introduction of a diabatization scheme in Sec. 2.3.1. According to that, composite states are constructed based on site states following the internal substructuring. In a first application in Sec. 2.3.2, excited states of molecular aggregates are introduced following the prominent Frenkel exciton model. Afterwards in Sec. 2.3.3, a generalized exciton ansatz is developed. It delivers a simple mean to correct the Frenkel model by taking into consideration effects of intermolecular dispersion. It describes the basement of the exciton studies in Chap. 8. In Sec. 2.3.4, a combined exciton theory is developed for hybrid structures based on Frenkel excitons of a molecular aggregate and Wannier–Mott excitons of a semiconductor part. It prepares the studies on phenomena of excitation energy transfer between aggregate and semiconductor in Chaps. 5 and 8. Finally, also the case of charge separation within hybrid interface systems is concerned in Sec. 2.3.5. Hybrid states which describe an excess electron in the semiconductor and a hole localized in the aggregate are created using anionic semiconductor states and cationic aggregate states. The derived model is applied to the studies on photoinduced charge separation processes and dissipative hole motion in Chaps. 6 and 7.

2.1. Molecules

The theoretical background of the description of many–electron systems is very common for molecules and semiconductors. However, the particular treatments of both types of matter are very distinct and adequate approximations up to practical computational realizations differ strictly. This first section is dedicated to the electronic ground, the first excited and the cationic state configurations of single molecules.

2.1.1. Molecular Schrödinger equation

In molecular structures, a number of N_{nuc} pointlike nuclei are surrounded by a number of N_{el} electrons. The latter are each specified by a set of Cartesian coordinates but also by an additional spin quantum number. All particles are in Coulomb interaction with each other and the molecular Hamilton operator reads

$$\hat{H}_{\mathrm{mol}} = \hat{T}^{\mathrm{nuc}} + \hat{V}^{\text{nuc-nuc}} + \hat{T}^{\mathrm{el}} + \hat{V}^{\text{el-el}} + \hat{V}^{\text{el-nuc}}. \tag{2.1}$$

It includes the kinetic energies of the nuclei and electrons, $\hat{T}^{\mathrm{nuc}}$ and $\hat{T}^{\mathrm{el}}$, respectively. Further, the Coulomb–like repulsive potential energies between the nuclei, $\hat{V}^{\text{nuc-nuc}}$, and between the electrons, $\hat{V}^{\text{el-el}}$, as well as the corresponding attractive potential between the manifold of electrons and nuclei, $\hat{V}^{\text{el-nuc}}$.[1]

The molecular wave function can be introduced as $\Psi(r, \sigma, R)$. It depends on the collective Cartesian coordinates of the electrons, $r = (\mathbf{r}_1, \mathbf{r}_2, ..., \mathbf{r}_{N_{\mathrm{el}}})$, and likewise collective spin quantum number σ. Further, it describes the nuclei behavior and carries their collective Cartesian coordinates indicated by $R = (\mathbf{R}_1, \mathbf{R}_2, ..., \mathbf{R}_{N_{\mathrm{nuc}}})$. Its particular form then obeys the stationary Schrödinger equation

$$\hat{H}_{\mathrm{mol}} |\Psi(r, \sigma, R)\rangle = \mathscr{E} |\Psi(r, \sigma, R)\rangle. \tag{2.2}$$

Since the Hamiltonian, Eq. 2.1, does not include spin–orbit coupling terms, the total molecular wave function can be directly written as

$$\Psi(r, \sigma, R) = \psi(r, R)\zeta(\sigma), \tag{2.3}$$

a direct product of the spatial molecular wave function $\psi(r, R)$ and the electron spin function $\zeta(\sigma)$.

2.1.2. Electronic system Hamiltonian

In this thesis, the main interest is on the spatial distribution of the electronic system. The related *electronic system Hamiltonian* is defined by

$$\hat{H}_{\mathrm{el}}(R) = \hat{T}_{\mathrm{el}} + \hat{V}_{\text{el-el}} + \hat{V}_{\text{el-nuc}}(R) \tag{2.4}$$

[1] Please note that the Hamiltonian does not contain spin–orbit coupling. Heavy atoms are not considered at this place (see instead Sec. 2.2).

and the electronic wave function (spatial orbital part) obeys the electronic Schrödinger equation

$$\hat{H}_{\mathrm{el}}(R)|\phi_a(r;R)\rangle = E_a(R)|\phi_a(r;R)\rangle. \tag{2.5}$$

Its solution delivers a set of *adiabatic electronic wave functions*, $\phi_a(r;R)$, and corresponding energies, $E_a(R)$, in dependence on R. The $\phi_a(r;R)$ decribe a complete orthogonal basis set in electronic sub Hilbert space. They can be utilized to expand the spatial part of the molecular wave function, according to

$$\psi(r,R) = \sum_a \chi_a(R)\phi_a(r;R). \tag{2.6}$$

The introduced expansion coefficients, $\chi_a(R)$, carry explicit dependence on the nuclear coordinate R and are interpreted as nuclear wave functions. The $\chi_a(R)$ obey a nuclear Schrödinger equation based on a nuclear Hamiltonian which depends again on the electronic wave functions $\phi_a(r;R)$.

In general, coupling of the nuclear and electronic sub Hilbert spaces appears in terms of the *non–adiabaticity operator*. The latter formulates the influence of the nuclear motion on the electronic wave functions. However, the nuclei and electron masses are at least in ratio 1800:1. Hence, their kinetics behavior can be rendered as rather slow and inert moving nuclei in comparison with much faster moving electrons [44]. Following this line, the action of the slow nuclei on the electrons changes only *adiabatically*. As expressed in the *Born–Oppenheimer approximation*, it is then assumed that the coupling terms of the non–adiabaticity operator can be completely neglected and that the $\phi_a(r;R)$ depend only parametrically on R.

Finally, the electron and nuclei degrees of freedom are decoupled and can be expressed in terms of two individual eigenvalue problems. The *molecular adiabatic wave functions* appears now in the simple product form

$$\psi_{aM}(r;R) = \chi_{aM}(R)\phi_a(r;R). \tag{2.7}$$

Such decoupled ansatz represents the fundament of the majority of molecular electronic structure treatments. For each electronic state a, the nuclear vibrational motion can be simply treated in terms of a harmonic oscillator model (based on a corresponding normal mode analysis of the molecule realizing $\phi_a(r;R)$).

Within this work, the $\phi_a(r;R)$ of single molecules describing their ground, their first singlet and their $+1e$ cationic charged electronic configuration are of primary interest. In Sec. 2.3, such single molecular electronic structures are merged adequately and different transfer states of molecular complexes are constructed. In practice, approximate schemes are generally required to compute the states $\phi_a(r;R)$. A direct attempt to the many–electron problem is not possible. It follows a brief overview on the Hartree–Fock and the density functional theory ansatzes. In this work, both methodologies were employed to describe the molecules considered in Chaps. 5–8.

2.1.3. Molecular ground state

It is the idea of the Hartree–Fock (HF) approach to treat a system of interacting electrons stepwise starting without electron–electron interaction, i.e., the case of $\hat{V}_{\text{el-el}} = 0$. In this case, the many–electron problem (see Eq. 2.5) decouples to a number of N_{el} equivalent single–electron problems in terms of N_{el} individual Schrödinger equations, according to $\hat{H}^k(\mathbf{r}_k, \sigma_k; R)\varphi_j(\mathbf{r}_k, \sigma_k; R) = \epsilon_j \varphi_j(\mathbf{r}_k, \sigma_k; R)$ with $k \in \{1, ..., N_{\text{el}}\}$. The latter equation gives excess to the single–electron molecular spin–orbitals φ_j as well as the single–electron energies ϵ_j. Without coupling, any electronic state of the molecule would resemble a *Hartree–product* state, $\Phi(r, \sigma; R) = \prod_k^{N_{\text{el}}} \varphi_{j_k}(\mathbf{r}_k, \sigma_k; R)$. However, the latter must be antisymmetrized in order to account for the fermionic character. So, each electronic states of the molecule appears as a *Slater–determinent*, according to

$$\Phi(r, \sigma; R) = \mathscr{A}\Big[\prod_k^{N_{\text{el}}} \varphi_{j_k}(\mathbf{r}_k, \sigma_k; R)\Big], \tag{2.8}$$

instead. It is based on the permutation operator $\mathscr{A}[...] = \sum_p (-1)^p \mathscr{P}[...]/\sqrt{N_{\text{el}}!}$. The summation runs over all possible electron index permutations $\mathscr{P}$ and contains also the proper renormalization factor. In this way, the $\Phi(r, \sigma; R)$ brings with the total antisymmetric character and further cares for the single occupation condition. The electronic ground state configuration, $\Phi_0(r, \sigma; R)$, of the molecular system is obtained when the number of N_{el} spin–orbitals contributing to the Slater determinant, Eq. 2.8, are the energetically lowest with respect to ϵ_j.

In the realistic case, i.e., for $\hat{V}_{\text{el-el}} \neq 0$, the segregation of the molecular system into N_{el} equivalent single–electron problems is not possible. Instead, the HF approach uses the single Slater determinant form for an approximate ansatz (suppressing electron correlation effects). The latter leads then to the Hartree–Fock equations describing an elegant self–consistent eigenvalue problem [132]. With an adequate expansion ansatz for the spatial part of the spin–orbitals (according to $\varphi_j(\mathbf{r}) = \sum_u \sum_l \mathscr{C}_{ul}(j)\chi_{ul}(\mathbf{r} - \mathbf{R}_u)$, based on the atomic orbital basis functions $\chi_{ul}(\mathbf{r} - \mathbf{R}_u)$ with index l and placed on atom u with coordinate $\mathbf{R}_u$), the equivalent Roothaan–Hall equation is deduced for computational practice. The converged eigenstates represent the set of N_{el} occupied spin–orbitals $\varphi_{j_k}(\mathbf{r}_k, \sigma_k; R)$. Together, they describe the molecular ground state configuration, $\Phi_0(r, \sigma; R)$, in terms of Eq. 2.8.

In this work, the simplified *Intermediate Neglect of Differential Overlap (INDO)* method was employed [133]. This method follows the HF scheme, but circumvents its computational drawback of too many electron–electron interaction integrals (of type $\int d\mathbf{r} \int d\mathbf{r}' \chi^*_{ul}(\mathbf{r}-\mathbf{R}_u)\chi^*_{vk}(\mathbf{r}'-\mathbf{R}_v)|\mathbf{r}-\mathbf{r}'|^{-1}\chi_{u'l'}(\mathbf{r}-\mathbf{R}_{u'})\chi_{v'k'}(\mathbf{r}'-\mathbf{R}_{v'})$). In approximation, the INDO includes only integrals over functions placed on different atoms with $k = k'$ and $l = l'$. All remaining terms of differential overlap are usually rather small and neglected for a semi–empirical ground state structure. In this work, the INDO approach is applied to compute the ground state configuration of the *para*–sexiphenyl molecule (for details, see the Appendix G.1). The latter is then used in a CIS scheme to determine the $S_0 \rightarrow S_1$ excitation energy (see Sec. 2.2.2).

The Kohn–Sham (KS) scheme of the density functional theory (DFT) describes a

Figure 2.1.: Chemical structures, relevant energy levels and illustrations of the HOMOs and LUMOs of the two molecules treated in this thesis. Panel a: the *para*–sexiphenyl molecule (6P). Panel b: the 5,5',6,6'–tetrachlorobenzimidacarbo–cyanine dye molecule (C8S3). H atoms: white, C atoms: cyan, N atoms: blue, S atoms: yellow, O atoms: red, Cl atoms: green. The visualized orbitals and energies are each taken from DFT ground state optimization (see Appendixes G.1 and G.2).

much less computationally bothersome approach than the above HF methods. The main difference lies in the electronic density perspective. In fact, all information about the ground state of an aspired system are provided by its ground state electronic density, $n_0(\mathbf{r})$ [134]. The many–electron problem appears not with $3N_{\mathrm{el}}$, but only in dependence on three Cartesian degrees of freedom. In order to find the $n_0(\mathbf{r})$ in practice, the KS scheme prepares the ground state density based on orbital–like functions, according to $n_0(\mathbf{r}) = \sum_{\lambda}^{N_{\mathrm{el}}} |\varphi_{\lambda}^{\mathrm{KS}}(\mathbf{r})|^2$. The latter KS orbitals, $\varphi_{\lambda}^{\mathrm{KS}}(\mathbf{r})$, obey the (one–electron Schrödinger–like) KS equation. In the KS equation the role of the Hamiltonian is played by the KS operator. The KS operator itself is fully determined by the electronic density and the $\varphi_{\lambda}^{\mathrm{KS}}(\mathbf{r})$ are obtained again self–consistently. Although the DFT, in principle, is able to describe the exact ground state density, the exchange–correlation functional (as part of the KS operator) is generally unknown until today and approximate models or semi–empirical expressions must be introduced instead. Nevertheless, once a form of the functional is defined, the KS operator acts equivalently on all $\varphi_{\lambda}^{\mathrm{KS}}(\mathbf{r})$, which means another essential computational benefit with respect to the HF.

Meanwhile there exist a broad spectrum of specific hybrid exchange–correlation functionals established for the application on the typical species and families of organic molecules. Based on these, the DFT provides accurate results concerning several quantities and molecular properties. In this work, it is applied to the *para*–sexiphenyl and cyanine molecule (see Appendixes G.1 and G.2). The obtained highest occupied and lowest unoccupied molecular orbitels (HOMOs and LUMOs) and their energies are visualized in Fig. 2.1. In particular, the optimized nuclear configuration of both molecules was obtained from DFT (see also Fig. 2.1) as well as the related electronic ground

state charge densities. Furthermore, the hole transfer integral between pairs of *para*–sexiphenyl molecules (needed in Chaps. 6 and 7) were computed more appropriately based on DFT instead of HF.

2.1.4. Molecular first excited state

The configuration interaction (CI) method [132] and the time–dependent density functional theory (TDDFT) [134] were stressed in order to determine the electronic structures of the excited molecules treated in this work. The CI improves the HF method by making a many–Slater determinent ansatz. It is based on the initially found HF ground state, $|\Phi_0\rangle$, and introduces further Slater determinants designed by lifting up different numbers of electrons from occupied to unoccupied orbitals. The superposition of them (together with the $|\Phi_0\rangle$) constitutes an advanced correlation consistent ansatz and provides excess to the manifold of excited state wave functions. The proper superpositioning (i.e., the weight of each determinants) is found in form of a secondary self–consistent solution of a HF–like equation [132]. Regarding the different replacement combinations, a huge number of different Slater determinants must be taken into account. Accordingly, the post–Hartree–Fock processes are of enormous computational demand and must be simplified in practice. The alternative TDDFT describes excited state properties in the picture of the KS ansatz. It relies on the idea to interprete an excited state electronic density as a state configuration in the presence of a (time–dependent) external potential. In this sense, the TDDFT directly simulates an excitation process of the electronic structure. The excitation energies and related excited state densities can be determined (in very simplified terms) by scanning the energy of the external field after poles of the linear susceptibility of the electronic density [134].

In comparison to the CI scheme, the TDDFT methodology is less demanding and maintains the computational benefits of the KS approach. The TDDFT is well–known for accurate electronic densities and excited state geometries. In this work, it provided electronic densities of the first excited (singlet S_1) state of the *para*–sexiphenyl and the C8S3 cyanine molecule as well as their $S_0 \rightarrow S_1$ transition densities (see Eq. 2.30). The latter were needed for computating excitonic coupling matrix elements later on in Chaps. 5, 6 and 8. Contrarily, the TDDFT may suffer from accuracy of the corresponding excitation energy and a CI approach can be more adequately. This is the case, e.g., concerning the *para*–sexiphenyl (see, e.g., Ref. [135]). For the latter, the excitation energy was obtained instead using the *CI–Singles* (CIS) solution ansatz (which takes into account singly excited determinants) based on the INDO semi–empirical HF approach (for details, see again Appendixes G.1 and G.2).

2.1.5. Molecular cationic ground state

The *para*–sexiphenyl aggregates, part of the investigations in Chaps. 6 and 7, are further subject to hole transfer processes. The presence of a hole means the removal of an electron. Correspondingly, the energy and electronic density of the *para*–sexiphenyl molecule in absence of an electron is required. Its electronic configuration then realizes the cationic ground state. The electronic properties of the molecular hole states can

be obtained by utilizing again the above ground state DFT scheme, but now with a number of $N_{\mathrm{el}} - 1$ electrons (see also Appendix G.1).

2.2. Semiconductor Nanocrystals

Besides molecules, nanoscopic semiconductor structures or nanocrystals (NC) are part of the hybrid systems investigated in this work. As finite structures, NCs cannot be modeled by introducing system periodicity. Therefore, a proper description must contain a hugh number of electrons. This essentially complicates electronic structure computations. On the one hand, established (molecular) all–electron theories (e.g., given in Sec. 2.1) cannot be applied to NCs. They become inappropriate concerning their computational effort. On the other hand, the finite size of NCs prevents introduction of band models from solid state physics, which would be only adequate for an idealized periodic bulk structure.

In this work, a ZnO cluster (as part of Chaps. 5 and 6) and a CdSe NC (as part of Chap. 8) are introduced. They are treated based on different types of tight–binding (TB) methodologies (see details below). In fact, only TB approaches can formulate a theoretical fundament of practical use concerning the present system sizes. In general, they are computationally cheap, operate based on a single electron picture and provide the electronic ground state structure in atomic resolution (see Sec. 2.2.1). Besides the electronic ground states of the ZnO cluster and the CdSe NC, adequate and practicable exciton theories are developed in Sec. 2.2.2. Singly charged semiconductor states are introduced as well (see Sec. 2.2.3).

2.2.1. Ground state

The self–consistent field treatments of the HF or KS ansatz are not of much use here. Instead, it is the idea to suppress the self–consistent character and to maintain only one essential diagonalization step. For this end, in a first step a corresponding TB Hamiltonian, $H_{ul\sigma,u'l'\sigma'}$, is constructed (with possible spin–orbit coupling). A minimum atomic orbital basis set, $\{\chi_{ul}\}$ (with atomic index u and orbital index l), and spin functions, ζ_σ (with spin index $\sigma \in \{+,-\}$), shall be introduced for its expansion. Such minimum basis set is motivated by the observation that the interesting electronic properties of semiconductors typically arise from the valence shell of the atoms. Moreover, the approach simplifies taking advantage of the regular nuclear structure. It justifies to restrict $H_{ul\sigma,u'l'\sigma'}$ uniformly to atomic nearest neighbor interactions. Then, the (spin–dependent) TB problem is written in matrix form as

$$\sum_{u',l',\sigma'} \Big[H_{ul\sigma,u'l'\sigma'} - \delta_{\sigma\sigma'} S_{ul,u'l'} - \delta_{ul\sigma,u'l'\sigma'} E_\lambda \Big] \mathscr{C}_{u'l'\sigma'}(\lambda) = 0, \tag{2.9}$$

with the overlap matrix of atomic orbitals $S_{ul,u'l'}$. As a simple eigenvalue problem, it is numerically cheap and can be straightforwardly implemented. Its solution delivers TB single–particle energies, E_λ, and related TB single–particle states, ψ_λ (in atomic orbital representation). Here and throughout this work, the index λ appears as a collective index for spatial and spin degrees of freedom. The ψ_λ are given by the coefficient

matrix $\mathscr{C}_{ul\sigma}(\lambda)$ (i.e., it is $\psi_\lambda = \sum_\sigma \sum_u \sum_l \mathscr{C}_{ul\sigma}(\lambda)\chi_{ul}\zeta_\sigma$). By energetic ordering, the $\{\psi_\lambda\}$ define a number of N_{VB} valence band (VB)–like (occupied) states ψ_λ (with energy E_λ and $\lambda \leq N_{\mathrm{VB}}$). These construct the total electronic ground state, written as

$$|\Psi_0\rangle = \prod_{\lambda=1}^{N_{\mathrm{VB}}} \hat{e}_\lambda^\dagger |\mathrm{vac}\rangle. \tag{2.10}$$

It is based on the second quantization operator $\hat{e}_\lambda^\dagger$ which creates an electron in the VB–like state ψ_λ. The remaining higher energetic, unoccupied states are collected in a number of N_{CB} conduction band (CB)–like states. For clarity, the latter are reintroduced as $\bar{\psi}_{\bar{\lambda}}$ (with energies $\bar{E}_{\bar{\lambda}}$ and $\bar{\lambda} \leq N_{\mathrm{CB}}$).

The key of the efficiency of TB approaches is clearly that by far the most elements of $H_{ul\sigma,u'l'\sigma'}$ are zero and moreover the most non–zero coupling elements are identical. Accordingly, it is the idea of the original (or empirical) TB scheme to treat the few remaining non–zero values of $H_{ul\sigma,u'l'\sigma'}$ and $S_{ul,u'l'}$ as universal parameters. These were once determined by fitting routines with the intention to directly reproduce certain experimental quantities (e.g., the electronic band structure). Meanwhile, diverse sets of fit values can be found in tabulated form for all typical semiconductors (including ZnO and CdSe). This allows computing band structures for, in principle, all kind of crystal types and shapes. In the framework of this thesis, the empirical TB ansatz are applied as an essential part of Chap. 8 (see Appendix G.4). By its mean, the electronic single–particle states of the CdSe NC are obtained which are then required for the formulation of the excitonic states (see Sec. 2.2.2). The density functional based TB (DFTB) technique was developed as a more sophisticated TB version [136]. It is applied to the ZnO cluster as a part of Chaps. 5 and 6 (see Appendix G.3). In general, it is the critical feature of wurtzite ZnO clusters that the Zn and O atoms realize especially high ionic character [137]. This typically leads to surface polarization effects and lattice distortion which essentially characterizes the band gap of the clusters (see, e.g., Refs. [94, 69, 66]). The standard TB suffers from that and turned out to be insufficient for the present ZnO cluster. Beyond the empirical TB, it is the intention of the DFTB to particularly account for such effects. In particular, in the DFTB approach the ground state density is modeled as a sum of a reference density and a small fluctuation. Terms related to the reference density are again tabulated, while the density fluctuation describes small corrections which have to be solved in a self–consistent way in the sense of the DFT (see Sec. 2.1.3).

2.2.2. Manifold of excited states

Contrarily to molecules, semiconductor nanostructures are generally known to offer a quasi–band of energetically very dense excited states over a broad energy range. Concerning the ZnO cluster (studied in Chap. 5) and the CdSe NC (see Chap. 8), a huge amount of excited states are equivalently relevant. All of them describe possible acceptor states for excitation energy transfer from the opponent molecular aggregates.

The following model describes excited semiconductor state based on a formerly determined TB ground state (see Sec. 2.2.2). As discussed, the latter renders a number

of N^{VB} occupied VB–like spin states, ψ_λ, and N^{CB} unoccupied states, $\bar{\psi}_{\bar{\lambda}}$. As the starting point, single *electron–hole pair states* are constructed as

$$|\Psi_\lambda^{\bar{\lambda}}\rangle = \hat{e}_{\bar{\lambda}}^\dagger \hat{h}_\lambda^\dagger |\Psi_0\rangle, \tag{2.11}$$

by moving a single electron from the VB–like state ψ_λ into the CB–like state $\bar{\psi}_{\bar{\lambda}}$. This creates a hole by means of $\hat{h}_\lambda^\dagger$ with the energy $\epsilon_\lambda = -E_\lambda$ and an electron by means of $\hat{e}_{\bar{\lambda}}^\dagger$ with energy $\bar{\epsilon}_{\bar{\lambda}} = \bar{E}_{\bar{\lambda}}$. For clarity, the indexes λ (in ψ_λ and ϵ_λ) and $\bar{\lambda}$ (in $\bar{\psi}_{\bar{\lambda}}$ and $\bar{\epsilon}_{\bar{\lambda}}$) are substituted occasionally by h or e to identify either the reference to hole or to electron states, respectively. This treatment clearly reminds to the CIS approach mentioned in Sec. 2.1.4 (though without the ab–initio background of the HF theory). The hole state ψ_h and the electron state $\bar{\psi}_e$ appear as a pair with respect to the ground state configuration $|\Psi_0\rangle$. Once created, both particles are aware of each other. Due to this common Coulomb–like interaction, the electron–hole pair states, $|\Psi_h^e\rangle$, can only serve as an expansion ansatz for the actual exciton states. The latter *Wannier–Mott excitons* (WXs) are introduced as $|\Psi_\gamma\rangle$ and constructed as superpositions of all $|\Psi_h^e\rangle$, i.e., it is

$$|\Psi_\gamma\rangle = \sum_{e,h} \mathfrak{C}_{eh}(\gamma) |\Psi_h^e\rangle. \tag{2.12}$$

The corresponding expansion coefficients $\mathfrak{C}_{eh}(\gamma)$ obey the WX equation, according to

$$(\bar{\epsilon}_e + \epsilon_h)\mathfrak{C}_{eh}(\gamma) + \sum_{e',h'} \Big[W_{eh,e'h'} - K_{eh,e'h'} \Big] \mathfrak{C}_{e'h'}(\gamma) = \mathfrak{E}_\gamma \mathfrak{C}_{eh}(\gamma). \tag{2.13}$$

The right hand side of the latter eigenvalue problem holds the number of $N^{\mathrm{VB}} \times N^{\mathrm{CB}}$ excitation energies $\mathfrak{E}_\gamma$. The terms on the left hand side of Eq. 2.13 render the energies and interactions in the "effective" electron–hole pair picture. The first term describes a diagonal energy shift (single–particle energies). It accounts for the seperate generation of the electron in $\bar{\psi}_e$ (energy: $\bar{\epsilon}_e$) and the hole in ψ_h (energy: ϵ_h). Both single–particle contributions, $\bar{\epsilon}_e$ and ϵ_h, must be completed by the mutual interaction between the electron and hole. This is represented by the second term in Eq. 2.13. The interaction is not limited to (diagonal) energy corrections, but also forms scattering and exchange terms which result in electron and hole transitions. Thereby, the Coulomb matrix, $W_{eh,e'h'}$, describes the direct interaction between the electron and hole. It follows as

$$W_{eh,e'h'} = e^2 \sum_{s,\bar{s}} \int d^3\mathbf{x} \int d^3\mathbf{y} \frac{\bar{\psi}_e^*(\mathbf{x},\bar{s})\bar{\psi}_{e'}(\mathbf{x},\bar{s})\psi_h(\mathbf{y},s)\psi_{h'}^*(\mathbf{y},s)}{|\mathbf{x}-\mathbf{y}|} \tag{2.14}$$

and mediates processes where an electron is scattered at a hole (and vice versa; under consideration of their spin). The additional appearance of exchange terms among the electron and hole in Eq. 2.13 becomes reasonable concerning the hole again in terms of an effective constellation of the $N_{\mathrm{el}} - 1$ electrons. The corresponding exchange matrix,

$K_{eh,e'h'}$, takes the form

$$K_{eh,e'h'} = e^2 \sum_{s,\bar{s}} \int d^3\mathbf{x} \int d^3\mathbf{y} \frac{\bar{\psi}_e^*(\mathbf{x},\bar{s})\psi_h(\mathbf{x},\bar{s})\bar{\psi}_{e'}(\mathbf{y},s)\psi_{h'}^*(\mathbf{y},s)}{|\mathbf{x}-\mathbf{y}|} \tag{2.15}$$

It determines processes where the electron–hole pair, Ψ_h^e, is annihilated and afterwards the electron–hole pair, $|\Psi_{h'}^{e'}\rangle$, is created.

An enormous number (including energetically high) excitons are relevant for the ZnO cluster modeled in Chap. 5. In view of that, a corresponding solution of the WX equation 2.13 was clearly beyond the scope of the present work. Instead, excited cluster states had to be approximately treated in terms of uncorrelated electron–hole states, $|\Psi_e^h\rangle$. Contrarily, much fewer (energetically low–lying) excitations are required for the CdSe NC in Chap. 8. These were computed by directly solving the WX equation 2.13.

2.2.3. Manifold of anionic states

In course of the study on photoinduced charge separation kinetics discussed in Chap. 6, the ZnO cluster further acts as an electron acceptor. Thereby, a single excess electron tunnels from a closely positioned molecular excitation into the manifold of available CB–like states of the cluster, $\bar{\psi}_{\bar{\lambda}}$. In view of the large number of electrons (concretely: $N_{\mathrm{el}} = 13750$, see Appendix G.3) a single electron injection hardly influences the neutral ground state structure. (Please note that this stands in contrast with the above molecular picture, where the removal or adding of electrons essentially influences the electronic ground state properties, cf. Sec. 2.1.5.) Following this *frozen orbital approximation*, the possible anionic charged ZnO cluster states can be expressed according to

$$|\Psi_{\bar{\lambda}}^-\rangle = \hat{e}_{\bar{\lambda}}^\dagger |\Psi_0\rangle. \tag{2.16}$$

By action of the creator $\hat{e}_{\bar{\lambda}}^\dagger$, the electronic TB ground state configuration $|\Psi_0\rangle$ (see Eq. 2.10) is augmented with another electron in one of the available CB states, $\bar{\psi}_{\bar{\lambda}}$.

2.3. Composite Systems

Aspects of modeling single molecules and isolated semiconductor nanocrystals were discussed in Secs. 2.1 and 2.2, respectively. In the remaining of this chapter, electronic states of molecular aggregates and *hybrid systems* (i.e., supermolecular complexes combined with semiconductor structures) are developed. After some general aspects described in Sec. 2.3.1, particular attention is paid to model the transfer states which are relevant in Chaps. 5–8. It begins with introducing the Frenkel exciton model for molecular aggregates in Secs. 2.3.2. An ansatz for a generalized formulation of the latter is provided in Sec. 2.3.3. In Sec. 2.3.4, the Frenkel exciton picture and the Wannier–Mott exciton model are merged for a combined aggregate/semiconductor exciton description. Likewise charge–separated states for hybrid systems are addressed in the framework of Sec. 2.3.5.

2.3.1. General concept of segmented electronic structures

Regarding composite systems, practical realizations of uniform electronic structure calculations are soon stretched to their limits. With increasing system size, it is more appropriate to develop electronic structure models which directly take advantage of the spatial segmentation of a composite system. Correspondingly, the electronic Hamiltonian of such system with a number of N_{sub} smaller segments (or substructures) can be expressed as

$$\hat{H}_{\mathrm{el}} = \sum_{s}^{N_{\mathrm{sub}}} \hat{H}_s + \sum_{s \neq s'}^{N_{\mathrm{sub}}} \hat{V}_{s,s'}, \tag{2.17}$$

in terms of a sum of N_{sub} sub Hamiltonians, $\hat{H}_s$. Each $\hat{H}_s$ is only related to the isolated substructure of segment s. The remaining interaction terms due to the mutual interaction between the latter are collected in the second sum in Eq. 2.17. Here, $\hat{V}_{s,s'}$ accounts for the electron–electron and electron–nucleus interaction between segment s and s'. Apparently, the interactions of electrons (and nuclei) between two spatial segments are generally much weaker than the interactions of electrons (and nuclei) on the same segment. This inspires the form of Eq. 2.17. The spatial separation further motivates the assumption that only negligible wave function overlap and correlation effects exist between the segments. Then, any electronic state $|\bar{\Phi}\rangle$ of the composite system is conveniently introduced as a simple Hartree product,[2]

$$|\bar{\Phi}\rangle = |\Phi^{(1)}\rangle \otimes |\Phi^{(2)}\rangle \otimes \cdots \otimes |\Phi^{(N_{\mathrm{seg}})}\rangle, \tag{2.18}$$

constructed based on the N_{sub} segment states $|\Phi^{(s)}(r_s)\rangle$. Each state $|\Phi^{(s)}(r_s)\rangle$ describes a separate electronic structure in relation to $\hat{H}_s$ with energy $E_s = \langle\Phi^{(s)}|\hat{H}_s|\Phi^{(s)}\rangle$. This *diabatization ansatz* provides the most convenient instrument for constructing different types of composite states. The $|\bar{\Phi}\rangle$ are furtheron denoted as *diabatic* or *localized states* of the composite. In the subsequent section, different basis sets of $|\bar{\Phi}\rangle$ are constructed in order to expand the electronic Hilbert space of the composite system.

On the one hand, when representing $\hat{H}_{\mathrm{el}}$ in a diabatic state basis, vast numbers of interaction terms $\hat{V}_{s,s'}$ must be computed. These are respondible for i) energy correction terms with respect to $\sum_s E_s$ (diagonal matrix elements), and ii) additional transfer coupling terms between the substructures (off–diagonal elements). On the other hand, the diabatization scheme enables to scale down the computational costs and to choose appealing electronic structure methods for each individual substructure. This is fully exploited in this work concerning the hybrid structures. Subsystem states related to molecules require for HF or DFT methods while the semiconductor components can only be computed based on the TB level.

[2] For convenience, the "bar" indication on the capital Greek letter is introduced here to flag a composite state. After this section, this indication form is exclusively applied in order to generally indicate molecular aggregate states.

2.3.2. Frenkel exciton model for molecular aggregates

This section is devoted to the standard *Frenkel exciton model* for supermolecular composite systems. It provides the basic and most popular tool for describing excited states and excitation energy transfer kinetics in molecular aggregates. In this work, it is directly applied to the molecular part of the *para*–sexiphenyl aggregate/ZnO system (see Chaps. 5 and 6). Further, it builds the fundament of the generalized exciton model developed in Sec. 2.3.3, which is utilized in Chap. 8 to describe exciton relaxation and transfer phenomena in the tubular dye aggregate/CdSe nanocrystal system.

In the following, a molecular aggregate is considered consisting of a number of N_{mol} individual molecules. With regard to the studies in Chaps. 5, 6 and 8, it is assumed that all molecules are of identical chemical structure. Furthermore, it is directly taken advantage of the fact that essentially the ground (S_0) and first excited singlet (S_1) state of each molecule is of interest. This restriction is very typical for basic treatments on energy transfer between molecules with an extended π–conjugated system after optical excitation [44]. The electronic system Hamiltonian of the molecular aggregate follows as, cf. Eq. 2.17,

$$\hat{H}_{\mathrm{agg}} = \sum_{m}^{N_{\mathrm{mol}}} \hat{H}_{\mathrm{mol}}^{(m)} + \sum_{m,n}^{N_{\mathrm{mol}}} \hat{V}_{\mathrm{mol\text{–}mol}}^{(m,n)}. \tag{2.19}$$

It consists of the individual electronic Hamiltonians of each molecule, $\hat{H}_{\mathrm{mol}}^{(m)}$ with $m \in \{1, ..., N_{\mathrm{mol}}\}$, and the corresponding intermolecular electrostatic Coulomb interactions, $\hat{V}_{\mathrm{mol\text{–}mol}}^{(m,n)}$ with $m \neq n$.[3]

Further, the excited aggregate states relevant for the Frenkel exciton model are straightly constructed. According to the diabatization ansatz (see Eq. 2.18), states of localized excitation follow as

$$|\bar{\Phi}_m^e\rangle = |\Phi_e^{(m)}\rangle \prod_{n\neq m}^{N_{\mathrm{mol}}} |\Phi_g^{(n)}\rangle, \tag{2.20}$$

with $m \in \{1, ..., N_{\mathrm{mol}}\}$. The diabatic state $|\bar{\Phi}_m^e\rangle$ is based on the S_1 first excited state of the mth molecule, $|\Phi_e^{(m)}\rangle$, and the respective molecular ground states, $|\Phi_g^{(n)}\rangle$, of the other molecules. So, each $|\bar{\Phi}_m^e\rangle$ represents the aggregate with a different molecule in the electronic first singlet excited state. Together, all $|\bar{\Phi}_m^e\rangle$ represent a complete basis set and expand the relevant Hilbert subspace of the excited aggregate. The related completeness relation expresses as

$$\hat{\mathbf{1}}_{\mathrm{el}} = \sum_{m}^{N_{\mathrm{mol}}} |\bar{\Phi}_m^e\rangle\langle\bar{\Phi}_m^e|. \tag{2.21}$$

The restricted expansion ansatz with only single excited states in Eq. 2.21 is typical and implicates that any contributions of multiple excitations are negligible. This is reasonable here and applies in the most cases on condition that the aggregate is subject

[3] Throughout this work, the indices m and n serve exclusively for indicating molecules.

to weak optical excitation.

Frenkel Hamiltonian

Making use of the latter completeness relation, the general form of $\hat{H}_{\mathrm{agg}}$ specifies to the famous *Frenkel exciton Hamiltonian* [44],

$$\hat{H}_{\mathrm{FX}} = \sum_{m}^{N_{\mathrm{mol}}} \mathscr{H}_m |\bar{\Phi}_m^e\rangle\langle\bar{\Phi}_m^e| + \Big(\sum_{m<n}^{N_{\mathrm{mol}}} \mathscr{J}_{mn} |\bar{\Phi}_m^e\rangle\langle\bar{\Phi}_n^e| + \mathrm{H.c.}\Big). \tag{2.22}$$

The first term (diagonal matrix element) holds the total energies of the different aggregate excited states, $\mathscr{H}_m = \langle\bar{\Phi}_m^e|\hat{H}_{\mathrm{agg}}|\bar{\Phi}_m^e\rangle$. In general, the $\mathscr{H}_m$ collects the energy of the mth isolated molecule in the excited state, the $N_{\mathrm{mol}}-1$ energies of other molecules (isolated ground state energies) and the electrostatic Coulomb interaction contributions between all molecules. (For convenience, the $\mathscr{H}_m$ are collectively refered to the aggregate ground state energy level, cf. Eqs. 2.24 and 2.28.) The remaining terms (offdiagonal matrix elements) in Eq. 2.22 are introduced according to $\mathscr{J}_{mn} = \langle\bar{\Phi}_m^e|\hat{H}_{\mathrm{agg}}|\bar{\Phi}_n^e\rangle$. They constitute the *excitonic coupling* between the states $|\bar{\Phi}_n^e\rangle$ and $|\bar{\Phi}_m^e\rangle$. In view of the transfer model, these terms are responsible for the translation of excitation energy from molecule n to molecule m. The actual excitation or de–excitation process of the aggregate is traditionally not contained in $\hat{H}_{\mathrm{FX}}$. Their possible inclusion is demonstrated at the end of this section after a detailed view on the above matrix elements $\mathscr{H}_m$ and $\mathscr{J}_{mn}$.

Intermolecular electrostatic interaction

All excited states, $|\bar{\Phi}_m^e\rangle$, "share" a common ground state $|\bar{\Phi}_0\rangle$. It is straightly introduced as

$$|\bar{\Phi}_0\rangle = \prod_{m}^{N_{\mathrm{mol}}} |\Phi_g^{(m)}\rangle. \tag{2.23}$$

Its energy $\mathscr{H}_0$ decomposes accoring to

$$\mathscr{H}_0 = E_0 + \frac{1}{2} \sum_{m,n\neq m}^{N_{\mathrm{mol}}} V_{\text{el-el}}^{(m,n)}(g,g) + \sum_{m,n\neq m}^{N_{\mathrm{mol}}} V_{\text{el-nuc}}^{(m,n)}(g), \tag{2.24}$$

where the intramolecular part E_0 is the sum over all single molecule S_0 ground state energies (i.e., $E_0 = N_{\mathrm{mol}} \times E_g$, since all molecules are identical). The second and third term collects all intermolecular energy corrections due to Coulomb coupling of type electron–electron[4] and electron–nucleus, respectively. The $\mathscr{H}_0$ takes here the role of a convenient reference level of the energies $\mathscr{H}_m$. The general form of the electron–electron Coulomb interaction between molecule m and n (realizing electronic state a

[4]The factor of $\frac{1}{2}$ cares for the inherent double counting in the case of electron–electron interaction. Please note therefore that it is $V_{\text{el-el}}^{(m,n)}(g,g) = V_{\text{el-el}}^{(n,m)}(g,g)$ but $V_{\text{el-nuc}}^{(m,n)}(g) \neq V_{\text{el-nuc}}^{(n,m)}(g)$

and b, respectively), follows as

$$V_{\text{el-el}}^{(m,n)}(a,b) = \int d^3\mathbf{x} \int d^3\mathbf{y} \frac{n_a^{(m)}(\mathbf{x}) n_b^{(n)}(\mathbf{y})}{|\mathbf{x}-\mathbf{y}|}. \tag{2.25}$$

The expression makes use of the *single–particle charge densities*,

$$n_a^{(m)}(\mathbf{r}) = -eN_{\text{el}}^{(m)} \int d\{r^{(m)}\} \delta(\mathbf{r}-\mathbf{r}_1^{(m)}) |\Phi_a^{(m)}(r^{(m)})|^2. \tag{2.26}$$

The $n_a^{(m)}(\mathbf{r})$ represents the many–electron charge density of the mth molecule (with a number of $N_{\text{el}}^{(m)}$ electrons) in state $|\Phi_a^{(m)}\rangle$ (with $a \in \{g,e\}$) at position $\mathbf{r}$. Similarly, a general expression of the electron–nucleus Coulomb interaction is found with

$$V_{\text{el-nuc}}^{(m,n)}(a) = +e \sum_{\mu}^{(n)} \int d^3\mathbf{r} \frac{n_a^{(m)}(\mathbf{r}) Z_\mu^{(n)}}{|\mathbf{r}-\mathbf{R}_\mu^{(n)}|}, \tag{2.27}$$

which is again based on the density $n_a^{(m)}(\mathbf{r})$. However, it interacts now with the nuclear structure of the nth molecule. The latter is represented by the set of discrete charges $\{Z_\mu^{(n)}\}$ (with atomic index μ and placed at nuclear coordinate $\mathbf{R}_\mu^{(n)}$). In Eq. 2.24, all molecules are in electronic S_0 ground state configuration, i.e., it is $a = g$ and $b = g$, respectively.

The matrix elements of the aggregate excited states, $\mathscr{H}_m$, are now introduced in reference to the $\mathscr{H}_0$ in Eq. 2.24. In this way, they appear directly as excitation energies,

$$\mathscr{H}_m = E_{eg} + \sum_{n}^{N_{\text{mol}}} \Big(V_{\text{el-el}}^{(m,n)}(e,g) - V_{\text{el-el}}^{(m,n)}(g,g) + V_{\text{el-nuc}}^{(m,n)}(e) - V_{\text{el-nuc}}^{(m,n)}(g) \Big). \tag{2.28}$$

The intramolecular excitation energy, $E_{eg} = E_e - E_g$, occurs again without molecular index (here with E_e, the energy of the electronic S_1 state). Further, the included intermolecular Coulomb interactions are given in reference to the gound state interaction energy. Thereby, the two interaction terms of positive sign, $V_{\text{el-el}}^{(m,n)}(e,g)$ and $V_{\text{el-nuc}}^{(m,n)}(e)$, carry the single–particle charge density $n_e^{(m)}(\mathbf{r})$, which is now related to the mth molecule in state $|\Phi_e^{(m)}\rangle$ (see Eq. 2.26, with index $a = e$).

Intermolecular excitonic coupling

The excitonic coupling $\mathscr{J}_{mn}$ (offdiagonal matrix element in Eq. 2.22) is a phenomenon of electron–electron interaction. The electron–nucleus Coulomb coupling cannot translate two aggregate excited states $|\bar{\Phi}_e^m\rangle$ and $|\bar{\Phi}_e^n\rangle$ (i.e., it does not mediate intermolecular excitation energy transfer). Similar to Eq. 2.25, the $\mathscr{J}_{mn}$ follows as

$$\mathscr{J}_{mn} = \int d^3\mathbf{x} \int d^3\mathbf{y} \frac{n_{eg}^{(m)}(\mathbf{x}) n_{ge}^{(n)}(\mathbf{y})}{|\mathbf{x}-\mathbf{y}|}. \tag{2.29}$$

However, here the two molecular *single–particle transition densities*, $n_{eg}^{(m)}(\mathbf{r})$ and $n_{ge}^{(m)}(\mathbf{r})$, are generally introduced according to

$$n_{ba}^{(m)}(\mathbf{r}) = eN_{\mathrm{el}}^{(m)} \int dr^{(m)} \delta(\mathbf{r} - \mathbf{r}_1^{(s)}) [\Phi_b^{(m)}(r^{(m)})]^* \Phi_a^{(m)}(r^{(m)}). \tag{2.30}$$

Instead of refering to the electronic charge density (see Eq. 2.26), $n_{ba}^{(m)}(\mathbf{r})$ now refers to the electronic transition density from state $|\Phi_a^{(m)}\rangle$ to state $|\Phi_b^{(m)}\rangle$ (of molecule m). It describes the change of the electronic structure by means of the transition $b \leftarrow a$ at the position $\mathbf{r}$. In this sense, $\mathcal{J}_{mn}$ facilitates the simultaneous excitation ($e \leftarrow g$) of the mth molecule (i.e., transition from its S_0 ground to the S_1 first excited state) and de–excitation ($g \leftarrow e$) of the nth molecule (i.e., transition from its S_1 excited to S_0 ground state).

Frenkel exciton states

Each possible excited system state can be described as a superposition of the diabatic states in Eq. 2.20 (see basis set in Eq. 2.21). In particular, the eigenstates of $\hat{H}_{\mathrm{FX}}$, known as *Frenkel excitons*, can be expressed as

$$|\bar{\Phi}_\alpha\rangle = \sum_m \mathscr{C}_m(\alpha) |\bar{\Phi}_m^e\rangle. \tag{2.31}$$

They describe delocalized excitations in the sense of a superposition state. Concerning each "molecular share", however, the excitation remains localized. This stands in contrast to the delocalized WX excitons, which are introduced for semiconductor structures and designed as a superposition of generally delocalized electron–hole pair excitations in Sec. 2.2.2 (see Eq. 2.12). The proper expansion coefficients $\mathscr{C}_m(\alpha)$ are found by solving the stationary Schrödinger equation (eigenvalue problem),

$$\hat{H}_{\mathrm{FX}} |\bar{\Phi}_\alpha\rangle = \mathscr{E}_\alpha |\bar{\Phi}_\alpha\rangle. \tag{2.32}$$

Besides the exciton states, Eq. 2.32 provides excess to the manifold of eigenenergies of the aggregate, $\mathscr{E}_\alpha$.

The diabatic state representation is very instructive regarding the spatial (or molecular) localization of the excitation. However, many types of kinetics are more conveniently studied from the energetic point of view. In particular, this is the case concerning the studies on the optical excitation processes in Secs. 6.4 and 6.5, the exciton relaxation process reported in Sec. 8.5 and the resonant excitation energy transfer processes in Secs. 5.5 and 8.7. In these cases, the use of the energy state representation based on $|\bar{\Phi}_\alpha\rangle$ and $\mathscr{E}_\alpha$ is more appropriate.

2.3.3. Generalization of the Frenkel exciton model

In what follows, a generalized version of the "standard" Frenkel exciton model (introduced in Sec. 2.3.2) is formulated. Thereby, it is the intention to take additionally into account polarization (or dispersion effects) between aggregated molecules. In general,

the polarization describes the change of a molecular electronic structure sensitive to the collective presence of the surrounding $N_{\mathrm{mol}} - 1$ molecules. As the electrostatic interaction, it affects each molecule specifically. In particular, it is demonstrated in application to the tubular cyanine aggregate in Chap. 8 that the impact of polarization may be very dominant – even stronger than the electrostatic interaction.

The surrounding of a molecule induces changes with respect to its isolated electronic structure. In the sense of perturbation theory, the exact ground and first excited state of an embedded molecule thus carry "correction contributions" from, in principle, all possible (higher excited) states of the isolated molecule. These corrections can only be handled in terms of a full configuration interaction approach.

Such configuration interaction approach is worked out in detail in Appendix B. In short, the derivation makes use of a projector operator formalism. Here, it allows concentrating solely on the dispersion effects of the ground and first excited molecular state. The derivation ends up with a practical correction prescript for each matrix element of the standard exciton Hamiltonian in Eq. 2.22. A generalized exciton model with approximate first–order polarization effects is finally segregated. The related *generalized Frenkel exciton Hamiltonian* reads, cf. Eq. B.14,

$$\hat{H}_{\mathrm{FX}}^{(\mathrm{disp})} = \sum_{m}^{N_{\mathrm{mol}}} \Big[\mathscr{H}_m - (\Delta E_{m,e}^{(\mathrm{disp})} - \Delta E_{m,g}^{(\mathrm{disp})}) \Big] |\bar{\Phi}_m^e\rangle\langle\bar{\Phi}_m^e| + \Big(\sum_{m<n}^{N_{\mathrm{mol}}} f_{mn} \mathscr{J}_{mn} |\bar{\Phi}_m^e\rangle\langle\bar{\Phi}_n^e| + \mathrm{H.c.} \Big). \tag{2.33}$$

In comparison with Eq. 2.22, it is based on excitation energies (diagonal matrix elements) corrected by two shifts of type

$$\Delta E_{m,a}^{(\mathrm{disp})} = - \sum_{n \neq m}^{N_{\mathrm{mol}}} \sum_{b,b'} \frac{|J^{(m,n)}(b \leftarrow a, b' \leftarrow g)|^2}{E_b^{(m)} - E_a^{(m)} + E_{b'}^{(n)} - E_g^{(n)}}, \tag{2.34}$$

The $\Delta E_{m,g}^{(\mathrm{disp})}$ in Eq. 2.33 represents that fraction of the polarization energy shift which is related to the mth molecule in the S_0 ground state, $|\Phi_g^{(m)}\rangle$. In this way, the total polarization shift related to the aggregate ground state $|\bar{\Phi}_0\rangle$ is given by the sum $\sum_m \Delta E_{m,g}^{(\mathrm{disp})}$ (collecting all molecular contributions). Likewise, the $\Delta E_{m,e}^{(\mathrm{disp})}$ describes the contribution related to the molecule m in the S_1 first excited state, $|\bar{\Phi}_m^e\rangle$. The difference of both fractions contained in Eq. 2.33 indicated the corresponding correction of the excitation energies.

The particular form of Eq. 2.34 results from the applied perturbative expansion series (see Appendix B). In principle, the expression tells about additional contributions of virtual transition paths. These virtual transitions to higher excited states (with state index b and b') represent the influence of an polarizable environment. Thereby, the $E_b^{(m)}$ in the denominator of Eq. 2.34 is the energy of the isolated mth molecule in state b. The numerator holds the generalized transfer coupling $J^{(m,n)}(b \leftarrow a, b' \leftarrow g)$. The latter coupling mediates the virtual (forward) transition happening simultaneously in molecule m (from state $|\Phi_a^{(m)}\rangle$ to $|\Phi_b^{(m)}\rangle$) and molecule n (from state $|\Phi_g^{(n)}\rangle$ to $|\Phi_{b'}^{(n)}\rangle$). Its complex conjugate form mediates the reverse process, respectively. (The restriction

to the virtual "single step" transitions results here from the first order treatment.)

Additionally, $\hat{H}_{\mathrm{FX}}^{(\mathrm{disp})}$ accounts for the influence of the dispersion on the excitonic coupling $\mathcal{J}_{mn}$ (for comparison, see Eq. 2.22). Therefore, the empirical *screening factor* f_{mn} is introduced on the off–diagonal matrix elements in Eq. 2.33 (according to Ref. [122]). As indicated, the screening factor depends on the local environment of the two interacting molecules (with indices m and n) and could be understood as a microscopic substitute of a refractive index (see also Sec. 8.3.3.

Once the dispersion shifts, Eq. 2.34, and the screening factors are determined, corrected Frenkel exciton states, $\bar{\Phi}_{\alpha}^{(\mathrm{disp})}$, are gained by solving

$$\hat{H}_{\mathrm{FX}}^{(\mathrm{disp})}|\bar{\Phi}_{\alpha}^{(\mathrm{disp})}\rangle = \mathscr{E}_{\alpha}^{(\mathrm{disp})}|\bar{\Phi}_{\alpha}^{(\mathrm{disp})}\rangle. \tag{2.35}$$

It resembles the eigenvalue problem of the standard Frenkel exciton model (see Eq. 2.32).

The practical realization of Eq. 2.34 describe an ultimate task. Molecular energies of an infinite number of excited states and transfer couplings of all possible transitions would be required. Here, further approximations must be introduced to make ready the exciton model for application to the tubular dye aggregate (see Chap. 8). Related details on the computation of the energy shifts and screening factors are provided later on in Secs. 8.3.2 and 8.3.3, respectively.

2.3.4. Excitations of molecular aggregate/semiconductor hybrid systems

In general, this work concerns hybrid systems which consist of molecular aggregates combined with semiconductor nanostructures. In Chaps. 5, excitation energy transfer processes are treated taking place from a *para*–sexiphenyl aggregate to a ZnO cluster. A similar study for a tubular dye aggregate/CdSe nanocrystal arrangement is provided in Chap. 8. Concerning both systems, a common exciton theory is required involving the organic and inorganic components. In an uniform ansatz, the electronic Hamiltonian of the hybrid systems shall be generally introduced as

$$\hat{H}_{\mathrm{hyb}} = \hat{H}_{\mathrm{agg}} + \hat{H}_{\mathrm{sc}} + \hat{V}_{\mathrm{agg–sc}}. \tag{2.36}$$

This form follows the segmentation approach in Eq. 2.17. The aggregate Hamiltonian, $\hat{H}_{\mathrm{agg}}$, is presented in Eq. 2.19. Moreover, Eq. 2.36 contains the Hamiltonian of the isolated semiconductor part, $\hat{H}_{\mathrm{sc}}$. The appearing Coulomb–type interaction terms between the aggregate and the semiconductor part are collected in the last term, $\hat{V}_{\mathrm{agg–sc}}$.

The basic diabatization scheme introduced in Sec. 2.3.1 is now reapplied. Therefore, negligible wave function overlap is assumed also between the semiconductor structure and the molecular aggregate. The diabatic excited states of the interface are constructed as states which describe excitations localized on the molecular aggregate or the semiconductor part. (Again exclusively single excitations are considered.) Accordingly, molecular–localized excitations (LX) are introduced as[5]

$$|\mathrm{LX}_m\rangle = |\bar{\Phi}_m^e\rangle \otimes |\Psi_0\rangle. \tag{2.37}$$

[5]Throughout this work, the abbreviated notation (with Latin letters) is used in order to indicate states of hybrid aggregate/semiconductor systems.

The latter states are equivalent to Eq. 2.20, however, here the molecular excited aggregate state, $|\bar{\Phi}^e_m\rangle$, is augmented with the electronic ground state of the semiconductor part $|\Psi_0\rangle$ (see Eq. 2.10). They describe the hybrid system with the mth molecule excited. Alternatively, excitations delocalized upon more than a single molecule (but still restricted to the aggregate part) can be described. In close relation with the above Frenkel excitons (see Eq. 2.31), these *Frenkel exciton–like (FX–like) states* are designed as

$$|\mathrm{FX}_\alpha\rangle = \sum_m^{N_\mathrm{mol}} \mathscr{C}_m(\alpha)|\mathrm{LX}_m\rangle. \tag{2.38}$$

However, here they represent a superposition of the number of the N_mol hybrid states in Eq. 2.37. Moreover, a single exitation may be centered on the semiconductor structure. In relation to the WXs in Eq. 2.12, these states are referred to as *Wannier–Mott exciton–like (WX–like) states* of the hybrid system. They are introduced as

$$|\mathrm{WX}_\gamma\rangle = |\bar{\Phi}_0\rangle \otimes |\Psi_\gamma\rangle \tag{2.39}$$

and constructed as a direct–product of the total ground state structure of the aggregate, $|\bar{\Phi}_0\rangle$ (see Eq. 2.20), and the semiconductor state, $|\Psi_\gamma\rangle$, which represents a correlated electron–hole pair excitation (see Eq. 2.12). If correlation effects are not of importance, the description of $|\Psi_\gamma\rangle$ can be reduced to the more basic picture based on single (uncorrelated) electron–hole pair states (see $|\Psi^e_h\rangle$ in Eq. 2.12). Consequently, a simplified treatment based on the uncorrelated (single) electron–hole pair (EHP) states,

$$|\mathrm{EHP}_{eh}\rangle = |\bar{\Phi}_0\rangle \otimes |\Psi^e_h\rangle, \tag{2.40}$$

can be utilized instead of the WX–like states in Eq. 2.39.

In Chap. 5, the LX and FX–like states the *para*–sexiphenyl aggregate/ZnO cluster system. In course of this study, further, the electron–hole pair correlation effects are not of particular interest and excitations localized on the semiconductor are treated in terms of Eq. 2.40. Then in Chap. 8, FX–like and WX–like states are modeled and resonant excitation energy transfer from a tubular dye aggregate to a CdSe nanocrystal is under inspection. In this particular study, energy corrections due to correlation effects have a vital role.

Exciton Hamiltonian of the hybrid system

Next, the hybrid system Hamiltonian (see Eq. 2.36) shall be represented adequately for studies on excitation energy transfer. In Chap. 5, two expansion basis sets are prepared based on either the LX states (see Eq. 2.37) or the FX–like states (see Eq. 2.38), each in combination with the EHP states (see Eq. 2.40). The completeness relation $\hat{\mathbf{1}}_\mathrm{el} = \sum_m |\mathrm{LX}_m\rangle\langle\mathrm{LX}_m| + \sum_{e,h} |\mathrm{EHP}_{eh}\rangle\langle\mathrm{EHP}_{eh}|$ is found in the first case (including LX

states and EHP states). In that basis, the Hamiltonian expresses as, cf. Eq. 2.36,

$$\begin{aligned}
&\hat{H}_{\mathrm{hyb}} = \\
&\sum_{m,n} \Big[\delta_{mn}\Big(\mathscr{H}_m + \int d^3\mathbf{x} \int d^3\mathbf{y} \frac{(n_e^{(m)}(\mathbf{x}) - n_g^{(m)}(\mathbf{x}))\Omega(\mathbf{y})}{|\mathbf{x}-\mathbf{y}|}\Big) + (1-\delta_{mn})\mathscr{J}_{mn}\Big] |\mathrm{LX}_m\rangle\langle \mathrm{LX}_n| \\
&+ \sum_{e,h} \Big[(\bar{\epsilon}_e + \epsilon_h) + \sum_m \int d^3\mathbf{x} \int d^3\mathbf{y} \frac{(n_g^{(m)}(\mathbf{x}) + e\sum_\mu Z_\mu^{(m)} \delta(\mathbf{x} - \mathbf{R}_\mu^{(m)}))\,(\bar{\rho}_e(\mathbf{y}) + \rho_h(\mathbf{y}))}{|\mathbf{x}-\mathbf{y}|}\Big] \\
&\quad \times |\mathrm{EHP}_{eh}\rangle\langle \mathrm{EHP}_{eh}| \\
&+ \sum_m \sum_{e,h} \Big[\mathscr{J}_{m,eh}^{\text{LX-EHP}} |\mathrm{LX}_m\rangle\langle \mathrm{EHP}_{eh}| + \mathrm{H.c.}\Big]. \qquad (2.41)
\end{aligned}$$

The diagonal elements in the first line hold the excitation energy of the hybrid system with the excitation placed on the mth molecule.[6] It consists of the aggregate–internal contribution $\mathscr{H}_m$ (including also intermolecular interaction terms, cf. Eq. 2.28) and the electrostatic interaction energy between the excitation placed on molecule m and the semiconductor in its electronic ground state configuration (integral term in the first line). Thereby, the excitation on the mth molecule is represented as the difference of charge density related to the electronic excited and ground state ($n_e^{(m)}(\mathbf{x})$ and $n_g^{(m)}(\mathbf{x})$, cf. Eq. 2.26). The semiconductor ground state structure (including all electrons and nuclei) is included as the density $\Omega(\mathbf{r})$. The third term in the first line of Eq. 2.41 describes the usual intermolecular excitonic coupling $\mathscr{J}_{mn}$. It translates the excitation from the nth to the mth molecule (see Eq. 2.29). Additional scattering effects of molecular excitations due to the presence of the ground state structure of the semiconductor are neglected in the present ansatz (i.e., it is assumed that $\langle \mathrm{LX}_m|\hat{V}_{\text{agg–sc}}|\mathrm{LX}_n\rangle \approx 0$ for $m \neq n$). The second line in Eq. 2.41 describes the hybrid system when the excitation is placed on the semiconductor part in form of electron–hole pair excitations. The semiconductor–internal contribution to the excitation energy is here simply given as $\langle \Psi_h^e|\hat{H}_{\mathrm{sc}}|\Psi_h^e\rangle \approx \bar{\epsilon}_e + \epsilon_h$. It contains the single–particle energies of the hole, ϵ_h, and the electron, $\bar{\epsilon}_e$ (introduced with Eq. 2.13). The integral term in the second line introduces again the energy correction due to electrostatic interactions. Each molecule in ground state configuration (represented by the total molecular density $n_g^{(m)} + e\sum_\mu Z_\mu^{(m)}\delta(\mathbf{x} - \mathbf{R}_\mu^{(m)})$, cf. Eqs. 2.25 and 2.27) interacts with the electron–hole pair. The latter is represented by the single–particle density $\bar{\rho}_e(\mathbf{y})$ of the electron in the CB (with total charge -1) and the density $\rho_h(\mathbf{y})$ of the hole in the VB (with total charge $+1$). Further details on $\bar{\rho}_e(\mathbf{y})$ and $\rho_h(\mathbf{y})$ are provided in Appendix G.3.3. Off–diagonal matrix elements appear not in the second line. (Also electron–hole pair scattering induced by the presence of the aggregate are neglected, i.e., it is $\langle \mathrm{EHP}_{eh}|\hat{V}_{\text{agg–sc}}|\mathrm{EHP}_{e'h'}\rangle \approx 0$ for $e,h \neq e',h'$.) The last line contains the excitonic couplings $\mathscr{J}_{m,eh}^{\text{LX-EHP}} = \langle \mathrm{LX}_m|\hat{V}_{\text{agg–sc}}|\mathrm{EHP}_{eh}\rangle$. These coupling terms are generally based on

[6] For clarity, the energy $\mathscr{E}_0$ of the overall ground state, $|\mathrm{G}\rangle = |\bar{\Phi}_0\rangle \otimes |\Psi_0\rangle$, was directly subtracted from all diagonal elements in Eq. 2.41 (as also done in Eq. 2.22). The $\mathscr{E}_0$ combines the energies of the aggregate ground state ($\mathscr{H}_0$, cf. Eq. 2.24), the semiconductor ground state ($\langle\Psi_0|\hat{H}_{\mathrm{sc}}|\Psi_0\rangle$) and the aggregate–semiconductor electrostatic interaction energy ($\langle \mathrm{G}|\hat{V}_{\text{agg–sc}}|\mathrm{G}\rangle$).

electronic transition densities of molecules as well as the semiconductor structure (see further details in Sec. 5.4). In general, they are responsible for the excitation energy transfer from the electron–hole pair excitation to the mth molecule (and vice versa).

In Chap. 5, furthermore the picture of exciton transfer based on FX–like states is applied. Then, the completeness relation $\hat{\mathbf{1}}_{\mathrm{el}} = \sum_{\alpha} |\mathrm{FX}_{\alpha}\rangle\langle\mathrm{FX}_{\alpha}| + \sum_{e,h} |\mathrm{EHP}_{eh}\rangle\langle\mathrm{EHP}_{eh}|$ is employed and the Hamiltonian is expressed according to

$$\begin{aligned}\hat{H}_{\mathrm{hyb}} = &\sum_{m}\Big[\mathscr{E}_{\alpha} + \int d^3\mathbf{x}\int d^3\mathbf{y}\frac{|\mathscr{C}_m(\alpha)|^2(n_e^{(m)}(\mathbf{x}) - n_g^{(m)}(\mathbf{x}))\Omega(\mathbf{y})}{|\mathbf{x}-\mathbf{y}|}\Big]|\mathrm{FX}_{\alpha}\rangle\langle\mathrm{FX}_{\alpha}| \\ &+ \sum_{e,h}\Big[(\bar{\epsilon}_e + \epsilon_h) + \sum_{m}\int d^3\mathbf{x}\int d^3\mathbf{y}\frac{(n_g^{(m)}(\mathbf{x}) + e\sum_{\mu} Z_{\mu}^{(m)}\delta(\mathbf{x}-\mathbf{R}_{\mu}^{(m)}))\,(\bar{\rho}_e(\mathbf{y}) + \rho_h(\mathbf{y}))}{|\mathbf{x}-\mathbf{y}|}\Big] \\ &\quad\times |\mathrm{EHP}_{eh}\rangle\langle\mathrm{EHP}_{eh}| \\ &+ \sum_{m}\sum_{e,h}\Big[\mathscr{J}_{\alpha,eh}^{\text{FX-EHP}}|\mathrm{FX}_{\alpha}\rangle\langle\mathrm{EHP}_{eh}| + \mathrm{H.c.}\Big]. \end{aligned} \tag{2.42}$$

By introducing the FX–like states, also the aggregate part of the Hamiltonian is now in diagonal form, i.e., the excitonic energies, $\mathscr{E}_{\alpha} = \langle\mathrm{FX}_{\alpha}|\hat{H}_{\mathrm{agg}}|\mathrm{FX}_{\alpha}\rangle$ (see Eq. 2.32), appear and intermolecular excitonic coupling terms are absent. The $\mathscr{E}_{\alpha}$ are corrected by means of the electrostatic interaction of the exciton (delocalized upon the aggregate) and the ground state structure of the semiconductor cluster. Thereby, the expansion coefficients $\mathscr{C}_m(\alpha)$ (see Eq. 2.38) must be introduced in order to properly account for superpositioned FX–like states. Moreover, concerning the off–diagonal excitonic coupling terms, the excitation energy transfer from the electron–hole pair excitations processes directly to the FX–like states by means of $\mathscr{J}_{\alpha,eh}^{\text{FX-EHP}} = \langle\mathrm{FX}_{\alpha}|\hat{V}_{\text{agg–sc}}|\mathrm{EHP}_{eh}\rangle$.

A third type of representation of the hybrid system Hamiltonian shall be introduced. It is utilized to study exciton transfer in the tubular dye aggregate/CdSe nanocrystal system in Chap. 8. The related expansion is based on the completeness relation $\hat{\mathbf{1}}_{\mathrm{el}} = \sum_{\alpha} |\mathrm{FX}_{\alpha}\rangle\langle\mathrm{FX}_{\alpha}| + \sum_{\gamma} |\mathrm{WX}_{\gamma}\rangle\langle\mathrm{WX}_{\gamma}|$. Thereby, it incorporates the generalized Frenkel exciton states (see Sec. 2.3.3). Accordingly, the FX–like states in Eq. 2.38 are here created based on the generalized Frenkel excitons $|\bar{\Phi}_{\alpha}^{(\mathrm{disp})}\rangle$ (see Eq. 2.35). Besides, in this study the electrostatic interaction energy between the semiconductor and aggregate turns out to be only of minor importance. Hence, they are suppressed and the hybrid system Hamiltonian simplifies to

$$\hat{H}_{\mathrm{hyb}} = \sum_{\alpha}\mathscr{E}_{\alpha}^{(\mathrm{disp})}|\mathrm{FX}_{\alpha}\rangle\langle\mathrm{FX}_{\alpha}| + \sum_{\gamma}\mathfrak{E}_{\gamma}|\mathrm{WX}_{\gamma}\rangle\langle\mathrm{WX}_{\gamma}| + \sum_{\alpha,\gamma}\Big[\mathscr{J}_{\alpha,\gamma}^{\text{FX-WX}}|\mathrm{FX}_{\alpha}\rangle\langle\mathrm{WX}_{\gamma}| + \mathrm{H.c.}\Big]. \tag{2.43}$$

Now, the two types of diagonal elements refer directly to the excitonic energies of the isolated aggregate, $\mathscr{E}_{\alpha}^{(\mathrm{disp})}$ (see Eq. 2.35), and the isolated nanocrystal, $\mathfrak{E}_{\gamma}$ (see Eq. 2.13). The third sum describes all exciton translations from the WXs in the nanocrystal to the generalized FXs in the aggregate (and vice versa).

2.3.5. Charge separation in molecular aggregate/semiconductor hybrid systems

This section is devoted to processes of charge separation (CS) at molecular aggregate/semiconductor interfaces. In particular, photoinduced ultrafast CS processes at the *para*–sexiphenyl/ZnO interface are investiagated in Chap. 6. The subsequent dissipative charge carrier dynamics is studied in Chap. 7. In both studies, charge–separated (CS) states describe a single positive hole charge in the *para*–sexiphenyl aggregate and a negative electron placed on the ZnO cluster. In total the hybrid system remains neutral. According to the general ansatz Eq. 2.18, such CS states generally follows as

$$|\mathrm{CS}_{m\bar{\lambda}}\rangle = |\bar{\Phi}^{+}_{m}\rangle \otimes |\Psi^{-}_{\bar{\lambda}}\rangle, \tag{2.44}$$

where the aggregate state $|\bar{\Phi}^{+}_{m}\rangle$ describes itself the direct product,

$$|\bar{\Phi}^{+}_{m}\rangle = |\Phi^{(m)}_{\mathrm{cat}}\rangle \prod_{n\neq m}^{N_{\mathrm{mol}}} |\Phi^{(n)}_{g}\rangle, \tag{2.45}$$

with the mth molecule in the cationic ground state, $|\Phi^{(m)}_{\mathrm{cat}}\rangle$ (see Sec. 2.1.5). The remaining molecules with $n \neq m$ are represented by their neutral ground state $|\Phi^{(n)}_{g}\rangle$. Opponent to the hole in the aggregate, the CS state in Eq. 2.44 describes the semiconductor part with the excess electron. It is represented by the anionic state $|\Psi^{-}_{\bar{\lambda}}\rangle$. An adequate approach to the latter is introduced in Sec. 2.2.3 (see Eq. 2.16). Following this picture (frozen orbital approximation), the charge density of $|\Psi^{-}_{\bar{\lambda}}\rangle$ is given by the the total charge density of the neutral ground state $|\Psi_0\rangle$ plus and the single–electron density related to the CB–like state $\bar{\psi}_{\bar{\lambda}}$.

Charge separation by exciton decay

Next, the Hamiltonian for CS shall can be constructed. In Chap. 6, CS is studied resulting from decay of molecular excitations, i.e., an electron is transfered from an excited *para*–sexiphenyl molecule into the CB of the ZnO cluster. An adequate expansion basis set for this purpose is found in terms of the completeness relation, $\hat{\mathbf{1}}_{\mathrm{el}} = \sum_m |\mathrm{LX}_m\rangle\langle\mathrm{LX}_m| + \sum_{m,\bar{\lambda}} |\mathrm{CS}_{m\bar{\lambda}}\rangle\langle\mathrm{CS}_{m\bar{\lambda}}|$. It combines the manifold of CS states (see Eq. 2.44) and local excited states (see Eq. 2.37).[7] By representing the interface Hamiltonian, Eq. 2.36, in this basis set, it appears the *Hamiltonian for charge separa-*

[7] As the CS results from molecular excitations, the alternative representation based on FX–like states (see Eq. 2.38) would be less instructive at this place.

tion by exciton decay,

$$\begin{aligned}
&\hat{H}_{\mathrm{CS}} = \\
&\sum_{m,n}\Big[\delta_{mn}\Big(\mathscr{H}_m + \int d^3\mathbf{x}\int d^3\mathbf{y}\frac{(n_e^{(m)}(\mathbf{x}) - n_g^{(m)}(\mathbf{x}))\Omega(\mathbf{y})}{|\mathbf{x}-\mathbf{y}|}\Big) + (1-\delta_{mn})\mathscr{J}_{mn}\Big]|\mathrm{LX}_m\rangle\langle\mathrm{LX}_n| \\
&+\sum_{m,n}\sum_{\bar{\lambda}}\Big[\delta_{mn}(\bar{\epsilon}_{\bar{\lambda}} + \mathscr{H}_m^{(\mathrm{cat})} + V_{\mathrm{agg\text{–}sc}}(m,\bar{\lambda})) + (1-\delta_{mn})\mathscr{V}_{mn}^{\mathrm{HT}}\Big]|\mathrm{CS}_{m\bar{\lambda}}\rangle\langle\mathrm{CS}_{n\bar{\lambda}}| \\
&+\sum_{m,\bar{\lambda}}\Big[\mathscr{V}_{m,\bar{\lambda}}^{\text{CS-LX}}|\mathrm{CS}_{m\bar{\lambda}}\rangle\langle\mathrm{LX}_m| + \mathrm{H.c.}\Big]. \qquad (2.46)
\end{aligned}$$

(According to Eq. 2.41, the total ground state energy, $\mathscr{E}_0$, is again subtracted from all diagonal energy terms.[8]) Apparently, the terms in the first line of Eq. 2.41 reappear here (also in the first line). The second and third line in Eq. 2.46 describe the situation of CS. The related diagonal matrix elements sum up terms of: i) $E_{\bar{\lambda}}$, the energy of the single electron (single–particle (TB) energy of the occupied CB–like state $\bar{\psi}_{\bar{\lambda}}$), ii) $\mathscr{H}_m^{(\mathrm{cat})}$, the aggregate–internal energy of the hole charge placed on the mth molecule including all intermolecular interactions (see details below), and iii) $\hat{V}_{\mathrm{agg\text{–}sc}}(m,\bar{\lambda})$, the mutual interaction energy of the electron and hole each with the opponent structure (see also below). The off–diagonal term $\mathscr{V}_{mn}^{\mathrm{HT}} = \langle\bar{\Phi}_m^e\rangle|\hat{H}_{\mathrm{agg}}|\bar{\Phi}_n^e\rangle$ accounts for the intermolecular hole transfer from molecule n to m. (Please note that a likewise electron transfer integral appears not in Eq. 2.46 due to the eigenstate character of the CB–like states $\bar{\psi}_{\bar{\lambda}}$.) The remaining matrix elements (last term in Eq. 2.46) are responsible for the actual CS process. They are introduced as transfer coupling elements $\mathscr{V}_{m,\bar{\lambda}}^{\text{CS-LX}} = \langle\bar{\Phi}_m^+\rangle|\langle\Psi_{\bar{\lambda}}^-|\hat{V}_{\mathrm{agg\text{–}sc}}|\Psi_0\rangle|\bar{\Phi}_m^e\rangle$. Each element reflects a different excess electron injection process from the mth molecule into the state $\bar{\psi}_{\bar{\lambda}}$. The localized excitation on molecule m is annihilated and a hole on the same molecule is created. (Particular details on $\mathscr{V}_{mn}^{\mathrm{HT}}$ and $\mathscr{V}_{m,\bar{\lambda}}^{\text{CS-LX}}$ are discussed in direct application to the *para*–sexiphenyl/ZnO system in Chap. 6.)

The potential energy of the hole within the aggregate, $\mathscr{H}_m^{(\mathrm{cat})}$, follows as

$$\mathscr{H}_m^{(\mathrm{cat})} = E_{+g} + \sum_n^{N_{\mathrm{mol}}}\Big(V_{\text{el-el}}^{(m,n)}(+,g) - V_{\text{el-el}}^{(m,n)}(g,g) + V_{\text{el-nuc}}^{(m,n)}(+) - V_{\text{el-nuc}}^{(m,n)}(g)\Big). \qquad (2.47)$$

The first term, $E_{+g} = E_{\mathrm{cat}} - E_g$, gives the intramolecular energy of the hole charge, i.e., the ionization energy. It describes the difference of the energies of the cationic and neutral electronic ground state of the molecule. (The molecular index is dropped again as all molecules in the *para*–sexiphenyl aggregate are identical.) The remaining terms account for the intermolecular electrostatic Coulomb–type interaction (similar

[8] Please note further that it is again assumed that $\langle\bar{\Phi}_m^e\rangle|\langle\Psi_0|\hat{V}_{\mathrm{agg\text{–}sc}}|\Psi_0\rangle|\bar{\Phi}_n^e\rangle\rangle \approx 0$ for $m \neq n$. Likewise, hole scattering effects within the aggregate by means of the semiconductor as well as vice versa electron scattering effects within the semiconductor by means of the aggregate are assumed to be of no importance here. In accordance with the former exciton treatment (see Eq. 2.41), the respective terms of type $\langle\bar{\Phi}_m^+\rangle|\langle\Psi_0|\hat{V}_{\mathrm{agg\text{–}sc}}|\Psi_0\rangle|\bar{\Phi}_n^+\rangle \approx 0$ with $m \neq n$ are suppressed in Eq. 2.46. Similarly, the terms of type $\langle\bar{\Phi}_m^+\rangle|\langle\Psi_{\bar{\lambda}}^-|\hat{V}_{\mathrm{agg\text{–}sc}}|\Psi_{\bar{\lambda}'}^-\rangle|\bar{\Phi}_n^+\rangle$ appear only for $m, \bar{\lambda} = n, \bar{\lambda}'$ in Eq. 2.46.

to Eq. 2.28). They are either of electron–electron type ($V_{\text{el-el}}^{(m,n)}$, cf. Eq. 2.25) or of electron–nucleus type ($V_{\text{el-nuc}}^{(m,n)}$, cf. Eq. 2.27). In particular, the first and third term is now based on the charge density related to the cationic state of the mth molecule,

$$n_{\text{cat}}^{(m)}(\mathbf{r}) = -e(N_{\text{el}}^{(m)} - 1) \int d\{r^{(m)}\} \delta(\mathbf{r} - \mathbf{r}_1^{(m)}) |\Phi_{\text{cat}}^{(m)}(r^{(m)})|^2. \tag{2.48}$$

It is equivalently with Eq. 2.26 but related to the configuration of the molecular cationic state $|\Phi_{\text{cat}}^{(m)}\rangle$. Please note that $n_{\text{cat}}^{(m)}(\mathbf{r})$ gives the total charge of $-(N_{\text{el}}^{(m)} - 1)e$. Together with the nuclei, it results the total molecular charging of $+1e$.

The third term in the second line of Eq. 2.46, $\hat{V}_{\text{agg–sc}}$, displays the electrostatic interaction between the aggregate and the semiconductor. Reminding that the total ground state energy is shifted to zero, the $\hat{V}_{\text{agg–sc}}$ can be grouped in three terms, according to

$$\begin{aligned} V_{\text{agg–sc}}(m, \bar{\lambda}) = &\int d^3\mathbf{x} \int d^3\mathbf{y} \frac{(n_{\text{cat}}^{(m)}(\mathbf{x}) - n_g^{(m)}(\mathbf{x}))\Omega(\mathbf{y})}{|\mathbf{x} - \mathbf{y}|} \\ &+ \sum_n^{N_{\text{mol}}} \int d^3\mathbf{x} \int d^3\mathbf{y} \frac{(n_g^{(m)}(\mathbf{x}) + e\sum_\mu Z_\mu^{(m)} \delta(\mathbf{x} - \mathbf{R}_\mu^{(m)}))\bar{\rho}_{\bar{\lambda}}(\mathbf{y})}{|\mathbf{x} - \mathbf{y}|} \\ &+ \int d^3\mathbf{x} \int d^3\mathbf{y} \frac{(n_{\text{cat}}^{(m)}(\mathbf{x}) - n_g^{(m)}(\mathbf{x}))\bar{\rho}_{\bar{\lambda}}(\mathbf{y})}{|\mathbf{x} - \mathbf{y}|}. \end{aligned} \tag{2.49}$$

The first and second term gives the electrostatic interaction of the hole with the (opponent) neutral ground structure of the semiconductor cluster and of the electron with the neutral aggregate, respectively. The charge density of the hole is again represented by the difference expression of the densities $n_{\text{cat}}^{(m)}(\mathbf{x})$ and $n_g^{(m)}(\mathbf{x})$. Such treatment is not necessary concerning the charge density of the excess electron in the CB–like state $\bar{\psi}_{\bar{\lambda}}$. According to Eq. 2.41, it is reintroduced as $\bar{\rho}_{\bar{\lambda}}(\mathbf{y})$. The third integral term in Eq. 2.49 describes the direct interaction between the electron and hole (in CB–like state $\bar{\psi}_{\bar{\lambda}}$ and placed on the mth molecule, respectively). In Sec. 6.2.2, the latter contribution turns out to be the dominant part of the aggregate–semiconductor interaction. Due to the effective $\pm 1e$ total charging, this is not surprising.

Charge separation by photoactivation

In Chap. 6, CS is studied after photoexcitaton of the *para*–sexiphenyl aggregate. The latter shall be directly simulated as part of the kinetics. Therefore, the interaction of the aggregate system with the radiation field must be treated explicitely and related off–diagonal coupling elements must be added to H_{CS}. Accordingly, the two types of matrix elements $\mathcal{J}_{m0}$ and $\mathcal{J}_{0m}$ are introduced. They mediate the excitation and de–excitation of the mth molecule in the aggregate, respectively. Added to H_{CS}, the *Hamiltonian for photoinduced charge separation* is generated as, cf. Eq. 2.46,

$$\hat{H}_{\text{CS}}^{(\text{opt})} = \hat{H}_{\text{CS}} + \sum_m^{N_{\text{mol}}} \Big(\mathcal{J}_{m0} |\text{LX}_m\rangle\langle \text{G}| + \mathcal{J}_{0m} |\text{G}\rangle\langle \text{LX}_m| \Big). \tag{2.50}$$

The ground state energy is shifted to zero following the above convention, i.e., the ground state diagonal element, $|\mathrm{G}\rangle\langle\mathrm{G}|$, vanishes. In general, $\mathcal{J}_{m0}$ and $\mathcal{J}_{0m}$ depend on the molecular transition densities. Further, they introduce time–dependence in H_{CS} as they carry the oscillating amplitude of the radiation field. Their particular expressions is clarified in Sec. 6.2.4.

Please note that, by definition, the semiconductor part is excluded from the optical excitation process. In principle, the direct treatment of excitations of the states $|\Psi_{\bar{\lambda}}^{\bar{\lambda}}\rangle$ (or $|\Psi_\gamma\rangle$) in the CS model would be also possible. However, such combined ansatz is beyond the scope of the studies presented in Chap. 6 and so it is not further considered at this place.

Hole motion and electron trapping

Finally, the special case of exclusive hole motion in the presence of an immobilized electron shall be considered. Corresponding interface states and a hole transfer Hamiltonian shall be developed in close relation with the former modeling (see Eqs. 2.44 and 2.46). Individual hole motion is studied in Chap. 7 in a layer of *para*–sexiphenyl molecules which is placed on a flat macroscopic ZnO surface. Concerning the kinetics is assumed that very fast CS appears and that the created electron charge becomes initially trapped at the ZnO surface. On longer time–scales, following such scenario, it remains to model the hole migration within the molecular aggregate.

By suppressing the electronic degree of freedom in the CS states (see Eq. 2.44), the Hamiltonian H_{CS} (see Eq. 2.46) reduces to the *hole transfer Hamiltonian*,

$$\hat{H}_{\mathrm{HT}} = \sum_{m,n} \Big[\delta_{mn}(\mathscr{H}_m^{(\mathrm{cat})} + V_{\mathrm{agg–sc}}(m)) + (1-\delta_{mn})\mathscr{V}_{mn}^{\mathrm{HT}}\Big]|\mathrm{HT}_m\rangle\langle\mathrm{HT}_n|. \tag{2.51}$$

It is based on the molecular localized hole transfer (HT) states, which are prepared according to

$$|\mathrm{HT}_m\rangle = |\bar{\Phi}_m^+\rangle \otimes |\Psi_{\mathrm{trap}}^-\rangle. \tag{2.52}$$

They are closely related to the CS states in Eq. 2.44 but assume an immediate electron trapping scenario. After electron injection, the electronic structure of the semiconductor part is directly translated into configuration $|\Psi_{\mathrm{trap}}^-\rangle$. The latter represents the semiconductor ground state and an excess electron in a certain trapped state, ψ_{trap}. The ψ_{trap} is considered as a superposition state, $\psi_{\mathrm{trap}} = C_{\bar{\lambda}}^{(\mathrm{trap})}\bar{\psi}_{\bar{\lambda}}$, of all CB–like states, $\psi_{\bar{\lambda}}$. In this way, a distinct spatial localization of the electron at the semiconductor surface shall be guaranteed. The total semiconductor state can then be formulated as

$$|\Psi_{\mathrm{trap}}^-\rangle = \sum_{\bar{\lambda}} C_{\bar{\lambda}}^{(\mathrm{trap})}|\Psi_{\bar{\lambda}}^-\rangle. \tag{2.53}$$

The introduced expansion coefficients $C_{\bar{\lambda}}^{(\mathrm{trap})}$ are directly related to the above superpositioning of $\bar{\psi}_{\bar{\lambda}}$. In the Hamiltonian $\hat{H}_{\mathrm{HT}}$, only potential energy terms depending on the hole index m are of relevance (see Eq. 2.51). (Terms of exclusive dependence on the

electron charge become constant and are withdrawn.) The remaining terms in Eq. 2.51 are: i) $\mathscr{H}_m^{(\mathrm{cat})}$, the aggregate internal potential energy matrix element (see Eq. 2.47), ii) $\mathscr{V}_{mn}^{\mathrm{HT}}$, the hole transfer coupling and iii) $V_{\mathrm{agg–sc}}(m)$, the aggregate–semiconductor interaction term which reads

$$V_{\mathrm{agg–sc}}(m) = \int d^3\mathbf{x} \int d^3\mathbf{y} \frac{\left(n_{\mathrm{cat}}^{(m)}(\mathbf{x}) - n_g^{(m)}(\mathbf{x})\right)\left(\Omega(\mathbf{y}) + \sum_{\bar{\lambda}} |C_{\bar{\lambda}}^{(\mathrm{trap})}|^2 \bar{\rho}_{\bar{\lambda}}(\mathbf{y})\right)}{|\mathbf{x} - \mathbf{y}|}. \quad (2.54)$$

The latter contains the potential energy correction of the hole due to its interaction with the opponent ground state electronic semiconductor structure, $\Omega(\mathbf{y})$, and the trapped electron with density $\sum_{\bar{\lambda}} |C_{\bar{\lambda}}^{(\mathrm{trap})}|^2 \bar{\rho}_{\bar{\lambda}}(\mathbf{y})$. A collective description of the potential energy (i.e., the full diagonal term in Eq. 2.51) is worked out in the framework of Chap. 7. In approximate manner, it introduces a polarizable continuum ansatz and finally opens the opportunity for a macroscopic picture of the *para*–sexiphenyl/ZnO interface.

3. Dynamics of Closed and Open Quantum Systems

Different forms of electronic structures for composite systems are developed in Chap. 2. Excited, charge–separated and charge–localized states are introduced together with the corresponding transfer Hamiltonians. In this chapter, different models for describing excitation energy transfer processes and charge separation kinetics are discussed.

A brief introduction of the different regimes of transfer phenomena and their adequate description is given in Sec. 3.1. Thereby, the concepts of closed and open quantum system kinetics are outlined. This overview is given in close relation to the concrete studies presented throughout Chaps. 5 to 8. In Sec. 3.2, closed quantum system kinetics are discussed more deeply. Thereby, Sec. 3.2.1 is dedicated to coherent state evolution alias wave packet motion according to the time–dependent Schrödinger equation. Subsequently in Sec. 3.2.2, incoherent transition rates are introduced for an approximate transfer model based on Fermi's golden rule.

Then, the discussion turns to open quantum systems in Sec. 3.3. Charge and exciton dynamics are modeled under permanent influence of a vibrational bath. In Sec. 3.3.1, therefore the concept of the reduced density operator is recaptured. The appearance of decoherence and energy dissipation is generally concerned in Sec. 3.3.2. In Sec. 3.3.3, the prominent bilinear coupling model of system–bath interaction is introduced. It is concretely employed in Chaps. 7 and 8 to describe dissipative hole and exciton dynamics, respectively. Then in Secs. 3.3.4, the spectral density and correlation function are discussed. They are integral parts of modeling the system–bath interaction. Based on them, in Sec. 3.3.5, the quantum master equation is considerd as the traditional ansatz to determine the evolution of the reduced density operator. It is the intention to illustrate its high computational costs in application to large–scale systems. Connonly utilized approximations are outlined. Motivated by that, the quantum state diffusion ansatz is introduced in Chap. 4. It indirectly approaches the evolution of the reduced density operator and is characterized by more efficient work flow in application to large–scale systems.

3.1. Regimes of the Studied Transfer Phenomena

Dynamics of excitation energy transfer, charge separation and charge transport mechanisms are studied in Chaps. 5–8. They can be classified into different regimes of electron–vibrational interaction (i.e., the influence of a surrounding vibrational bath (nuclear motion) on the actual transfer system as a measure). In principle, different regimes can be characterized using directly the ratio of the system–bath interaction strength and the system–internal coupling strengths (e.g., excitonic coupling or hole transfer integrals). More convienent, in what follows the times t_{el} and t_{vib} shall be introduced instead for categorization. Respectively, they describe characteristic times of the motions within the electronic subsystem and the vibrational bath. (The t_{el} describes, e.g., a characteristic time–scale of some transfer of particular interest.)

In Chaps. 5 and 6, exciton transitions and photoinduced charge separation kinetics in the *para*–sexiphenyl aggregate/ZnO cluster system interface are investigated. Thereby, the focus is on the initial femtosecond time–scale and it shall be assumed that $t_{\mathrm{vib}} \gg t_{\mathrm{el}}$. In this regime, the electronic motion is much faster than the response of the vibrational degrees of freedom and effects of the nuclei dynamics on the exciton or charge separation kinetics can be neglected. Accordingly, the influence of the vibrations can be simplified to static modulations of the electronic system. These can be realized by introducing minor random shifts added to the energies of exciton and charge–separated states. The random shifts are simply generated from adequate distribution functions (see Secs. 5.5.2 and 6.6). Attributed with the random energy shifts, the electronic system is modeled as a closed quantum system, i.e., the states obey wave packet dynamics according to the time–dependent Schrödinger equation (see Sec. 3.2.1). Further approximations are possible in the presence of a quasi–continuum of transfer acceptor states and a weakly coupled single donor state. Then, the wave packet motion approximately turns to an *incoherent* type of motion. In Chap. 5, this is demonstrated for excitation energy transfer from the *para*–sexiphenyl aggregate to the ZnO cluster. A likewise incoherent ansatz is also applied to exciton transfer in the tubular dye aggregate/CdSe nanocrystal system as a part of Chap. 8. In both cases, unidirectional transfer dynamics are modeled and rates based on Fermi's golden rule are computed (see Sec. 3.2.2). A somewhat special scenario is thereby encountered in Sec. 8.7.2. There, the transfer is much slower than the nuclear motion and vibronic effects can be included as a thermalized distribution of initial population upon all available acceptor states. The reverse of the determined rate values represent characteristic times of exciton translation in the systems.

In Chap. 7, hole transfer in a *para*–sexiphenyl layer on a flat ZnO surface is under inspection. The study concentrates on the picosecond time–scale which means that it is $t_{\mathrm{vib}} \approx t_{\mathrm{el}}$. Hence, the system kinetics can be treated neither in terms of coherent motion with static disordered hole states nor based on incoherent rate expressions. In the same regime, also the exciton relaxation process within the tubular dye aggregate studied in Sec. 8.5 takes place. In both studies, the electronic system kinetics are characterized equivalently by means of coherent (hole or exciton) motion as well as dephasing and dissipation due to vibronic effects. Consequently, they must be treated in terms of open system dynamics. In this formalism, the evolution within the system is approached in terms of the reduced density operator by introducing a quantum master

equation. The latter explicitly takes into account the contact with the vibrational bath which introduces loss of coherence and dissipative effects like population relaxation [44]. In the special case of a *Markovian* bath (i.e., the vibrations shows very fast response, $t_{\mathrm{vib}} \ll t_{\mathrm{el}}$, without any memory effects), the reduced density matrix can be computed using the simplified multilevel Redfield equations (see Sec. 3.3.5 and Ref. [44]). This approach is applied in Chap. 4 to the Fenna–Metthews–Olson complex. The latter describes a very small chromophore complex with only seven molecular states. The transfer systems studied in Chaps. 7 and 8, however, contain each several thousand electronic states. On that scale, the concept of directly solving a master equation becomes generally inefficient. Therefore, such approaches are of less practical use for the main studies presented in this work. Instead, then quantum state diffusion approaches are more adequate. In Chap. 4, one such particular strategy is developed as a powerful alternative.

3.2. Closed System Dynamics

In general, a closed quantum system is identified by the existance of a complete set of commutating observable operators [44]. Accordingly, any possible realization of a closed system, in principle, can be described in terms of a "pure" state in Hilbert space which generally obeys the Schrödinger equation.

3.2.1. Wave packet dynamics

In Chaps. 5, exciton transfer phenomena in the *para*–sexiphenyl aggregate/ZnO cluster are described in terms of wave packet propagation. The same is done concerning photoinduced charge separation kinetics in Chap. 6. Thereby, the evolution of the system (i.e., the time–dependence of the wave packet) obeys the *time–dependent Schrödinger equation* (TDSE),

$$i\hbar\partial_t|\psi(t)\rangle = \hat{H}_{\mathrm{el}}(t)|\psi(t)\rangle. \tag{3.1}$$

The TDSE provides the evolving system state, $\psi(t)$, based on the (possibly time–dependent) electronic system Hamiltonian, $\hat{H}_{\mathrm{el}}(t)$. Several Hamiltonians concerning different transfer scenarios are generally formulated in Secs. 2.3.4 and 2.3.5 (see particularly Eq. 2.41 for exciton transfer and Eq. 2.50 for treating photoinduced charge separation). In practice, the system state is obtained as a set of time–dependent expansion coefficients $\mathbf{c}_j(t)$ (i.e., it is $\psi(t) = \sum_j \mathbf{c}_j(t)\psi_j$, based on a complete Hilbert space basis set $\{|\psi_j\rangle\}$). The wave packet character of $\psi(t)$ is expressed in the superposition of the different complex–valued phase oscillations of each $\mathbf{c}_j(t)$.

An unambiguous solution is possible for the wave function $\psi(t > t_0)$. This means onward wave function kinetics are conditioned critically by an initial state $\psi(t_0)$, which hence has to be defined carefully. The formal integration of Eq. 3.1 expresses the state propagation,

$$|\psi(t)\rangle = \hat{\mathcal{U}}(t, t_0)|\psi(t_0)\rangle, \tag{3.2}$$

where the time–evolution operator, $\hat{\mathcal{U}}(t,t_0) = T\exp\{-i/\hbar\int_{t_0}^{t} d\tau\ \hat{H}_{\mathrm{el}}(\tau)\}$, is involved. Assuming that a system wave function trajectory is found, the temporal behavior of a certain physical observable $\mathcal{O}(t)$ is computed straightforwardly with

$$\langle\mathcal{O}(t)\rangle = \langle\psi(t)|\hat{\mathcal{O}}|\psi(t)\rangle = \sum_{j,j'} \mathbf{c}_j^*(t)\mathbf{c}_{j'}(t)\langle\psi_j|\hat{\mathcal{O}}|\psi_{j'}\rangle. \tag{3.3}$$

The right hand side of Eq. 3.3 illustrates the oscillative features of $\mathcal{O}(t)$ in direct consequence of the wave packet motion of $\psi(t)$. For instance in Chap. 6, this is nicely visualized concerning the kinetics of molecular excitation across the *para*–sexiphenyl aggregate. Details on the efficient numerical propagation of Eq. 3.2 are provided in Appendix H.2.1.

3.2.2. Fermi's golden rule

Obviously, the numerical integration of the TDSE (see Eq. 3.1) can become very bothersome regarding systems with very high numbers of relevant states. Fortunately though, transfer kinetics can be oftenly described more simple in terms of a single initially populated donor state and a weakly coupled quasi–continuum of "opponent" acceptor states. Typically in such case, only the depletion time of the acceptor state population is of interest. The individual populations of acceptor states are not important and the manifold of acceptor states can be treated as a whole. In Chap. 5, such scenario is identified when the focus is on the excitation energy transfer from Frenkel exciton (or molecular excitation) in the *para*–sexiphenyl aggregate to electron–hole pair excitation in the ZnO cluster.

A convenient formalism of the depletion process can be found starting with the transfer rate model based on of Fermi's golden rule [44, 138]. Accordingly, the depletion rate from a single donor (or initial) to a single acceptor (or final) state reads

$$k_{i\to f} = \frac{2\pi}{\hbar}|V_{fi}|^2\delta(E_i - E_f), \tag{3.4}$$

with, E_i and E_f, being the energies of the initial and the final state, respectively. The V_{fi} describes their interstate coupling term. The squared form of V_{fi} in Eq. 3.4 gives evidence on an underlying second–order approximation. In fact, the rate $k_{i\to f}$ is only valid in the weak coupling limit when the population transfer can be treated as unidirectional process. Moreover, the delta–distribution conditions a sharp energy conservation during the state transition.

In assumption of a quasi–continuum of acceptor states, Eq. 3.5 can be utilized to derive a formula of enormous practical value. In summation with respect to all possible transfer paths, the total depletion rate of the donor state follows as

$$k = \frac{2}{\hbar}\sum_{f}|V_{fi}|^2\frac{\Delta}{(E_i - E_f)^2 + \Delta^2}, \tag{3.5}$$

where further a life–time broadening is introduced and a Lorentzian line shape function replaces the above occuring delta distribution. Similarly, a Gaussian line shape function

can be introduced in order to account for inhomogeneous broadening (see, e.g., the disorder effect in Sec. 5.5.1). With Eq. 3.5, in principle, a much simpler excess to transfer processes is obtained. Its applicability as an alternative to direct wave function propagation is intensively discussed in Chap. 5 when studying exciton transfer across the *para*–sexiphenyl aggregate/ZnO interface.

3.3. Open System Dynamics

The concept of open quantum systems is required whenever the transfer system cannot be treated as "clearly isolated" from the influence of an environment. The interaction with the latter describes a source of fluctuation and friction in the "active" system part. Accordingly, its dynamics cannot be determined based on the time–dependent Schrödinger equation 3.1 involving only the transfer system Hamiltonian. Many optical experiments take place under such circumstances measuring time–dependent electronic processes under persistent impact of nuclear vibrations (see, e.g., Refs. [139, 125]).

In particular, after ultrafast laser–pulse excitation charge migration processes at the *para*–sexiphenyl/ZnO interface take place on the picosecond time–scale (see Chap. 7). These "slow" charge kinetics are critically influenced by vibronic effects and can no longer be captured in terms of coherent wave packet dynamics. The same is valid for the exciton migration within the tubular dye aggregates discussed in Chap. 8 (see Sec. 8.5). Then, vibrational–induced exciton relaxation processes can be observed on the picosecond time–scale.

3.3.1. Reduced density operator

In order to study transfer processes in the framework of an open quantum system, the total system Hamiltonian is generally departed according to

$$\hat{H} = \hat{H}_{\mathrm{S}} + \hat{H}_{\mathrm{B}} + \hat{H}_{\mathrm{S\text{–}B}}. \tag{3.6}$$

Its first term, $\hat{H}_{\mathrm{S}}$, describes the Hamiltonian of the transfer system. Abstracting both concrete studies in Chaps. 7 and 8, the $\hat{H}_{\mathrm{S}}$ is related to the moving object (i.e., the charge or exciton) and generally formulated as,

$$\hat{H}_{\mathrm{S}} = \sum_{m,n} \Big(\delta_{m,n} E_m + (1 - \delta_{m,n}) V_{mn} \Big) |m\rangle\langle n|, \tag{3.7}$$

using a basis of molecular localized states, $\{|m\rangle\}$. The $\hat{H}_{\mathrm{S}}$ covers site–energies, E_m, and inter–site transfer coupling elements, V_{mn}. In Chaps. 7 and 8, the $\hat{H}_{\mathrm{S}}$ is substituted by the hole transfer Hamiltonian (see Eq. 2.51) and exiton Hamiltonian (see Eq. 2.33), respectively. In accordance to that, the states of molecular localized holes (see Eq. 2.52) or excitations (see Eq. 2.37) are casted for the states $|m\rangle$ in Eq. 3.7, respectively. The second and third term in $\hat{H}$ (see Eq. 3.6) represent the vibrational Hamiltonian of the macroscopic vibrational bath, $\hat{H}_{\mathrm{B}}$, and the vibronic interaction part among system and bath, $\hat{H}_{\mathrm{S\text{–}B}}$, respectively.

The "macroscopic" character of the bath prohibits any declaration of a pure wave function state of the complete system. Instead, the density matrix formalism must be applied [45, 44]. (The concrete form of $\hat{H}_{\mathrm{B}}$ and $\hat{H}_{\mathrm{S–B}}$ is specified below in Sec. 3.3.3.) In particular, the *reduced density operator* (RDO),

$$\hat{\rho}(t) = tr_{\mathrm{B}}\{\hat{W}(t)\}, \tag{3.8}$$

is typically employed. According to the trace expression, $tr_{\mathrm{B}}\{...\}$, the density operator (introduced as $\hat{W}$) becomes reduced by the vibrational degrees of freedom. (This operation is motivated since only observables of the transfer system are relevant. The concrete knowledge of the bath part, however, is not of interest.) In convenient manner, hence, the RDO describes the time–dependent statistics of the transfer system under influence of the vibrational bath.

The evolution of $\hat{\rho}(t)$ is prescribed by $\hat{W}(t)$, which itself obeys the Liouville–von Neumann equation [45], $i\hbar\partial_t\hat{W}(t) = [\hat{H}, \hat{W}(t)]$ with $\hat{H}$ given in Eq. 3.6. Accordingly, the general equation of motion of the RDO is then found as

$$i\hbar\partial_t\hat{\rho}(t) = [\hat{H}_{\mathrm{S}}, \hat{\rho}(t)] + tr_{\mathrm{B}}\{[\hat{H}_{\mathrm{S\text{-}R}}, \hat{W}(t)]\}. \tag{3.9}$$

The first term describes the evolution of the transfer system on condition that the bath would be absent (i.e., in case of pure coherent motion for $\hat{H}_{\mathrm{S–R}} = 0$). However, this behavior is disturbed by the second part of Eq. 3.9. This one holds the influence of the vibrational bath on the transfer kinetics as further discussed in the subsequent Secs. 3.3.2–3.3.4.

3.3.2. Dissipation and coherence dephasing

In Chaps. 7 and 8, the RDO is represented using either states of a molecular localized holes or excitations, respectively (see Eqs. 2.52 and 2.37). Both shall be further on generalized as $\{|m\rangle\}$ (see also Eq. 3.7). The corresponding *reduced density matrix* (RDM) emerges as

$$\rho_{mn}(t) = \langle m|\hat{\rho}(t)|n\rangle. \tag{3.10}$$

This expression is of particular interest in this work. On the diagonal, the RDM carries the population of the mth transfer state introduced as $P_m(t) = \rho_{mm}(t)$. Later on, the $P_m(t)$ renders the probability that a charge or excitation is localized on the mth molecule. In contrary to that, the offdiagonal elements of the RDM, $\rho_{mn}(t)$ with $m \neq n$, quantify the quantum coherence between the mth and nth transfer state.

The RDM provides the transfer process in spatial resolution. However, especially in course of the exciton relaxation studies in Chap. 8, also the energetic perspective of the transfer is of interest. In such cases, it is more adequate to represent the RDO using the eigenstate basis $\{|\alpha\rangle\}$, where it is $\hat{H}_{\mathrm{S}}|\alpha\rangle = E_\alpha|\alpha\rangle$. With this, the evolution of the internal energy stored in the transfer system follows as

$$E_{\mathrm{S}}(t) = tr_{\mathrm{S}}\{\hat{\rho}(t)\hat{H}_{\mathrm{S}}\} = \sum_\alpha E_\alpha P_\alpha(t), \tag{3.11}$$

with the eigenstate population $P_\alpha(t) = \langle\alpha|\hat{\rho}(t)|\alpha\rangle$. Since continuous energetic exchange takes place with the vibrational bath, the transfer system steadily converges to thermal equilibrium (see *principle of detailed balance* [45, 44]). This status manifests in the limit $t \to \infty$. Then, the energy state populations $P_\alpha(t)$ obey the canonical distribution. In the study on exciton relaxation in Chap. 8, this dissipation process is directly monitored after initial preparation of different high–energy excitonic wave packets. During time–evolution, continuous energy flow (i.e., continuous decay of $E_\mathrm{S}(t)$) is clearly documented. Energy funnels from the exciton system into the bath aligned with an irreversible spatial energy migration within the tubular dye aggregate. Besides the dissipative energy current, the interaction with the bath raises continuous loss of coherence within the transfer system. Considering again $\rho_{\alpha\beta}$, such dephasing is observed as a collective decay of the offdiagonal elements with the limit $\rho_{\alpha\neq\beta}(t \to \infty) = 0$. The action of dephasing is particularly visualized when discussing the dissipative charge transfer kinetics in Chap. 7. There, dephasing is identified as the decreasing ability of the hole wave packet to interfere and the continuous transformation from ballistic motion to diffusive drift (see also Ref. [53]).

3.3.3. System–bath interaction

In order to derive an equation of motion of practical use, the bath Hamiltonian, H_B, as well as the system–bath interaction, $\hat{H}_\mathrm{S\text{–}B}$, must be further specified. In this thesis, the molecular vibrational motion is treated in terms of the standard harmonic oscillator model [44]. Accordingly, (mass–weighted) normal modes are introduced and the bath Hamiltonian translates to

$$\hat{H}_\mathrm{B} = \sum_\xi \hbar\omega_\xi \hat{b}_\xi^\dagger \hat{b}_\xi, \tag{3.12}$$

with frequencies ω_ξ (where the index ξ indicates the individual vibrational modes) and the creation and annihilation operators, $\hat{b}_\xi^\dagger$ and $\hat{b}_\xi$, respectively. Fundamentally, Eq. 3.12 relies on the assumption that the ω_ξ are independent on the configuration of the transfer system. So, changes in the electronic state mean only a displacement of the potential energy surface along the vibrational coordinates [45, 44]. In concert with the harmonic vibrational model, typically a bilinear type of system–bath interaction model is introduced. (This approach is adequate in the presence of weak vibronic coupling strength [44].) In the bilinear model, the interaction Hamiltonian factorizes into $\hat{H}_\mathrm{S\text{–}B} = \sum_u \hat{S}_u \hat{B}_u$. The two linear operators $\hat{S}_u$ and $\hat{B}_u$ describe individual parts from the transfer system and the vibrational bath, respectively. In relation to Eq. 3.12, the bath coupling operator is straightly found as $\hat{B}_u \propto (\hat{b}_\xi + \hat{b}_\xi^\dagger)$ [45, 44].

In principle, both the state energies, E_m, as well as the corresponding intersite couplings, V_{mn}, are influenced by the vibrational motion (see Eq. 3.7). However, a combined treatment of modulations of E_m and V_{mn} is beyond the scope of this thesis. Regarding the present studies on charge and energy transfer it is therefore argued that the vibrations influence the transfer properties primarily via the former type of energetic fluctuations. Although recent studies on different molecular transfer systems demonstrated that also intermolecular vibrations can be an important issue (see, e.g.,

Ref. [55]), this type of influence shall not be further considered here. Accordingly, the general system operator part, $\hat{S}_u$, is specified as the projector of type $\hat{L}_m = |m\rangle\langle m|$. Together, the $\hat{H}_{\text{S–B}}$ follows as, cf. Ref. [44],

$$\hat{H}_{\text{S–B}} = \sum_m \sum_\xi \hbar\omega_{m\xi} g_\xi(m) [\hat{b}_{m\xi} + \hat{b}^\dagger_{m\xi}] \hat{L}_m. \tag{3.13}$$

By definition, each molecular localized state $|m\rangle$ couples to an independent set of bath modes. The $g_\xi(m)$ represents a dimensionless vibronic coupling constant. It measures the strength of the fluctuation of energy E_m induced by the bath mode ξ of the mth molecule.

3.3.4. Correlation function and spectral density

The correlation function describes a fundamental quantity in the field of open quantum dynamics. Merged to a single quantity, it generally provides the complete information about the system–bath interaction processes according to Eq. 3.13. The form introduced next appears in the master equation discussed in Sec. 3.3.5 and plays an important role in the quantum state diffusion approach developed in Chap. 4.

Following the bilinear model of $\hat{H}_{\text{S–B}}$ (see Sec. 3.3.3), the correlation function is generally defined as [44]

$$C_{uv}(t,\tau) = \langle \hat{B}^{(\text{I})}_u(t) (\hat{B}^{(\text{I})}_v(\tau))^\dagger \rangle_{\text{B}} - \langle \hat{B}^{(\text{I})}_u(t) \rangle_{\text{R}} \langle (\hat{B}^{(\text{I})}_v(\tau))^\dagger \rangle_{\text{B}}. \tag{3.14}$$

The time–dependent bath coupling operators are introduced in the interaction picture as $\hat{B}^{(\text{I})}_u(t) = \hat{U}^+_{\text{S}}(t-t_0)\hat{U}^+_{\text{B}}(t-t_0)\hat{B}_u(t)\hat{U}_{\text{B}}(t-t_0)\hat{U}_{\text{S}}(t-t_0)$, where $U_{\text{S(B)}}(t-t_0) = \exp\{H_{\text{S(B)}}(t-t_0)/i\hbar\}$ is the time–evolution operator in the transfer system (bath) Hilbert space. Further, Eq. 3.14 makes use of $\langle ... \rangle_{\text{B}} = tr_{\text{B}}\{\hat{W}_{\text{eq}} ...\}$. It represents the expectation value with respect to the bath system degrees of freedom, based on the canonical bath density operator, $\hat{W}_{\text{eq}} = \mathfrak{Z}^{-1} e^{-\hat{H}_{\text{B}}/k_B T}$, with the partition function $\mathfrak{Z} = tr_{\text{B}}\{\exp(-\hat{H}_{\text{B}}/k_B T)\}$. In the form of Eq. 3.14, the $C_{uv}(t,\tau)$ correlates the fluctuation of $\hat{B}^{(\text{I})}_u(t)$ and $\hat{B}^{(\text{I})}_v(\tau)$ at two different times (with respect to their equilibrium values). Using the model in Eq. 3.13, the correlation function simplifies straightly to

$$C_m(t-\tau) = \frac{1}{\pi} \int_0^\infty d\omega J_m(\omega) \Big[(n(\omega)+1) e^{-i\omega(t-\tau)} + n(\omega) e^{i\omega(t-\tau)} \Big]. \tag{3.15}$$

The Bose–Einstein distribution is introduced as $n(\omega) = 1/(\exp\{\hbar\omega/k_B T\} - 1)$. Here, the bath operators are Hermitian which is why the correlation function depends not directly on t and τ, but only on their delay, i.e., $t-\tau$. A second subindex of $C_m(t,\tau)$ in Eq. 3.15 is directly removed due to the fact that exclusively intramolecular vibrational modes shall be considered, i.e., it is $C_{mn} = 0$ for $m \neq n$. Finally, the *spectral density* is introduced in Eq. 3.15. It is defined as

$$J_m(\omega) = \pi \sum_\xi \big(\hbar\omega_\xi g_m(\xi)\big)^2 \delta(\omega - \omega_\xi), \tag{3.16}$$

and compresses the spectrum of the electron–vibrational interaction strength expressed to functional form with $J_m(\omega) = 0$ for $\omega < 0$. Further computational details on $J_m(\omega)$ and $C_m(t-\tau)$ are stated in direct application in Chaps. 4, 7 and 8.

3.3.5. Master equations for weak system–bath coupling

The time–evolution of the RDO generally obeys Eq. 3.9, however it cannot be solved straightly. Instead, the involving second dissipative term must be subject to further treatment in order to find an adequate equation of motion. Typically, the dissipative term is reformulated in a perturbative expansion series with respect to $H_{\text{S–B}}$. Here, the concrete open system studies on charge and exciton transfer (see Chaps. 7 and 8) rely on the assumption of weak to moderate vibronic coupling strength. Correspondingly, the evolution of the reduced density matrix is adequately described in restriction to second order in $H_{\text{S–B}}$. Indeed, this second Born approximation represents the basic approach in application to molecular aggregates [45, 44]. Utilizing Eq. 3.13, the non–Markovian quantum master equation (QME) is found with,

$$\partial_t \hat{\rho}(t) = \frac{1}{i\hbar}\big[\hat{H}_{\text{S}}, \hat{\rho}(t)\big]_- - \frac{1}{\hbar^2}\sum_m \int_0^t d\tau \Big\{ C_m(\tau)\big[\hat{L}_m, \hat{U}_{\text{S}}^\dagger(\tau)\hat{L}_m\hat{\rho}(t-\tau)\hat{U}_{\text{S}}(\tau)\big]_- - C_m^*(\tau)\big[\hat{L}_m, \hat{U}_{\text{S}}^\dagger(\tau)\hat{\rho}(t-\tau)\hat{L}_m\hat{U}_{\text{S}}(\tau)\big]_- \Big\}. \quad (3.17)$$

Its second order character is covered in the correlation function $C_m(t)$ given in Eq. 3.15. As generally explained in Chap. 1, the numerical solution of the QME 3.17 suffers critically from very unfavorable scaling of computational cost with increasing size of the transfer system (see also Sec. 4.1). By that virtue, the application of Eq. 3.17 to larger systems becomes extremely inefficient and further simplification (e.g., concerning the memory kernel) are very likely in practice. As one of these, the Markov approximation is utilized in a great many cases in literature. Then the Eq. 3.17 transforms to the popular multilevel Redfield equations [44]. Additional introduction of the secular approximation would further transform the Redfield equations to the Bloch equation. The latter describes a very simple modeling, which is equivalent with the famous phenomenological Lindblad type of dissipation [45].

In this thesis, it is the intention to follow a fundamentally different strategy to compute large–scale open system dynamics in Chaps. 7 and 8. Instead of using approximations to essentially simplifiy the direct propagation of $\hat{\rho}(t)$, the above QME 3.17 is simulated indirectly based on the quantum state diffusion method in application of a stochastic Schrödinger equation (see Chap. 4). The difference to the QME lies basically in the fact that stochastic quantum state trajectories are simulated in Hilbert space. Such procedure, in principle, means a significantly advantaged scaling behavior which promises a substantial computational benefit concerning large–scale open systems compared with QME 3.17. Chap. 4 is devoted to that issue. A general debate on the equivalence of the quantum state diffusion method and the QME is given (see Sec. 4.2) and a particular algorithm is discussed which was specially developed in this work to unravel Eq. 3.17 with the intention to compute truly large–scale open system dynamics.

4. Quantum State Diffusion

The demand for computationally cheap and robust theoretical methodologies for studying open quantum system dynamics grows continuously. In what follows, a novel approach to a quantum state diffusion method with particularly cheap numerics is presented. Its enormous value lies in its specific applicability to extremely large–scale open systems including several thousand states. The presented strategy was published in Ref. [140] and represents a fundamental part of this thesis.

In very short terms, the quantum state diffusion method describes the quantum analogue to the famous Langevin theory in classical stochastic physics. In this sense, it allows unraveling open quantum system dynamics by means of stochastic state propagation in Hilbert space. Especially regarding large–scale systems, solving such a stochastic Schrödinger equation (SSE) means a clear numerical benefit compared with quantum master equations. Although the general concept of this is known for more than 30 years, so far it has been utilized only rarely in studies on truly large–scale systems. Only recently, a very promising approach was suggested based on a non–Markovian SSE. It was applied to studies on hot exciton and charge motion in a chain–like 1d system of up to 150 molecular sites. These publications motivated to work out an own novel strategy which allows for going beyond that scale and to study open quantum systems of several thousand states. The particular theoretical model and numerical routine is discussed in the framework of this chapter. Later on in Chaps. 7 and 8, it is applied to two gigantic systems of realistic size.

The chapter starts with an introductory part on the general principles and the theoretical background of the quantum state diffusion method (see Sec. 4.1). In Sec. 4.2, a microscopic ansatz for the transfer system and its environment is described in the weak coupling limit. The developed model is clearly related to existing approaches in literature. Then in Sec. 4.3, a Monte–Carlo integration scheme is introduced for proper stochastic reinterpretation of the analytic ansatz. It directly leads to the formulation of a linear type of SSE based on a stochastic force and a dissipative damping operator. The price for the linearity and the remarkable simple implementation of the obtained SSE is paid with a critical drift of the norm of the propagated state (see Sec. 4.4). In order to execute performance tests of different of such linear SSE algorithms, an additional nonlinear SSE is introduced. The latter brings with numerical stability but can only be applied to medium–scale systems. Therefore, the small Fenna–Matthews–Olson complex is chosen for first test simulations. A particular type of numerical force generation is figured out which results in excellent numerical performance of the cheap linear SSE. Finally in Sec. 4.6, a brief summary and a simple strategy for the adequate application of the linear SSE in cases of large–scale systems is exposed.

4.1. Background and Motivation

In general, the time–dependence of classical systems in interaction with an environment obeys the master equation

$$\frac{d}{dt}P_m(t) = \sum_n \left[r_{n\to m}P_n(t) - r_{m\to n}P_m(t)\right]. \tag{4.1}$$

It describes the evolution of the probability distribution, $P_m(t)$, with respect to the configuration space of the system (here with the discretized index m). Its apparent "gain–and–loss" structure with the transition rates, $r_{n\to m}$, preserves the positivity of each $P_m(t)$ in the same way as the norm of the total probabilty is guaranteed. These $r_{n\to m}$ quantize the influence of the environment on the system evolution. In the way of Eq. 4.1, the modeling of the system evolution is directly related to the probability distribution over the phase space. For instance, the Fokker–Planck equation discribes the random (Brownian) motion of a particle [141]. However, the solution resembles a continuous probability distribution and not a destinct trajectory. Hence, such ansatz must be understood as an ensemble related mean. The Langevin equation provides the alternative formalism from the single particle's perspective. While the Fokker–Planck equation concerns the time–dependence of the probability distribution, the Langevin approach directly formulates a random spatio–temporal evolution of a single particle. The influence of the environment is thereby modeled in terms of fluctuations introduced by a stochastic process (Wiener process). Both ansatzes to the stochastic behavior are *completely equivalent*. In fact, predictions on the probability distribution (over phase space) can be straightly prepared by means of a sufficiently large number of random trajectories (i.e., individual solution of the Langevin equation).

In the quantum domain, the reduced density operator (RDO), $\hat{\rho}(t)$, replaces the classical $P(t)$ (see Sec. 3.3.1). In 1976, Lindblad proposed its popular *axiomatic form* of a quantum master equation [142]. It was solely based on mathematical properties and expressed as

$$\frac{d}{dt}\hat{\rho}(t) = \frac{1}{i\hbar}[\hat{H}_{\mathrm{S}}, \hat{\rho}(t)] + \frac{1}{2\hbar^2}\sum_m \Big\{[\hat{L}_m, \hat{\rho}(t)\hat{L}_m^\dagger] + [\hat{L}_m\hat{\rho}(t), \hat{L}_m^\dagger]\Big\}, \tag{4.2}$$

with the system Hamiltonian, $\hat{H}_{\mathrm{S}}$, and certain bounded operators of the system Hilbert space, $\hat{L}_m$, with $\sum_m \hat{L}_m = \mathbf{1}$ (see, e.g., the projectors introduced in Sec. 3.3.3). The non–Hermitian term in the brackets represents again the typical "gain–and–loss" structure. The master equation 4.2 describes the most general approach of quantum Markovian master equations. In fact, a diversity of other master equations were developed starting from alternative more direct *constructive* ansatzes. One particular form of such master equations with a concrete ab–initio background is introduced in Sec. 3.3.5 (see Eq. 3.17). Nevertheless, at this place the above Lindblad form shall serve for convenient introduction of the principle aspects on quantum state diffusion ansatzes.

By analogy to the Langevin equation, alternative stochastic approaches to $\hat{\rho}(t)$ were uncovered in quantum theory. In particular, 10 years after the work of Lindblad, the

axiomatic *Ito–Schrödinger equation*[1] was worked out by Alicki et al. [143, 144]. It was designed as an Ito stochastic differential equation and follows as

$$\frac{d}{dt}|\psi(t)\rangle = \frac{1}{i\hbar}\hat{H}_{\mathrm{S}}|\psi(t)\rangle + \frac{1}{i\hbar}\sum_m \hat{L}_m|\psi(t)\rangle\frac{dB_m}{dt} - \frac{1}{2\hbar^2}\sum_m \hat{L}_m^\dagger \hat{L}_m|\psi(t)\rangle, \tag{4.3}$$

where the stochastic process dB_m/dt appears in form of a complex Wiener process (i.e., Gaussian white noise). According to the equivalence of Langevin and Fokker–Planck equation, the Ito–Schrödinger equation is totally equivalent with the above Lindblad equation 4.2. Indeed, the evolution of the RDO is straightly recovered in terms of the arithmetic mean operation $\mathscr{M}[...]$ with respect to the stochastic process, cf. Appendix F.1.1,

$$\frac{d}{dt}\hat{\rho}(t) = \frac{d}{dt}\mathscr{M}\Big[|\psi(t)\rangle\langle\psi(t)|\Big]. \tag{4.4}$$

This relation illustrates an essential goal of the *stochastic unraveling* of the RDO. In fact, the solution of the master equation 4.2, (i.e., its computational demand) scales with N^4 (where N describes the number of system states). Thereby, the power four scaling must be understood as numerical scaling. In fact, integration of the master equations requires computing the superoperator for time–evolution in Liouville space. Like the popular Redfield tensor (in matrix representation [44]), its computation scales with N^4 and so does the direct propagation of Eq. 4.2. In comparison to that, the computational cost of the wave function based equation 4.3 scales only with N^2. Like before this refers now to the computation of the time–evolution operator for a vector state in Hilbert space (which scales quadratically with N). In principle, this means that a computational benefit of Eq. 4.4 can be anticipated whenever the number M of required stochastic trajectories for $\mathscr{M}[...]$ (i.e., number of different solutions of Eq. 4.3) is smaller than N^2. In the framework of this thesis, a correspondingly promising ratio is generally found for systems with $N > 100$ (see Chaps. 7 and 8). Besides, it is another very important benefit of approaching Eq. 4.4 that simulations of individual stochastic trajectories can be executed trivialy on parallel computing infrastructures.

While the early works of Alicki et al. [143, 144] were originally proposed without physical background, Eq. 4.3 soon founds its way into concrete application studies on open quantum system – especially in the field of quantum optics [145, 146]. Several different and specific forms of Eq. 4.3 were established and are still frequently utilized or further developed nowadays.[2] In particular, in 1992 a series of several works by Gisin and Percival et al. started [149, 150, 151]. Physically relevant forms of Eq. 4.3 were discussed for the first time. By that, they prepared the Ito–Schrödinger equation

[1] Although the Heisenberg picture would be the more intuitive analogue to classical physics, the Schrödinger picture was followed instead. In fact, the Heisenberg representation would lead to substantial difficulties concerning the description of a stochastic process in terms of quantum noise operators. Compared to that, its modeling particularly simplifies to complex–valued random numbers when related to a wave function based description in the Schrödinger picture [46].

[2] One very prominent form is the Monte–Carlo wave function method developed by Carmichael et al. [147] and Dalibard et al. [148]. It is based on substitution of the axiomatic stochastic process (dB_m/dt in Eq. 4.3) by a (random) quantum–jump process. However, in the framework of this thesis the focus shall be further on diffusion–like descriptions of Eq. 4.3.

for open system simulations where the term *quantum state diffusion* was introduced. During these works, they proposed an alternative nonlinear equation based on the normalized wave function, $|\bar{\psi}(t)\rangle = |\psi(t)\rangle/|\psi(t)|$, according to,

$$\frac{d}{dt}|\bar{\psi}(t)\rangle = \frac{1}{i\hbar}\hat{H}_{\mathrm{S}}|\bar{\psi}(t)\rangle + \frac{1}{i\hbar}\sum_m (\hat{L}_m - \langle\hat{L}_m\rangle)|\bar{\psi}(t)\rangle\frac{dB_m}{dt} \\ + \frac{1}{\hbar^2}\sum_m \Big(\langle\hat{L}_m^\dagger\rangle\hat{L}_m - \frac{1}{2}\hat{L}_m^\dagger\hat{L}_m - \frac{1}{2}\langle\hat{L}_m^\dagger\rangle\langle\hat{L}_m\rangle\Big)|\bar{\psi}(t)\rangle. \tag{4.5}$$

Its nonlinearity is due to the occuring expectation values, $\langle ...\rangle = \langle\bar{\psi}(t)|...|\bar{\psi}(t)\rangle$. The evolution of the RDO is again recovered in terms of Eq. 4.4, where it is straightly proved that, despite the inclusion of the additional terms proportional to $\langle\hat{L}_m\rangle$ and $\langle\hat{L}_m^\dagger\rangle$, the Lindblad form of Eq. 4.2 is received straightly and it is again $\hat{\rho}(t) = \mathscr{M}[|\bar{\psi}(t)\rangle\langle\bar{\psi}(t)|]$ (see Appendix F.1.2). The development of Eq. 4.5 was motivated since the norm of the state $|\psi(t)\rangle$ in the linear Eq. 4.3 is not preserved during its evolution. The additional terms in Eq. 4.5 take care of this issue and intrinsically compensate the drift of the wave function norm (see Appendix F.2). On the one hand, Eq. 4.5 provides an essential goal concerning numerical simulations. On the other hand, this numerical stability is paid with the requirement to compute the less appealing nonlinear terms and the above described scaling benefit of the computational costs of Eq. 4.4 is lowered again.

Then in 1997, the exclusively axiomatic descriptions of the quantum state diffusion methods were basically supported by Strunz and Diósi et al. [47, 48]. Together, they presented the first of many theoretical studies on a *constructive* approach and worked out the first ab–initio ansatz of the quantum state diffusion based on an uniform microscopic model of the open system together and its environment. Their description started directly with the time–dependent Schrödinger equation of the complete system (and the bilinear coupling model discussed in Sec. 3.3.3). In the end, a generalization of Eq. 4.3 (and Eq. 4.5) was obtained, which they called the *non–Markovian stochastic Schrödinger equation*,

$$\frac{d}{dt}|\psi_z(t)\rangle = \frac{1}{i\hbar}\Big(\hat{H}_{\mathrm{S}} + \sum_m \hat{L}_m z_m(t)\Big)|\psi_z(t)\rangle - \frac{1}{\hbar^2}\sum_m \hat{L}_m^\dagger\int_0^t d\tau C_{T=0}(t-\tau)\frac{\delta|\psi_z(t)\rangle}{\delta z_m(\tau)}. \tag{4.6}$$

Thereby, the function $z_m(t)$ takes over the role of the former stochastic process dB_m/dt. The integral term in Eq. 4.6 contains the correlation function at zero–temperature (see Eq. 3.15) and the non–trivial functional derivative of the state vector with respect to the stochastic process $z(t)$. This term represents the generalized non–Markovian "memory kernel". In order to derive more appealing forms, Strunz and Diósi et al. substituted the functional derivative by the action of an operator in terms of $\frac{\delta|\psi_z(t)\rangle}{\delta z(\tau)} = O(t,\tau,z)|\psi_z(t)\rangle$. This was the central point of their model. Although the operator $O(t,\tau,z)$ is generally unknown, appealing approximate expressions can be straightly deduced by different expansion ansatzes. For instance, the axiomatic model of quantum state diffusion (see Eq. 4.3) could be recovered in assumption of a Markovian bath which is weakly coupled to the system [152, 153, 154, 155, 156, 157, 158, 159]. Further, Strunz and Diósi et

al. honoured the work of Gisin and Percival and developed a nonlinear non–Markovian stochastic Schrödinger equation [47, 155]. Accordingly, this version preserves the norm of the state trajectory in course of time–evolution and generalizes the Markovian nonlinear equation 4.5.

Recently, Zhao and Zhong et al. presented a series of application related studies of a *time–dependent wavepacket diffusion method* on energy migration and charge carrier transport in realistic molecular systems [160, 49, 50, 51]. They utilized a microscopic ansatz related to the one of Refs. [47, 48], but other argumentation led them to an equation (in the weak coupling limit) which is not strictly obtained from Eq. 4.6. In their studies, they presented results obtained from a linear equation of motion, i.e., without the intrinsic feature of the norm–conservation. Nevertheless, very convincing kinetics of energy relaxation within the popular Fenna–Matthews–Olson chromophore complex were shown from their linear approach [49].

The present chapter is devoted to a novel convenient simulation technique based on a stochastic Schrödinger equation approach. Its development describes an essential part of this thesis. From the beginning, it is the intention to establish a methodology which is ready for application to large–scale open quantum systems including several thousand states using standard computational work stations. As motivated above, therefore the focus is directly on the development of a linear stochastic Schrödinger equation method which computational demand scales only with N^2. The works of Zhao and Zhong et al. (particularly Ref. [49] served as important inspiration for that). However, as already indicated above, the studies of Strunz and Diósi et al. give rise to some questions concerning the treatment in Ref. [49]. In this regard, the approach of Zhao and Zhong et al. is supplemented here. Special modifications are introduced following the basic concepts of Refs. [47, 48, 152, 153, 154, 155, 156, 157, 158, 159] and also new ideas by own work are incorporated. By that, different uncertain aspects of the former works are clarified.

The following ansatz directly formulates a temperature–dependent wave function trajectory. This differs from the methods of Refs. [160, 49, 50, 51] as well as the one followed in Refs. [48, 157]. Here, it turns out to be very instructive for a consequent introdcution of a temperature–dependent stochastic force (which finally acts on the quantum particle) in terms of a Monte–Carlo integration scheme. Additionally, it was of particular interest to find a possible interrelation of the existing types of stochastic Schrödinger equations (the one derived in Refs. [47, 48] and the one proposed in Ref. [49]). Such a relationship is demonstrated here in the limit of weak system–bath coupling. Finally, the here developed approach is integrated in a general strategy for highly efficent computations of non–Markovian open system dynamics including more than 1000 states. Therefore, a practical implementation guide of a linear stochastic Schrödinger equation method is offered and the varying norm of the propagated quantum state is considered carefully. Its numerical computational cost scales quadratically. This is pioneering and describes an enormous step forward in the field of open system dynamics.

In Chap. 7, the workability of the discussed treatment is demonstrated in detail when studying dissipative charge carrier kinetics within an aggregate of 2553 *para*–sexiphenyl molecules on a ZnO interface. In a second study, the developed scheme is applied to

investigate energy relaxation processes in an even larger tubular dye aggregate of 4140 molecules (see Chap. 8). Both numbers are one order of magnitude larger and outstanding in comparison with existing work on an equivalent level of theory (see for comparison, e.g., Refs. [49, 50, 53, 51, 161, 54]). The here developed scheme demonstrates that existing numerical limitations of computationally inefficent conventional approaches can be overcome and that novel large–scale and non–Markovian dynamics can be achieved in future.

4.2. System and Bath in the Schrödinger Picture

In the following, a Schrödinger equation for an open system "conditioned" by its surrounding bath is developed. In Sec. 4.3, the outcome of this section is reinterpreted in a stochastic sense. This finally results in the non–Markovian stochastic Schrödinger equation (SSE).

The general concept of open quantum systems and related dynamics are discussed in the framework of Sec. 3.3. The system–bath Hamiltonian is introduced as the sum $\hat{H} = \hat{H}_{\mathrm{S}} + \hat{H}_{\mathrm{B}} + \hat{H}_{\mathrm{S–B}}$ (see Eq. 3.6), with the Hamiltonian of the "active" transfer system, $\hat{H}_{\mathrm{S}}$ (see Eq. 3.7), and the Hamiltonian of the heat bath, $\hat{H}_{\mathrm{B}}$ (see Eq. 3.12). Further, the system–bath interaction is collected in the third term, $\hat{H}_{\mathrm{S–B}}$ (see Eq. 3.13). All three parts are specified according to the bilinear coupling model (see Sec. 3.3.1). In particular, the system–bath coupling is introduced as, cf. Eq. 3.13,

$$\hat{H}_{\mathrm{S–B}} = \sum_{m,\xi} \mathscr{K}_{m\xi}(\hat{b}_{m\xi} + \hat{b}^{\dagger}_{m\xi})\hat{L}_m, \tag{4.7}$$

with the oscillator creation and annihilation operators $\hat{b}^{\dagger}_{m\xi}$ and $\hat{b}_{m\xi}$, respectively. They refer to the bath vibrational mode ξ coupled to the mth state of the active system. The related frequency is indicated by $\omega_{m\xi}$. Further, the system coupling operator is reduced to the diagonal form,

$$\hat{L}_m = |m\rangle\langle m|. \tag{4.8}$$

In general, this type of system–bath interaction model has a long history. In the field of quantum state diffusion, it was extensively discussed by Diósi, Strunz, Gaspard or Eisfeld et al. [47, 48, 152, 153, 154, 155, 156, 157, 158, 159].

4.2.1. Coherent state unraveling of the reduced density operator

The SSE presented in the following is mainly motivated by the work of Zhao et al. [160, 49, 50, 51]. The general ansatz, however, was originally presented in the earlier studies of Diósi and Strunz et al. [47, 48, 155]. According to the latter, a typical approach starts with applying the interaction picture with respect to $\hat{H}_{\mathrm{S–B}}$ and describing the bath environment in terms of Bargmann coherent states, according to $|\alpha_{m\xi}\rangle = \exp(\alpha_{m\xi}\hat{b}^{\dagger}_{m\xi})|0\rangle$ [146]. The latter states correspond to the various intramolecular vibrational modes. The $\alpha_{m\xi}$ are complex numbers and it is $\hat{b}_{m\xi}|\alpha_{m\xi}\rangle = \alpha_{m\xi}|\alpha_{m\xi}\rangle$. The coherent state ansatz makes possible a straight and instructive expansion series of

the wave function trajectories with respect to the system–bath interaction. Here, the coherent states are used to express the RDO, $\hat{\rho}(t)$ (see Sec. 3.3.1). This is one possible way for an appealing stochastic unraveling of the RDO later on.[3]

The RDO in the interaction representation (note the index I, cf. Eq. 3.14) reads

$$\hat{\rho}^{(\mathrm{I})}(t) = \mathrm{tr}_{\mathrm{R}}\{\hat{S}(t,0)|\psi(0)\rangle\langle\psi(0)|\hat{R}_{\mathrm{eq}}\hat{S}^{\dagger}(t,0)\}. \tag{4.9}$$

The operator $\hat{S}(t,0) = \hat{T}\exp\{-i\int_0^t d\tau\ H^{(\mathrm{I})}_{\mathrm{S\text{-}B}}(\tau)/\hbar\}$ performs the time–evolution of the complete statistical operator $\hat{W}^{(\mathrm{I})}(t)$ starting from $\hat{W}^{(\mathrm{I})}(0) = |\psi(0)\rangle\langle\psi(0)|\hat{R}_{\mathrm{eq}}$. In this form, the transfer system is initially prepared in the pure state $|\psi(0)\rangle$ and decoupled from the surrounding bath. The latter is in thermal equilibrium at temperature T. Correspondingly, the bath statistical operator $\hat{R}_{\mathrm{eq}} = 1/\mathfrak{Z} \times \exp(-H_{\mathrm{B}}/k_{\mathrm{B}}T)$ appears. The trace in Eq. 4.9 (with respect to the bath states) can be computed straightly making use of the completeness relation of the coherent states,

$$\hat{\mathbf{1}} = \prod_{m,\xi}\frac{1}{\pi}\int d^2\alpha_{m\xi}e^{-|\alpha_{m\xi}|^2}|\alpha_{m\xi}\rangle\langle\alpha_{m\xi}| \equiv \int d\alpha e^{-|\alpha|^2}|\alpha\rangle\langle\alpha|. \tag{4.10}$$

Here and in the following the multi–site and multi–mode integration is abbreviated by a single complex α–integral (including all the $1/\pi$). Moreover, the $|\alpha\rangle$ stands for the whole product state, and the shorthand notation $|\alpha|^2 = \sum_{m,\xi}|\alpha_{m\xi}|^2$ is introduced. Making use of some further algebra leads straightly to the RDO represented as (see Supporting Information of Ref. [140]),

$$\hat{\rho}^{(\mathrm{I})}(t) = \int d\alpha \int d\beta\ e^{-|\alpha|^2-|\beta|^2}|\psi_{\alpha\beta}(t)\rangle\langle\psi_{\alpha\beta}(t)| \equiv \mathscr{M}\Big[|\psi_{\alpha\beta}(t)\rangle\langle\psi_{\alpha\beta}(t)|\Big]. \tag{4.11}$$

The expression on the right hand side indicates that all the information of the RDO is now translated to the state vectors,

$$|\psi_{\alpha\beta}(t)\rangle = \langle\alpha|\hat{S}(t)|\theta\beta\rangle|\psi(0)\rangle/\sqrt{\mathfrak{Z}}. \tag{4.12}$$

The ket $|\theta\beta\rangle$ abbreviates the multitude of states $|\theta_{m\xi}\beta_{m\xi}\rangle$ with $\theta_{m\xi} = \exp\{-\hbar\omega_{m\xi}/k_{\mathrm{B}}T\}$. The state vector $|\psi_{\alpha\beta}(t)\rangle$ is exclusively defined in the system Hilbert space. However, it is conditioned by the presence of bath which is indicated by the dependences on α and β. A Gaussian averaging with respect to the multiple dependencies on the $\alpha_{m\xi}$ and $\beta_{m\xi}$ defines the RDO $\hat{\rho}^{(\mathrm{I})}(t)$. The $\mathscr{M}[...]$ in Eq. 4.11 symbolizes the related multidimensional Gaussian weighted mean value operation.

The here presented relation differs crucially from the one used by Zhao et al. [49]. In particular, Eq. 4.11 describes a simple Gaussian averaging which is independent on T. All the temperature dependence is condensed in $|\psi_{\alpha\beta}(t)\rangle$. Contrarily to that, the approach in Ref. [49] starts with a quantum trajectory which shows no temperature dependence at all, while the Gaussian averaging process is temperature dependent. To finally fix this, in Ref. [49] an expression for temperature dependent state trajectories is finally introduced phenomenologically.

[3] Alternatively, e.g., a path–integral approach can be applied to formulate a more generalized derivation with identical result [47, 48, 155].

In order to determine the kinetics of the RDO according to Eq. 4.11, the evolution of $|\psi_{\alpha\beta}(t)\rangle$ is required in dependence on the complex numbers α and β. Hence, an equation of motion for $|\psi_{\alpha\beta}(t)\rangle$ must be deduced. By taking the time–derivative of Eq. 4.12, one directly obtains in a first step

$$i\hbar\frac{\partial}{\partial t}|\psi_{\alpha\beta}(t)\rangle = \sum_{m,\xi}\left(\hat{A}_{m\xi}(t) + \hat{D}_{m\xi}(t)\right)|\psi_{\alpha\beta}(t)\rangle \;, \tag{4.13}$$

based on the two introduced operator definitions,

$$\hat{A}_{m\xi}(t) = \mathcal{K}_{m\xi}\hat{L}_m(t)e^{i\omega_{m\xi}t}\alpha^*_{m\xi} \tag{4.14}$$

and

$$\hat{D}_{m\xi}(t) = \mathcal{K}_{m\xi}\hat{L}_m(t)e^{-i\omega_{m\xi}t}\frac{\partial}{\partial\alpha^*_{m\xi}}, \tag{4.15}$$

with $\hat{L}_m(t) \equiv \hat{L}^{(\mathrm{I})}_m(t)$ (see Eq. 3.14). Besides, a third operator,

$$\hat{B}_{m\xi}(t) = \mathcal{K}_{m\xi}\hat{L}_m(t)e^{i\omega_{m\xi}t}\beta^*_{m\xi}, \tag{4.16}$$

is employed later on. The partial derivatives which appears in $\hat{D}_{m\xi}(t)$ let become Eq. 4.13 clearly less suited for further analysis. It is the next task to replace them by a perturbative expansion ansatz.

So far, the approach Eq. 4.13 is in close relation to the ansatz presented by Strunz et al. [155] and identical finite temperature SSE expressions are finally obtained. However, the explicit inclusion of the temperature in the present ansatz describes a novel feature. Contrarily to that, the finite temperature description in Refs. [155, 48, 157] was finally introduced by applying a Bogoliubov transformation to the bath ladder operators of their original zero–temperature model. Such transformation is not required here because the trajectory is already considerd as a finite temperature expression (see Eq. 4.12).

Different strategies to handle the derivative term in Eq. 4.13 are conceivable. For instance, in Ref. [48] (and other studies of Strunz, Diósi and Gisin et al.), this term is first reinterpreted as a functional derivative term which then allows developing more appealing expressions. Most sophisticated, the non–perturbative hierachical equation of motion approach could be derived based on such transformation step [162]. Another approximate approach was used by Zhao et al. [49] on their temperature independent form of Eq. 4.13 which contained a similar derivative term. They simplified that term by means of an expansion with respect to the system–bath coupling. In what follows, a likewise perturbative treatment is worked out with respect to the system–bath interaction. However, now the expansion is collectively applied to the complete expression Eq. 4.12.

In the present interaction picture, expansion with respect to time equals expansion with respect to system–bath interaction. An adequate approximate form of the state

trajectory $|\psi_{\alpha\beta}(t)\rangle$ (see Eq. 4.12) is thus straightly achieved with the time–series

$$|\psi_{\alpha\beta}(t)\rangle \approx \Big\{\mathbf{1} + \frac{1}{i\hbar}\int_0^t d\tau \sum_{m,\xi}\Big[\hat{A}_{m\xi}(\tau) + \hat{D}_{m\xi}(\tau)\Big] \tag{4.17}$$
$$+ \frac{1}{(i\hbar)^2}\int_0^t d\tau \int_0^\tau d\tau' \sum_{m,\xi}\sum_{n,\zeta}\Big[\hat{A}_{m\xi}(\tau)\hat{A}_{n\zeta}(\tau') + \hat{D}_{m\xi}(\tau)\hat{D}_{n\zeta}(\tau')$$
$$+ \hat{D}_{m\xi}(\tau)\hat{A}_{n\zeta}(\tau') + \hat{A}_{m\xi}(\tau)\hat{D}_{n\zeta}(\tau')\Big]\Big\}|\psi_{\alpha\beta}(0)\rangle,$$

which results formally from an integration scheme of Eq. 4.13 up to second order terms. This stands in clear contrast to the Ref. [49]. Instead, it was inspired by a perturbative ansatz applied in Ref. [158]. Now realizing that it is $|\psi_{\alpha\beta}(t=0)\rangle = \exp\{\theta\alpha^*\beta\}|\psi(0)\rangle/\sqrt{\mathfrak{E}}$ (see Eq. 4.12), the action of the derivative terms $\hat{D}_{m\xi}(t)$ is straightly replaced by the (derivation free) projector–type operators $\hat{B}_{m\xi}(t)$ already introduced in Eq. 4.16. The time–derivative of Eq. 4.17 leads then to the second order expression

$$\frac{\partial}{\partial t}|\psi_{\alpha\beta}(t)\rangle \approx \Big\{\frac{1}{i\hbar}\sum_{m,\xi}\Big[\hat{A}_{m\xi}(t) + \theta_{m\xi}\hat{B}^*_{m\xi}(t) + \frac{1}{i\hbar}\int_0^t d\tau \mathcal{K}^2_{m\xi}\hat{L}_m(\tau)\hat{L}_m(\tau')e^{-i\omega_{m\xi}(t-\tau)}\Big] \tag{4.18}$$
$$+\frac{1}{(i\hbar)^2}\sum_{m,\xi}\sum_{n,\zeta}\int_0^t d\tau\Big[\hat{A}_{m\xi}(t)\hat{A}_{n\zeta}(\tau) + \theta_{m\xi}\theta_{n\zeta}\hat{B}^*_{m\xi}(t)\hat{B}^*_{n\zeta}(\tau)$$
$$+ \theta_{n\zeta}\hat{A}_{m\xi}(t)\hat{B}^*_{n\zeta}(\tau) + \theta_{m\xi}\hat{A}_{n\zeta}(\tau)\hat{B}^*_{m\xi}(t)\Big]\Big\}|\psi_{\alpha\beta}(0)\rangle.$$

4.2.2. Weak system–bath coupling

Perturbative ansatzes for the RDO are commonly introduced up to second order [44, 45]. An equivalent level of accuracy shall be achieved here by considering the expression

$$\frac{\partial}{\partial t}\hat{\rho}^{(\mathrm{I})}(t) = \mathscr{M}\Big[\big[\frac{\partial}{\partial t}|\psi_{\alpha\beta}(t)\rangle\big]\langle\psi_{\alpha\beta}(t)|\Big] + \text{H. c.}. \tag{4.19}$$

It results directly as the derivative of Eq. 4.11 and represents the general form of a master equation. A strict restriction of Eq. 4.19 up to second order can be formulated when inserting the expansion series given in Eq. 4.18. For this purpose, several redundant terms in Eq. 4.18 can be figured out and a correspondingly simplified but equivalent version of Eq. 4.18 can be introduced.

Therefore, one firstly notices the product form of $|\psi_{\alpha\beta}(t)\rangle$ and its derivative in $\partial_t\hat{\rho}^{(\mathrm{I})}(t)$. Concerning the state expansion Eq. 4.18, now only these terms are relevant which finally contribute to terms of second order (or below) in $\partial_t\hat{\rho}^{(\mathrm{I})}(t)$. Vice versa, all terms which exclusively contribute to higher order terms in $\partial_t\hat{\rho}^{(\mathrm{I})}(t)$ describe only irrelevant corrections and can be excluded right in the expansion series of Eq. 4.18. For this reason, a second order ansatz in Eq. 4.18 is generally sufficient. Closer examination uncovers that further terms in the second and third line of Eq. 4.18 can be eliminated. Therefore, one has to realize their dependences on α and β together

with the Gaussian averaging in Eq. 4.19. In fact, all of them are already of second order and must be attended in $\partial_t\hat{\rho}^{(\mathrm{I})}(t)$ only as products with the respective zero order counterpart of $|\psi_{\alpha\beta}(t)\rangle$. The majority of these product terms average to zero. In particular, all terms from the second line in Eq. 4.18 disappear in $\partial_t\hat{\rho}^{(\mathrm{I})}(t)$ due to $\mathscr{M}[\hat{A}_{m\xi}(t)\hat{A}_{n\zeta}(\tau)|\psi_{\alpha\beta}(0)\rangle\langle\psi_{\alpha\beta}(0)|]_{\alpha\beta} = 0$ and $\mathscr{M}[\hat{B}_{m\xi}(t)^*\hat{B}_{n\zeta}(\tau)^*|\psi_{\alpha\beta}(0)\rangle\langle\psi_{\alpha\beta}(0)|]_{\alpha\beta} = 0$. Non–vanishing contributions of these terms are at least of fourth order in $\partial_t\hat{\rho}^{(\mathrm{I})}(t)$ [140]. Similar restrictions can be applied concerning the remaining terms in the third line of Eq. 4.18. These terms are of the type $\mathscr{M}[\hat{A}_{m\xi}(t)\hat{B}^*_{n\zeta}(\tau)|\psi_{\alpha\beta}(0)\rangle\langle\psi_{\alpha\beta}(0)|]_{\alpha\beta}$, where one notices that only terms with $m,\xi = n,\zeta$ give non–zero contribution. So, removing all remaining terms with $m,\xi \neq n,\zeta$ in Eq. 4.18 is adequate as well. Together, the "adjusted" version of Eq. 4.18 is found as

$$\begin{aligned}\frac{\partial}{\partial t}|\psi_{\alpha\beta}(t)\rangle \approx \Big\{ &\frac{1}{i\hbar}\sum_{m,\xi}\Big[\hat{A}_{m\xi}(t) + \theta_{m\xi}\hat{B}^*_{m\xi}(t) + \frac{1}{i\hbar}\int_0^t d\tau \mathscr{K}^2_{m\xi}\hat{L}_m(\tau)\hat{L}_m(\tau')e^{-i\omega_{m\xi}(t-\tau)}\Big] \\ &+ \frac{1}{(i\hbar)^2}\sum_{m,\xi}\int_0^t d\tau\Big[\theta_{m\xi}\hat{A}_{m\xi}(t)\hat{B}^*_{m\xi}(\tau) + \theta_{m\xi}\hat{A}_{m\xi}(\tau)\hat{B}^*_{m\xi}(t)\Big]\Big\}|\psi_{\alpha\beta}(0)\rangle.\end{aligned} \tag{4.20}$$

(Please note that the former wave function notation, $\psi_{\alpha\beta}(t)$, is kept for convenience.) The Eq. 4.20 describes a remarkable simplification with respect to Eq. 4.18. Nevertheless, it generates the identical master equation 4.19 in second order perturbation theory. The presented considerations can be straightly generalized and also applied to unravel higher order master equations.

4.2.3. Preparation of the initial state vector

Next, the $|\psi_{\alpha\beta}(t)\rangle$ is normalized to a state which is initially independent on α and β. Such transformational step is sensible with regard to an equation of motion of practical use (see Sec. 4.2.4). In particular, it ensures physical and identical initial conditions independent on the influence of the bath. The initially normalized state is found directly with

$$|\tilde{\psi}_{\alpha\beta}(t)\rangle = \sqrt{\mathfrak{X}}/\langle\alpha|\theta\beta\rangle \times |\psi_{\alpha\beta}(t)\rangle. \tag{4.21}$$

Correspondingly, the master equation 4.19 must be adapted. It reexpresses as

$$\frac{\partial}{\partial t}\hat{\rho}^{(\mathrm{I})}(t) = \tilde{\mathscr{M}}\Big[\big[\frac{\partial}{\partial t}|\tilde{\psi}_{\alpha\beta}(t)\rangle\big]\langle\tilde{\psi}_{\alpha\beta}(t)|\Big] + \mathrm{H.\,c.}, \tag{4.22}$$

with the trajectories following from Eq. 4.21. The usage of $|\tilde{\psi}_{\alpha\beta}(t)\rangle$ must be compensated by substitution of the former Gaussian averaging (see Eq. 4.11), according to

$$\tilde{\mathscr{M}}[...] = \mathscr{M}\Big[|\langle\alpha|\theta\beta\rangle|^2/\mathfrak{X} \times ...\Big]. \tag{4.23}$$

In order to return again to the more straight Gaussian averaging of type $\mathscr{M}[...]$, the helpful integral transformations of the type,

$$\tilde{\mathscr{M}}\left[\alpha_{m\xi}\alpha^{*}_{n\zeta}\right] = \mathscr{M}\Big[\sqrt{1+n_{m\xi}}\;\alpha_{m\xi}\sqrt{1+n_{n\zeta}}\alpha^{*}_{n\zeta}\;\Big], \tag{4.24}$$

can be employed. The $n_{m\xi} = 1/(\exp\{\hbar\omega_{m\xi}/k_{\mathrm{B}}T\}-1)$ abbreviate the Bose–Einstein distributions at frequency $\omega_{m\xi}$. Analogue integral translation rules are available to translate back all terms in Eq. 4.22 in similar way to the more appealing averaging operation $\mathscr{M}[...]$ (see also Supplementing Materials in Ref. [140]). As the result of the simple transformation one finds the form

$$\frac{\partial}{\partial t}\hat{\rho}^{(\mathrm{I})}(t) = \mathscr{M}\Big[\big[\frac{\partial}{\partial t}|\phi^{(\mathrm{I})}_{\alpha\beta}(t)\rangle\big]\langle\phi^{(\mathrm{I})}_{\alpha\beta}(t)|\Big] + \text{H. c.}, \tag{4.25}$$

which is equivalent with Eq. 4.22 (and Eq. 4.19). The new wave function state $|\phi^{(\mathrm{I})}_{\alpha\beta}(t)\rangle$ is introduced. Its time–evolution obeys

$$\begin{aligned}\frac{\partial}{\partial t}|\phi^{(\mathrm{I})}_{\alpha\beta}(t)\rangle =& \Big\{\frac{1}{i\hbar}\sum_{m,\xi}\sqrt{1+n_{m\xi}}\Big(\hat{A}_{m\xi}(t)+\theta_{m\xi}\hat{B}^{*}_{m\xi}(t)\Big)\\ &+\frac{1}{(i\hbar)^2}\int_0^t d\tau\sum_{m,\xi}\mathscr{K}^2_{m\xi}\hat{L}_m(t)\hat{L}_m(\tau)\Big[(1+n_{m\xi})\theta^2_{m\xi}\big(e^{-i\omega_{m\xi}(t-\tau)}+e^{i\omega_{m\xi}(t-\tau)}\big)\\ &+e^{-i\omega_{m\xi}(t-\tau)}\Big]\Big\}|\phi_{\alpha\beta}(0)\rangle,\end{aligned} \tag{4.26}$$

The $n_{m\xi}$ appears now directly in the prefactors of the terms.[4] The explicit label (I) is reapplied in Eq. 4.26 to remind on interaction representation. A more convenient version of Eq. 4.26 is obtained when introducing the functions

$$\eta^{+}_{m}(t;\alpha) = \sum_{\xi}\mathscr{K}_{m\xi}\sqrt{1+n_{m\xi}}\alpha_{m\xi}e^{-i\omega_{m\xi}t}, \tag{4.27}$$

and

$$\eta^{-}_{m}(t;\beta) = \sum_{\xi}\mathscr{K}_{m\xi}\sqrt{n_{m\xi}}\beta_{m\xi}e^{-i\omega_{m\xi}t}. \tag{4.28}$$

Insertion of Eqs. 4.27 and 4.28 in Eq. 4.26 gives

$$\begin{aligned}\frac{\partial}{\partial t}|\phi^{(\mathrm{I})}_{\alpha\beta}(t)\rangle =& \Big\{\frac{1}{i\hbar}\sum_{m}\Big(\big(\eta^{+}_{m}(t;\alpha)\big)^{*}\hat{L}_m(t)+\eta^{-}_{m}(t;\beta)\hat{L}_m(t)\Big)\\ &+\frac{1}{(i\hbar)^2}\int_0^t d\tau\sum_{m}C_m(t-\tau)\hat{L}_m(t)\hat{L}_m(\tau)\Big\}|\phi_{\alpha\beta}(0)\rangle.\end{aligned} \tag{4.29}$$

[4] Please note that the latter transformation affects not the initial form of the state vector. As achieved above, the latter is free of α and β–dependences and therefore directly recaptured as $|\phi^{(\mathrm{I})}_{\alpha\beta}(t=0)\rangle \equiv |\psi(0)\rangle$ (see Eqs. 4.21 and 4.12).

The correlation function of the system–bath coupling,

$$C_m(t) = \sum_\xi \mathscr{K}_{m\xi}^2 \big[(1+n_{m\xi})e^{-i\omega_{m\xi}t} + n_{m\xi}e^{i\omega_{m\xi}t}\big], \tag{4.30}$$

is finally identified in Eq. 4.26 and introduced according to Eq. 3.15.

4.2.4. Equation of motion

In the following, it is the task to establish an equation of motion for computational determination of $|\phi^{(\mathrm{I})}_{\alpha\beta}(t)\rangle$. Therefore, the Eq. 4.29 shall be moved back to the Schrödinger picture (based on $|\phi_{\alpha\beta}(t)\rangle = \hat{U}_\mathrm{S}(t)|\phi^{(\mathrm{I})}_{\alpha\beta}(t)\rangle$). In the Schrödinger picture, the term $\hat{L}_m(t)|\phi_{\alpha\beta}(0)\rangle$ can be approximated by $\hat{U}_\mathrm{S}^\dagger(t)\hat{L}_m|\phi_{\alpha\beta}(t)\rangle$. The involved replacement of $\hat{U}_\mathrm{S}(t)|\phi_{\alpha\beta}(0)\rangle$ by the complete wave function at t (i.e., by $|\phi_{\alpha\beta}(t)\rangle$) goes along with the consequent second order treatment of the system–bath coupling started in Sec. 4.2.2. This can be realized immediately by introducing $|\phi_{\alpha\beta}(t)\rangle = \hat{\mathcal{U}}(t,\tau)|\phi_{\alpha\beta}(\tau)\rangle$, with the exact time–evolution operator, $\hat{\mathcal{U}}(t,\tau) = \hat{T}\exp\{-\frac{i}{\hbar}\int_\tau^t d\tau'\,[\hat{H}_\mathrm{S} + \hat{H}^{(\mathrm{I})}_{\mathrm{S\text{–}B}}(\tau')]\}$ (taken in the partial interaction picture). When expressed as expansion series with respect to the system–bath coupling, the evolution of the state follows as

$$|\phi_{\alpha\beta}(t)\rangle = \hat{U}_S(t-\tau)\Big(\mathbf{1} + \mathcal{O}\big[K_{m\xi}\big] + ...\Big)|\phi_{\alpha\beta}(\tau)\rangle. \tag{4.31}$$

According to the argumentation in Sec. 4.2.2, it is possible to restrict the time–evolution on the right hand side of Eq. 4.29 in zeroth order (with respect to $\hat{H}_{\mathrm{S\text{–}B}}$), i.e., to approximately apply $|\phi_{\alpha\beta}(t)\rangle \approx U_S(t)|\phi_{\alpha\beta}(0)\rangle$. In particular, concerning the last term in Eq. 4.29, substitution of $\hat{L}_m(t)\hat{L}_m(\tau)|\phi_{\alpha\beta}(0)\rangle$ by $\hat{L}_m U_\mathrm{S}(t-\tau)\hat{L}_m|\phi_{\alpha\beta}(\tau)\rangle$ is possible when changing to the Schrödinger picture. The latter term is further identical with $\hat{L}_m\hat{L}_m(\tau-t)|\phi_{\alpha\beta}(t)\rangle$. An equivalent argumentation is employed by Vega et al. [158] with the purpose to generate a more appealing *time–convolution less* equation of motion (though they start from a different approach). One finally arrives at the equation of motion[5]

$$i\hbar\frac{\partial}{\partial t}|\phi_{\alpha\beta}(t)\rangle = (\hat{H}_\mathrm{S} + \hat{\mathscr{F}}(t;\alpha,\beta) - i\hbar\hat{\mathscr{D}}(t))|\phi_{\alpha\beta}(t)\rangle. \tag{4.32}$$

In second order approximation, it unravels the finite temperature RDO by the simple mean

$$\hat{\rho}(t) = \mathscr{M}\big[|\phi_{\alpha\beta}(t)\rangle\langle\phi_{\alpha\beta}(t)|\big]. \tag{4.33}$$

The compact function

$$\hat{\mathscr{F}}(t;\alpha,\beta) = \sum_m \mathscr{F}_m\hat{L}_m = \sum_m \Big(\big(\eta_m^+(t;\alpha)\big)^* + \eta_m^-(t;\beta)\Big)\hat{L}_m, \tag{4.34}$$

[5] Please note that also a substitution of τ in Eq. 4.29 by the new integration variable $\bar{t} = t - \tau$ is utilized to arrive at Eq. 4.32.

based on the terms Eqs. 4.27 and 4.28 is introdcued. For later purpose, further Eq. 4.32 makes use of the expression

$$\hat{\mathscr{D}}(t) = \frac{1}{\hbar^2}\int_0^t d\bar{t}\ \sum_m C_m(\bar{t})\hat{L}_m\hat{L}_m(-\bar{t}). \tag{4.35}$$

Solving the equation of motion 4.32 is fundamental to unravel the RDO. However, the $\hat{\mathscr{F}}(t;\alpha,\beta)$ depends on the continuous variables α and β and any concrete computation would require an infinite number of wave function trajectories. So far, the Eq. 4.32 is only of analytical but not of practical use. To change this, the $\hat{\mathscr{F}}(t;\alpha,\beta)$ and the mean operation, $\mathscr{M}[...]$, must be approached in a stochastic scheme instead. In particular, in Sec. 4.3 the $\hat{\mathscr{F}}(t;\alpha,\beta)$ is reinterpreted as a fluctuative function $\hat{\mathscr{F}}(t;z)$, which depends no longer on α and β but on a stochastic process indicated by z. The equation of motion 4.32 appears then as a stochastic Schrödinger equation. Thereby, analogously to the Langevin theory of (classical) Brownian motion [141]), the $\mathscr{F}_m(t,z)$ represents a random influence of the bath acting on the system realizing the state $|m\rangle$. The collective stochastic *driving force* of $\hat{\mathscr{F}}(t)$ on the system is accompanied by $\hat{\mathscr{D}}(t)$. It describes the corresponding *damping process* (or friction). Here, $\hat{\mathscr{D}}(t)$ takes the form of a non–Markovian integral kernel including the finite temperature system–bath correlation function, $C_m(t)$.

This stochastic reinterpretation is demonstrated in Sec. 4.3. Beforehand, the analytic properties of $\hat{\mathscr{F}}(t;\alpha,\beta)$ shall be closer inspected (see Sec. 4.2.5) and also the damping term, $\hat{\mathscr{D}}(t)$, requires further reflection (see Sec. 4.2.6).

4.2.5. Relevant properties of the force function

In the following, important properties of the analytic form of the force components, η_m^+ and η_m^-, (see Eqs. 4.27 and 4.28, respectively) are prepared. In Sec. 4.3, the analytic forms are reinterpreted and replaced by stochastic analogues. Then, the here declared properties become relevant in terms of stochastic moments. With respect to the Gaussian averaging, one directly finds the mean values, cf. Eq. 4.11,

$$\mathscr{M}\big[\eta_m^+(t;\alpha)\big] = \mathscr{M}\big[\eta_m^-(t;\beta)\big] = 0. \tag{4.36}$$

Further, the correlation functions,

$$\begin{aligned}\mathscr{M}\big[\eta_m^+(t;\alpha)\big(\eta_n^+(\tau;\alpha)\big)^*\big] &= \delta_{mn}C_m^+(\omega)e^{-i\omega(t-\tau)}\\ \mathscr{M}\big[\eta_m^-(t;\beta)\big(\eta_n^-(\tau;\beta)\big)^*\big] &= \delta_{mn}C_m^-(\omega)e^{-i\omega(t-\tau)},\end{aligned} \tag{4.37}$$

can be straightly deduced. For convenience, the two parts of the bath correlation function in frequency domain are introduced as

$$C_m^+(\omega) = \sum_\xi \mathscr{K}_{m\xi}^2[1+n(\omega_{m\xi})]\delta(\omega-\omega_{m\xi}) \tag{4.38}$$

and

$$C_m^-(\omega) = \sum_\xi \mathscr{K}_{m\xi}^2 n(\omega_{m\xi})\delta(\omega - \omega_{m\xi}). \tag{4.39}$$

Further, it is $\mathscr{M}\left[\eta_m^+(t;\alpha)\eta_n^+(\tau;\alpha)\right] = \mathscr{M}\left[\eta_m^+(t;\alpha)(\eta_n^-(\tau;\beta))^*\right] = \mathscr{M}\left[\eta_m^+(t;\alpha)\eta_n^-(\tau;\beta)\right] = 0$ (what is also valid interchanging + and −, respectively). Together, the moments of the force $\mathscr{F}_m(t;\alpha,\beta)$ acting on molecular site m follow as, cf. Eq. 4.34,

$$\begin{aligned}
\mathscr{M}\left[\mathscr{F}_m(t;\alpha,\beta)\right] &= 0 \\
\mathscr{M}\left[\mathscr{F}_m(t;\alpha,\beta)\mathscr{F}_n^*(\tau;\alpha,\beta)\right] &= \delta_{mn}C_m(t-\tau) \\
\mathscr{M}\left[\mathscr{F}_m(t;\alpha,\beta)\mathscr{F}_n(\tau;\alpha,\beta)\right] &= 0.
\end{aligned} \tag{4.40}$$

4.2.6. The damping operator

Before turning to the stochastic reinterpretation in Sec. 4.3, the present form of the damping term (see Eq. 4.35) shall be discussed in relation to the other works in literature.

The general stochastic ansatz derived by Diósi and Strunz et al. [47, 155, 158] results in a very general functional expression of the damping term $\hat{\mathscr{D}}$. In the limit of weak system–bath coupling, it essentially simplifies and becomes identical to the damping in Eq. 4.35. This is demonstrated for instance in Ref. [155], where a second order approximation of the functional term is derived (starting from the finite temperature treatment of Ref. [47] and in direct application to quantum Brownian motion). Here, the Eq. 4.35 is obtained straightly by applying the same level of approximation right from the beginning (see Sec. 4.2.2). Also the present shape of the force terms can be related to the works of Diósi and Strunz et al. [48]. In fact, they deduce a finite temperature expression of the force which resembles exactly the one derived here with Eq. 4.34 (though they utilize a Bogoliubov transformation to change from the situation of zero temerature to the finite temperature). Together the comparison confirms the identity of Eq. 4.32 and the weak coupling limit of the general non–Markovian ansatz developed by Diósi, Gisin, Strunz, and Gaspard et al. [47, 48, 153, 154, 155, 157, 158, 159]. The present treatment (of starting directly with the finite temperature RDO in Eq. 4.9 and transforming subsequently the Gaussian averaging according to Eq. 4.24) describes an instructive direct alternative to their general ansatz.

Also the equation of motion introduced by Zhao et al. [160, 49, 50, 51] shall be related to Eq. 4.32. An obvious difference lies in the form of the damping term. In fact, they propose the form

$$\hat{\mathscr{D}}_{T=0}(t) = \frac{1}{\hbar^2}\int_0^t d\bar{t}\sum_{m,\xi}\mathscr{K}_{m\xi}^2 e^{-i\omega_{m\xi}\bar{t}}\hat{L}_m\hat{L}_m(-\bar{t}). \tag{4.41}$$

As indicated, this expression resembles the $T = 0$ limit of the present ansatz (see Eq. 4.35 with Eq. 4.30). In Refs. [160, 49, 50, 51], it is introduced also for situations of finite temperature. In particular, Zhao et al. first derived an exact expression of $\hat{\mathscr{D}}$ which, in a second step, was expanded to lowest order with respect to the coupling

strength. However, the force term was thereby not subject to the expansion. This stands clearly in contrast to the collective time expansion set–up which leads here directly to Eq. 4.32 (see Sec. 4.2.2).

In order to align, nevertheless, the present work and the ansatz of Zhao et al. [49], a further transformation step of the above Eq. 4.32 was figured out. As demonstrated more detailed in Appendix F.3, it is possible to emulate in the present ansatz the selective perturbative treatment of their damping term. This treatment changes only slightly the unraveled RDO in second–order approximation. According to that, it is proved that the substitution of the zero temperature part of Eq. 4.35 (coinciding with the damping term proposed in Ref. [49]) results in an optional alternative equation of motion equivalent to Eq. 4.32. Its concrete form is provided in Eq. F.24.

Although the appearance of the zero temperature damping term of Zhao et al. could be explained in the present ansatz, their equation of motion is still different concerning the force expressions. In fact, in constrast to the present approach, in Ref. [49] a temperature dependent stochastic force must be installed phenomenologically in order to achieve RDO kinetics at finite temperature. The proper introduction of a stochastic force following the present ansatz is demonstrated next in Sec. 4.3. Later on in Sec. 4.5.3, the particular force algorithm suggested in Ref. [49] is revisited.

4.3. Stochastic Interpretation

As clarified in Sec. 4.2.4, the equation of motion 4.32 is not of practical use so far. To change this, the discussion turns now to the combined stochastic reformulation of the analytic force $\hat{\mathscr{F}}(t;\alpha,\beta)$ (see Eq. 4.34) and the related analytic operation $\mathscr{M}[...]$ (see Eqs. 4.33). For this purpose, an approximate Monte–Carlo integration scheme is introduced. The here provided translation is direct and very instructive. Inspired by other works (see, e.g., Ref. [155]), it is worked out as an essential part of this thesis. By substituting $\hat{\mathscr{F}}(t;\alpha,\beta)$ and $\mathscr{M}[...]$ by approximate stochastic analogues, the equation of motion 4.32 finally turns to the aspired stochastic form.

4.3.1. Transformation of the Gaussian averaging

Two transformation steps are required to prepare the Monte–Carlo integration scheme executed later on in Sec. 4.3.3. It is the first one to transform the infinite integral range in $\mathscr{M}[...]$ to finite integration boundaries. Most conveniently, the Monte–Carlo scheme is done on the range of $[0,1]$. Concerning an arbitrary function $f(\{\alpha_{n\zeta},\beta_{n\zeta}\})$ which generally depends on all α and β variables, the mean $\mathscr{M}[...]$ operates as the multi–dimensional complex–valued integration, cf. Eq. 4.11,

$$\mathscr{M}[f(\{\alpha_{n\zeta},\beta_{n\zeta}\})] = \Big[\prod_{m,\xi}\frac{1}{\pi^2}\int_{-\infty}^{\infty}d\alpha_{m\xi}\int_{-\infty}^{\infty}d\beta_{m\xi}e^{-|\alpha_{m\xi}|^2-|\beta_{m\xi}|^2}\Big]f(\{\alpha_{n\zeta},\beta_{n\zeta}\}. \quad (4.42)$$

Each single integration runs upon the complete complex plane (reminding, e.g., $d\alpha_{m\xi} = d\mathrm{Re}[\alpha_{m\xi}] + i\cdot d\mathrm{Im}[\alpha_{m\xi}]$). Now, polar coordinates coordinates are introduced as $R^{+}_{m\xi} = \sqrt{\mathrm{Re}[\alpha_{m\xi}]^2+\mathrm{Im}[\alpha_{m\xi}]^2}$ and $\varphi^{+}_{m\xi} = \arctan\{\mathrm{Im}[\alpha_{m\xi}]/\mathrm{Re}[\alpha_{m\xi}]\}$ (both related to each of

the $\alpha_{m\xi}$'s). Similarly, $R^-_{m\xi} = \sqrt{\mathrm{Re}[\beta_{m\xi}]^2 + \mathrm{Im}[\beta_{m\xi}]^2}$ and $\varphi^-_{m\xi} = \arctan\{\mathrm{Im}[\beta_{m\xi}]/\mathrm{Re}[\beta_{m\xi}]\}$ are defined for every $\beta_{m\xi}$. When substituting into Eq. 4.42, it follows

$$\mathscr{M}[f] = \Big[\prod_{m,\xi}\prod_{j=+,-}\frac{1}{\pi^2}\int_0^\infty dR^j_{m\xi}\int_0^{2\pi} d\varphi^j_{m\xi}e^{-(R^j_{m\xi})^2}\Big]f(\{R^+_{n\zeta}e^{i\varphi^+_{n\zeta}}, R^-_{n\zeta}e^{i\varphi^-_{n\zeta}}\}). \quad (4.43)$$

The desired finite integration boundaries in the range of $[0,1]$ are finally achieved with the further substitution of $A^\pm_{m\xi} = \exp\{-(R^\pm_{m\xi})^2\}$ and $B^\pm_{m\xi} = \varphi^\pm_{m\xi}/2\pi$ (not to be confused with Eqs. 4.14 and 4.16). By that, Eq. 4.43 changes to the very appealing form

$$\mathscr{M}[f] = \Big[\prod_{m,\xi}\prod_{j=+,-}\int_0^1 dA^j_{m\xi}\int_0^1 dB^j_{m\xi}\Big]f(\{X(A^+_{n\zeta}, B^+_{n\zeta}), X(A^-_{n\zeta}, B^-_{n\zeta})\}), \quad (4.44)$$

where the function

$$X(A^j_{n\zeta}, B^j_{n\zeta}) = \sqrt{-\log(A^j_{n\zeta})}\exp\{i2\pi B^j_{n\zeta}\} \quad (4.45)$$

is introduced for convenience.

4.3.2. Transformation of the force function

With the latter transformation from Eq. 4.42 to Eq. 4.44, also the functions η^+_m and η^-_m (see Eqs. 4.27 and 4.28) must be translated. They reexpress straightly according to

$$\eta^+_m(t; A^+, B^+) = \sum_\xi \mathscr{K}_{m\xi}\sqrt{1+n_{m\xi}}X(A^+_{m\xi}, B^+_{m\xi})e^{-i\omega_{m\xi}t} \quad (4.46)$$

and

$$\eta^-_m(t; A^-, B^-) = \sum_\xi \mathscr{K}_{m\xi}\sqrt{n_{m\xi}}X(A^-_{m\xi}, B^-_{m\xi})e^{-i\omega_{m\xi}t}. \quad (4.47)$$

In this form, however, they cannot be computed because specific information about the bath vibrational modes (i.e., values of $\mathscr{K}_{m\xi}$ and $\omega_{m\xi}$) are not available (see Sec. 3.3.4). Instead, it is required to substitute the correlation function terms, $C^+_m(\omega)$ and $C^-_m(\omega)$ (see Eqs. 4.38 and 4.39) into the Eqs. 4.46 and 4.47, respectvely.

At this place, the properties of η^+_m and η^-_m discussed in Sec. 4.2.5 become relevant. As demonstrated, the average of the functions η^+_m and η^-_m vanishes. Relevant non–zero averages appear only for correlation–type terms (see Eq. 4.37). Using the transformed expressions in Eqs. 4.46 and 4.47, these follow now as

$$\begin{aligned}\mathscr{M}[(\eta^+_m(t))^*\eta^+_m(\tau)] = \mathscr{M}\Big[\Big(\sum_\xi \mathscr{K}_{m\xi}\sqrt{1+n_{m\xi}}X(A^+_{m\xi}, B^+_{m\xi})e^{-i\omega_{m\xi}t}\Big)^* \\ \times\Big(\sum_\xi \mathscr{K}_{m\xi}\sqrt{1+n_{m\xi}}X(A^+_{m\xi}, B^+_{m\xi})e^{-i\omega_{m\xi}\tau}\Big)\Big],\end{aligned} \quad (4.48)$$

and

$$\mathscr{M}\left[(\eta_m^-(t))^*\eta_m^-(\tau)\right] = \mathscr{M}\Big[\Big(\sum_\xi \mathscr{K}_{m\xi}\sqrt{n_{m\xi}}X(A_{m\xi}^-, B_{m\xi}^-)e^{-i\omega_{m\xi}t}\Big)^* \times\Big(\sum_\xi \mathscr{K}_{m\xi}\sqrt{n_{m\xi}}X(A_{m\xi}^-, B_{m\xi}^-)e^{-i\omega_{m\xi}\tau}\Big)\Big], \tag{4.49}$$

respectively. Both expressions are given here in detail as they prove that, in awareness of the relation of $\mathscr{M}[X^*(A_{m\xi}^s, B_{m\xi}^s)X(A_{n\zeta}^{s'}, B_{n\zeta}^{s'})] = \delta_{ss'}\delta_{mn}\delta_{\xi\zeta}$, the explicite dependence on the bath modes can be exchanged and "coarsened" in terms of

$$\sum_\xi \mathscr{K}_{m\xi}^2(1+n_{m\xi})e^{-i\omega_{m\xi}t} = \int d\omega C_m^+(\omega)e^{-i\omega t} \approx \sum_k^K \Delta\omega C_m^+(\omega_k)e^{-i\omega_k t}, \tag{4.50}$$

and

$$\sum_\xi \mathscr{K}_{m\xi}^2 n_{m\xi}e^{-i\omega_{m\xi}t} = \int d\omega C_m^-(\omega)e^{-i\omega t} \approx \sum_k^K \Delta\omega C_m^-(\omega_k)e^{-i\omega_k t}. \tag{4.51}$$

To obtain Eqs. 4.50 and 4.51, in the first steps, the two correlation function terms, $C_m^+(\omega)$ and $C_m^-(\omega)$ (see Eqs. 4.38 and 4.39) are introduced. Based on $C_m^+(\omega)$ and $C_m^-(\omega)$, in the second steps, then discretized summations are reintroduced for numerical implementation. The intention of introducing $C_m^+(\omega)$ and $C_m^-(\omega)$ is to collect the complete information on the bath modes in compact form. In practice, both correlation function terms are approximately replaced by functional analytic ansatzes (see Sec. 3.3.4).

Next, noise–like functions based on $C_m^+(\omega)$ and $C_m^-(\omega)$ shall be identified. For this purpose, the discretized expressions found with the right hand sides of Eqs. 4.50 and 4.51 are inserted back into Eqs. 4.48 and 4.49, respectively. Then, the sums (with respect to k) must be defactorized again to obtain two noise–like expressions. Basically, the argumentation which led once to Eqs. 4.50 and 4.51 is rewind again, but now based on the discretized bath modes with index k. The defactorization is simply executed when reintroducing the function X in dependence on the variables A_{mk}^+, B_{mk}^+, A_{mk}^- and B_{mk}^-. The appealing noise–like functions are then deduced in terms of,

$$\bar{\eta}_m^+(t; A^+, B^+) = \sum_k^K \sqrt{\Delta\omega C_m^+(\omega_k)}X(A_{mk}^+, B_{mk}^+)e^{-i\omega_k t} \tag{4.52}$$

and

$$\bar{\eta}_m^-(t; A^-, B^-) = \sum_k^K \sqrt{\Delta\omega C_m^-(\omega_k)}X(A_{mk}^-, B_{mk}^-)e^{-i\omega_k t}. \tag{4.53}$$

The mean value operation is recaptured as, cf. Eq. 4.44,

$$\bar{\mathcal{M}}[f] = \Big[\prod_{m}^{M}\prod_{k}^{K}\prod_{j=+,-}\int_0^1 dA^j_{m\xi}\int_0^1 dB^j_{m\xi}\Big] f(\{X(A^+_{nk'},B^+_{nk'}),X(A^-_{nk'},B^-_{nk'})\}). \quad (4.54)$$

As shown, the $\bar{\mathcal{M}}[...]$ is now realied with respect to a finite number of $2\cdot KM$ variables A^+_{mk}, B^+_{mk}, A^-_{mk} and B^-_{mk}. They replace the former infinite number of integration variables (with mode index ξ). As desired, now the functions $\bar{\eta}^+_m$ and $\bar{\eta}^-_m$ rely only on the correlation functions. Commonly, analytic ansatzes are used for the bath correlation function and the $\bar{\eta}^+_m$ and $\bar{\eta}^-_m$ can be determined straightforwardly. Furthermore, the sums in Eqs. 4.52 and 4.53 are very conveniently determined in practice. In fact, the $C(\omega)$ usually decays rapidly with increasing ω and an upper frequency cutoff can be introduced. Such cutoff would identify the fastest bath vibration which relevantly couples to the transfer system (for details, see Sec. 4.5.1).

4.3.3. Monte–Carlo integration scheme

It follows the last step which is the reformulation of the mean operation in Eq. 4.54 based on the Monte–Carlo integration technique [163]. By its mean, the multidimensional integration with respect to all A^+_{mk}, B^+_{mk}, A^-_{mk} and B^-_{mk} is approximated in terms of a descrete sum with respect to only over a certain selection of values of all A^+_{mk}, B^+_{mk}, A^-_{mk} and B^-_{mk}. According to the general Monte–Carlo processing, these values are generated as uniform random numbers from $[0,1]$.

Concretely, the Monte–Carlo scheme is introduced according to, cf. Eq. 4.54,

$$\bar{\mathcal{M}}[...] \longrightarrow \bar{\mathcal{M}}_z[...] = \frac{1}{\mathcal{N}}\sum_{z}^{\mathcal{N}}[...]_z, \quad (4.55)$$

together with, cf. Eq. 4.52,

$$\bar{\eta}^+_m(t;A^+,B^+) \longrightarrow \bar{\eta}^+_m(t;z_+) = \sum_{k}^{K}\sqrt{\Delta\omega C^+_m(\omega_k)}W^{(z_+)}_{mk}e^{-i\omega_k t} \quad (4.56)$$

and similarly, cf. Eq. 4.53,

$$\bar{\eta}^-_m(t;A^-,B^-) \longrightarrow \bar{\eta}^-_m(t;z_-) = \sum_{k}^{K}\sqrt{\Delta\omega C^-_m(\omega_k)}W^{(z_-)}_{mk}e^{-i\omega_k t}. \quad (4.57)$$

When sampling $A^\pm_{mk}$ and $B^\pm_{mk}$ uniformly from $[0,1]$, the function $X(A^\pm_{mk},B^\pm_{mk})$ produces a complex–valued random number from a normal distribution with zero mean (see Eq. 4.45). This echoes exactly the Box–Muller algorithm [164, 165]. For the sake of convenience, therefore the $W^{(z_+)}_{mk}$ and $W^{(z_-)}_{mk}$ are here directly introduced as such independently generated Gaussian random numbers. The indices m refers still to the mth state of the "active" system (see Eqs. 4.7 and 4.8). The second index $k\in\{1,...,K\}$ is related to the kth discretized vibrational bath mode (see again Eqs. 4.52 and 4.53).

The upper labels z_+ and z_- count the different random realizations of $W_{mk}^{(z_+)}$ and $W_{mk}^{(z_-)}$, respectively.

Both functions $\bar{\eta}_m^+(t;z_+)$ and $\bar{\eta}_m^-(t;z_-)$ appear finally as complex–valued Gaussian colored noise processes[6]. Their stochastic moments are equivalent with the relations Eqs. 4.36 and 4.37. In this light, the operation $\bar{\mathcal{M}}_z[\mathcal{O}]$ (given with Eq. 4.55) renders the stochastic mean of some observable $O(z)$ with respect to the noise processes $\bar{\eta}_m^+(t;z_+)$ and $\bar{\eta}_m^-(t;z_-)$, where the z_+ and z_- are conveniently united to $z=(z_+,z_-)$. It is computed in terms of the simple arithmetic mean of a number of $\mathcal{N}$ different stochastic realizations of $O(z)$.

4.3.4. The stochastic Schrödinger equation

Finally, the stochastic noise functions $\bar{\eta}_m^+(t;z_+)$ and $\bar{\eta}_m^-(t;z_-)$ (see Eqs. 4.56 and 4.57) can be substituted into the original equation of motion deduced in Sec. 4.2.4 (see 4.32). The resulting equation,

$$i\hbar\frac{\partial}{\partial t}|\phi_z(t)\rangle = \big(\hat{H}_{\mathrm{S}} + \hat{\mathcal{F}}_z(t) - i\hbar\hat{\mathcal{D}}(t)\big)|\phi_z(t)\rangle. \tag{4.58}$$

is called (linear) *stochastic Schrödinger equation* (SSE) further on.[7] The two types of noise functions contribute to the fluctuative force operator,

$$\hat{\mathcal{F}}_z(t) = \sum_m \mathcal{F}_m(t;z)\hat{L}_m = \sum_m \big((\bar{\eta}_m^+(t;z_+))^* + \bar{\eta}_m^-(t;z_-)\big)\hat{L}_m. \tag{4.59}$$

The (non–Markovian) dissipative damping operator, $\hat{\mathcal{D}}(t)$ (see Eq. 4.35) is left unchanged with respect to the equation of motion 4.32. The original dependence on α and β in Eq. 4.32 is now removed and the dependence on the complex–valued stochastic process is introduced with $\hat{\mathcal{F}}_z(t)$ (and indicated by the label z).

According to Eq. 4.33 and making use of Eq. 4.55, the desired unraveling of the RDO is finally found in terms of the trivial expression

$$\hat{\rho}(t) = \frac{1}{\mathcal{N}}\sum_z^{\mathcal{N}} |\phi_z(t)\rangle\langle\phi_z(t)|. \tag{4.60}$$

It describes a simple arithmetic mean value operation based on an appropriate manifold of $\mathcal{N}$ independent stochastic trajectories $\phi_z(t)$ (i.e., different solutions of Eq. 4.58). Since $\mathcal{N}$ (besides K in Eq. 4.56 and 4.57) is finite, Eq. 4.60 describes an approximate expression of the RDO. However, in course of the concrete studies the Monte–Carlo integration scheme shows surprisingly good convergence features for increasing numbers of stochastic realization.

[6] Please be aware that here the functions $\bar{\eta}_m^+(t;z_+)$ and $\bar{\eta}_m^-(t;z_-)$ are treated in terms of stochastic noises although their time–dependence is apparently continuous as well as deterministic (based on the knowledge of the random numbers $W_{mk}^{(z_+)}$ and $W_{mk}^{(z_-)}$). Hence, both actually describe not stochstic prosesses in the narrow sense [141, 166].

[7] The SSE 4.58 describes a linear equation of motion because the operators $\hat{\mathcal{F}}_z(t)$ and $\hat{\mathcal{D}}(t)$ are independent on the state vector $|\phi_z(t)\rangle$. Further discussions on that are given in Secs. 4.4 and 4.5.

The present form of the linear SSE 4.58 raises serious concerns about its practical value. The following sections are therefore devoted to an elaborate discussions on the numerical performance of Eq. 4.58. The discussion closes finally with developing a very straight strategy which instructs proper implementation of Eq. 4.58 even to very large transfer systems. In Chaps. 7 and 8, it is then applied to study dissipative charge migration and exciton relaxation mechanism phenomena at the large–scale *para*–sexiphenyl/ZnO interface and the gigantic tubular dye aggregate/CdSe nanocrystal system, respectively.

4.4. The Stochastic Schrödinger Equation in Practice

In this section, the particular focus lies on the practicability of the linear SSE derived with Eq. 4.58. The discussion begins in Sec. 4.4.1 with concerning the critical numerical features of the state vector. An alternatively applicable but computationally more expansive nonlinear SSE is introduced in Sec. 4.4.2. A strategy to apply the linear SSE on large–scale systems, like the ones studied in Chaps. 7 and 8, is then sketched in Sec. 4.4.3. Later on in Secs. 4.5 and 4.6, it is further worked out to a concrete simulation technique.

4.4.1. Norm of the state vector

In Sec. 4.2.3, the state vector is prepared in order to guarantee initial normalization (see Eq. 4.21). This initial normalization is preserved throughout the stochastic reinterpretation in Sec. 4.3. Concerning the stochastic wave function, $\phi_z(t)$, it follows then $|\phi_z(0)| = \langle\phi_z(0)|\phi_z(0)\rangle^{1/2} = 1$. However, the norm starts to vary during time–propagation. This results from the non–Hermitian parts of $\hat{\mathscr{F}}_z(t)$ and $\hat{\mathscr{D}}(t)$ and can be realized for $t > 0$ according to, cf. Eq. 4.58,

$$d\langle\phi_z(t)|\phi_z(t)\rangle = \langle\phi_z(t)|\big[\frac{1}{i\hbar}\hat{\mathscr{F}}_z(t) - \hat{\mathscr{D}}(t)\big]|\phi_z(t)\rangle dt + \text{H.c.} \neq 1. \tag{4.61}$$

Consequently, the linear SSE 4.58 cannot be straightly utilized for computer simulations. Critical aspects must be expected concerning the numerics. In practice, the norm diverges extremely within only few time steps. Independent on the numerical integration scheme, this feature is a typical observation documented in literature also when other linear SSEs were utilized [158, 162]. In order to minimize the numerical error originated from the drifting norm, ultimative computational precission would be required. The nonlinear form of the SSE 4.58 shall be considered next. It is attributed with intrinsic norm conservation but much more computationally costly.

4.4.2. Nonlinear stochastic Schrödinger equation

As generally discussed in Sec. 4.1, Gisin and Percival [149, 150, 151] proposed early an alternative nonlinear type of equation which directly approaches the normalized state $|\bar{\phi}_z(t)\rangle = |\phi_z(t)\rangle/|\phi_z(t)|$. They arrived at the nonlinear (Markovian) quantum state diffusion approach discussed in Sec. 4.1 (see Eq. 4.5). Concerning the unraveling of

the RDM (see Eq. 4.4), the $|\bar{\phi}_z(t)\rangle$ is absolutely equivalent with the solution $|\phi_z(t)\rangle$ (see Eq. 4.3) and can be straightly propagated using standard numerical integration schemes. In what follows, the nonlinear version of the present (non–Markovian) SSE 4.58 shall be introduced.

Following Diósi, Gisin and Strunz et al., the linear SSE 4.58 is first interpreted as a stochastic differential equation of Stratonivich type [48, 141]. The derivative $d|\bar{\phi}_z(t)\rangle/dt$ (with $|\bar{\phi}_z(t)\rangle = |\phi_z(t)\rangle/\sqrt{\langle\phi_z(t)|\phi_z(t)\rangle}$) follows then by basic algebraic rules based on $d|\phi_z(t)\rangle/dt$. Concerning the unnormalized trajectories $|\phi_z(t)\rangle$, the RDO is obtained with $\hat{\rho}(t) = \hat{\mathcal{M}}_z[|\phi_z(t)\rangle\langle\phi_z(t)|]$ (see Eq. 4.60). However, this relation cannot be used straightly for the normalized trajectories $|\bar{\phi}_z(t)\rangle$. Indeed, it is $|\phi_z(t)\rangle\langle\phi_z(t)| = |\phi_z(t)|^2|\bar{\phi}_z(t)\rangle\langle\bar{\phi}_z(t)|$. The occuring prefactor $|\phi_z(t)|^2$ would modulate the mean value operation as time goes on and so would make this operation impracticable. In order to circumvented this the method of importance sampling must be employed. Thereby, the stochastic noise itself is attributed with an additional time–dependent drift. This drift is adjusted in that way that it mimicks the action of the $|\phi_z(t)|^2$ in the averaging [48, 155]. By virtue of that, the prefactor is omitted and the original time–independent averaging recovered $\hat{\rho}(t) = \hat{\mathcal{M}}_z[|\phi_z(t)\rangle\langle\phi_z(t)|]$ (see below Eq. 4.65). The entire treatment represents a mathematical Girsanov transformation (see also Refs. [156, 167]). It finally results in the nonlinear SSE

$$\begin{aligned} i\hbar\frac{d}{dt}|\bar{\phi}_z(t)\rangle =& \hat{H}_s|\bar{\phi}_z(t)\rangle + \sum_m [\hat{L}_m - \langle\hat{L}_m\rangle_t]\xi_m(t;z)|\bar{\phi}_z(t)\rangle \\ & - i\hbar\sum_m \Big\{ [\hat{L}_m - \langle\hat{L}_m\rangle_t]\hat{O}(t) - \Big\langle [\hat{L}_m - \langle\hat{L}_m\rangle_t]\hat{O}(t)\Big\rangle_t \Big\}|\bar{\phi}_z(t)\rangle. \end{aligned} \tag{4.62}$$

The nonlinearity of Eq. 4.62 arises from the expectation values $\langle ...\rangle_t = \langle\bar{\phi}_z(t)|...|\bar{\phi}_z(t)\rangle$. They appear due to the inclusion of the inverse norm (i.e., the factor $\langle\phi_z(t)|\phi_z(t)^{-1/2}$) in the derivative. The related Girsanov transformation results in the adjusted noise terms $\xi_m(t;z)$, which are introduced according to

$$\xi_m(t;z) = \mathcal{F}_m(t;z) - \frac{1}{i\hbar}\int_0^t d\tau C^*(t-\tau)\langle\hat{L}_m\rangle_\tau, \tag{4.63}$$

based on $\mathcal{F}_m(t;z)$ (see Eq. 4.59), but now shifted by the time–dependent integrative term. Moreover, the dissipative memory kernel in Eq. 4.62 is abbreviated with $O(t)$. According to the present strict second order treatment, it is here, cf. Eq. 4.35,

$$\hat{O}(t) = \int_0^t d\tau C(t-\tau)\hat{U}(t-\tau)\hat{L}_m\hat{U}^\dagger(t-\tau)/\hbar^2. \tag{4.64}$$

With the nonlinear SSE 4.62, an alternative to Eq. 4.58 is obtained. (Please note that when suppressing all expectation value terms, one recaptures the original linear SSE 4.58.) In equivalence to the latter, the RDO is unraveled according to, cf. Eq. 4.60,

$$\hat{\rho}(t) = \frac{1}{\mathcal{N}}\sum_z^{\mathcal{N}} |\bar{\phi}_z(t)\rangle\langle\bar{\phi}_z(t)|, \tag{4.65}$$

based on an appropriate number of trajectories $|\bar{\phi}_z(t)\rangle$.

On one side, the norm conservation of $|\bar{\phi}_z(t)\rangle$ describes an elementary technical advantage. On the other side, this numerical stability is dearly paid with the nonlinearity of Eq. 4.5 which brings with significant increase of computational costs. In particular, the additional expectation values and the time–dependent convolution in Eq. 4.63 make simulations generally expansive.

On the bottom line, the numerical propagation of the nonlinear SSE is not featured with the same promising computational scaling properties as expected from the linear SSE 4.58. Like the direct master equation ansatz, also the nonlinear SSE 4.62 seems to be inappropriate for application to truly large–scale open system studies. Indeed, no application study of Eq. 4.62 to systems larger than few ten states was found in literature so far. (An elaborate computer study comparing linear and nonlinear implementations was presented by Vega et al. [158]. A manifold of works on smaller systems were, e.g., studied by Strunz and Eisfeld et al. [162, 168])

In this work, the nonlinear SSE serves for generation of exact RDO kinetics considering small up to intermediate sized systems. For large–scale systems (including 1000 states and more), however, it only remains to apply the linear SSE in combination with a numerical renormalization scheme. The latter technique is discussed next in Sec. 4.4.3. Later on in Secs. 4.5 and 4.6, a strategy to simulate large–scale systems based on the linear SSE is explained. Thereby, also the nonlinear SSE plays a role.

4.4.3. Numerical renormalization procedure

In view of large–scale systems, it is the intention to preserve the advantageous computational scaling properties of the original linear SSE 4.58. For this end, a simple numerical renormalization routine applied on the state vector $\phi_z(t_n)$ is imperative. It means that the norm of the trajectory is restored between each integration step of Eq. 4.58, according to the following scheme:

$$|\phi_z(t_0)\rangle \;\Rightarrow\; |\phi'_z(t_1)\rangle \;\Rightarrow\; |\phi_z(t_1)\rangle = \frac{|\phi'_z(t_1)\rangle}{|\phi'_z(t_1)|} \;\Rightarrow\; |\phi'_z(t_2)\rangle \;\Rightarrow\; |\phi_z(t_2)\rangle = \frac{|\phi'_z(t_2)\rangle}{|\phi'_z(t_2)|} \;\Rightarrow\; \ldots \tag{4.66}$$

It describes an alternating sequence of propagation steps of $|\phi_z(t)\rangle$ from t_n to t_{n+1} (according to Eq. 4.58; blue arrows) and approximate renormalization steps of $|\phi_z(t)\rangle$ (red arrows). Due to the renormalization steps, the treatment 4.66 must be clearly characterized as numerical manipulation of the wave function kinetics. These might produce essential numerical error and also the resulting RDO kinetics might be corrupted.

The drift of the norm (i.e., $1 - |\phi_z(t)|$) and so the introduced error of the renormalization is determined by the non–Hermitian contribution of $\hat{\mathfrak{F}}_z(t)$ and $\hat{\mathfrak{D}}(t)$ (see again Eq. 4.61). In the first place, the imaginary parts of the complex–valued terms $\mathfrak{F}_m(t;z)$ in $\hat{\mathfrak{F}}_z(t)$ describe a source of error and it can be expected that the RDO kinetics show sensitivity for the choice of the particular algorithm applied to generate the $\mathfrak{F}_m(t;z)$. This motivates the search for a noise algorithm which minimizes the introduced numerical error. For this purpose, one reminds the numerically exact nonlinear SSE 4.62. In direct comparison, it provides now a helpful instrument to evaluate the actual ap-

proximate character of the numerical linear propagation scheme 4.66. The subsequent sections are devoted to that issue. A first test on the numerical performance of the scheme 4.66 is offered in Sec. 4.5. Subsequently, a concrete strategy on its proper application to large–scale systems is worked out in Sec. 4.6.

4.5. Performance of the Linear Algorithms

In this section, results from four different linear SSE algorithms are compared. All four applied linear algorithm unravel analytically the same RDO (on second order). Their computational simulation, however, must be based on the renormalization scheme 4.66, introduced before in Sec. 4.4.3. So numerical discrepancies of the four obtained kinetics are anticipated. The four algorithms are based on the SSE 4.58. Their concrete forms, however, distinguishes in that each one represents a different combination of damping operator and force generation function. Thereby, two versions of damping and force shall be probed in alternation.

The popular Fenna–Matthews–Olson (FMO) complex is chosen as a small–scale and well–established molecular system. In Sec. 4.5.1, a brief introduction of the Fenna–Matthews–Olson (FMO) complex and further details on the computational studies are provided. The four obtained kinetics based on the approximate scheme are compared with exact data from the nonlinear SSE algorithm. This ensures proper evaluation of the four underlying algorithms.

Behind all this lay the intention to possibly discover a linear SSE algorithm with minimal numerical error due to the renormalization scheme. In particular, the search for an adequate noise function described a key challenge of this thesis. Its success decided basically about the applicability of the linear propagation scheme and so the possibility to study large–scale open systems.

4.5.1. The Fenna–Matthews–Olson complex as a model system

The FMO complex is a biological chromophore complex of the photosynthetic apparatus of green sulfur bacteria [169, 170, 171, 172]. It is small and well–understood and so it served as a trial system already many times in literature (see, e.g., Refs. [49, 173, 174]). In its center, seven bacteriochlorophyll molecules are arranged in a protein environment (see Fig. 4.1). In nature, the FMO complex funnels energy from the antenna complexes to the photosynthetic reaction center. Here, it is considered as an open system which is subject to internal intermolecular excitation energy transfer. The surrounding protein matrix is treated in terms of a vibrational bath introducing vibronic effects.

According to Sec. 3.3.1, the system Hamiltonian can be introduced as H_{S} (see Eq. 3.7). The basis states $|m\rangle$ (with $m \in \{1, ..., 7\}$) represent the seven molecular excited states of the complex. The diagonal elements, E_m, describe the energies related to the $|m\rangle$ and the off–diagonal elements, V_{mn}, give the corresponding excitonic couplings between the chromophores. Here, the widely used parameterization of

Figure 4.1.: The Fenna–Matthews–Olson (FMO) complex in the photosynthetic reaction center of green sulfur bacteria. It consists of seven bacteriochlorophylls (see labels 1 to 7). The protein matrix is not shown. It is subject to excitation energy transfer (EET) from the antenna complex to the reaction center. Colored curves in the graphic show the excited state population kinetics of the three prominent chromophores (colored labels) based on the nonlinear SSE 4.62 (solid) and the Redfield equations (dashing); for more details, see the main text.

Refs. [175, 173, 176] is reapplied. The Hamiltonian matrix (in units cm^{-1}) follows as

$$\langle\varphi_m|\hat{H}_\mathrm{S}|\varphi_n\rangle = \begin{pmatrix} 200 & -87.7 & 5.5 & -5.9 & 6.7 & -13.7 & -9.9 \\ & 320 & 30.8 & 8.2 & 0.7 & 11.8 & 4.3 \\ & & 0 & -53.5 & -2.2 & -9.6 & 6.0 \\ & & & 110 & -70.7 & -17.0 & -63.3 \\ & & & & 270 & 81.1 & -1.3 \\ & & & & & 420 & 39.7 \\ & & & & & & 230 \end{pmatrix}, \tag{4.67}$$

where only the upper triangle is shown and a constant energy offset of 12210 cm^{-1} is introduced on the diagonal. As typical, the coupling of the molecules to the vibrational bath is uniformly characterized by a spectral density $J(\omega)$ of Drude–Lorentz type [49, 173, 174]. Its concrete form is provided in Appendix E (see Eq. E.3). The $J(\omega)$ is fully specified in terms of the bath reorganization energy λ and relaxation time γ^{-1}. With $J(\omega)$ the correlation functions $C^+(\omega)$ and $C^-(\omega)$ (see Eqs. 4.38 and 4.39) can be computed for room temperature simulations. Based on $C^+(\omega)$ and $C^-(\omega)$, the noise terms $\bar{\eta}_m^+(t, z_+)$ and $\bar{\eta}_m^-(t, z_-)$ (see Eqs. 4.56 and 4.57) are determined immediately and so are the stochastic forces $\mathscr{F}_m(t; z)$ (see Eq. 4.59).

According to Eq. 4.59 (and Eqs. 4.56 and 4.57), each $\mathscr{F}_m(t; z)$ renders a superposition

Figure 4.2.: Time–dependence of the correlation function $C(t)$. Panel a: Stochastic versus analytic (see Eq. 3.15) versions of $C(t)$ for $t_{\max} = 1000$ fs via the spectral density $J(\omega)$. Stochastic form follows from $C(t) = \bar{\mathscr{M}}_z[\mathscr{F}_m(t;z)\mathscr{F}_m^*(0;z)]$ (see Eq. 4.59, based on $\mathcal{N} = 1000$ different noise realizations). The discretization of $J(\omega)$ uses $\omega_{\max} = \pi/\text{fs}$ with $K = 1000$ frequency points (for details, see the main text). Panel b: The same as in panel a but with $K = 500$.

of different complex oscillating terms with random amplitudes. The frequencies of the latter are thereby prescribed from discretizing the spectral interval $[0, \omega_{\max}]$. By definition a number of K equally spaced intervals are introduced together with a cutoff frequency $\omega_{\max}$ giving the upper limit of the relevant frequency range of $J(\omega)$. In turn, the discrete frequencies follow as $\omega_k = k \cdot \Delta\omega$ with the spacings $\Delta\omega = \omega_{\max}/K$.

It is a general feature of the equally spaced discretization in $\bar{\eta}_m^+(t, z_+)$ and $\bar{\eta}_m^-(t, z_-)$ (see Eqs. 4.56 and 4.57) that all $\mathscr{F}_m(t;z)$ become periodic. The duration of the repetitive cycle is $\tau = 2\pi/\Delta\omega$. In order to avoid related recurrence phenomena, it is needed to choose the number of grid points K in such a way that the condition $T_{\text{sim}} < \tau/2$ is ensured (where T_{sim} denotes the total simulation time).[8] The described unphysical behavior, which would be obtained if this prescript is violated, is exemplarily illustrated in Fig. 4.2. Both panels give the stochastic determination of $C(t) = \bar{\mathscr{M}}_z[\mathscr{F}_m(t;z)\mathscr{F}_m^*(0;z)]$ based on the above $J(\omega)$. The $C(t)$ in Fig. 4.2a was simulated using a proper number of grid points ($T_{\text{sim}} = 1000$ fs, $\omega_{\max} = \pi \times$ 1/fs and $K = 1000$) and indeed, no recurrence effects are observable. The $C(t)$ shown in Fig. 4.2b results from the same parameterization, however, only each second of the grid points were applied (i.e., it was $K = 500$). This stochastic simulation is improper and the unphysical recurrence can

[8] Please note that the symmetric time–dependence of the generated correlation function $C(t)$ is also taken into account. The latter symmetry consideration is responsible for the factor of 1/2.

be recognized clearly (see blue arrows).

4.5.2. Variation of the damping operator

In this first part, the performance of the linear SSE 4.58 is studied under variation of the damping operator. Therefore, two simulation runs each with one of the two damping operators $\hat{\mathfrak{D}}(t)$ or $\hat{\mathfrak{D}}_{T=0}(t)$ (see Eqs. 4.35 and 4.41) were executed. Both simulation runs were further based on the same stochastic noise generation function $\mathfrak{F}_m(t;z)$ (see Eq. 4.59). This ensures proper comparison. According to the approximate numerical scheme 4.66, the state vector $|\phi_z(t_n)\rangle$ was renormalized after each propagated time–step t_n (see further computational details in Appendix H.2.2). In total, an ensemble of each $\mathcal{N} = 3500$ system state trajectories was computed to achieve converged RDO kinetics according to the Eq. 4.60. The two kinetics were aligned with a third simulation run based on the nonlinear SSE 4.62, which holds the corresponding exact solution. Besides the three SSE algorithms, another computation run based on the multilevel Redfield equations was executed. It describes the popular quantum master equation in Markov approximation and directly simulates the kinetics of the RDO [44]. The parameters $\lambda = 35\,\mathrm{cm}^{-1}$ and $\gamma^{-1} = 10$ fs were applied to specify the spectral density $J(\omega)$. It should be noted that the chosen parameter set is a somewhat arbitrary one indicating fast phonon relaxation. However, it is utilized here since it represents the weak vibronic coupling Markov limit, i.e., proper comparison of the kinetics from the non–Markovian SSE algorithms and the Markovian Redfield equations is guaranteed.[9]

The time–evolution of the molecular excited state populations,

$$P_m(t) = \langle\varphi_m|\hat{\rho}(t)|\varphi_m\rangle, \tag{4.68}$$

are computed illustrated. For simplicity, the present study only concentrates on the three most relevant $P_m(t)$ with $m = 1$, 2 and 3. The respective chromophores are indicated by the colored labels in Fig. 4.1. All following simulations start from $P_m(0) = \delta_{m,1}$ and are carried out at $T = 300$ K. The graphic in Fig. 4.1 visualizes the expected coincidence of the data from the Redfield theory (dashed lines) and the nonlinear SSE (solid lines). It should be further mentioned that the convergences of the kinetics from the linear SSE were very carefully approved. In fact, due to the inherent numerical error, the proper convergence of these RDO kinetics could not be taken for granted. Their observed proper reproducibility was regarded here as an indirect consequence of the inherent averaging process (see Eq. 4.60).

In Fig. 4.3a and b, the exact data from the nonlinear SSE (pink lines) is each compared with the population kinetics from one of the two linear SSEs (see the displayed legend). The kinetics obtained with $\hat{\mathfrak{D}}(t)$ (see Eq. 4.35) are visualized by the green lines in Fig. 4.3a. The blue lines in Fig. 4.3b result from simulations based on $\hat{\mathfrak{D}}_{T=0}(t)$ (see Eq. 4.41). One realizes that the two linear SSEs give almost identical results independent on the implemented damping operator. According to Sec. 4.2.6, this is reasonable here and had to be expected due to the installed weak coupling parametrization. More

[9] In fact, it was demonstrated by Kreisbeck et al. that, based on these parameters, the second order Markovian Redfield approach is able to accurately reproduce exact results from a hierarchical equation of motion (HEOM) ansatz [177].

Figure 4.3.: Excitation energy transfer dynamics of site state populations, $P_m(t)$, in the FMO complex (for the parameters see text). Solid lines: $P_1(t)$, dashed lines: $P_2(t)$, dotted lines: $P_3(t)$ (see again Fig. 4.1). Panel a: Comparison of results from using the nonlinear SSE (pink coloring) and the linear SSE 4.58 (green coloring) with the integration scheme 4.66 and based on force $\mathscr{F}(t;z)$ (see Eq. 4.59) and damping $\hat{\mathscr{D}}(t)$ (see Eq. 4.35). Panel b: The same comparison as in panel a, but the linear SSE was simulated using $\hat{\mathscr{D}}_{T=0}(t)$ (see Eq. 4.41), instead.

importantly, both direct comparisons with the exact data (pink colored lines) are very unsatisfactory. In fact, significant diagreements are clearly recognizable. Likewise poor performances were recorded for both linear algorithms in simulations with $\gamma^{-1} = 50$ fs (not shown) – though using $\hat{\mathscr{D}}_{T=0}(t)$ produces slightly better coincidence in that case.

It can be concluded that the actual choice of damping operator (i.e., using $\hat{\mathscr{D}}(t)$ or $\hat{\mathscr{D}}_{T=0}(t)$) seems not an essential criteria for the performance of the linear SSE with the approximate propagation scheme 4.66. A second trial study is offered in the next section. It concentrates on the influence of the force generation algorithm.

4.5.3. Variation of the force function

The simulations discussed in the foregoing Sec. 4.5.2 showed that the conceived integration scheme 4.66 for the linear SSE 4.58 suffers strongly from accuracy. These results were computed based on the noise function $\hat{\mathscr{F}}(t;z)$ (see Eq. 4.59). In this section, therefore, the performance of the scheme 4.66 based on an alternative stochastic force generator shall be probed.

In general, different algorithms exist which generate noise with the same stochastic

properties (see, e.g., Ref. [165]). Concerning the analytical expression of the RDO, $\hat{\rho}(t) = \mathscr{M}[|\phi_z(t)\rangle\langle\phi_z(t)|$, the individual stochastic trajectory of the state vector is irrelevant. In this sense, the particular noise algorithm (underlying the stochstic force) may be simply replaced by another one. Under the condition that the substitute obeys the same stochastics, in principle, the unraveled RDO is kept unchanged. However, this changes critically regarding the numerical error introduced with the propagation scheme 4.66 for the linear SSE. Even if two force generating functions obey the same statistics, they may then lead to very distinct population kinetics.

Here, the introduction of the stochastic process in Sec. 4.3 straightly led to the formulation of the force according to $\mathscr{F}_m(t;z)$ (see Eq. 4.59) with the statistical moments $\mathscr{M}[\mathscr{F}_m(t)] = 0$, $\mathscr{M}[\mathscr{F}_m(t)\mathscr{F}_n(\tau)] = 0$ and $\mathscr{M}[\mathscr{F}_m(t)\mathscr{F}_n^*(\tau)] = \delta_{mn}C_m(t-\tau)$ (see Sec. 4.2.5). Several other algorithms with the same statistics were meanwhile proposed from alternative ansatzes in literature (see, e.g., Ref. [178]). It is now the intention to search for an alternative algorithm which works with the same stochastics as $\mathscr{F}_m(t)$, but which causes on average less dramatic drift of the vector norm of $|\phi_z(t)\rangle$ in the linear SSE. Such algorithm would consequently operate more accurately during the propagation scheme Eq. 4.66.

An alternative force algorithm with equivalent statistics is obtained, cf. Eq. F.33,

$$\mathscr{F}_m^{(2)}(t) = \sum_k^K \sqrt{\frac{\Delta\omega J(\omega_k)}{\pi}}\Big(A(\omega_k)\cos(\omega_k t + \zeta_{mk}) + iB(\omega_k)\sin(\omega_k t + \zeta_{mk})\Big), \tag{4.69}$$

as motivated by the earlier works of Refs. [160, 49, 50, 51]. Its phenomenological derivation is demonstrated together with its stochastic moments in Appendix F.4. As proved, it brings with the same stochastic properties but clearly distinguishes from $\mathscr{F}_m(t)$ in Eq. 4.59. The random phases ζ_{mk} are here uniformly generated from the interval $[0, 2\pi]$ and the two functions $A(\omega_k)$ and $B(\omega_k)$ follow according to

$$A(\omega_k) = \sqrt{\coth(\frac{\hbar\omega_k}{2k_\mathrm{B}T}) + \sinh(\frac{\hbar\omega_k}{2k_\mathrm{B}T})^{-1}} \tag{4.70}$$

and

$$B(\omega_k) = \sqrt{\coth(\frac{\hbar\omega_k}{2k_\mathrm{B}T}) - \sinh(\frac{\hbar\omega_k}{2k_\mathrm{B}T})^{-1}}. \tag{4.71}$$

As discussed in Secs. 4.4.1 and 4.4.3, a main cause of the drift of the state vector norm is found with the imaginary part of the complex–valued force. In this concern, a trivial but important feature can be realized in Eq. 4.69: the function $B(\omega_k)$ is generally smaller than the function $A(\omega_k)$. Especially for high temperatures, it means that the imaginary parts of the slowly oscillating terms (with small ω_k) in Eq. 4.69 are smaller than the real parts. This is different reconsidering $\mathscr{F}_m(t)$ (see Eq. 4.59), where the fluctuations of real and imaginary part are of equal amplitude. The latter observation is a very important issue of this thesis. In particular, it can be now expected that the scheme 4.66 works superior when it is applied to linear SSE algorithms based on $\mathscr{F}_m^{(2)}(t)$ instead of $\mathscr{F}_m(t)$.

Figure 4.4.: Excitation energy transfer dynamics of site state populations $P_m(t)$ in the FMO complex as in Fig. 4.3. Panel a and b: Same comparison between data from the nonlinear and linear SSE (see legend), but now concentrating on the linear SSE based on the alternative force algorithms $\mathscr{F}^{(2)}(t;z)$ defined with Eq. 4.69.

In order to prove this, further test simulations were executed in the fashion of Sec. 4.5.2. The FMO kinetics from the linear SSE 4.58 with the numerical scheme 4.66 were repeated twice (once based on $\hat{\mathscr{D}}(t)$ and once using $\hat{\mathscr{D}}_{T=0}(t)$), but now the force $\mathscr{F}_m^{(2)}(t)$ is utilized. The resulting data are illustrated in Fig. 4.4. The population kinetics obtained from $\hat{\mathscr{D}}(t)$ are colored green (see Fig. 4.4a) and the results from $\hat{\mathscr{D}}_{T=0}(t)$ are given in blue coloring (see Fig. 4.4b). Both simulations runs are again directly confronted with the exact data from the nonlinear SSE (pink coloring; overtaken from Fig. 4.3). Regarding the former rather bad performance of the linear SSE, both here observed kinetics using $\mathscr{F}_m^{(2)}(t)$ show surprisingly good agreement. As expected, the $\mathscr{F}_m^{(2)}(t)$ causes only minor drift of the norm of $|\phi_z(t)\rangle$.

Together, the four different kinetics give an impression that the propagation scheme 4.66 is more sensitive to the applied force generation function than to the choice of the damping operator. In general, this observation might be simply related to the fact that the force influences $|\phi_z(t)\rangle$ in first order of the system–bath coupling while the damping operator occurs in terms of second order in the SSE 4.58.

With the force generation function, $\mathscr{F}_m^{(2)}(t)$, an algorithm is found which significantly reduces the numerical error of the propagation scheme 4.66 applied to the linear SSE 4.58. The demonstrated great performance motivates its further application to the large–scale systems studied in Chaps. 7 and 8. A special strategy to indirectly evaluate

its performance in such cases is developed in Sec. 4.6.

4.6. Strategy for Application to Large–Scale Systems

In large–scale studies, the performance of a linear SSE algorithm based on the integration scheme 4.66 cannot be evaluated directly against results from the nonlinear SSE 4.62. The latter simulations are simply too computationally intensive and inefficient on that scale (see Sec. 4.4.2). Instead, it is the idea to judge indirectly about the suitability of a linear SSE algorithm. In fact, many interesting large–scale systems are based on a repetitive unit cell structure (e.g., molecular aggregates). Those systems can be constructed easily in different sizes. Also the systems studied later on in Chaps. 7 and 8 are of such type. In these cases, it can be argued that an algorithm applies properly to a large–scale systems if it performs appealingly on a related small–scale system and on condition that this performance is preserved or even improved when extending the system stepwise to larger sizes. This strategy allows judging the applicability of a linear SSE algorithm to extremely huge systems in indirect manner without the direct comparison with alternative exact methods. Instead, only several small to intermediate–scale comparative studies are required.

The described simulation technique is impressive due to its outstanding simplicity and, in principle, application to any kind of scalable large–scale system is possible. In Chap. 7, the procedure is exemplarily showcased in a study on hole transfer in a huge regular film of 2553 *para*–sexiphenyl molecules aggregated on a ZnO surface. Therefore, it is firstly demonstrated that the numerical error of the approximate propagation scheme even decreases impressively when increasing the size of the aggregate. In the second concrete application Chap. 8, the same strategy is followed to study exciton relaxation processes in a gigantic (also regular) tubular cyanine dye aggregate including the vast number of 4110 excitons.

4.7. Concluding Remarks

By virtue of its remarkable computational scaling properties, the linear SSE is of enormous practical value in application to large–scale open system studies. In comparison with the linear SSE, quantum master equations as well as the nonlinear SSE become swiftly inefficient when increasing the system size. In the foregoing sections, the methodology of the SSE is presented as a computationally cheap alternative to the direct solution of the quantum master equation. Different algorithms of linear SSEs and the nonlinear SSE are discussed.

In Sec. 4.2, novel aspects on deriving a linear SSE from first principles are offered. The derivation starts thereby directly from a finite temperature formulation of the RDO based on a coherent state description of the bath vibrational modes. In course of the discussion, the two different damping operators occuring in literature for the weak coupling scenario could be interrelated. This describes an important contribution to an unified microscopic ansatz. As another keypoint, in Sec. 4.3 the proper translation of the algebraic into the stochastic equation of motion is demonstrated by making use of a Monte–Carlo integration scheme.

The meaning of the linear SSE in practice is discussed elaborately in Sec. 4.4. Its computational demand scales only linearly when increasing the size of the system. This scaling benefit is the motivation to tackle the unavoidable numerical disadvantage of the linear SSE – the drifting norm of the trajectory $|\phi_z(t)\rangle$. Therefore, a straight numerical renormalization scheme of the linear SSE is introduced. It allows for approximately propagating the $|\phi_z(t)\rangle$ while the beneficial scaling feature is preserved.

In the framework of Sec. 4.5, first performance tests of the linear SSE based on the approximate propagation scheme are demonstrated. The FMO complex serves here as an adequate trial system. It only consists of seven chromophores and exact data (for comparison) can be straightly produced with the nonlinear SSE algorithm. Very good performance of the renormalization scheme is observed when the force generation function $\mathfrak{F}_m^{(2)}(t)$ (see Eq. 4.69) is applied. Although $\mathfrak{F}_m^{(2)}(t)$ was already utilized earlier, it describes a key challenge of this thesis to document and to clarify its particular value for the numerical implementation of the linear SSE. The superior performance based on $\mathfrak{F}_m^{(2)}(t)$ is demonstrated and explained as the result of the special feature of $\mathrm{Im}[\mathfrak{F}_m^{(2)}(t)] < \mathrm{Re}[\mathfrak{F}_m^{(2)}(t)]$. This is discussed here for the first time.

Finally, in Sec. 4.6 a simple strategy to evaluate the performance of the linear SSE in application to large–scale open systems is developed. In particular, in such cases it is the task to judge the performance of the approximate integration routine without parallel simulations based on other more expansive methods. Instead, evaluation must then rely on impressions obtained from a series of related systems with reduced size.

The here worked out simulation technique using a linear SSE is of enormous value for large–scale open system studies including more than 1000 states. In Chaps. 7 and 8, it opens the opportunity to study dissipative charge and exciton transfer mechanisms in two nanoscale interface structures with the impressive numbers of 2553 and 4110 electronic states, respectively.

5. Excitation Energy Transfer at the *para*–Sexiphenyl/ZnO Nano–Interface

Detailed insights into electronic transfer processes at organic/inorganic interfaces are recently of tremendous interest. Understanding the energy transfer from Frenkel excitons or molecular excitations in organic aggregates to electron–hole pair excitations in semiconductor nanostructures opens opportunities for designing novel hybrid devices for optoelectronics. In the following, excitation energy transfer is simulated in a prototypical para–sexiphenyl/ZnO nano–interface system. Though the system describes a huge finite structure, the presented modeling is based on a single–particle treatment. All computations are carried out in atomistic resolution. By virtue of that, the offered insights are of immense value. Major parts of this chapter were published in Ref. [179].

The particular focus lies on the scenario of initially populated Frenkel excitons. The first part of the study is devoted to their detailed investigation. Excitonic energies and spatial localizations are analysed. Thousands of excitonic couplings between Frenkel excitons (considered as energy donor states) and electron–hole pair excitations (considered as energy acceptor state) are determined. Subsequently, the energy level alignment of both types of excited states is inspected. It gives message on whether efficient resonant energy transfer can be expected or not. The entire discussion is supported by drawing comparison with the situation of intially prepared single–molecule excitations.

In general, only very weak excitonic couplings are computed and significant effects from "hybrid interface excitons" can be ruled out. At first place, this encourages a simplified model based on transfer rates according to Fermi's golden rule. In order to prove the validity of the rate ansatz in the present case, its prognosed exponential decay of Frenkel exciton population is compared to exciton wave packet dynamics according to the time–dependent Schrödinger equation. Very different time–scales of energy transfer into the ZnO are observed under variation of the initially prepared energy donor states. Thereby, the higher Frenkel exciton levels decay most rapidly. These top levels are characterized by lifetimes in the ps–region. Contrarily, energy transfer initialized in the lower part of the Frenkel exciton band are blocked by a reduced number of available energy acceptor states and lifetimes in the ns–region are uncovered.

The here obtained insights into the energy transfer can be straightly related to the investigations on photoinduced charge separation process presented in Chap. 6. Their direct comparison informs about unwanted quenching effects of the charge separation mechanism (e.g., in a photovoltaic module). Please note that the stochastic Schrödinger equation method is not employed in this chapter.

5.1. Background and Motivation

Many innovative ideas in the field of optoelectronics are expected from further nanotechnological development of organic/inorganic hybrid materials (see Chap. 1). The discovery of specific excitonic properties of such materials is of paramount interest. The steadily growing research community concentrating on excitation energy transfer (EET) between organic molecules and semiconductor nanostructures gives evidence on that [1, 2]. Meanwhile, an overwhelming amount of spectroscopic studies can be found in literature. Many of these report on features of small complexed hybrid structures based on few molecules and small quantum dots of nanocrystals [30, 31, 7, 4, 129]. Often these studies also include simple Förster resonant energy transfer calculations. Other works focus on excitonic processes in essentially larger hybrid architectures [5, 26, 28], especially in form of multilayers of different materials [180, 128, 181, 6, 15, 10, 14].

Detailed knowledge on the excitonic effects between both material classes can only be gathered from concrete computational studies. Quantifying the excitonic coupling is the first important step towards specific creation of hybrid devices. In general, studies of such concern are recently of great value and tremendous importance. In contrast to the experimental works, however, the list of theoretical studies on excitonic properties of related hybrid systems is rather short. As discussed in Chap. 1, theoretical studies on EET dynamics at hybrid interfaces become extremely cumbersome when turning to realistic nanoscale. In turn, so far ab–initio ansatzes were only applied to very small finite molecule/nanocrystal systems in order to deliver excitonic properties [76, 182]. Other studies concentrate on systems of molecular layers deposited on flat semiconductor surface. In such cases, corresponding computations can profit from system periodicity and so ab–initio models become possible as well. Excitonic properties and transfer processes were studied recently in this fashion [35, 38, 36]. However, also the periodic simulation cells in these computations cannot become too large and insights into, e.g., wide–range exciton transfer are restricted.

In the present work, the *para*–sexiphenyl (6P)/ZnO interface is studied. It is generally introduced and motivated in Chap. 1 (see Fig. 1.2). As discussed, ZnO components are chosen favorably for materials in industrial sectors of optoelectronics because of their rather straightly tuneable band gap and a diversity of possible nanoscale designs and flat surface structures which can be prepared cheaply and easily [58, 24, 61, 72]. The 6P is a very promising candidate for building optically active molecular layers on plane ZnO surfaces. As illustrated in Fig. 1.2c and d, deposited 6P molecules start to assemble regularly according to two favored molecular orientations – either in up–right standing or in flat lying position [68, 65]. These interfaces show interesting excitonic features. In particular, diverse EET processes at related oligo–phenyl/ZnO interfaces were measured after specific optical excitation of either the molecular aggregate or the ZnO part (see, e.g., Refs. [180, 181, 68, 65, 67]). Here, the focus shall be on the EET from the 6P aggregate to the ZnO part.

A finite and nanoscopic 6P/ZnO interface structure is designed (see details below). Due to its impressive size, it cannot be approached in an uniform ab–initio modeling (as a whole). Instead, energies and wave functions of the interface states are here introduced in terms of a diabatization ansatz of the entire system, i.e., in the shape of

direct products of individual substructure states. In consequence, each substructure can be modeled using the best suited electronic structure method. Concretely, here a combination of ab–initio TD–DFT (for the isolated 6P) and semi–empirical DFT–based tight–binding approach (for the ZnO cluster) [80] is employed. Thanks to that, an atomistic exciton theory can be formulated for a system which appears huge in comparison with all formerly investigated systems [76, 130, 182]. The price for it, however, is paid with an enormous number of different electrostatic and excitonic coupling terms between Frenkel excitons on the one hand side and electron–hole pair excitations on the other hand side of the interface. As the fundamental quantity, here the excitonic coupling receives special attention. Their computation in atomistic resolution is a key challenge of this study.

It is an important advantage of the present large–scale model that Frenkel excitons in the molecular aggregate may also couple to electron–hole pair states which are localized further remote from the interface zone (i.e., "deeper" in the "bulk–like" region of the ZnO cluster). Another benefit of the present ansatz is that it also allows studying mechanisms of charge separation, which are of relevance when following the idea of a photovoltaic or light emitting device (see, e.g., Refs. [15, 10, 183]). In this regard, the present investigation is standalone but closely related to the work presented in the framework of Chap. 6. There, simulations on photoinduced charge separation kinetics at the model interface are discussed and the interface EET is considered as a possible quenching process which could lower the yield of free charge carrier generation (see also Chap. 1). Later on, its actual potential is estimated based on the here determined characteristic exciton transfer times.

According to Ref. [80], the excitonic coupling between both types of excitations can be expected to stay in the meV–range or less on condition that the distance between the 6Ps and the ZnO surface is in the Ångström–range or larger (chemically non–bonded configuration without significant wave function overlap). In most cases, this justifies a transfer models based on incoherent rate expression according to Fermi's golden rule [80] or the simplified Förster theory [76, 5]. In the aspired scenario, the multitude of electron–hole pair excitations may form a quasi–continuum of energy acceptor states. This would further support an exponential and unidirectional picture of the EET process. Attention however must be paid for stronger coupling and, in particular, for a rather restricted number of energy acceptor states of the transition, i.e., less dense electron–hole pair excitations. In these cases, one has to go beyond the latter convenient picture. Instead of a rate ansatz, the transfer dynamics are then more adequately approached in terms of exciton wave packet motion based on the time–dependent Schrödinger equation (see also Sec. 3.2). In this regard, it is of general interest to present here a rate approach in direct comparison with direct wave function propagation. While the Förster transfer rate (based on point–dipole approximation of the excitonic coupling with the famous $1/R^6$–distance dependence) is the usual choice (see, e.g., Refs. [12, 130, 5, 30, 7, 129, 26]), here the more general rates expressions (deduced from Fermi's golden rule) shall be utilized. Its computation is based on excitonic coupling terms in atomistic resolution. This provides results which are more accurate than any multipole expansion and hold clear indications on the applicability of the approximate Förster theory. (Sec. 8.7.3 is further devoted to that important

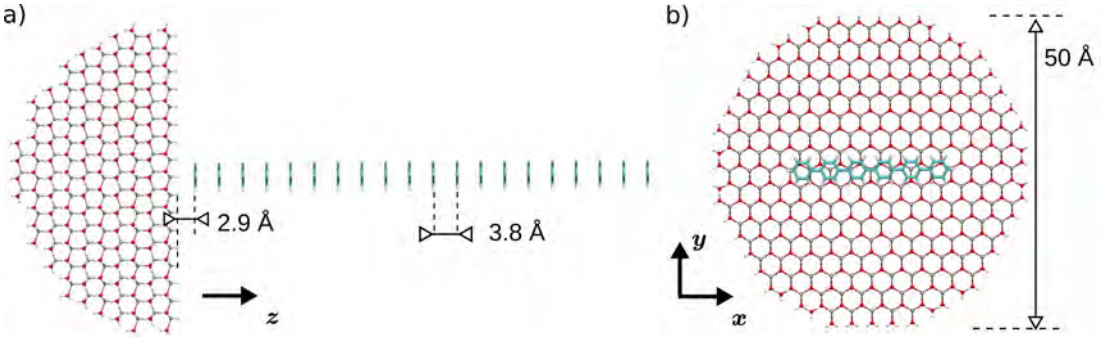

Figure 5.1.: Structure of the 6P/ZnO model interface system. Panel a: Side view on the system with the hemispherical ZnO cluster (left) and the 20 π–stacked molecules (right). Panel b: Top view on the system (please note the Cartesian coordinate axes).

issue.)

5.2. Atomistic Structure of the Interface System

The atomic structure of the studied model system is depicted in Fig. 5.1. It describes a regular arrangement of 20 π–stacked 6Ps placed on the (0001) surface of a wurtzite ZnO cluster. The latter is of hemispherical shape with 5 nm diameter and contains 3903 atoms. Its artificial shape is the result of a special ansatz, where the system can be considered as an outtake of a larger interface system. The hemispherical ZnO cluster and the laterally aggregated 6P stacking allow adequately studying wide–range EET (and charge–separation, cf. Chap. 6), on condition that its total volume is hold modest (see also Chap. 1). The flat "front" surface is terminated with pseudo–hydrogen saturated zinc atoms and renders one of the three prominent ZnO plane faces [65, 180, 24, 67] (see also Fig. 1.2b). The spherical "backside" of the cluster is exclusively terminated by oxygen atoms (also covered with an pseudo–hydrogen saturation shell). This exclusive oxygen shell seems exceptional but, for the present purpose, it describes the "backside" of the cluster more realistically. Instead of a mixed zinc and oxygen saturation, it only generates surface states which lie energetically very apart from the band–gap region. Hence, the here relevant electronic structure of the cluster appears reasonably as an outtake of a much larger surface. The 6P molecules are arranged in about van der Waals contact distances (see Fig. 5.1a). At the ZnO surface, this corresponds to the physisorption process observed in experiments [65, 64, 68]. Instead of the 6P herringbone lattice, however, a one–dimensional variant of π–stacking is chosen here in completely flat configuration (i.e., untwisted phenyl–rings). The first molecule is placed in separation of 2.9 Å to the cluster and the intermolecular distance amounts 3.8 Å. For simplicity the cluster–molecule orientation is conceived in such way that the 6P longitudinal axis is aligned with the axis defined by the "rail" of zinc atoms in the middle of the surface (see Fig. 5.1b). Further aspects of the 6P alignment could be surely addressed concerning concrete electrostatic and van der Waals interaction with

the ZnO surface atoms (for related ab–initio modelings, see, e.g., Refs. [184, 185, 69]). Here, a force field–driven alignment of the 6Ps is spared right from the beginning in order not to overload the transfer model.

5.3. Modeling the Excitonic Interface System

As stated in Sec. 5.1, diverse experimental investigations were already executed on 6P/ZnO interfaces (see also Chap. 1). As illustrated in Fig. 1.2e, the HOMO–LUMO energy gap of 6P molecules aggregated on the (0001) ZnO surface was measured to be about 0.2 eV larger than the band gap of macroscopic ZnO substrate [68]. In principle, this opens opportunities for resonant EET from the 6P part to the ZnO slab (see also the discussion in Chap. 1). The following description is solely focused on decay of Frenkel excitons (FXs) of the 6P aggregate into the manifold of electron–hole pair excitations residing in the ZnO cluster (see also Sec. 5.1).

In order to construct the excited electronic states of the 6P/ZnO interface, very small wave function overlap between the 20 6P molecules as well as between the ZnO cluster and the 6Ps is assumed (see again Fig. 5.1). This allows making use of the diabatization scheme generally introduced in Sec. 2.3.1. A certain electronic state of the interface follows then by the direct–product ansatz according to, cf. Eq. 2.18,

$$|\bar{\Psi}\rangle = \prod_{m}^{N^{6\mathrm{P}}} |\Phi_m\rangle \otimes |\Psi\rangle. \tag{5.1}$$

In general, it consists of $N^{6\mathrm{P}} = 20$ separate molecular states, $|\Phi_m\rangle$, and a many–electron state of the ZnO nanocrystal, $|\Psi\rangle$. Further, the exciton transfer Hamiltonian is straightly considered in terms of, cf. Eq. 2.36,

$$\hat{H} = \hat{H}_{\mathrm{agg}} + \hat{H}_{\mathrm{sc}} + \hat{H}_{\text{agg-sc}} \, . \tag{5.2}$$

It covers the FXs in the molecular aggregate, $\hat{H}_{\mathrm{agg}}$, and the excitations in semiconductor part, $\hat{H}_{\mathrm{sc}}$. The $\hat{H}_{\text{agg-sc}}$ describes the coupling part between the 6P aggregate and the ZnO cluster. It accounts for the EET processes of interest and is assumed to be free of exchange and correlation contributions. Corrections of the excitation energies of the FXs as well as the electron–hole pair excitations due to electrostatic interaction (i.e., of direct Coulomb–type) shall be instead already incorporated in $\hat{H}_{\mathrm{agg}}$ and $\hat{H}_{\mathrm{sc}}$.

5.3.1. Frenkel–like excitons of the *para*–sexiphenyl aggregate

First of all, interface states of molecular localized excitations shall be introduced in order to formulate the aggregate Hamiltonian. In the fashion of Sec. 2.3.4 (see Eq. 2.37), these are defined according to,

$$|\mathrm{LX}_m\rangle = |\bar{\Phi}^e_m\rangle \otimes |\Psi_0\rangle = |\Phi^{(m)}_e\rangle \otimes \Big[\prod_{n\neq m}^{N^{6\mathrm{P}}} |\Phi^{(n)}_g\rangle \Big] \otimes |\Psi_0\rangle. \tag{5.3}$$

They describe an excitation localized on the mth 6P molecule, which correspondingly realizes the S_1 first excited state $|\Phi_e^{(m)}\rangle$. The other molecules (with $n \neq m$) and the ZnO cluster stay in their electronic ground state configurations, $|\Phi_g^{(n)}\rangle$ and $|\Psi_0\rangle$, respectively. If expanded with respect to these states, the Hamiltonian of the molecular sub system takes the standard form,

$$\hat{H}_{\mathrm{mol}} = \sum_{m}^{N^{6\mathrm{P}}} \mathscr{E}_m |\mathrm{LX}_m\rangle\langle \mathrm{LX}_m| + \sum_{m\neq n}^{N^{6\mathrm{P}}} \mathscr{J}_{mn} |\mathrm{LX}_m\rangle\langle \mathrm{LX}_n|. \tag{5.4}$$

Its diagonal elements describe the excitation energies of the individual molecules (being aware of the ZnO cluster). In the fashion of the Eq. 2.28, they follows as,

$$\begin{aligned}\mathscr{E}_m = E_e^{6\mathrm{P}} - E_g^{6\mathrm{P}} + \sum_{n\neq m} \int d^3\mathbf{x} d^3\mathbf{y} \frac{[n_e^{(m)}(\mathbf{x}) - n_g^{(m)}(\mathbf{x})][n_g^{(n)}(\mathbf{y}) + \sum_\mu Z_\mu^{(n)} \delta(\mathbf{y} - \mathbf{R}_\mu^{(n)})]}{|\mathbf{x}-\mathbf{y}|} \\ + \int d^3\mathbf{x} d^3\mathbf{y} \frac{[n_e^{(m)}(\mathbf{x}) - n_g^{(m)}(\mathbf{x})]\Omega(\mathbf{y})}{|\mathbf{x}-\mathbf{y}|}.\end{aligned} \tag{5.5}$$

The first two terms, $E_g^{6\mathrm{P}}$ and $E_e^{6\mathrm{P}}$, represent the ground state energy of a 6P in gas phase and its related first excited state energy, respectively. As announced above, additional electrostatic interaction energy corrections enter. According to the general expression Eq. 2.28 based on Eqs. 2.25 and 2.27, all electrons and nuclei of the surrounding (here the remaining aggregate and the ZnO cluster) interact with the excitation localized on the mth 6P molecule. The latter is rendered in terms of the difference of the electronic charge densities, $n_e^{(m)}(\mathbf{x}) - n_g^{(m)}(\mathbf{x})$ (see Eq. 2.26). The charge density of the surrounding 6P aggregate structure is decomposed into individual molecular charge densities related to electronic ground state configuration, $n_g^{(n)}(\mathbf{y}) + \sum_\mu Z_\mu^{(n)} \delta(\mathbf{y} - \mathbf{R}_\mu^{(n)})$ (with $n \neq m$). The latter molecular densities carry contributions of all electron and nuclei according to Eqs. 2.25 and 2.27. Equivalently, the density $\Omega(\mathbf{y})$ is introduced in $\mathscr{E}_m$. It represents the charge distribution of the entire ZnO nanocrystal (nuclei plus electrons; also in the electronic ground state). The offdiagonal elements of $\hat{H}_{\mathrm{mol}}$ represent the EET couplings among all 6P pairs according to, cf. Eq. 2.29,

$$\mathscr{J}_{mn} = \int d^3\mathbf{x} d^3\mathbf{y} \frac{n_{eg}^{(m)}(\mathbf{x}) [n_{eg}^{(n)}(\mathbf{y})]^*}{|\mathbf{x}-\mathbf{y}|} \,. \tag{5.6}$$

The $\mathscr{J}_{mn}$ is determined by the molecular transition density $n_{eg}^{(m)}(\mathbf{x})$. Its general form is detailed discussed in Sec. 2.3.2 (see Eq. 2.30). Here, the $n_{eg}^{(m)}(\mathbf{x})$ is defined via spatial overlap of the ground and excited state wave functions $|\Phi_g^{(m)}\rangle$ and $|\Phi_e^{(m)}\rangle$. It characterizes the excitation of the mth 6P molecule. The complex conjugate density in Eq. 5.6 accounts for the vice versa de–excitation process of the nth 6P.

Different computations were performed on the DFT and INDO/CIS level in order to obtain all quantities related to the 6P molecule (see Secs. 2.1.3 and 2.1.4). Detailed computational protocols are provided in Appendix G.1. Thereby, the molecular exci-

Figure 5.2.: Frenkel exciton (FX) formation in the 6P stack. Panel a: Excitonic coupling $\mathcal{J}_{mn}$ (see Eq. 5.6) versus intermolecular distance from atomistic and point–dipole modeling (see indication). Panel b: FX energies $\mathscr{E}_{\alpha}^{\mathrm{FX}}$ (inset: molecular excitation energies $\mathscr{E}_m$, cf. Eq. 5.5). Panel c: Excitonic expansion coefficents $\mathscr{C}_{\alpha}(m)$ versus the moleuclar index m and exciton quantum number α (see Eq. 5.7). The green dashed ellipse marks the spatial area of great localization close to the ZnO surface (for details, see the main text).

tation energy was determined as $E_e^{6\mathrm{P}} - E_g^{6\mathrm{P}} = 4.02$ eV. For more efficient calculation of the integral expressions in Eq. 5.5 (and Eq. 5.6), the continuous 6P charge densities of the ground and excited state (and transition density) were approximately substituted by atomic centered partial (transition) charges (see Appendix G.1). Moreover, for more reasonable values of $\mathscr{E}_m$, the size of the 6P aggregate was extended up to 40 molecules (i.e., the integral part in Eq. 5.5 includes further 20 molecules elongating the aggregate offside the ZnO surface). In this way, the interaction energy of a somewhat larger aggregate is simulated. The electronic ground state configuration of the ZnO cluster and the related density $\Omega(\mathbf{r})$ (also approximated in terms of atomic centered charges) was computed based on the semi–empirical DFTB scheme introduced in Sec. 2.2.1 (for computational details, see Appendix G.3).

An atomistic modeling of the intermolecular EET coupling, $\mathcal{J}_{mn}$, is employed although this clearly means a greater numerical effort in comparison with the more conventional point–dipole interaction model (lowest order multipole expansion). To work with such accuracy was advisable here, because the intermolecular distances within the 6P stacking are essentially smaller than the 6P molecular length (see Fig. 5.1). The computed values of $\mathcal{J}_{mn}$ between molecule m and n are illustrated in Fig. 5.2a. They

are drawn against the intermolecular distance (i.e., $d = |m - n| \cdot 3.8$ Å). The data connected by the blue line (with blue squares) is obtained by applying the atomistic interaction model. As indicated, the chosen discretization of the distance axis corresponds to the repetitive step size of the 6P stack. To emphasize the need for the atomsitic resolution, also related values based on the more approximate point–dipole model were computed. In direct comparison, they are given by the purple line with pink triangles. Very large discrepancies can be figured out and a clear overestimation of the dipole coupling results especially in cases of intermolecular distances closer than 35 Å (i.e., within ranges of about 10 nearest neighbor units). Moreover, as depicted in Fig. 5.2a, it is $\mathscr{J}_{m,m+1} = 75$ meV (excitonic coupling between nearest neighbors). This value gives evidence on rather prominent excitonic couplings. Indeed, even the $\mathscr{J}_{mm+3}$ still amounts about 12 meV. The uncovered strong excitonic coupling dictates to go beyond a nearest neighbor coupling model in the present study.

Next, the possible FX states of the interface system are obtained as the eigenstates of $\hat{H}_{\rm mol}$ (see Eq. 5.4). This treatment is generally discussed in Sec. 2.3.4 and equivalent with the "standard" Frenkel exciton approach (see Eq. 2.32). Here, the related FX energies, $\mathscr{E}_\alpha^{\rm FX}$, follow as the corresponding eigenvalues of $\hat{H}_{\rm mol}$. By making use of the above basis set of localized excited states, Eq. 5.3, the FXs follow as, cf. Eq. 2.38,

$$|{\rm FX}_\alpha\rangle = \sum_m^{N^{\rm 6P}} \mathscr{C}_m(\alpha)|{\rm LX}_m\rangle, \tag{5.7}$$

with the exciton expansion coefficients, $\mathscr{C}_m(\alpha)$. The main panel of Fig. 5.2b holds the $\mathscr{E}_\alpha^{\rm FX}$. The inset panel depicts the molecular excitation energies $\mathscr{E}_m$ (see Eq. 5.5). The 20 levels of the FX spectrum cover the energy range from 3.91 up to 4.32 eV and show the typical features of a H–aggregate. This is reasonable here, because the vector of the transition dipole moment points along the long molecular axis. In the present 6P stack, this leads to the H–aggregate formation. The observed strong level splitting in the exciton spectrum is the direct consequence of the effective excitonic coupling. As shown in the inset of Fig. 5.2b, the variation of the energies $\mathscr{E}_m$ is much too small to be responsible for such a wide spectral range. In fact, only very small electrostatic interaction energies modulate the $\mathscr{E}_m$ in the meV–range.

Details on the spatial structure of the FXs upon the 6P stacking are illustrated in Fig. 5.2c. Precisely, the expansion coefficients $\mathscr{C}_m(\alpha)$ (see Eq. 5.7) are drawn versus the molecular index m (see z–axis in Fig. 5.1a). The color–code of the 20 horizontal strips renders the route of the $\mathscr{C}_m(\alpha)$ across the stacking including sign. The map highlights impressively the nodal structure of the exciton wave functions. As shown, the $|{\rm FX}_{\alpha=20}\rangle$ is node–free, the $|{\rm FX}_{\alpha=19}\rangle$ has one node, and so on. This behavior with respect to index m is an important observation and a keypoint of the discussion later on in Secs. 5.4 and 5.5.

5.3.2. Electron–hole pair excitations of the ZnO cluster

The electronic ground state structure of the ZnO nanocrystal was generated using the TB methodology described in Sec. 2.2.1. In particular, a number of $N_{\rm VB} = 12253$ VB–like single–particle states and a number of $N_{\rm CB} = 6003$ CB–like single–particle states

were obtained. Based on that, the excited states of the ZnO would be modeled in form of Wannier–Mott–like excitons. This ansatz is generally introduced in Sec. 2.2.2 (see Eq. 2.12). For practical reasons, however, its implementation cannot be mastered in the present case. The number of relevant excited states is simply too large (see below). In fact, the inclusion of the electron–hole correlation effects (see Eqs. 2.14 and 2.15) significantly rises computational costs and a straight solution of the Wannier–Mott exciton equation 2.13 is beyond the scope of this thesis.

Here, it has to be assumed instead that correlation effects are less important regarding the huge amount of available excitations forming a quasi–band of energy acceptor states. Based on that argumentation, the excited states of the ZnO cluster are approximately treated in terms of (uncorrelated) electron–hole pair excitations (EHPs), cf. Sec. 2.2.2,

$$|\Psi_{as}^{\bar{a}s}\rangle = \hat{e}_{\bar{a}s}^{\dagger}\hat{h}_{a-s}^{\dagger}|\Psi_0\rangle. \tag{5.8}$$

The $\hat{e}_{\bar{a}s}^{\dagger}$ and $\hat{h}_{a-s}^{\dagger}$ create an electron in the CB–like state $\bar{\psi}_a$ (with spin s) and a hole in the VB–like state ψ_a (with spin $-s$), respectively.[1] Then, the excited states of the complete interface system, where a single excitation resides on the ZnO cluster, can be directly identified as, cf. Eq. 2.40,

$$|\mathrm{EHP}_{\bar{a}s,as}\rangle = |\bar{\Phi}_0\rangle \otimes |\Psi_{as}^{\bar{a}s}\rangle. \tag{5.9}$$

Because the electron–hole pair correlation is suppressed, now also the ZnO cluster part of the Hamiltonian in Eq. 5.2 simplifies to

$$\hat{H}_{\mathrm{sc}} = \sum_{s}\Big(\sum_{\bar{a}}^{N_{\mathrm{CB}}}\bar{E}_{\bar{a}}\hat{e}_{\bar{a}s}^{\dagger}\hat{e}_{\bar{a}s} + \sum_{a}^{N_{\mathrm{VB}}}E_a\hat{h}_{a-s}^{\dagger}\hat{h}_{a-s}\Big). \tag{5.10}$$

Accordingly, the energies of the EHPs in Eq. 5.9 are directly given as

$$\mathscr{E}_{\bar{a}s,as}^{\mathrm{EHP}} = \bar{E}_{\bar{a}} + E_a, \tag{5.11}$$

with the electron energy, according to

$$\bar{E}_{\bar{a}} = \bar{\epsilon}_{\bar{a}} + \sum_{m}^{N^{6\mathrm{P}}}\int d^3\mathbf{x}d^3\mathbf{y}\frac{\bar{\rho}_{\bar{a}}(\mathbf{x})n_g^{(m)}(\mathbf{y})}{|\mathbf{x}-\mathbf{y}|}. \tag{5.12}$$

The first term, $\bar{\epsilon}_{\bar{a}}$, represents the energy of the electron in the isolated ZnO system (CB–like single–particle energy). The second integral term introduces the energy correction due to the Coulomb coupling between the CB–like electron with density $\bar{\rho}_{\bar{a}}(\mathbf{x})$ (introduced in Eq. 2.41) and the 6P molecules in electronic ground state configuration (represented by the density $n_g^{(m)}(\mathbf{y})$). The hole energy E_a in Eq. 5.11 is written in similar way, but based on the hole energy ϵ_a and the hole density $\rho_a(\mathbf{x})$, instead (see

[1] In general, spin–orbit coupling effects are conceivable (see, e.g., Sec. 8.4 and Refs. [80, 186]), but were not part of the applied TB parametrization for ZnO. The modeled singlet character of the excitons (i.e., zero total spin) is prescribed by introducing FXs of singlet type in Sec. 5.3.1. States of other spin configuration are irrelevant here as they cannot serve as energy acceptor states.

Figure 5.3.: Energy level scheme of the interface excited states. Energy levels $\mathscr{E}_{\gamma}^{\mathrm{EHP}}$ (see Eq. 5.11) of the ZnO electron–hole pair excitations (EHPs; pink coloring) are compared with the energies, $\mathscr{E}_{\alpha}^{\mathrm{FX}}$ (see Fig. 5.2b), of the 20 Frenkel–like excitons residing on the 6P stacking (FXs; cyan coloring).

again Eq. 2.41). In practice, again sets of atomic centered partial charges were utilized to compute the interaction terms in $\bar{E}_{\bar{a}}$ and E_a (see Appendix G.3.3).

Further on, the more convenient notation of $|\mathrm{EHP}_{\gamma}\rangle$ and $\mathscr{E}_{\gamma}^{\mathrm{EHP}}$ shall be used to abbreviate $|\mathrm{EHP}_{\bar{a}s,as}\rangle$ and $\mathscr{E}_{\bar{a}s,as}^{\mathrm{EHP}}$ in Eqs. 5.9 and 5.11, respectively. Thereby, the exciton index $\gamma \in \{1, ..., N^{\mathrm{ZnO}}\}$ counts all possible combinations of created electron–hole pair excitations including spin alternation (N^{ZnO} labels their total number). In Fig. 5.3, the computed levels of $\mathscr{E}_{\gamma}^{\mathrm{EHP}}$ are compared to the FX levels $\mathscr{E}_{\alpha}^{\mathrm{FX}}$ (also shown in Fig. 5.2b). Thereby, the pink band structure represents only the energetically lower part of the vast number of $N^{\mathrm{ZnO}} = 2 \times N_{\mathrm{CB}} \times N_{\mathrm{CB}} = 147109518$ EHPs which are presently available. In the following, this number is by far too much for an explicit treatment (even without electron–hole pair correlation). Fortunately, the major part of the band, however, lies in energetically far beyond the highest FX level at 4.32 eV. Therefore, it can be expected that these have only an negligible influence on the exciton kinetics discussed in Secs. 5.5. In this view, a strict restriction of the EHPs to only those with $\mathscr{E}_{\gamma}^{\mathrm{EHP}} < 5$ eV is used from now on. The limit reduces the amount of relevant EHPs to a manageable number of $N^{\mathrm{ZnO}} = 68388$. As given in Fig. 5.3, the lowest EHP energy lies at 3.97 eV. This value also accounts for a small electrostatic correction of +3.5 meV (see Eq. 5.12). In general, the observed electrostatic shifts lie in the range of about ±60 meV. As further shown, the lowest energy $\mathscr{E}_{1}^{\mathrm{EHP}}$ is positioned within the Frenkel excitonic band. Moreover, when going higher in energy one realizes that the density of EHPs increases. This is a plausible and a typical observation because of the higher the energy the larger the number of different electron and hole pair combinations.

Figure 5.4.: Excitonic coupling $\mathscr{J}_{\gamma m}^{\text{6P-EHP}}$ (see Eq. 5.15) between molecular excitations (6P*) and ZnO electron–hole pair excitations (EHPs) versus energy $\mathscr{E}_{\gamma}^{\text{EHP}}$. Panel a-d: Four sets of $\mathscr{J}_{\gamma m}^{\text{6P-EHP}}$ related to $m = 1$, 2, 10, 20, respectively. The blue Gaussians (with FWHM of 50 meV) point to the 6P* energies, $\mathscr{E}_m$ (see Eq. 5.5). Panel e: Comparison of $\mathscr{E}_{\gamma}^{\text{EHP}}$ (pink) and $\mathscr{E}_m$ (blue).

5.4. Excitonic Coupling across the Interface

Making use of the excited states $|\mathrm{FX}_\alpha\rangle$ (see Eq. 5.7) and $|\mathrm{EHP}_\gamma\rangle$ (see Eq. 5.9), the interface system Hamiltonian in Eq. 5.2 is expanded resulting in

$$\hat{H} = \tag{5.13}$$
$$\sum_\alpha \mathscr{E}_\alpha^{\mathrm{FX}} |\mathrm{FX}_\alpha\rangle\langle\mathrm{FX}_\alpha| \quad + \sum_\gamma \mathscr{E}_\gamma^{\mathrm{EHP}} |\mathrm{EHP}_\gamma\rangle\langle\mathrm{EHP}_\gamma| + \sum_{\alpha,\gamma} \Big(\mathscr{J}_{\gamma\alpha}^{\text{FX-EHP}} |\mathrm{EHP}_\gamma\rangle\langle\mathrm{FX}_\alpha| + \mathrm{H.c.} \Big).$$

In general form, this expansion is introduced in Sec. 2.3.4 (see Eq. 2.42). The energies, $\mathscr{E}_\alpha^{\mathrm{FX}}$ and $\mathscr{E}_\gamma^{\mathrm{EHP}}$, on the diagonal are already discussed in detail in Secs. 5.3.1 and 5.3.2. The offdiagonal terms describe the excitonic couplings across the interface. Precisely, the coupling element $\mathscr{J}_{\gamma\alpha}^{\text{FX-EHP}}$ is responsible for EET from FX with index α to EHP with index γ. It decomposes into according to

$$\mathscr{J}_{\gamma\alpha}^{\text{FX-EHP}} = \sum_m^{N^{6\mathrm{P}}} \mathscr{C}_m(\alpha) \mathscr{J}_{\gamma m}^{\text{6P-EHP}}, \tag{5.14}$$

with (reminding that γ unifies the index pair $\bar{a}s, a-s$)

$$\mathscr{J}_{\gamma m}^{\text{6P-EHP}} = \int d^3\mathbf{x} d^3\mathbf{y} \frac{\big(n_{eg}^{(m)}(\mathbf{x})\big)^* \rho_\gamma^{(\text{e-h})}(\mathbf{y})}{|\mathbf{x}-\mathbf{y}|}. \tag{5.15}$$

The latter expression, $\mathscr{J}_{\gamma m}^{\text{6P-EHP}}$, formulates the EET coupling between $|\mathrm{LX}_m\rangle$ with the 6P molecular transition density $n_{eg}^{(m)}(\mathbf{x})$ (see Eq. 5.3) and $|\mathrm{EHP}_\gamma\rangle$ with the transition density $\rho_\gamma^{(\text{e-h})}(\mathbf{y})$. For details on the latter, see Appendix G.3. (Please note further that the complex conjugate of the $n_{eg}^{(m)}(\mathbf{x})$ in Eq. 5.15 accounts for the de–excitation process of the mth 6P molecule. In superposition and weighted with the coefficients $\mathscr{C}_m(\alpha)$ (introduced in Eq. 5.7), these terms generate the FX–related coupling expression in Eq. 5.14. As found with Eq. 5.14, not only the spatial distribution (i.e., the $|\mathscr{C}_m(\alpha)|^2$), but also the sign of the individual $\mathscr{C}_m(\alpha)$ potentially influence the coupling strength $\mathscr{J}_{\gamma\alpha}^{\text{FX-EHP}}$. Their interplay can be barely foreseen. Moreover, particular attention must be paid regarding the great diversity of spatial localizations of the EHP states within the ZnO cluster. Altogether, this implies that the very commonly utilized point–dipole approximation of the excitonic coupling according to the Förster theory (see, e.g., Refs. [180, 12, 130, 5, 30, 7, 129, 26]) is very insufficient at this place.

The EET coupling, $\mathscr{J}_{\gamma\alpha}^{\text{FX-EHP}}$, is the central quantity for the present analysis. However, it is more conveniently to discuss first the behavior of the quantities $\mathscr{J}_{\gamma m}^{\text{6P-EHP}}$ (see Eq. 5.15). In fact, the $\mathscr{J}_{\gamma m}^{\text{6P-EHP}}$ give a more clear impression on the distance dependence of the interface excitonic coupling mechanism than the $\mathscr{J}_{\gamma\alpha}^{\text{FX-EHP}}$. Moreover, in cases of weak FX delocalization (e.g., in presence of strong energetic disorder), also the $\mathscr{J}_{\gamma m}^{\text{6P-EHP}}$ would be directly physically relevant. Then, the latter would mediate the EET from the individual 6P units to the EHPs. The computed values of $\mathscr{J}_{\gamma m}^{\text{6P-EHP}}$ are displayed in Fig. 5.4. The depicted data was obtained by Eq. 5.15, but based on atomic centered partial transition charges (for details, see Appendixes G.3 and G.1). In Figs. 5.4a–d,

Figure 5.5.: Excitonic coupling $\mathcal{J}_{\alpha\gamma}^{\text{FX-EHP}}$ (see Eq. 5.14) between Frenkel excitons (FXs) of the 6P stack and ZnO electron–hole pair excitations (EHPs) versus energy $\mathscr{E}_{\gamma}^{\text{EHP}}$ (see Eq. 5.11). Panel a-h: Eight sets of $\mathcal{J}_{\alpha\gamma}^{\text{FX-EHP}}$ for different FX levels (see indication of α). The Gaussians (with FWHM of 50 meV) point to the related FX energies $\mathscr{E}_{\alpha}^{\text{FX}}$. Panel i: Comparison of $\mathscr{E}_{\gamma}^{\text{EHP}}$ (pink) and $\mathscr{E}_{\alpha}^{\text{FX}}$ (cyan).

four exemplarily chosen sets of $|\mathcal{J}_{\gamma m}^{\text{6P-EHP}}|$ are illustrated. As indicated, these four sets are related to four different excited 6P donor molecules. The donor states $|\text{LX}_{m=1}\rangle$, $|\text{LX}_2\rangle$, $|\text{LX}_{10}\rangle$ and $|\text{LX}_{20}\rangle$ are considered, respectively. The positions of the pink peaks along the x–axis provide the dependence of $|\mathcal{J}_{\gamma m}^{\text{6P-EHP}}|$ on the EHP energy $\mathscr{E}_{\gamma}^{\text{EHP}}$. The blue Gaussians indicate the related 6P excitation energy $\mathscr{E}_m$ and are part of the discussions in Sec. 5.5. As expected, the values of $|\mathcal{J}_{\gamma m}^{\text{6P-EHP}}|$ decrease two orders of magnitude when changing from the first 6P molecule (closest to the ZnO surface) to the furthermost 6P (with index $m = 20$). Moreover, a certain variation of $|\mathcal{V}_{m\gamma}^{\text{6P-WX}}|$ with the EHP index γ is enlightened in Figs. 5.4a–d. This must be addressed to the manifold of different localizations of the EHPs within the ZnO cluster.

The situation is different turning next to $\mathcal{J}_{\gamma\alpha}^{\text{FX-EHP}}$, i.e., the coupling between the FXs and EHPs (see Eq. 5.14). In Figs. 5.5a-h, the $\mathcal{J}_{\gamma\alpha}^{\text{FX-EHP}}$ are exemplarily displayed for eight FX levels (see indication). Again, the EHP energy $\mathscr{E}_{\gamma}^{\text{EHP}}$ is drawn against the abscissa. Now, the related FX energies $\mathscr{E}_{\alpha}^{\text{FX}}$ are indicated by the blue Gaussians with a FWHM of 50 meV. The eight panels in Fig. 5.5 expose directly that in general the coupling $|\mathcal{J}_{\gamma\alpha}^{\text{FX-EHP}}|$ lies in the 1–meV–region. Moreover, in comparison with Fig. 5.4 one directly notices that the $\mathcal{J}_{\gamma\alpha}^{\text{FX-EHP}}$ of the upper FXs are of about half of the maximum absolute values observed for the 6P related $\mathcal{J}_{\gamma m}^{\text{6P-EHP}}$.

The positions of the Gaussians emphasize that the most of the FX levels are far–off the lowest EHP energy at the ZnO band gap. In particular, concerning the upper FXs, a manifold of EHP acceptor states is available in energetic resonance with $\mathscr{E}_{\alpha}^{\text{FX}}$. This

changes turning to the energetically lower FX levels. Indeed, though the interface coupling strength decreases not dramatically when moving from higher to lower FXs, the $|\mathrm{FX}_{\alpha=10}\rangle$ can be suggested to be the energetically lowest donor state which noticeable transfers energy to the ZnO system. As shown in Fig. 5.5i, energetically lower FXs (i.e., with index $\alpha < 10$) are simply out of resonance with possible EHP acceptor states.

Comparing the 8 panels in Figs. 5.5a-h uncovers that the excitonic coupling strengthes generally weaken when moving from the high FX levels to the lower ones. This can be understood by reconsidering the nodal structure of the FX expansion coefficients $\mathscr{C}_m(\alpha)$ in Eq. 5.7. As already recognized in Fig. 5.2c, the higher the energy the lower the number of nodes. Further, each node is responsible for a sign change in the sum over the molecular terms contributing to $\mathscr{J}_{\gamma\alpha}^{\text{FX-EHP}}$ (see again Eq. 5.14). The more nodes the more cancellation of the individual terms. Hence, it can be generally understood that any further node leads to more reduction of the $\mathscr{J}_{\gamma\alpha}^{\text{FX-EHP}}$.

On closer inspection, however, Fig. 5.5a-c enlighten that values of the $|\mathscr{J}_{\gamma\alpha}^{\text{FX-EHP}}|$ with $\alpha = 19$ and 18 are slightly larger than the one of the FX with $\alpha = 20$. An explanation for this detail is found by concerning further the absolute value of the $\mathscr{C}_m(\alpha)$. In particular, also maximum positions of $|\mathscr{C}_m(\alpha)|$ with respect to the interface (i.e., at index $m = 1$) have a primary influence on the $|\mathscr{J}_{\gamma\alpha}^{\text{FX-EHP}}|$. This is demonstrated best in an exemplary way for the $\mathscr{C}_{\alpha=19}(m)$, i.e., for the case of a single node in the center of the stacking. Obviously, the described node produces some cancellation in the middle of the stack. However, it also leads to an exciton localization which is crucially squeezed to the ZnO surface. In this fashion, the coupling strength is effectively increased in comparison to the case of $\alpha = 20$ (where the exciton is localized right in the middle of the stack). In complex interplay, two effects are at work – the cancellation effect and the distance dependence. In general, both should be expected for all H–aggregate like arrangements. Nevertheless, their interplay can hardly be quantified generally. Instead, it should be computed concretely for each structure.

Finally, it must be stated that presently no evidence can be given to support the proclamation of hybrid interface excitons which were often hopefully announced concerning oligo–phenyl/ZnO interfaces (see also Chap. 1). On the basis of the here uncovered weak excitonic coupling values, noticeable effects of hybridization cannot be anticipated.

5.5. Excitation Energy Transfer

In what follows, kinetics of exciton transfer from the 6P stack to the ZnO cluster are approached in two different ways and finally compared. In the first place, a Golden Rule–like rate expression is introduced. Its inverse measures a characteristic transfer time starting from a certain initially poulated FX donor state. The resulting exponential decay process is then compared with exciton population kinetics obtained from solving the time–dependent Schrödinger equation.

5.5.1. Interface transfer rates

As discussed in Sec. 5.4, only moderate values on the coupling $|\mathcal{J}_{\gamma\alpha}^{\text{FX-EHP}}|$ across the interface are found and a related second order perturbative treatment of the EET process is adequate. On that basis, a simple rate expression based on Fermi's golden rule is introduced in Sec. 3.2.2. Adapted to the present situation of EET from a single FX into the quasi–band of EHPs[2], the rate expression specifies to, cf. Eq. 3.4,

$$k_{\alpha}^{\text{FX}\to\text{EHP}} = \frac{2\pi}{\hbar} \sum_{\gamma}^{N^{\text{ZnO}}} |\mathcal{J}_{\gamma\alpha}^{\text{FX-EHP}}|^2 \mathcal{G}(\mathscr{E}_{\alpha}^{\text{FX}} - \mathscr{E}_{\gamma}^{\text{EHP}}). \tag{5.16}$$

In order to simulate inhomogeneous broadening effects, the sharp energy conservation introduced in Sec. 3.2.2 is removed in Eq. 5.16 and a Gaussian with FWHM of 50 meV is employed instead. The latter value is taken to be smaller than the overall width of the FX band and to be equivalent to Gaussian fluctuation of the state energies with a standard deviation compared to $k_{\text{B}}T$ at room temperature (see also Sec. 5.5.2). Please note also that the sum in Eq. 5.16 is restricted by the condition of $\mathscr{E}_{\gamma}^{\text{EHP}} < 5.0$ eV (as explained in Sec. 5.3.2). For instructuve reasons, additional transition rates shall be determined for the case of EET from individual initially excited 6P molecules, according to

$$k_{m}^{\text{6P}\to\text{EHP}} = \frac{2\pi}{\hbar} \sum_{\gamma}^{N^{\text{ZnO}}} |\mathcal{J}_{\gamma m}^{\text{6P-EHP}}|^2 \mathcal{G}(\mathscr{E}_{m} - \mathscr{E}_{\gamma}^{\text{EHP}}). \tag{5.17}$$

Now, the rate expression is based on the coupling $\mathcal{J}_{\gamma m}^{\text{6P-EHP}}$ (see Eq. 5.15). Further it is related to the excitation energy of the mth 6P molecule $\mathscr{E}_m$. In Fig. 5.6, $k_m^{\text{6P}\to\text{EHP}}$ and $k_{\alpha}^{\text{FX}\to\text{EHP}}$ are drawn against the initial state quantum number m (lower frame) and α (upper frame), respectively. The largest values are generally about 10^{12}/s. This gives evidence on only moderate transfer times in the picosecond region.

The blue line (with triangle markers) in Fig. 5.6 shows the $k_m^{\text{6P}\to\text{EHP}}$. Its dependence on index m enlightens straightly the dependence of the decay time on the distance d between the 6P molecule and the ZnO surface. When increasing d from the smallest value of 2.9 Å to the largest value of 78.9 Å (i.e., from $m = 1$ to $m = 20$), the rate drastically decreases by four orders of magnitude from 4.0×10^{12}/s to 1.7×10^{8}/s. Thereby, the change of the rate shows a $\propto 1/d^{2.6}$–behavior in the stacking part close to the interface ($m < 10$). For molecules further apart, however, a $1/d^{5.0}$–dependence was fitted. This result clarifies strikingly that the Förster's point–dipole interaction model (with the uniform $1/d^6$–behavior) should be applied very carefully to extended donor/acceptor objects. (Please note at this place that the very small change of the $\mathscr{E}_m$ with m (see inset Fig. 5.2b) is surely of negligible influence and has surely not to be involved in the latter concern.) The same issue is recaptured and further discussed in

[2]Please note that, in principle, also a thermal averaged initial FX population could be modeled. Therefore, the rate $k^{\text{FX}\to\text{EHP}} = \sum_{\alpha} f(\mathscr{E}_{\alpha}^{\text{FX}}) \times k_{\alpha}^{\text{FX}\to\text{EHP}}$ would have to be introduced with weights according to the Boltzmann distribution function $f(E) = 1/Z \times \exp(-E/k_{\text{B}}T)$ and the partition function $Z = \int dE\ f(E)\delta(E - \mathscr{E}_{\alpha}^{\text{FX}})$. However, such treatment is of less interest here due to the energetically rather isolated FX levels.

Figure 5.6.: Rates of EET into the multitude of ZnO electron–hole pair excitations (EHPs) starting from a single 6P molecule (rate $k_m^{\mathrm{6P}\rightarrow\mathrm{EHP}}$; blue triangles) or from a Frenkel–exciton (rate $k_\alpha^{\mathrm{FX}\rightarrow\mathrm{EHP}}$; green squares).

Sec. 8.7.3 concerning the EET from an even larger tubular dye aggregate to a spherical nanocrystal.

In general, the appropriateness of using the dipole–approximation to nanoscale objects is of recent concern (see, e.g., Refs. [130, 187, 131, 80, 27] and an elaborate discussion on this topic in Sec. 8.7.3). In agreement with earlier findings on realistic molecule/semiconductor systems [80, 186] and other idealized nanostructures semiconductor junctions [187, 131], here a significantly more complicated behavior is documented.

Next, the rate $k_\alpha^{\mathrm{FX}\rightarrow\mathrm{EHP}}$ shall be discussed in detail. It is critically influenced by: i) the energy level alignment of the FX donor states of the aggregate and the EHP acceptor states in the ZnO cluster, and ii) the nodal structuring of the FX (see discussion Sec. 5.4). The green line (with squared markers) in Fig. 5.6 displays the values of $k_\alpha^{\mathrm{FX}\rightarrow\mathrm{EHP}}$ drawn against the exciton index α, i.e., ordered from low to high energy. It is clearly shown that the $k_\alpha^{\mathrm{FX}\rightarrow\mathrm{EHP}}$ corresponding to the high energetic part of the FX spectrum are as large as the maximum values of $k_m^{\mathrm{6P}\rightarrow\mathrm{EHP}}$. To understand this finding, one has to remind the formerly observed different number of EHP acceptor states which are in energetic resonance with the respective energy donor state. In particular, significantly more EHP states are available in the energetic range of the upper FXs (see again Fig. 5.5i) than in the region of molecular excitations (see again Fig. 5.5e). The different energetic alignment is also clearly visualized by the Gaussians added to Figs. 5.4a-d and Figs. 5.5a-h. This effect is very potential and compensates the fact that the maximum values of $|\mathcal{J}_{\gamma m}^{\mathrm{6P\text{-}EHP}}|$ actually exceed the values of $|\mathcal{J}_{\gamma\alpha}^{\mathrm{FX\text{-}EHP}}|$. It appears mostly pronounced from $\alpha = 20$ to $\alpha = 15$. For lower lying FX acceptor levels, very rapidly decreasing values of $k_\alpha^{\mathrm{FX}\rightarrow\mathrm{EHP}}$ are obtained. This distinct decrease from $\alpha = 13$ to $\alpha = 1$ is finally the consequence of: i) the deteriorating energetic alignment, and ii) the increasing delocalization and nodal structuring of the FXs. In this region both properties jointly attenuate the rate.

In general, it can be stated that the EET from the upper FX donor states are strongly assisted by the denser band of available acceptor states. Since this increase of the density of energy acceptor states is a general feature of semiconductors, the presented results is also important to other H–aggregate/semiconductor nanosystems. Besides, the here computed excitonic couplings are generally of extremely high relevance. They provide insights into the complex EET mechanisms at a nanoscale hybid interface based on an atomistic modeling.

5.5.2. Coherent transfer kinetics

Finally, the uniform FX decay shall be compared against more sophisticated population kinetics resulting from the exact wave function propagation approach. By means of that, the reliability of the rate concept introduced in Sec. 5.5.1 can be evalueated. The latter kinetics are directly based on the interface Hamiltonian $\hat{H}$ (see Eq. 5.13) and obey the time–dependent Schrödinger equation, i.e., it is $\partial_t|\Phi(t)\rangle = \hat{H}|\Phi(t)\rangle$ (see Eq. 3.1). The overall wave function is introduced as $|\Phi(t)\rangle$ and an adequate expansion ansatz is found with

$$|\Phi(t)\rangle = \sum_{\alpha}^{N^{6\mathrm{P}}} \mathscr{C}_{\alpha}^{\mathrm{FX}}(t)|\mathrm{FX}_{\alpha}\rangle + \sum_{\gamma}^{N^{\mathrm{ZnO}}} \mathscr{C}_{\gamma}^{\mathrm{EHP}}(t)|\mathrm{EHP}_{\gamma}\rangle. \tag{5.18}$$

Then, the total populations of each the FXs and EHPs express as

$$P^{\mathrm{FX}}(t) = \sum_{\alpha}^{N^{6\mathrm{P}}} |\mathscr{C}_{\alpha}^{\mathrm{FX}}(t)|^2 \quad \text{and} \quad P^{\mathrm{EHP}}(t) = \sum_{\gamma}^{N^{\mathrm{ZnO}}} |\mathscr{C}_{\gamma}^{\mathrm{EHP}}(t)|^2, \tag{5.19}$$

respectively. Apparently, both populations are related according to $P^{\mathrm{EHP}}(t) = 1 - P^{\mathrm{FX}}(t)$.

Concerning the rate model for FX decay in Sec. 5.5.1 (see Eqs. 5.16), the energetic resonance condition of energy donor and acceptor states is somewhat relaxed by substituting a Gaussian line shape function. The evolution of $|\Phi(t)\rangle$ shows similar sensitivity for energetic resonance or off–resonance of states. Therefore, also the present coherent ansatz shall be augmented by energetic disorder. It simply means that the randomly generated shifts $\Delta\mathscr{E}_{\alpha}^{\mathrm{FX}}$ and $\Delta\mathscr{E}_{\gamma}^{\mathrm{EHP}}$ are added to all energy levels, according to

$$\mathscr{E}_{\alpha}^{\mathrm{FX}} \rightarrow \mathscr{E}_{\alpha}^{\mathrm{FX}} + \Delta\epsilon_{\alpha}^{\mathrm{FX}} \quad \text{and} \quad \mathscr{E}_{\gamma}^{\mathrm{EHP}} \rightarrow \mathscr{E}_{\gamma}^{\mathrm{EHP}} + \Delta\epsilon_{\gamma}^{\mathrm{EHP}}, \tag{5.20}$$

respectively. Instead of running a single simulation, an ensemble of W different solutions of the Schrödinger equation ($|\Phi_w(t)\rangle$ with $w \in \{1, ..., W\}$) is required. Each trajectory $|\Phi_w(t)\rangle$ and the population kinetics $P_w^{\mathrm{FX}}(t)$ and $P_w^{\mathrm{EHP}}(t)$ are determined by somewhat different energies. Finally, the mean of the latter provides the disorder attributed FX population,

$$\bar{P}^{\mathrm{FX}}(t) = \langle P_w^{\mathrm{FX}}(t)\rangle_W = \frac{1}{W}\sum_{w} P_w^{\mathrm{FX}}(t). \tag{5.21}$$

Figure 5.7.: Time–evolution of the 6P Frenkel–exciton (FX) population, $\bar{P}^{\mathrm{FX}}(t;\alpha)$ (solid line, see Eq. 5.21) compared with the rate determined exponential decay, $\exp(-k_{\alpha}^{\mathrm{FX}\to\mathrm{EHP}}t)$ (dashed line). Panel a: Kinetics sarting from initially populated FX levels $\alpha = 20$ (pink) and $\alpha = 19$ (blue). Panel b: Kinetics with initially populated FX $\alpha = 10$. (TDSE+sd: time–dependent Schrödinger equation plus static disorder).

In practice, all Gaussian fluctuations in Eq. 5.20 were generated equivalently using a standard deviation of 21.2 meV. This value corresponds to a distribution function with a FWHM of 50.0 meV and guarantees a proper confrontation with the data from Sec. 5.5.1. Converged data of the $\bar{P}^{\mathrm{FX}}(t)$ were gained by involving $W = 1000$ disorder realizations. (For further details on the system state propagation, see Appendix H.2.1.)

Following the rate ansatz of Sec. 5.5.1, the kinetics realize the exponential decay $\exp(-k_{\alpha}^{\mathrm{FX}\to\mathrm{EHP}}t)$. This common model assumes unidirectional population flow from a single donor state $|\mathrm{FX}_{\alpha}\rangle$ into a continuum of EHPs. Any energy backward transport (from the EHPs to the $|\mathrm{FX}_{\alpha}\rangle$) is neglected and so is any contribution of the other $|\mathrm{FX}_{\alpha'}\rangle$ with $\alpha' \neq \alpha$. The corresponding population kinetics are achieved in terms of $\bar{P}^{\mathrm{FX}}(t;\alpha)$ by starting the wave packet propagation from $|\Phi(t=0)\rangle = |\mathrm{FX}_{\alpha}\rangle$. (For the sake of convenience, the index α is added to $\bar{P}^{\mathrm{FX}}(t;\alpha)$ to indicate the initially prepared FX.)

The temporal behavior of the two types of kinetics, $P^{\mathrm{FX}}(t;\alpha)$ and $\exp(-k_{\alpha}^{\mathrm{FX}\to\mathrm{EHP}}t)$, are compared in Fig. 5.7. Exemplarily, the kinetics are illustrated for the FXs with $\alpha = 20$, 19 and 10. The cases of $\alpha = 20$ and 19 are depicted in Fig. 5.7a. One realizes that somewhat faster decay starts from $|\mathrm{FX}_{19}\rangle$ compared with the energetically higher $|\mathrm{FX}_{20}\rangle$. This finding is clearly in agreement with the discussion in Sec. 5.5.1 (see also Fig. 5.5). Comparing the rate ansatz and wave function–based ansatz with each other, one further notices that the population dynamics prognosed by both methodologies agree rather well until about 500 fs. After 500 fs, however, the exponential decay moves the population further to zero while the $P^{\mathrm{FX}}(t;\alpha)$ (from the wave function ansatz) approaches a finite value. The latter behavior is explained by the fact that the wave packet motion generally accounts also for back transfer processes. Based on the assumption of a continuum of acceptor states, these are not accounted for in the single

rate ansatz.[3]

Next, the discussion turns to the case of EET close to the ZnO band gap energy. The respective results are shown in Fig. 5.7b. Exemplarily, the FX with index $\alpha = 10$ are populated initially. The unidirectional decay from the rate ansatz is visualized in the main panel and the inset gives the population kinetics based on the wave packet propagation (please note the different scales of the ordinates). Now, the rate model and wave packet motion apparently give basically different kinetics. When applying the rate formalism, on the one hand, the FX population decays to zero within 100 ps. On the other hand, the data obtained from the Schrödinger equation describe only minor population decay to a steady state value of $\bar{P}^{\mathrm{FX}} = 0.975$ (see inset panel of Fig. 5.7b). This decay is not continuously but happens very initially within 5 ps. After that sudden initial drop, the population stays balanced but shows oscillatory behavior. An explanation can be given as follows. In comparison to the two cases discussed above, now the observed kinetics are strongly characterized by the small number of EHPs available at the band edge. Hence, only few acceptor states contribute to the EET process and very long–lived wave packet motion takes place. The fluctuative features observed with unchanged amplitude and frequency (up to a simulation time of 1 ns) proves this quite clearly. The particular oscillation features as well as the high steady state value must be attributed to the presently rather off–resonant energetic alignment of the initially populated FX and the few available EHPs (see again Fig. 5.5i). With decreasing number of EHP states in the lower band region, a basic assumption of the rate model is more and more violated. Especially concerning EET at the band edge region, the direct Schrödinger equation ansatz should be favoured instead.

The latter finding can be summarized: i) the fastest EET takes place on the picosecond time–scale and originates from the upper FXs of the aggregate (i.e., when the 6P stack is excited in the high energetic region), ii) the EET is much less efficient in the lower band region, and iii) especially close to the band edge the application of the simplified rate model suffers strongly from the small number of available EHP states in the ZnO cluster. Finally it is figured out that essentially the EET from the high–energy FXs is worth considering as quenching process of charge separation at the interface (see Chap. 6).

5.6. Summary and Concluding Remarks

The presented study examines excitation energy transfer (EET) processes in a finite *para*–sexiphenyl aggregate/ZnO model interface system. The focus lies on an atomistic exciton model and the computation of EET kinetics from initially populated Frenkel excitons in the molecular aggregate to electron–hole pair excitations residing at the ZnO part. The obtained decay times of the Frenkel excitons reach from few picoseconds (in the upper energetic region) to the nanosecond range (for the lower Frenkel excitons).

Kinetics from a rate ansatz based on Fermi's golden rule are confronted with direct excitonic wave packet propagation. The latter dynamics are obtained by disorder at-

[3] Please note that additional back transfer rate could be generally introduced and, in cases of two opponent state continua, a Pauli master equation system [44] be could be solved instead to obtain more reasonable population kinetics. However, here, this approach would be conceptually questionable.

tributed simulations of the time–dependent Schrödinger equation. In the higher part of the Frenkel exciton band, both approaches deliver EET kinetics in compliance. This general result supports the application of the simplified model of unidirectional energy transport. In particular, only minor back transfer from the ZnO system to the molecular aggregate can be recognized. Concerning the high–energy Frenkel excitons, more efficient backflow is prevented by the huge amount of available resonant energy acceptor states in the ZnO cluster. Also the low–energy Frenkel excitons are employed as EET donor states. In these cases, the reduced number of acceptor states in the ZnO, however, increasingly blocks the interface EET. In turn, the Frenkel excitons decay more slowly. With the same reasoning, the incoherent transfer model of Fermi's golden rule fails at all in the complete lower part of the FX band.

The above findings are very meaningful regarding the discussion given in Chap. 6. There, photoinduced charge separation kinetics are studied at the similar interface. In comparison, the here uncovered EET from the aggregate to the ZnO seems to be somewhat slower than the mechanism of charge separation. If, e.g., the highest two exciton levels are addressed with a laser–pulse, the charge separation appears clearly on the time–scale below 500 fs. With this, it is somewhat faster than the interface EET presented above. In view of the complexity of the interface kinetics, however, at the present state it is cumbersome to give a more specific answer on the initial question about which subprocess describes the dominant one. In general, quenching of the charge separation process is conceivable in different manner. As introduced in Chap. 1, photoinduced charge separation can be generally classified into: i) the indirect mechanism starting with Frenkel exciton population (and migration) and ending with electron transfer across the interface (see Fig. 1.3b), and ii) the direct way via the activation of charge transfer excitons (see Fig. 1.3c). By its nature, the latter direct activation should not be quenched as dramatically as it is surely the case considering the former indirect process after primary Frenkel exciton population.

The concrete interplay of EET and charge separation processes needs to be clarified further on. For instance, the above excitonic Hamiltonian and wave function ansatz could be merged with the manifold of charge separated states introduced in Chap. 6 (see Eq. 6.3). Furthermore, the inclusion of phonon–mediated relaxation and dephasing processes should be considered prospectively. For this purpose, the time–dependent Schrödinger equation could be replaced by the more sophisticated stochastic Schrödinger equation approach introduced in Chap. 4. Its way of including vibronic interaction effects is demonstrated later on in Chaps. 7 and 8. Unfortunately, employing the stochastic Schrödinger equation approach here was beyond the scope of this thesis. If applied to the present excitonic system, different aspects of possible energy reflux and exciton relaxation processes could be precisely studied.

6. Photoinduced Charge Separation at the *para*–Sexiphenyl/ZnO Nano–Interface

Besides phenomena of excitation energy transfer, also photoinduced charge separation kinetics at hybrid nano–interfaces are recently of high interest. Their understanding is elementary for developing novel nanotechnological devices with exciting optoelectronic features. In continuation of the studies on exciton transfer across the para–sexiphenyl/ZnO model interface in Chap. 5, now ultrafast photoinduced charge separation kinetics shall be simulated. Major parts of this chapter were published in Refs. [188] and [189].

During the last decade, different types of interfaces with ZnO substrate and molecular multilayers have been investigated a lot. Thereby, not only excitonic processes but also mechanisms of charge separation were identified. Accordingly, an excitation of the organic part may lead to the translation of an excited electron into the ZnO conduction band and, due to that, to the creation of a hole in the organic part. Beyond that basic picture, the understanding of that mechanism, however, is still very incomplete. In this light, now a combined simulation study on the processes of photon absorption, intermolecular excitation energy transfer, interface charge separation and the initial phase of correlated electron and hole motion is presented.

For this purpose, the atomistic interface model developed in Chap. 5 is now adapted to treat i) laser–pulse excitations of the interface, ii) Frenkel exciton migration, and iii) the formation of charge–separated states. The enormous computational ansatz involves more than 125000 interface states. An own intuitive picture for the interface electron transfer is developed. It describes the center piece of the model Hamiltonian. Based on it, ultrafast laser–pulse induced kinetics are computed in terms of wave packet dynamics which obey the Schrödinger equation. Here, the focus is on the femtosecond time–scale and temperature effects are assumed to be of minor impact. On larger scales, dissipative effects may become important. Then, the stochastic Schrödinger equation ansatz should be employed instead (see Chap. 4).

The elaborate modeling delivers very detailed insights into the complex interplay of the different interface processes. A discussion on the efficiency of the charge separation kinetics in dependence on the exciting photon energy is provided. These photoinduced dynamics are then compared with simulations starting from different initially prepared excited states. Furthermore, the charge–separation process is investigated in dependence on the intermolecular hole transfer coupling and the influence of energetic disorder in the system is examined.

6.1. Background and Motivation

The theoretical understanding of charge separation (CS) processes at nanohybrid interfaces is of paramount importance for an improvement of existing photovoltaic systems and, more generally, for the development of novel devices in the entire field of optoelectronics. As described in Chap. 1, many experimental studies have been published on different types of organic/inorganic hybrid systems during the last two decades [1, 23]. Thereby, there is an overwhelming amount of studies which follow the concept of the dye–sensitized solar cell (made popular by the pioneering work of O'Regan and Grätzel in 1991 [190]). Likewise systems consist of porously conglomerates of dye–covered semiconductor nanoparticles which are dissolved in an electrolyte solution. Their way of working is related to the large reactive surface of the nanoparticles [190, 6, 2]. Another general concept of hybrid structures is to prepare regular or amorphous molecular multilayers on top of flat semiconductor substrates (frequently ZnO surfaces [68, 3, 10]). By that, rather flat interfaces are generated which can be designed with extreme accuracy [24, 65, 14]. Each layer can be thereby customized individually based on a large variety of organic substances [15, 14, 183]. In particular, in order to bring forward these advanced multilayer designs, it immediately needs for detailed understanding of the CS processes happening at such interfaces.

General knowledge on the CS can be taken from computational studies related to bulk hetero junctions (i.e., organic/organic interface structures) [191, 29, 73, 83, 84, 81, 85, 192, 86]. However, concerning flat organic/inorganic interfaces, there is a massive lack of time–domain simulations on CS kinetics (see also Chap. 1). Moreover, the most of the few existing works are based on ab–initio nonadiabatic molecular dynamics [32, 76, 33] – an accurate but very costly methodology. The latter can only be applied to periodic interfaces based on rather small unit cells [91, 34, 37] and many aspects, especially of CS processes at large–scale interface structures, are still very unclear to date. Surprisingly, there is another particular topic which has attracted less attention so far, namely the explicit consideration of the exciting radiation field [193]. Indeed, explicit simulations of, e.g., an incident laser–pulse are commonly avoided by starting the CS kinetics directly from a certain prepared excited state. However, the excitation process is of central importance whenever ultrafast pump–probe experiments shall be understood in detail [66, 67].

In the following, concrete simulations are performed on laser–pulse induced charge separation kinetics at the *para*–sexiphenyl (6P)/ZnO interface [68, 65] (see also Chap. 1). Therefore, the finite 6P/ZnO interface model introduced in Chap. 5 is reapplied (for details, see Sec. 5.2). The particular design of the model interface allows studying also rather wide–range processes. In Chap. 5, it is investigated concerning excitation energy transfer (EET) from the 6P aggregate to the ZnO cluster, i.e., the transition of Frenkel excitons across the interface into electron–hole pair excitations (see Fig. 1.3a). Now, these EET studies are confronted with time–domain simulations on ultrafast formation of charge–separated interface states after laser–pulse excitation of the 6P aggregate (see Fig. 1.3b and c). The direct comparison finally clarifies whether the EET describes a serious quenching channel of the CS process or not.

According to Chap. 5, an interface model is built up using diabatic (localized site)

states in form of direct products of individual substructure site states (i.e., the 6Ps and the ZnO cluster). In this way, enormous numbers of (here more than 125000) interface states can be mastered rather straightforwardly. However, that simple state picture means vice versa that ambitious calculations on a diversity of transfer coupling terms must be accomplished. For the sub processes 2 and 4 indicated in Fig. 1.3b, intermolecular excitonic coupling (see Sec. 5.3.1) and hole transfer integrals are required, respectively. Furthermore, the actual charge separation process (process 3 in Fig. 1.3b) relies on a third kind of transfer coupling elements.

The modling of this latter type of interface electron transfer is very critical. Typically, the computation of the related transfer integrals demands for advanced ab–initio methodologies. This is circumvented here by developing an own approximate single–particle ansatz for the electron injection process. It is based on a very intuitive picture and inspired by the elaborate ab–initio works of Troisi et al. [95, 96, 194]. They introduced an elegant partitioning scheme for modeling electron injection rates from molecules into large TiO_2 clusters (based on several uniform DFT calculations). Unfortunately, a related ansatz is not practicable here concerning the ZnO cluster. Instead, the own conceived technique introduces electron donor and acceptor states in a phenomenological way. By that, the most critical computational parts of the 6P/ZnO junction can be avoided and a more adequate semi–empirical single–particle picture can be applied to the ZnO cluster. The approach is demonstrated for 6P on ZnO(0001), but can be used for any other surface design as well.

The following simulation studies exclusively describe scenarios of CS starting from laser–pulse excitation of the 6P molecules (process 1 in Fig. 1.3b). Although also the ZnO cluster could be optically addressed and additional electron–hole pair excitations could be incorporated (see Sec. 5.3.2), this is ignored here in order to avoid interference of the two types of excited states. Moreover, decoherence and dissipative effects due to vibronic (or electron–phonon) interaction should not be of primary relevance. As the present focus lies on ultrafast processes, the interface kinetics are simply deduced in terms of coherent wave packet dynamics obeying the time–dependent Schrödinger equation.

The achieved wave packet dynamics are illustrated in remarkable spatio–temporal resolution. This precission is vital for a detailed discussions. Also a preliminary analysis of the eigenstates and the absorption spectrum of the interface turns out to be very insightful. Altogether many simulation runs are executed and compared to understood in which way laser–pulse excitations in different spectral regions promote the CS process. Thereby, the efficient direct optical pumping of the prominent charge transfer excitons (see Fig. 1.3b) [15, 72] but also the more slowly CS mechanisms via Frenkel exciton decay can be clearly identified (see Fig. 1.3c). Besides the action of the laser–pulse, more fundamentally, also the importance of its explicit consideration as part of the simulation is investigated. This is an important issue and very elaborately discussed. In particular, ultrashort laser–pulses generally activate wave packet–like superposition states. In general, kinetics based on initial excited state ansatzes must be expected to differ significantly [32]. Nevertheless, many recent time–domain simulations dispense direct laser–pulse simulation in favor of simple excited state ansatzes [92, 84, 34]. Here, data resulting from different prominent initial state preparations are exemplarily

compared with related kinetics induced by laser–pulse excitation.

The obtained interface kinetics are further investigated regarding the influence of small energetic disorder. Related disorder attributed and ensemble averaged kinetics hold valueable information. For instance, very sensitive scenarios of CS along single resonant transfer pathways can be uncovered. Also the influence of molecular vibrations and lattice phonons can be adressed in a first attempt. In fact, under condition that rather slow vibrational motion can be assumed, such static disorder ansatz resembles the dephasing model according to Haken, Strobl and Reineker [195, 196, 197].

6.2. Modeling the Electronic System

A detailed introduction of the 6P/ZnO model system is provided in Sec. 5.2. The interface set–up describes a regular arrangement of 20 π–stacked *para*–sexiphenyl molecules placed on a flat surface of a finite wurtzite ZnO cluster (see Fig. 5.1). For the sake of completeness, two minor changes shall be mentioned, i) the here applied intermolecular 6P–6P distance measures 3.4 Å (instead of 3.8 Å utilized in Chap. 5), and ii) a somewhat other passivation technique of the spherical "backside" of the ZnO cluster is employed (see Appendix G.3).

The interesting CS processes at the 6P/ZnO interface are illustrated in the level schemes offered in Fig. 1.3b and c. As motivated in Sec. 6.1, the description concentrates on the CS kinetics starting from excitations of the 6P stack (see also Chap. 1). In Fig. 1.3b the indirect CS process is sketched. It includes optical excitations of the 6Ps (1), subsequent EET within the aggregate (2) and the process of CS by electron transfer across the interface into the ZnO cluster (3). Subsequently, it describes correlated electron and hole migration within the ZnO and 6P parts (4), respectively. The model accounts further for the direct optical excitation of *charge transfer excitons* (see Fig. 1.3c). Here, these are introduced as interface states attributed with significant charge–seperated state character and at the same time also with high oscillator strength [73, 23, 15, 72] (see Sec. 6.4.1).

6.2.1. Electronic states and interface Hamiltonian

The basis set for expanding the electronic Hilbert space consists of the ground state (G) of the full system, the states of 6P molecular excitations (LX) and the CS states with a molecular localized hole and an electron residing in the ZnO cluster. According to Sec. 5.2 (see Fig. 5.1), wave function overlap between the 6Ps and the ZnO cluster is assumed to be zero within the present model, which means that the diabatization scheme of Sec. 2.3.1 can be reapplied. Again, the full system electronic states are constructed as Hartree products of a number of $N^{6\mathrm{P}} = 20$ individual 6P states and a single ZnO cluster many–electron state (see also Sec. 5.3). Correspondingly, the ground state of the 6P/ZnO interface system follows as

$$|\mathrm{G}\rangle = \prod_{m}^{N^{6\mathrm{P}}} |\Phi_g^{(m)}\rangle \otimes |\Psi_0\rangle \; . \tag{6.1}$$

It consists of the 20 molecular (S_0) ground states, $|\Phi_g^{(m)}\rangle$ (with molecular index m), and the ground state of the ZnO cluster, $|\Psi_0\rangle$. Likewise, the expression,

$$|\mathrm{LX}_m\rangle = |\Phi_e^{(m)}\rangle \prod_{n\neq m}^{N^{6\mathrm{P}}} |\Phi_g^{(n)}\rangle \otimes |\Psi_0\rangle, \tag{6.2}$$

has to be interpreted. According to Sec. 2.3.4 (see Eq. 2.37), it represents the full system realizing a local excitation on the mth 6P molecule. That mth 6P is in its first (S_1) excited state, $|\Phi_e^{(m)}\rangle$, while its entire surrounding is in ground state configuration. These states are also part of the exciton model in Sec. 5.3.1 (see Eq. 5.3). Here, they are accompanied with a manifold of interface CS states, represented as

$$|\mathrm{CS}_{ma}\rangle = |\Phi_{\mathrm{cat}}^{(m)}\rangle \prod_{n\neq m}^{N^{6\mathrm{P}}} |\Phi_g^{(n)}\rangle \otimes |\Psi_a^-\rangle \,, \tag{6.3}$$

which follows the discription of Sec. 2.3.5 (see Eqs. 2.44 and 2.45). It contains the state $|\Phi_{\mathrm{cat}}^{(m)}\rangle$ of the mth 6P in the cationic S_0 ground state configuration (see Sec. 2.1.5). Respectively, the $|\Psi_a^-\rangle$ represents a certain anionic many–electron state of the ZnO cluster. The treatment of the $|\Psi_a^-\rangle$ based on the frozen orbital approximation is explicitly discussed in Sec. 2.2.3. According to that, it is constructed as the TB ground state with an additional occupation of the conduction band (CB)–like state $\bar{\psi}_a$ (see Eq. 2.16). For the present ZnO cluster, a number of $N_{\mathrm{CB}} = 6285$ CB–like states are computed resulting in $N^{6\mathrm{P}} \times N_{\mathrm{CB}} = 125700$ possible CS states. Apparently, they constitute the vast majority of states in the model. (Details on the molecular (TD)DFT and the DFTB calculations are given in Appendixes G.1 and G.3, respectively.)

According to Sec. 2.3.5, the electronic system Hamiltonian for photoactivated CS is constructed as, cf. Eqs. 2.50 and 2.46,

$$\begin{aligned} H(t) = & \\ & \sum_{m}^{N^{6\mathrm{P}}} \mathscr{E}_m^{\mathrm{LX}} |\mathrm{LX}_m\rangle\langle \mathrm{LX}_m| + \sum_{m}^{N^{6\mathrm{P}}} \sum_{a}^{N_{\mathrm{CB}}^{\mathrm{ZnO}}} \mathscr{E}_{ma}^{\mathrm{CS}} |\mathrm{CS}_{ma}\rangle\langle \mathrm{CS}_{ma}| + \Big(\sum_{m}^{N^{6\mathrm{P}}} \mathscr{V}^{\mathrm{opt}}(t) |\mathrm{LX}_m\rangle\langle \mathrm{G}| \\ & + \sum_{m<n}^{N^{6\mathrm{P}}} \mathscr{J}_{mn} |\mathrm{LX}_m\rangle\langle \mathrm{LX}_n| + \sum_{a}^{N_{\mathrm{CB}}^{\mathrm{ZnO}}} \mathscr{V}_a^{\mathrm{CT}} |\mathrm{CS}_{1a}\rangle\langle \mathrm{LX}_1| + \sum_{a}^{N_{\mathrm{CB}}^{\mathrm{ZnO}}} \sum_{m<n}^{N^{6\mathrm{P}}} \mathscr{V}_{mn}^{\mathrm{HT}} |\mathrm{CS}_{ma}\rangle\langle \mathrm{CS}_{na}| + \mathrm{H.c.} \Big), \end{aligned} \tag{6.4}$$

by using the states Eqs. 6.1, 6.2 and 6.3 for expansion. The $\mathscr{E}_m^{\mathrm{LX}}$ and $\mathscr{E}_{ma}^{\mathrm{CS}}$ give the excitation energies associated with the interface states $|\mathrm{LX}_m\rangle$ and $|\mathrm{CS}_{ma}\rangle$, respectively. Both terms refer commonly to the full system ground state energy which is set equal to zero (for details, see Sec. 6.2.2). The remaining terms in Eq. 6.4 indicate the couplings responsible for the different appearing state transitions. The $\mathscr{V}^{\mathrm{opt}}(t)$ represents the laser–pulse excitation and mediates the transition between the interface ground state and the state with the mth 6P excited (see Sec. 6.2.4). Further, the element $\mathscr{J}_{mn}$ is responsible for the EET from the nth to the mth 6P (see Sec. 6.2.3). Likewise, the $\mathscr{V}_{mn}^{\mathrm{HT}}$ represents the intermolecular coupling for hole transfer (from the nth to the mth

6P molecule). It is commonly restricted to only nearest–neighbor coupling, i.e., it is $\mathscr{V}_{mn}^{\mathrm{HT}} = \delta_{mm\pm1}\mathscr{V}^{\mathrm{HT}}$ (see Sec. 6.2.3). Finally, the $H(t)$ contains the term $\mathscr{V}_a^{\mathrm{CT}}$ for the charge (electron) transfer across the interface (the actual CS process). This terms mediates the excess electron injection from the 6P with index $m = 1$ (closest to the surface) into the ath ZnO CB–like state (see Sec. 6.3).

6.2.2. Interaction energies

According to the fundamental discussion in Sec. 2.3.5 (see Eq. 2.46), the diagonal terms of $H(t)$ contain the energies of the isolated substructures as well as further corrections due to their electrostatic Coulomb–like interaction. The $\mathscr{E}_m^{\mathrm{LX}}$ is discussed in Eq. 5.5 as part of the exciton model in Sec. 5.3. Here, similarly small interaction corrections of the $\mathscr{E}_m^{\mathrm{LX}}$ (less than 10 meV) must be noted (see the inset of Fig. 5.2b). The diagonal term $\mathscr{E}_{ma}^{\mathrm{CS}}$ in Eq. 6.4 is associated with $|\mathrm{CS}_{ma}\rangle$ and follows as, cf. Eqs. 2.46, 2.47 and 2.49,

$$\begin{aligned}\mathscr{E}_{ma}^{\mathrm{CS}} &= E_+^{\mathrm{6P}} - E_g^{\mathrm{6P}} + E_a^{\mathrm{CB}} + \\ &+ \int d^3\mathbf{x}d^3\mathbf{y}\Big[n_{\mathrm{cat}}^{(m)}(\mathbf{x}) - n_g^{(m)}(\mathbf{x})\Big]\frac{1}{|\mathbf{x}-\mathbf{y}|}\Big[\sum_{n\neq m}^{N^{\mathrm{6P}}}\big[n_g^{(n)}(\mathbf{y}) + \sum_\mu eZ_\mu\delta(\mathbf{y}-\mathbf{R}_\mu^{(n)})\big] + \Omega(\mathbf{y})\Big] \\ &+ \sum_n^{N^{\mathrm{6P}}}\int d^3\mathbf{x}d^3\mathbf{y}\frac{\big[n_g^{(n)}(\mathbf{x}) + \sum_\mu eZ_\mu\delta(\mathbf{y}-\mathbf{R}_\mu^{(n)})\big]\bar{\rho}_a(\mathbf{y})}{|\mathbf{x}-\mathbf{y}|} \\ &+ \int d^3\mathbf{x}d^3\mathbf{y}\frac{\big[n_{\mathrm{cat}}^{(m)}(\mathbf{x}) - n_g^{(m)}(\mathbf{x})\big]\bar{\rho}_a(\mathbf{y})}{|\mathbf{x}-\mathbf{y}|}.\end{aligned} \tag{6.5}$$

The intramolecular energy of the 6P cationic state E_+^{6P} are introduced in reference to the ground state energy E_g^{6P}. The related 6P ionization potential $E_{\mathrm{I}}^{\mathrm{6P}} = E_+^{\mathrm{6P}} - E_g^{\mathrm{6P}}$ represents the energy of the hole on an isolated 6P molecule. Further, the E_a^{CB} appears as the ZnO CB–like state energy. The latter is the energy of the excess electron (i.e., the electron affinity of the ZnO cluster). The remaining terms in Eq. 6.5 formulate the Coulomb–like interaction energy within the system. The related terms are generally worked out with Eqs. 2.47 and 2.49 in Sec. 2.3.5. The term $n_g^{(n)}(\mathbf{x}) + \sum_\mu Z_\mu\delta(\mathbf{x}-\mathbf{R}_\mu^{(n)})$ represents the electronic charge density of the nth 6P in the electronic ground state (see Eq. 2.26) plus the related nuclear charges placed at the atomic coordinate $\mathbf{R}_\mu^{(n)}$ (with nuclear index μ). Similarly, the term $n_{\mathrm{cat}}^{(n)}(\mathbf{x}) + \sum_\mu Z_\mu\delta(\mathbf{x}-\mathbf{R}_\mu^{(n)})$ would give the cationic molecular charge distribution of the nth 6P (see Eq. 2.48) plus nuclear charge contributions. Together, the term $n_{\mathrm{cat}}^{(m)}(\mathbf{x}) - n_g^{(m)}(\mathbf{x})$ therefore describes then the hole charge density which resides on the mth 6P. Concerning the ZnO cluster, the density $\Omega(\mathbf{y})$ appears. It renders the total charge density of the ground state of the ZnO cluster (nuclei plus VB–electrons, cf. Eq. 2.49). Further, the $\bar{\rho}_a(\mathbf{y})$ is reintroduced as the charge density of the excess electron (see also Eq. 2.49). Based on the different densities, the first integral term in Eq. 6.5 represents the coupling of the hole on the mth 6P with its complete surrounding in the absence of the excess electron. The counterwise coupling of the electron charge in the ath CB–like state with the aggregate structure in the

Figure 6.1.: Interaction energies of charge–separates (CS) states. The $\mathscr{E}_{ma}^{\mathrm{CS}}$ is drawn against 6P hole index m (see Eq. 6.5). Panel a: Hole interaction with the excess electron. Three cases of different populated CB–like states $\bar{\psi}_a$ are shown (see coloring). Panel b and c: Hole interaction with neutral ZnO cluster and surrounding 6Ps, respectively. Panel d: Isosurface plots of $|\bar{\psi}_a|^2$ (for panel a). Panel e: Total interaction potentials.

absence of the hole is given by the second integral term. The last term in Eq. 6.5 finally describes the mutual interaction of the two excess charges with each other.

The 6P ionization potential was determined as $E_{\mathrm{6P}}^{\mathrm{I}} = 6.83$ eV based on DFT (for details, see Appendix G.1). Further, the CB–like state energies E_a^{CB} were computed from the DFTB methods (for details, see Appendix G.3). The Coulomb–type integrals in Eq. 6.5 were determined in atomic resolution by approximating all density expressions in terms of atomic centered partial charges (for details, see Appendix D). For computing the electrostatic interaction energies, furthermore, the 6P aggregate was extended to a size of 40 molecular units (see also Sec. 5.3).

The interaction energy shift $\mathscr{E}_m^{\mathrm{LX}}$ in Eq. 6.4 carries different contributions of the cluster and the molecules, but all are neutral and essentially homogeneously charged. Only minor electrostatic effects were observed (see and Fig. 5.2b). This is different concerning $\mathscr{E}_{ma}^{\mathrm{CS}}$. Due to the charge separation character, it can be generally expected that the $\mathscr{E}_{ma}^{\mathrm{CS}}$ carries much stronger interaction. In fact, the strongest contributions to $\mathscr{E}_{ma}^{\mathrm{CS}}$ were found with: i) the direct electron–hole interaction, ii) the interaction of the hole with the surrounding 6P molecules, and iii) the interaction of the hole with the neutral ZnO cluster. The three prominent terms are computed for all 20 hole positions (i.e., sampled along index m) and illustrated as potential energy curves in Fig. 6.1.

The correction due to the attractive coupling between electron and hole is displayed in

Fig. 6.1a. Each of the three colored curves results from a different electron localization in the ZnO cluster (by populating three different CB–like states $\bar{\psi}_a$). The three charge distributions (i.e., the $|\bar{\psi}_a|^2$) are rendered in Fig. 6.1d (labeled with related colorings). The blue and green cases are exemplarily chosen because they result in the strongest and weakest electron–hole interaction, respectively. According to Fig. 6.1e, the electrons are localized rather closely to and far away from the interface, respectively. The third density (pink label) represents a CB–state which is localized rather in the bulk zone of the ZnO cluster and its related potential energy curve lies between the former two in Fig. 6.1a. As generally expected, in all three cases the electron–hole interaction energy decreases with increasing hole distance from the ZnO interface (i.e., moving from smaller to larger values of m). The different slopes, however, give a clear message on very distinct spatial localizations of the electron within the cluster.

The curve in Fig. 6.1b illustrates the energy contribution due to the interaction of the hole with the opponent ground state ZnO cluster (without additional occupation of $\bar{\psi}_a$). Although the cluster is neutrally charged, surprisingly the values appear in similar strength like in Fig. 6.1a. The reason is found in the atomic structuring of the flat ZnO surface. The present Zn–termination is responsible for a partial positively charged top layer. This feature resulted directly from the employed DFTB single–particle treatment of the cluster. The created positive surface charging is exposed right to the 6P aggregate (see again Fig. 5.1), which is why the curve in Fig. 6.1b renders a repulsive potential with respect to the interface.

The electrostatic interaction of the hole with the surrounding 6P aggregate is illustrated in Fig. 6.1c. If the hole is localized inside the aggregate, the energy correction settles to a value of about -0.51 eV. Being placed at the boundary of the aggregate (i.e., on 6P with index $m = 1$), the energy contribution amounts -0.26 eV.

Finally, the remaining energy shift due to interaction of the excess electron charge with the ground state 6P aggregate was examined (not shown). In general, it causes another positive energy correction of about 20 meV on average. Only few ψ_a produce shifts up to 80 meV (see Supplementary Information of Ref. [188] and Ref. [189]). The total correction shifts, again making use of the three prominent electron occupations (see colorings), are presented in Fig. 6.1e. It is clearly demonstrated that potential energy gaps of more than 100 meV can appear between neighbored molecular sites (especially in the close surface zone). These are rather large values which play a decicive role later on in Sec. 6.5.2, when the hole evacuation from the interface zone is concerned.

6.2.3. Intermolecular excitation energy and hole transfer coupling

The intermolecular EET coupling $\mathcal{J}_{mn}$ (off–diagonal element in Eq. 6.4) is generally introduced as part of Sec. 2.3.2 (see Eq. 2.29) and further specified to the 6P aggregate in Sec. 5.3.1 (see Eq. 5.6). The same computational procedure is reapplied here. For nearest neighbored 6P pairs and next nearest neighbor 6Ps, it amounts $\mathcal{J}_{mm\pm1} = 81$ meV and $\mathcal{J}_{mm\pm2} = 42$ meV, respectively.[1]

As a type of intermolecular tunneling process the hole transfer, i.e., the strength

[1] As the present 6P–6P distances are somewhat smaller related to the one in Sec. 6.1, the EET coupling appears here slightly increased compared with Sec. 5.3.1.

of the transfer integral $\mathscr{V}_{mn}^{\mathrm{HT}}$ critical depends on the distance between the donor and acceptor molecule. For that reason, the $\mathscr{V}_{mn}^{\mathrm{HT}}$ is usually restricted to nearest neighbor interaction [198, 199]. For the present 6P stack, it suffices to determine the single quantity $\mathscr{V}^{\mathrm{HT}} = \mathscr{V}_{mm\pm1}^{\mathrm{HT}}$, where the value of $\mathscr{V}^{\mathrm{HT}} = 0.2$ eV was computed on the DFT level (for details, see Appendix G.1). That value lies in the typical range of hole transfer integrals known for customary π–conjugated molecular stackings [198, 199, 200, 52].

6.2.4. Laser–pulse excitation

In this study, the focus is on CS kinetics resulting from photoinduced excitation of the organic 6P aggregate (see Sec. 6.1). The related laser–field strength is chosen to guarantee weak optical excitation of the 6Ps. Then, the coupling expression entering Eq. 6.4 follows as,

$$\mathscr{V}^{\mathrm{opt}}(t) = -\hbar\Omega_R \cos(\omega_{\mathrm{L}} t)\mathscr{G}(t). \tag{6.6}$$

The function $\mathscr{G}(t) = \exp\{-4\log(2)(t-\tau_0)^2/\tau_p^2\}$ is a Gaussian envelope with the center at $t = \tau_0$ and the FWHM of τ_p. The photon energy is given by $\hbar\omega_{\mathrm{L}}$. The $\Omega_{\mathrm{R}} = \mathbf{d}_m^{6\mathrm{P}}\mathbf{E}_0/\hbar$ gives the Rabi frequency, which would be associated with a 6P two–level system with the transition dipole moment $\mathbf{d}_m^{6\mathrm{P}}$ and the field strength $\mathbf{E}_0$. The incident laser–pulse is defined with parallel polarization to the molecular transition dipole moments. While the values of $\tau_p = 100$ fs, $\tau_0 = 150$ fs, $|\mathbf{d}_m^{6\mathrm{P}}| = 12.7$ D (see Appendix G.1) and $|\mathbf{E}_0| = 10^6$ V/m are taken as constant parameters throughout this work, the influence of different $\hbar\omega_{\mathrm{L}}$ on the CS kinetics is intensively investigated as part of this work.

6.3. Interface Charge Transfer Coupling

The charge transfer coupling across the interface (see $\mathscr{V}_a^{\mathrm{CT}}$ in Eq. 6.4) features the CS process in the first place. It mediates the injection of the electron from the excited 6P molecule (localized right at the interface) into the unoccupied CB–like state $\bar{\psi}_a$ of the ZnO clluster. As described in Sec. 6.1, computing transfer integrals, especially concerning nanoscale molecule/semiconductor interfaces, is very costly. In what follows, the main aspects of the own developed interface transfer model shall be outlined. A more detailed description is provided in Appendix A.

6.3.1. Electron injection process

Intermolecular electron transfer is commonly modeled based on two relevant states – a molecular donor state and an opponent molecular acceptor state, usually the lowest unoccupied molecular orbitals (LUMOs). Here, the electron injection takes place into an entire manifold of $N_{\mathrm{CB}}^{\mathrm{ZnO}} = 6285$ CB–like states $\bar{\psi}_a$ and the clear discrimination of relevant acceptor states is rather intricate. In consequence, careful considerations are required concerning energy and spatial localization of in principle all individual $\bar{\psi}_a$.

As a tunneling process, efficient electron injection relies again on the spatial distance between a certain $\bar{\psi}_a$ and the molecular donor state. From the spatial point of view (i.e., excluding energetic aspects), the excess electron is transfered into the surface zone

Figure 6.2.: Interface charge transfer (CT) coupling. Panel a: Illustrations of the 6P–ZnO interface zone (front, side and top view, the H–passivation is not shown). The focus lies on the 25 Zn atoms colored black and white. A superposition of atomic orbital wave functions is conceived to construct the electron transfer acceptor state ϕ_{A} (for details, see the main text). Panel b: CT couplings $\mathscr{V}_a^{\mathrm{CT}}$ against energy of the related CB–like state $\bar{\psi}_a$ (pink coloring: values smaller 1 meV; inset: view on the complete CB band).

of the ZnO cluster. The closer a certain $\bar{\psi}_a$ is localized to the donor molecule the higher is the transfer probability to it. From the energetic point of view, it is clear that the electron can only enter the CB of the ZnO. In this light, it is the idea to construct a wave function state, ϕ_{A}, which serve as a phenomenological electron acceptor state at the ZnO surface. It has to be fully unoccupied (i.e., $\phi_{\mathrm{A}} = \sum_a \kappa_a \bar{\psi}_a$) and it should be localized in immediate proximity to the 6P donor. By that, it is finally possible to collectively parameterize the electron transfer into each of the $\bar{\psi}_a$ by means of only a single estimate value related to the transfer coupling for the injection into ϕ_{A}.

The prescribed spatial localization of ϕ_{A} is achieved best by making use of the atomic orbital (AO) representation (available as part of the TB description of the ZnO cluster, cf. Sec. 2.2.1). The Fig. 6.2a illustrates the atomistic structure of the interface region (magnified; three perspectives). The LUMO of the 6P attached to the ZnO represents the electron donor state. As visualized in the isosurface plot in the inset of Fig. 2.1a, it is rather equally distributed upon the 6 phenylene rings. So, in the first step, the 25 surface atoms are selected which are positioned closest to the aromatic system of the attached 6P. They are highlighted by the white and black spheres in Fig. 6.2a. In the present situation, these selected 25 atoms are exclusively of Zn–type. In the second step, the ($4p_x$–type) AOs of each of the 25 Zn atoms in Fig. 6.2a are considered. They are now utilized to create in superposition a first localized wave function state ϕ'_{A} which is the particular surface zone. Appropriate weights of the 25 AOs for ϕ'_{A} can be derived from a simple analytic modeling under condition that each of the 7 centrally aligned (black colored) atoms and each the surrounding 18 (white colored) atoms contribute equally (see Eq. A.3).

In the final step, the constructed ϕ'_{A} is "cleaned" from the unwanted shares of VB–like states. After normalization, so far the ϕ'_{A} would be still partially occupied and cannot

host the "complete" electron. In order to strictly remove any VB–like state contribution, the ϕ'_{A} is represented in the eigenstate basis using all single–particle cluster states (i.e., all VB–like states and all CB–like states). In this representation, the VB–like state partition is finally identified and withdrawn (see Eq. A.4). After its normalization, the adequately localized and unoccupied acceptor state ϕ_{A} is obtained (see Eq. A.5).

6.3.2. Electron migration into the ZnO cluster

In the moment the electron is transfered to the ϕ_{A}, it starts migrating further into the cluster. That migration process is already included in the interface model. To realize this, one has to reconsider the ϕ_A in terms of the wave packet of delocalized CB–like states $\bar{\psi}_a$,

$$\phi_{\mathrm{A}} = \sum_{a}^{N_{\mathrm{CB}}} \kappa_a \bar{\psi}_a. \tag{6.7}$$

The concrete expressions for the expansion coefficients κ_a are provided in Eq. A.6. During time–evolution, now each individual term is subject to a different phase factor. From the spatial perspective, the initially localized acceptor state dissolves continuously and the electron starts migrating within the ZnO cluster. In the same manner, electron migration appears after injection when propagating a full system state.

6.3.3. Charge transfer integrals for the CB–like acceptor states

The transfer coupling of the 6P donor state to the initial ZnO acceptor state, ϕ_{A}, shall be introduced as $\mathscr{V}^{\mathrm{CT}}$. Based on this definition, the transfer coupling to each CB–like state $\bar{\psi}_a$ follows immediately from the expansion in Eq. 6.7, according to, cf. Eq. A.7,

$$\mathscr{V}_a^{\mathrm{CT}} = \kappa_a \mathscr{V}^{\mathrm{CT}}. \tag{6.8}$$

The value $\mathscr{V}^{\mathrm{CT}}$ parameterizes the strength of the interface transfer. Here, the physically plausible value of $\mathscr{V}^{\mathrm{CT}} = 0.2$ eV is applied. It describes a rough estimate concerning the close 6P attachment and lies in the range of typical values from literature (see, e.g., Refs. [201, 202, 203]). The computed values of $|\mathscr{V}_a^{\mathrm{CT}}|$ are depicted by the peaks in Fig. 6.2b. Their positions along the abscissa give the energy E_a^{CB} (see Eq. 6.5) corresponding to $\bar{\psi}_a$. Certain energetic regions of prominent transfer couplings can be clearly identified. In fact, they can be related to single states $\bar{\psi}_a$ with great shares in the particular surface zone "beneath" the 6P donor molecule. Nevertheless, the most of the $|\mathscr{V}_a^{\mathrm{CT}}|$ echo very weak coupling. To quantify this, all peaks smaller than 1 meV are highlighted in Fig. 6.2b with the pink coloring. That are about 73 % of all couplings.

6.4. Interface Excited States

In general, each ultrafast optical excitation results in a certain spectral broadening. The shorter the exciting laser–pulse in time, the broader the formed wave packet–like superposition state from the energetic point of view. In the following, the full system

eigenstates (FSE) of the interface Hamiltonain $\hat{H}(t)$ with $\mathscr{V}^{\mathrm{opt}}(t) = 0$ (see Eq. 6.4) are discussed. Their spectral positioning decides about whether a certain pulsed excitation results in the population of a single eigenstate or in the formation of a wave packet of multiple eigenstates. Moreover, different types of available bright interface states are figured out. The following detailed analysis is very important for understanding the characteristic types of CS kinetics uncovered in Secs. 6.5 and 6.6.

6.4.1. Character of the interface states

The FSEs are expressed in expansion of the diabatic states introduced in Eqs. 6.2 and 6.3, according to

$$|\mathrm{FSE}_\alpha\rangle = \sum_m \mathscr{C}_m^{\mathrm{LX}}(\alpha)|\mathrm{LX}_m\rangle + \sum_{m,a} \mathscr{C}_{ma}^{\mathrm{CS}}(\alpha)|\mathrm{CS}_{ma}\rangle, \tag{6.9}$$

with the FSE index α, where it is $1 < \alpha < 125720$ (excluding the decoupled interface ground state). The $|\mathrm{FSE}_\alpha\rangle$ obey the interface Schrödinger equation, i.e., it is $\hat{H}|\mathrm{FSE}_\alpha\rangle = \mathscr{E}_\alpha^{\mathrm{FSE}}|\mathrm{FSE}_\alpha\rangle$, with the $\hat{H}$ (see Eq. 6.4) under condition that $\mathscr{V}^{\mathrm{opt}}(t) = 0$. Their energies $\mathscr{E}_\alpha^{\mathrm{FSE}}$ and the related expansion coefficients $\mathscr{C}_m^{\mathrm{LX}}(\alpha) = \langle \mathrm{LX}_m|\mathrm{FSE}_\alpha\rangle$ and $\mathscr{C}_m^{\mathrm{CS}}(\alpha) = \langle \mathrm{CS}_{ma}|\mathrm{FSE}_\alpha\rangle$ are determined by solving the respective eigenvalue problem[2]. The latter two different types of expansion coefficients echo the character of the FSE. When switching off the matrix elements $\mathscr{V}_a^{\mathrm{CT}}$ in $\hat{H}$, the bright FSEs of the interface system would appear as the Frenkel excitons (FXs), which are intensively discussed in Chap. 5 (see Eq. 5.7) and generally introduced in Sec. 2.3.4 (see Eq. 2.38). However, by the action of $\mathscr{V}_a^{CT}$, the FSEs now generally describe hybridizations of the FXs (or LX states) and the CS states. A qualitative measure of the *character of hybridization* shall be introduced with,

$$\mathrm{char}(\alpha) = -\sum_m |\mathscr{C}_m^{\mathrm{LX}}(\alpha)|^2 + \sum_a \sum_m |\mathscr{C}_{am}^{\mathrm{CS}}(\alpha)|^2. \tag{6.10}$$

This quantity varies between $\mathrm{char}(\alpha) = -1.0$ (i.e., 100% FX character) and $\mathrm{char}(\alpha) = 1.0$ (i.e., 100% CS character). In dependence on $\mathrm{char}(\alpha)$, the direct optical excitation implies population of CS states.

The computed energies, $\mathscr{E}_\alpha^{\mathrm{FSE}}$, and the FSE characters, $\mathrm{char}(\alpha)$, are displayed in Fig. 6.3a (the essential part is magnified). With regard to the following discussion, it was chosen to concentrate on a tenfold weaker hole transfer coupling of $\mathscr{V}^{\mathrm{HT}} = 0.02$ eV for the beginning (see also Sec. 6.5.2).[3] Against the ordinate, Fig. 6.3a shows the positions of the different energy levels $\mathscr{E}_\alpha^{\mathrm{FSE}}$. In order to illustrate the character of the related $|\mathrm{FSE}_\alpha\rangle$, the levels are positioned against the abcissa (and colored) according to the computed values $\mathrm{char}(\alpha)$, respectively. In the left part, a band of eigenstates of almost pure (> 99.9 %) FX character can be clearly identified (green coloring). The majority of the individual coupling values $\mathscr{V}_a^{\mathrm{CT}}$ is very weak (see Fig. 6.2b). Conse-

[2] In practice, an approximate ansatz for its diagonalization was inevitable concerning the dimensionality of $\hat{H}$ with 125721x125721 elements. The here specially conceived technique for reduction of the dimensionality is described in Appendix H.1.

[3] Please note that such coupling strength still represents typical π–stacked organic clusters [204].

Figure 6.3.: Eigenstates of the 6P/ZnO model interface ($\mathscr{V}^{\mathrm{CT}} = 0.2$ eV, $\mathscr{V}^{\mathrm{HT}} = 0.02$ eV). Panel a: Excitation energy levels of the hybridized interface states. The coloring and horizontal positioning of the levels represents their Frenkel exciton (FX) and charge–separated (CS) state character, char(α) (see Eq. 6.10 and indication). The frame magnifies the region with relevant hybridization effects. Panel b: Full absorption profile of the interface (blue line) and differential spectrum (dashed pink line with the scale factor). The latter is obtained from the blue curve by removing the pure H–aggregate contribution (obtained in case of $\mathscr{V}^{\mathrm{CT}} = 0$ eV). The labels 1 to 6 mark the six dominant hybridized states (for details, see the main text). Labels I and II mark the two brightest states in the band. Letters A to D mark the four photon energies $\hbar\omega_L$ applied in the time–domain simulations presented in Figs. 6.4–6.10.

quently, the related $\mathscr{E}_{\alpha}^{\mathrm{FSE}}$ are still ordered according to the H–aggregate arrangement of the 6P molecules (for comparison, see $\mathscr{E}_{\alpha}^{\mathrm{FX}}$ in Fig. 5.2b).

The vast majority of the FSEs levels up at the right part of Fig. 6.3a (blue coloring). They are almost complete CS character. It can be recognized that only few FSEs with apparently mixed character appear in the middle part of the abscissa. These must be related to the individual larger values of $|\mathscr{V}^{CT}|$ found beforehand as peaks in Fig. 6.2b. Typically, the terminus *charge transfer (CT) exciton* is used in literature for all such FSEs which hold both essential oscillator strength and CS character [15, 72]. While the CS character of a certain FSE can be directly identified from $\mathrm{char}(\alpha)$, this value contains no information about the actual oscillator strength of the incorporated Frenkel exciton partition. Correspondingly, also FSEs of almost complete CS character (i.e., with $\mathrm{char}(\alpha) \approx +1$) can appear as charge transfer excitons, if the remaining FX contributions bring with very high oscillator strength to represent a prominent CT exciton. Equivalently, FSEs with equal shares of FXs and CS states ($\mathrm{char}(\alpha) \approx 0$) may not have the required oscillator strength. The proper picture on the oscillator strengthes of the FSEs is obtained from the interface absorption spectrum.

6.4.2. Interface absorption coefficient

The absorption coefficient $\mathscr{A}(\omega)$ provides a first impression on the response of the interface system to an incident laser–pulse. By arranging the squared transition dipole moments of the FSE versus energy, the related stick spectrum [44] follows as,

$$\mathscr{A}(\omega) \propto \omega \sum_{\alpha} |\mathbf{d}_{\alpha}|^2 \delta(\mathscr{E}_{\alpha}^{\mathrm{FSE}} - \hbar\omega). \tag{6.11}$$

The FSE transition dipole moments, $\mathbf{d}_{\alpha}$, are obtained by the expression,

$$\mathbf{d}_{\alpha} = \sum_{m} \mathscr{C}_{m}^{\mathrm{LX}}(\alpha) \mathbf{d}_{m}^{\mathrm{6P}} \mathbf{e}_{eg}, \tag{6.12}$$

which is based on the 6P transition dipole moment $\mathbf{d}_{m}^{\mathrm{6P}}$, introduced in Sec. 6.2.4, and the fact that all 6Ps have the same spatial orientation (given by the unit vector $\mathbf{e}_{eg}$).

When the stick spectrum is finally lifetime broadened, it represents the absorption profile of the interface. The total interface absorption is given by the full blue line in Fig. 6.3b (using a Gaussian broadening of 50 meV). Despite the CT coupling, it is still dominated by Frenkel–like exciton formation within the 6P aggregate. As typical for H–aggregates, the oscillator strength decreases strongly when going from higher to lower energies. The energetically highest FX–like FSE marks the largest absorption peak (see Roman label I in Figs. 6.3a and b). The second highest absorption peak results from the energetically third highest FX–like FSE (see Roman label II). According to the H–aggregate effect, bright and dark FX–like FSEs are energetically ordered in alternation.

Next, the differential spectrum $\Delta\mathscr{A}$ is consulted in order to visualize only the contribution of the CT excitons to the absorption. It is obtained when removing the pure FX absorption (i.e., the spectrum for $\mathscr{V}^{CT} = 0$) from the full system absorption (i.e., the full blue line in Fig. 6.3b). The remaining $\Delta\mathscr{A}$ is exclusively subject to the generated CT excitons. It is given in Fig. 6.3b by the dashed and pink colored line. (Please con-

sider also the pink scaling factor of 10^{-2}.) By the direct comparison, clear evidence is given that the absorption of the CT excitons is about two orders of magnitude smaller than the full absorption. Besides that general observation, a certain "rule of thumb" concerning the energetic positions of the brightest CT excitons with respect to the full interface absorption however cannot be figured out.

The $\Delta\mathscr{A}$ essentially renders contributions of only six CT excitons. This is highly surprising in view of the many ten thousands of interface states. Instead of few individual states, one would intuitively anticipate a rather band–like structure. The reasoning for the isolated appearance of the levels is complex. Basically, however, it can be understood based on two arguments. Firstly, only these LX states and CS states are directly coupled, which realize the hole and excitation, respectively, localized on the first 6P (with $m = 1$; closest to the ZnO surface). All the remaining hybridizations between the much greater number of LX and CS states must therefore be mediated additionally by the action of the intermolecular couplings $\mathscr{V}^{\mathrm{HT}}_{m,m\pm1}$ and $\mathscr{J}_{mn}$ and hence appear as much less pronounced. And secondly, only few of the $\mathscr{V}^{CT}_{a}$ themself reach values high enough to efficiently couple states $|\mathrm{CS}_{1a}\rangle$ and $|\mathrm{LX}_1\rangle$ across the interface (see again Fig. 6.2b). Altogether, the missing CT band structure can be explained.

Now, the six dominant CT excitons diserve some closer attention. They are indicated by labels 1 to 6 in Figs. 6.3a and b. Accordingly, the spectral decomposition of the $\Delta\mathscr{A}$ (pink coloring) in Fig. 6.3b can be rather well realized. Turning to Figs. 6.3a, it can be clearly seen that the FSEs 1 and 2 have FX character of about 99.9 % (see energy levels on the very left side). In contrast to these two, the three highest lying states 4 to 6 represent CT excitons of more than 99 % CS character. However, despite the strong CS character, they carry rather similar oscillator strength as the former two CT excitons with labels 1 and 2 (see $\Delta\mathscr{A}$ in Figs. 6.3b again). This observation can be explained when taking additionally into account the above identified H–aggregate character of the 6P stacking. In fact, the energetically lower FX–like states carry only very weak oscillator strength by themself. Hence, even if the energetically lower FSEs (with labels 1 and 2) have very strong FX character, they only contain contributions from very weakly absorbing FXs. Vice versa, the CT excitons with labels 4 – 6 are mainly attributed with the energetically higher and much brighter excitons of the formed H–aggregate. However, in these cases the actually provided high oscillator strength is effectively decreased by the much lower FX character of the CT excitons. The FSE with the label 3 describes the brightest CT exciton. It still carries great shares of the second brightest FX state and at the same time it is of very high CS character.

6.5. Photoinduced Charge Separation Kinetics

After considering time–independent properties in the foregoing sections, now the interface kinetics are up for discussion. Only the direct simulation of the laser–pulse excitation makes possible the proper comparison with state–of–the–art measurements based on ultrafast pump–probe spectroscopy. The most simple description of the CS kinetics could be based on rate equations (see, e.g., Ref. [192], but also the work on interface EET provided in Chap. 5). The present investigation, however, is dedicated to femtosecond laser–pulse excitations of the interface. This induces coherences in the

system and therefore requires a reduced density matrix approach (for some general aspects on that, see Sec. 3.3). In the present case, the direct application of the density matrix theory would be unpractical concerning the vast number of $N = 120081$ interface states. Instead, it should be the intention to utilize the stochastic Schrödinger equation (SSE) approach developed, cf. Eq. 4.58,

$$i\hbar\frac{\partial}{\partial t}|\Psi(t)\rangle = \hat{H}_{\text{eff}}(t)|\Psi(t)\rangle. \tag{6.13}$$

It is defined by an effective Hamiltonian, $\hat{H}_{\text{eff}}(t) = \hat{H}(t) + \hat{\mathscr{F}}(t) + \hat{\mathscr{D}}(t)$. Besides the interface Hamiltonian $H(t)$ (see Eq. 6.4), the $H_{\text{eff}}(t)$ additionally account for dissipative contributions (i.e., molecular vibrations and ZnO phonons). These enter via the time–dependent stochastic force operator $\hat{\mathscr{F}}(t)$ and the damping operator $\hat{\mathscr{D}}(t)$. The time–dependence of the interface state is expanded following

$$|\Psi(t)\rangle = \mathscr{C}^{\text{G}}(t)|\text{G}\rangle + \sum_{m}\mathscr{C}^{\text{LX}}_{m}(t)|\text{LX}_m\rangle + \sum_{m,a}\mathscr{C}^{\text{CS}}_{ma}(t)|\text{CS}_{ma}\rangle, \tag{6.14}$$

using the diabatic basis states of Eqs. 6.1–6.3 (now including the interface ground state). Correspondingly, in total 120081 different time–dependent expansion coefficients are introduced, according to $\mathscr{C}^{\text{G}}(t) = \langle\text{G}|\Psi(t)\rangle$, $\mathscr{C}^{\text{LX}}_{m}(t) = \langle\text{LX}_m|\Psi(t)\rangle$ and $\mathscr{C}^{\text{CS}}_{ma}(t) = \langle\text{CS}_{ma}|\Psi(t)\rangle$.

As explained in Chap. 1 and Sec. 4.1, solving Eq. 6.13 would then tremendously lower computational costs in comparison with a direct density matrix calculation on equivalent level of theory. Here, however, the response to a 100 fs laser–pulse excitation is of interest and, regarding a desired time–scale below 1 ps, it is simply assumed that dephasing and dissipation have only minor influence on the interface kinetics. Consequently, the stochastic transfer model is limited to its coherent part. It means, the time–dependent Schrödinger equation is stressed neglecting $\hat{\mathscr{F}}(t)$ and $\hat{\mathscr{D}}(t)$. Though of preliminary character, this study already gives an important impression on the short–time coherent dynamics. It shall be the aim of future studies to get an idea of the influence of vibrational relaxation (see, e.g., Chap. 7). Here, the ordinary Schrödinger equation,

$$i\hbar\frac{\partial}{\partial t}|\Psi(t)\rangle = \hat{H}(t)|\Psi(t)\rangle, \tag{6.15}$$

is solved instead of Eq. 6.13. It is solely based on $\hat{H}(t)$ given in Eq. 6.4. Initially, the $|\Psi(t=0)\rangle$ represent the interface ground state configuration (i.e., it is $\mathscr{C}^{\text{G}}(0) = 1.0$ and $\mathscr{C}^{\text{LX}}_{m}(0) = \mathscr{C}^{\text{CS}}_{ma}(0) = 0$). When formally integrating Eq. 6.16, the wave packet dynamics of the interface state arise as, cf. Eq. 3.2,

$$|\Psi(t)\rangle = \hat{T}\exp\Big\{\frac{1}{i\hbar}\int_0^t d\tau\ \hat{H}(\tau)\Big\}|\text{G}\rangle. \tag{6.16}$$

Details on its efficient numerical integration are provided in Appendix H.2.1. Based on the simulation data, the probability to have the organic part in its excited state is then

deduced as

$$P_{\mathrm{X}}(t) = \sum_{m} |\langle \mathrm{LX}_m | \Psi(t) \rangle|^2 = \sum_{m} P_{\mathrm{X}}(m,t). \tag{6.17}$$

It collects the individual probabilities $P_{\mathrm{X}}(m,t) = |\mathscr{C}_m^{\mathrm{LX}}(t)|^2$ of an excitation localized on the mth 6P (see Sec. 6.14). The probability $P_{\mathrm{X}}(t)$ is confronted with

$$P_{\mathrm{CS}}(t) = \sum_{m,a} |\langle \mathrm{CS}_{ma} | \Psi(t) \rangle|^2 = \sum_{m} P_{\mathrm{H}}(m,t), \tag{6.18}$$

which echos the probability that CS appears across the interface (i.e., the total population of all CS states at time t). The latter can be further decomposed by introducing $P_{\mathrm{H}}(m,t) = \sum_a |\mathscr{C}_{ma}^{\mathrm{CS}}(t)|^2$, the probability to measure an hole localized on the mth 6P (independent on the electron localization). Accordingly, one immediately realizes that it is $P_{\mathrm{CS}}(t) = \sum_m P_{\mathrm{H}}(m,t)$. In similar way, $P_{\mathrm{CS}}(t)$ can also be dissected more precisely concerning the electron localization in the ZnO cluster. For this purpose, the Löwdin AOs $\zeta_{l_u}^{(u)}$ (with atomic index u, orbital index l_u and atomic coordinates $\mathbf{R}_u$) describe an adequate basis set (see also Sec. 2.2.1 and Appendix G.3). Based on the AOs, the excess electron in the CB–like states $\bar{\psi}_a$ can be extreme accurately rendered within the ZnO cluster. Making use of the expansion coefficients $\mathscr{C}_{u,u_l} = \langle \zeta_{l_u}^{(u)} | \bar{\psi}_a \rangle$ (see Eq. 2.9; here without the spin quantum number σ), the $P_{\mathrm{CS}}(t)$ decomposes according to

$$P_{\mathrm{CS}}(t) = \sum_{m,a} \sum_{u} \sum_{l_u} |\mathscr{C}_{ma}^{\mathrm{CS}}(t)|^2 |\mathscr{C}_{u,u_l}|^2 = \sum_{u} P_{\mathrm{E}}(\mathbf{R}_u, t) \ , \tag{6.19}$$

The probability to find the electron on atom $\mathbf{R}_u$ (independent on hole and CB–like state indexes m and a) reads $P_{\mathrm{E}}(\mathbf{R}_u, t) = \sum_{m,a} \sum_{l_u} |\mathscr{C}_{ma}^{\mathrm{CS}}(t)|^2 |\mathscr{C}_{u,u_l}|^2$.

6.5.1. Variation of laser–pulse excitation energy

For the beginning, the computational results on the net degree of excitation and CS shall be discussed ignoring any information on its spatial distribution. The temporal behaviors of $P_{\mathrm{X}}(t)$ and $P_{\mathrm{CS}}(t)$ (see Eqs. 6.17 and 6.18, respectively) are drawn versus time in Fig. 6.4. Kinetics from four different cases of photon energy: $\hbar\omega_L = 4.35$ eV, 4.2 eV, 4.0 eV and 3.9 eV are given as indicated in the subpanels Fig. 6.4a–d, respectively. While $\hbar\omega_L$ is varied, the other laser–pulse parameters are kept constant as introduced in Sec. 6.2.4. Besides, all four simulation runs were performed in continuation of Sec. 6.4 with the hole coupling of $\mathscr{V}^{HT} = 0.02$ eV and the CT coupling of $\mathscr{V}^{\mathrm{CT}} = 0.2$ eV.

As depicted in Fig. 6.4d, the smallest value of $P_{\mathrm{X}}(t)$ results from applying the photon energy of $\hbar\omega_L = 3.9$ eV. Moving upwards with $\hbar\omega_L = 4.35$ eV, the values of $P_{\mathrm{X}}(t)$ become essentially larger (see Fig. 6.4a). At the same time, $P_{\mathrm{CS}}(t)$ moves through a maximum found at $\hbar\omega_L = 4.2$ eV (see Fig. 6.4b).

A detailed understanding of the kinetics is possible. In Secs. 6.4.1 and 6.4.2, the interface absorption spectrum and the appearance of CT excitons are discussed elaborately (see Fig. 6.3). Based on that, the dramatic difference of the maximum values of $P_{\mathrm{X}}(t)$ (when moving $\hbar\omega_L$ from 4.35 to 3.9 eV) can be now directly explained with the

Figure 6.4.: Time–evolution of the total 6P excited state population P_{X} (solid green lines, see Eq. 6.17) and the total probability of CS state formation P_{CS} (dashed blue lines, see Eq. 6.18) following laser–pulse excitation with different photon energies $\hbar\omega_L$ (black lines, with pulse duration of 100 fs) and applying $\mathscr{V}^{\mathrm{CT}} = 0.2$ eV and $\mathscr{V}^{\mathrm{HT}} = 0.02$ eV. The used $\hbar\omega_L$ are displayed in each panel as well as the different scale factors for P_{X} and P_{CS} (box in the upper center).

pronounced H–aggregate character shown in Fig. 6.3b. (Please note that for the sake of clarity the relevant regions of the four photon energies $\hbar\omega_L = 4.35$ eV, 4.2 eV, 4.0 eV and 3.9 eV are indicated by the capital Latin labels A–D in Fig. 6.3.) Furthermore, hybridized states of very strong CS character are directly populated by exciting the system with $\hbar\omega_L = 4.35$ eV. This is confirmed in Fig. 6.4a by an increase of P_{CS} during the laser–pulse and the subsequent oscillation behavior. This oscillation is attributed to the pulsed femtosecond excitation. Different interface states with energies around $\hbar\omega_L$ are simultaneously excited according to the width of the spectral broadening inherent to the ultrashort pulses (here, it is $\hbar/\tau_p \approx 7$ meV). By virtue of that, a wave packet is formed and may move in CS state space.

The previous argumentation is footed on the picture of prompt CS via optical activation of CT excitons introduced in Chap. 1 (see Fig. 1.3c). Contrarily, a distinction between optical excitation and CS process (see Fig. 1.3b) is more adequate when considering the kinetics obtained with $\hbar\omega_L = 4.0$ eV. They are given in Fig. 6.4c. In this case, one may interpret the CS as a slower process resulting from the decay of an initially formed FX. This reasoning is supported by the continuous increase of $P_{\mathrm{CS}}(t)$ during the simulation. The kinetics related to $\hbar\omega_L = 3.9$ eV are illustrated in Fig. 6.4d. They show different features. A short but strong CS occurs simultaneously with a fast

Figure 6.5.: Spatio–temporal evolution of the 6P excited state population $P_{\mathrm{X}}(m,t)$ (see Eq. 6.17) using $\mathscr{V}^{\mathrm{CT}} = 0.2$ eV, $\mathscr{V}^{\mathrm{HT}} = 0.02$ eV and each the indicated $\hbar\omega_L$ in panel a–d. (Continuous presentation with respect to the m–dependence indicated at the 6P/ZnO interface system in the lower left). Panel d: Case of $\hbar\omega_L = 3.9$ eV. Pink dash–dotted line points to the center of the 100 fs laser–pulse. Highest population occurs within the green and cyan dashed zones. The blue dashed arrows indicate exciton wave packet motion from the top of the 6P stack to the ZnO interface at the bottom (for details, see the main text).

but transient exciton formation. Afterwards, both populations stay rather constant. This case is very interesting and shall be further inspected in detail below.

The pronounced CS efficiency in Fig. 6.4b is obtained when applying $\hbar\omega_{\mathrm{L}} = 4.2$ eV. Its appearance can be understood better when analyzing the spatially resolved probability $P_{\mathrm{X}}(m,t)$ (see Eq. 6.17). It is offered by the four contour plots in the Figs. 6.5a–d (related to the Figs. 6.4a–d, respectively). For better illustration, they present each interpolations of the data with discrete m–dependence. The color codes are separately adapted to the respective minimum and maximum values. Both, the $P_{\mathrm{X}}(m,t)$ from $\hbar\omega_L = 4.35$ eV and the one belonging to $\hbar\omega_L = 4.2$ eV display each sinusoidal patterns of the exciton wave function (rendered in Figs. 6.5a and b, respectively). According to the detailed discussion on the exciton formation in Sec. 5.3.1, such patterns are suggested at this place. There stability, however, is somewhat astonishing. Initiated by wave packet formation, one would actually expect the observation of exciton migration, i.e., clear indications for EET among the 6Ps. This is presently not the case which is due to the fact that, in this high–energy region, the laser–pulse of 100 fs duration is still too long in order to sufficiently populate eigenstates with inherent shares of other FXs. Indeed, a closer view on the energy level diagram in Fig. 6.3b testifies that the highest as well as the third highest FX–like FSE lies very isolated. Because of that, the FSE wave packets prepared in the range of $\hbar\omega_L = 4.35$ and 4.2 eV contain exclusively exciton partition from the highest and third highest FX level, respectively, and so

exciton migration remains off.

Concerning the case of $\hbar\omega_L = 4.35$ eV (see Figs. 6.4a and 6.5a), this explains: i) the stable and high $P_{\mathrm{X}}(m,t)$ in Fig. 6.5a, ii) the much weaker P_{CS} in Fig. 6.4a, and iii) the oscillating behavior of the $P_{\mathrm{CS}}(t)$. Similarly, the stable exciton pattern in Fig. 6.4b (with $\hbar\omega_L = 4.2$ eV) can be explained by the excitation of interface states which only hold shares of the third highest FX. It is a special feature of this exciton, however, to generate a significant localization of molecular excitation very close to the ZnO surface (see Fig. 6.5b, green dashed area at index $m = 1$). Likewise "squeezed" localizations are also enlightened and discussed in Chap. 5 (see Sec. 5.3.1). That close exciton localization right at the ZnO surface greatly supports efficient hybridization of FX and CS states which furthermore suggests that in the present case much more CS states are involved in the kinetics. Indeed, the continuously increasing type of CS process give evidence on that (see Fig. 6.4b). Finally, it is also plausible to observe the strongest CS process under these conditions reminding that excitation with $\hbar\omega_L = 4.2$ eV goes along with the second highest oscillator strength.

Contrarily to the latter two stable exciton localizations (from $\hbar\omega_L = 4.2$ and 4.35 eV), a superimposed exciton oscillation upon the entire 6P aggregate is monitored in Fig. 6.5c when exciting with $\hbar\omega_L = 4.0$ eV. The spatially resolved continuous wave packet migration confirms the above characterization of the kinetics as exciton diffusion and subsequent decay (see again Fig. 6.4c). This reasoning is also valid in the case of $\hbar\omega_L = 3.9$ eV. By analysing Fig. 6.5d, it is now possible to resolve a short–term initial localization of the excitation on the first and last 6P molecule (see the green and cyan dashed areas, respectively). The excitation close to the surface (green dashed area) leads to the rapid CS and explains the initial steplike increase of the $P_{\mathrm{CS}}(t)$ monitored in Fig. 6.4d. After the laser–pulse, the 6P excitation diminishes. The localization of the remaining excitation clearly signifies wave packet migration that origins from the end of the stacking (blue dashed arrows in Fig. 6.5d). Minor fluctuations of both populations $P_{\mathrm{CS}}(t)$ and $P_{\mathrm{X}}(t)$ in Fig. 6.4d at around 600 and 800 fs coincides with the approaching and reflection of the exciton wave packet at the ZnO surface (the lower margin of Fig. 6.5d) with partial CS state formation.

6.5.2. Variation of hole transfer coupling

For photovoltaic devices, it is of fundamental importance that the electron and hole move away from the interface. It follows a detailed study on the spatial distribution of the created electron and hole. The probability $P_{\mathrm{H}}(m,t)$ to find the hole at the mth 6P (see Eq. 6.18) is analysed for the four computed kinetics with different $\hbar\omega_L$. Throughout all four simulations, it is found that the hole stays completely localized at the interface (not shown). This distinct localization reflects the weak hole transfer coupling of $\mathscr{V}^{\mathrm{HT}} = 0.02$ eV. As discussed in Sec. 6.2.2 (see particularly Fig. 6.1e), the energy levels of the hole localized on neighbored 6P molecules close to the surface are rather off–resonant. These energy gaps are too large for efficient hole delocalization or coherent transport (i.e., it is $|\mathscr{E}_{1a}^{\mathrm{CS}} - \mathscr{E}_{2a}^{\mathrm{CS}}| \gg \mathscr{V}^{\mathrm{HT}}$) and the hole stays trapped at the interface.

Such strict hole trapping is not observed when the simulations are based on the hole

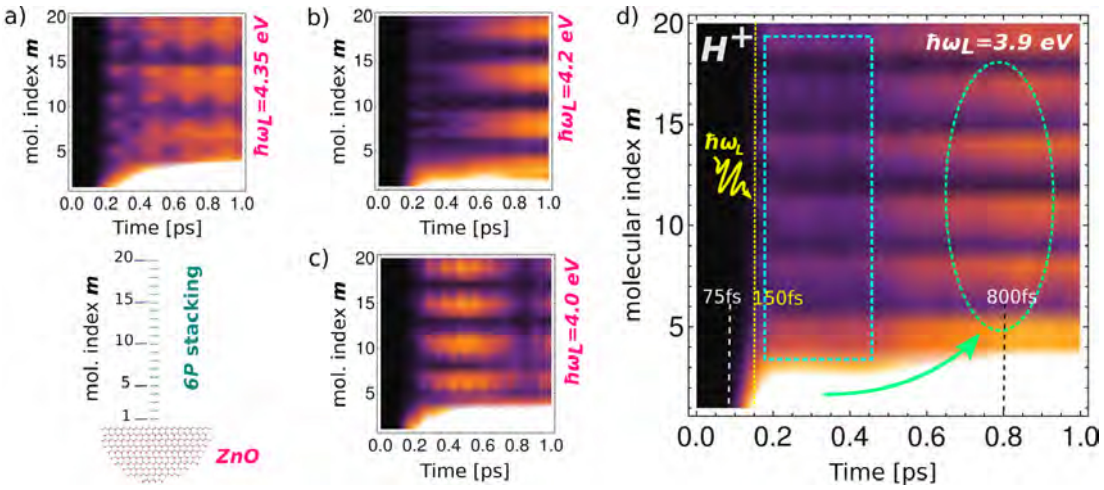

Figure 6.6.: Spatio–temporal evolution of the hole population $P_{\mathrm{H}}(m,t)$ (see Eq. 6.18) using $\mathscr{V}^{\mathrm{CT}} = 0.2$ eV, $\mathscr{V}^{\mathrm{HT}} = 0.2$ eV and each the indicated $\hbar\omega_L$ in panel a–d. The yellow dashed line gives the center of the 100 fs laser pulse. Cyan rectangular and green oval dashed zones mark direct CS processes and more diffusive hole motion, respectively. White dashed lines point to the time–steps displayed in Fig. 6.7 concerning the electron localization (for details, see the main text).

coupling of $\mathscr{V}^{\mathrm{HT}} = 0.2$ eV. The related $P_{\mathrm{H}}(m,t)$ (see Eq. 6.18) are displayed in the Figs. 6.6. As in Sec. 6.5.1, four simulation runs were executed under variation of the photon energy $\hbar\omega_L$ (see indication in each panel of Fig. 6.6). For better illustration, again a continuous presentation in the fashion of Fig. 6.5 is chosen. With the increased coupling, now the hole is able to overcome much better the discussed off–resonances. The obtained hole delocalization can be understood as CS states with holes which are more scattered apart from the interface. All $P_{\mathrm{H}}(m,t)$ in Fig. 6.6 reveal sinusoidal patterns occurring upon all 20 molecules. However, the localizations are still pronounced in the vicinity of the interface (white area at $m < 4$). For instance, the data resulting from $\hbar\omega_L = 3.9$ eV are given in Fig. 6.6d. In response to the laser–pulse (centered at 150 fs), a specific hole distribution can be identified which is immediately delocalized over all 20 6P molecules (marked by the cyan squared zone). Its incident appearence gives evidence of the direct excitation of CS states. For later times the delocalization is further enhanced. Slower and more diffusive hole migration accompanies by evacuating the region close to the interface (starting after 500 fs; marked by the green oval ellipse).

The above described hole migration can be confronted with the motion of the opponent excess electron in the ZnO cluster. This shall be demonstrated examplarily for the two case of $\hbar\omega_L = 4.35$ and 3.9 eV. For spatial analysis of the electron motion, the Figs. 6.7a and b visualize the $P_{\mathrm{E}}(\mathbf{R}_u,t)$ via side views on the ZnO cluster. As introduced in Eq. 6.20, the $P_{\mathrm{E}}(\mathbf{R}_u,t)$ reflects the probabilty to have the excess electron at atomic position $\mathbf{R}_u$ in the ZnO cluster. The electron distributions are depicted for time–frames of $t = 75$ fs, 150 fs and 800 fs, respectively. Very fast initial redistribution

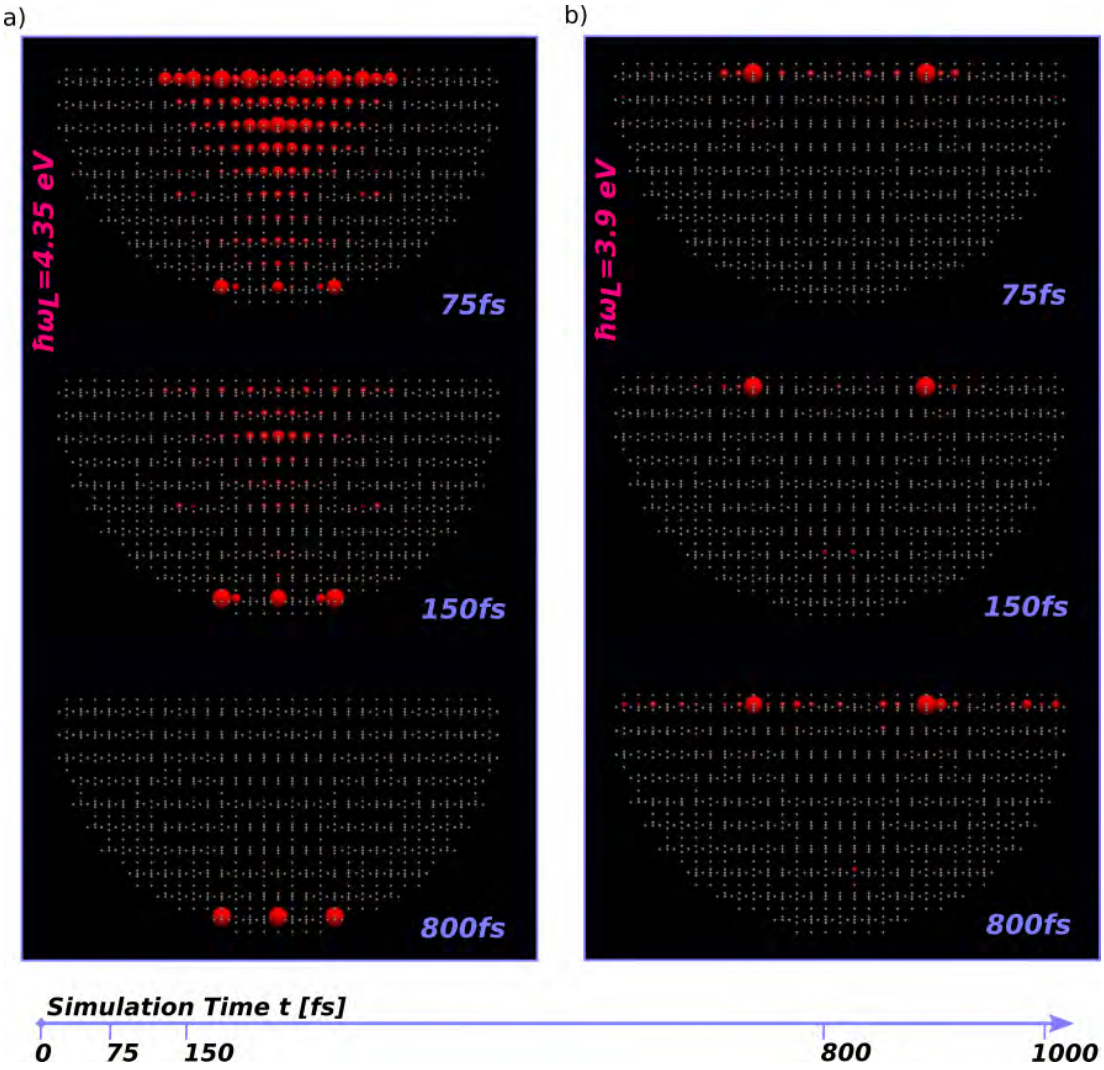

Figure 6.7.: Spatio–temporal evolution of the electron population in the ZnO cluster, $P_{\mathrm{E}}(\mathbf{R}, t)$ (see Eq. 6.20). Panel a: Electron delocalization upon the Zn and O atoms at three different time–steps related to the hole dynamics shown in Fig. 6.6a (front view on the cluster, see also the interface sketch in the lower left corner of Fig. 6.6). Panel b: Similar visualization of $P_{\mathrm{E}}(\mathbf{R}, t)$ related to the hole dynamics shown in Fig. 6.6d (for details, see the main text).

from the primary acceptor region (introduced in Sec. 6.3, cf. Fig. 6.2a) was uncovered in all cases within less than 50 fs (not shown). This is due to the universally strong interatomic transfer coupling between the atoms in the ZnO cluster. After this initial phase, however, the electron shows very unspecific behavior. For instance, deep electron injection into the bulk region appears when using $\hbar\omega_L = 4.35$ eV (see Fig. 6.7a). Until 800 fs, a stable electron accumulation at the "bottom" of the cluster takes place. Contrarily to that, the electron stays in the top layers of the ZnO cluster during the entire kinetics with photon energy $\hbar\omega_L = 3.9$ eV (see Fig. 6.7b).

The previous argumentation must be carefully reviewed when introducing long–term dissipative effects in the interface model. According to the particular potential energy gradient discussed in Sec. 6.2.2 (see Fig. 6.1e), on one side, hole relaxation processes would obviously accelerate the hole evacuation from the interface. On the other side, however, ZnO materials are well–known for unoccupied surface states which lie energetically close to the CB edge. Due to dissipative, now also electron relaxation to the CB edge would happen. It manifests in terms of critical accumulation of the injected electron at the ZnO surface instead of the actually aspired delocalization into more "deeper" ZnO bulk regions. This problematic of ZnO is a well–known issue of recent concern [94, 66, 34]. The topic is recaptured in Chap. 7, when simulation studies on dissipative hole motion the hole at the 6P/ZnO interface are presented.

6.6. Effects of Static Energetic Disorder

In the foregoing sections, the interface system is set up with regularly arranged 6P molecules. In order to relax this idealized picture, the effect of energetic disorder on the CS kinetics is investigated in what follows. As discussed in Sec. 6.1, in this way a rough initial impression on the inclusion of vibronic effects is provided and the "robustness" of the interface kinetics against minor changes of the system can be probed.

Static fluctuations of the energy terms shall be introduced as $\Delta\epsilon_m^{\mathrm{LX}}$ and $\Delta\epsilon_{ma}^{\mathrm{CS}}$. Both types are substituted into the $\hat{H}(t)$ (see Eq. 6.4) according to,

$$\mathscr{E}_m^{\mathrm{LX}} \rightarrow \mathscr{E}_m^{\mathrm{LX}} + \Delta\epsilon_m^{\mathrm{LX}} \tag{6.20}$$

and

$$\mathscr{E}_{ma}^{\mathrm{CS}} \rightarrow \mathscr{E}_{ma}^{\mathrm{CS}} + \Delta\epsilon_{ma}^{\mathrm{CS}}. \tag{6.21}$$

To keep things simple, all fluctuations are randomly generated from the same Gaussian probability distribution with zero mean and $\sigma = 30$ meV. The latter choice was taken as a reasonable value. It is somewhat larger than thermal energy at room temperature and in the range of the value introduced in the study on EET in Sec. 5.5.2. Then, disorder attributed solutions $|\Psi_w(t)\rangle$ of the Schrödinger equation 6.16 were computed. The subindex w is utilized to label the individual solutions. Ensemble averaged population kinetics corresponding to Eqs. 6.17 and 6.18 follow from a number of W different

simulation runs with

$$\bar{P}_{\mathrm{X}}(t) = \sum_{m} \langle \mathrm{LX}_m | \Big[\frac{1}{W} \sum_{w}^{W} |\Psi_w(t)\rangle\langle\Psi_w(t)| \Big] | \mathrm{LX}_m \rangle \tag{6.22}$$

and

$$\bar{P}_{\mathrm{CS}}(t) = \sum_{m,a} \langle \mathrm{CS}_{ma} | \Big[\frac{1}{W} \sum_{w}^{W} |\Psi_w(t)\rangle\langle\Psi_w(t)| \Big] | \mathrm{CS}_{ma} \rangle, \tag{6.23}$$

respectively. The averaged kinetics of $\bar{P}_{\mathrm{X}}$ and $\bar{P}_{\mathrm{CS}}$ are given in the right column of Fig. 6.8 (Roman subfigure index i–iv). The data from the regular system (overtaken from Fig. 6.4) is presented in the left column (Latin subfigure index a–d). In practice, $W = 500$ different simulation runs were computed to achieve well–converged results.

The comparison of the disorder attributed $\bar{P}_{\mathrm{X}}(t)$ and $\bar{P}_{\mathrm{CS}}(t)$ with the $P_{\mathrm{X}}(t)$ and $P_{\mathrm{CS}}(t)$ uncovers moderate changes. Most evident, the $\bar{P}_{\mathrm{X}}(t)$ and $\bar{P}_{\mathrm{CS}}(t)$ appear smoother. Due to the averaging, the oscillations discussed in Sec. 6.5 as an essential indication for coherent wave function propagation are not recovered in Figs. 6.8i–iv. Furthermore, the disorder–attributed kinetics from $\hbar\omega_L = 4.35$ eV and $\hbar\omega_L = 4.2$ eV (shown in Figs. 6.8i and ii) show decreased maximum values of the excited state population with respect to the related non–averaged kinetics in Figs. 6.8a and b, respectively (i.e., with both photon energies it is $\bar{P}_{\mathrm{X}}^{\max} < P_{\mathrm{X}}^{\max}$). Also this finding could be very well explained. In fact, the $\hbar\omega_L$ are defined in Sec. 6.5 as rather resonant with the two brightest FX–like FSEs. On average, now the random energy shifts result in a somewhat detuned optical excitation. In both cases of very isolated FX–like FSEs (see again the level scheme in Fig. 6.3a), the missing resonance explains the overall reduced excitation. As an evidence for this, very equivalent ratios of $\bar{P}_{\mathrm{X}}^{\max}/P_{\mathrm{X}}^{\max} = 1/2.5$ and $1/2.7$ are obtained for $\hbar\omega_L = 4.35$ eV and 4.2 eV, respectively. In cases of low–energy region of the band (i.e., when using photon energies $\hbar\omega_L = 4.0$ eV and 3.9 eV), the FX–like FSEs lie much denser (in particular, when applying $\hbar\omega_L = 3.9$ eV). There, a detunded optical excitation has not the same effect. In the case of $\hbar\omega_L = 4.0$ eV, very similar maximum values of excited state populations are obtained (i.e., $\bar{P}_{\mathrm{X}}^{\max}/P_{\mathrm{X}}^{\max} \approx 1.0$ and when applying $\hbar\omega_L = 3.9$ eV, the disorder–averaged kinetics show even vice versa enhanced excited state populations (i.e., $\bar{P}_{\mathrm{X}}^{\max}/P_{\mathrm{X}}^{\max} = 2.8$).

The relative CS efficiency can be concerned in terms of the relation $\eta_{\mathrm{CS}} = P_{\mathrm{CS}}^{\max}/P_{\mathrm{X}}^{\max}$. Its ensemble averaged version follows as $\bar{\eta}_{\mathrm{CS}} = \bar{P}_{\mathrm{CS}}^{\max}/\bar{P}_{\mathrm{X}}^{\max}$. Only minor quantitative differences result for the three cases of $\hbar\omega_L = 3.9$ eV, 4.0 eV and 4.2 eV. However, a uniform trend could not be realized. Instead, the relative CS efficiency $\bar{\eta}_{\mathrm{CS}}$ increases for $\hbar\omega_L = 4.35$ eV by one order of magnitude ($\bar{\eta}_{\mathrm{CS}}/\eta_{\mathrm{CS}} = 11.2$). Though the disorder leads to off–resonant excitation, in this energetic region, it strongly enhances the efficiency of the CS process on average.

Finally, the disorder–attributed and averaged $\bar{P}_{\mathrm{X}}$ is reconsidered in spatio–temporal resolution. The Figs. 6.9a–d illustrate the averaged kinetics resulting from the four photon energies. Very similar excitonic patterns for the two cases of $\hbar\omega_L = 4.35$ eV and 4.2 eV are realized in direct comparison with the earlier results from the regular system provided in Figs. 6.5a and b. As discussed above in Sec. 6.4, the upper FX levels

Figure 6.8.: Effect of energetic disorder on the time–evolution of the total 6P excited state (LX) and charge–separated (CS) state populations. Panel a-d: Population kinetics of $P_{\mathrm{X}}(t)$ (green solid line, cf. Eq. 6.17) and $P_{\mathrm{CS}}(t)$ (blue dashed line, cf. Eq. 6.18). The latter data is overtaken from Fig. 6.4. The applied photon energies are each indicated. Panel i-iv: Respective population kinetics of $\bar{P}_{\mathrm{X}}(t)$ (yellow solid line, cf. Eq. 6.22) and $\bar{P}_{\mathrm{CS}}(t)$ (purple dashed line, cf. Eq. 6.23), averaged with respect to disorder (note again the scale factors to get the correct values).

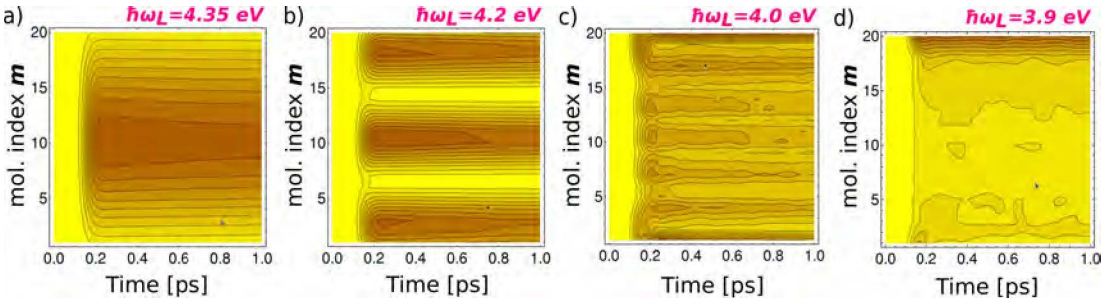

Figure 6.9.: Effect of energetic disorder on the spatio–temporal evolution of the 6P excited state population. The averaged kinetics $\bar{P}_{\mathrm{X}}(m,t)$ are visualized based on the same parametrization as applied in Fig. 6.5 (there without disorder). Panel a-d: Applied photon energies $\hbar\omega_L$ correspond to Fig. 6.5a-d, respectively (see indication).

are energetically very isolated (see again Fig. 6.3b) and the applied fluctuations are too small to mix contributions of several FXs into $\bar{P}_{\mathrm{X}}(m,t)$. These findings agree very well with the discussion in Sec. 6.5. Clear distinctions are visible when studying $\bar{P}_{\mathrm{X}}(m,t)$ for $\hbar\omega_L = 4.0$ eV and 3.9 eV, instead. Therefore, the Fig. 6.9c and Fig. 6.9d must be compared with Fig. 6.5c and Fig. 6.5d, respectively. In this lower energetic region, the FX band is essentially more dense and by means of the energetic fluctuations many different FXs come into range of the laser–pulse. The absence of the typical patterns of exciton wave packet motion is not surprising. They are superimposed and compensated due to the ensemble averaging.

6.7. Kinetics from Prepared Initial States

In literature, the explicit treatment of the excitation by means of direct laser–pulse simulation is commonly avoided (see, e.g., Refs. [92, 84, 34]). Instead, it is more likely to start simulations directly from certain localized excited state. Here, this would mean introducing a certain formal ansatz for the initial state wave function $\Psi(t=0)$ according to a set of $\mathscr{C}_m^{\mathrm{LX}}(t=0) \neq 0$ (see Eq. 6.14). In what follows, the populations, P_{X} and P_{CS}, as well as the disorder affected populations, $\bar{P}_{\mathrm{LX}}$ and $\bar{P}_{\mathrm{CS}}$, obtained from accurate laser–pulse treatment (see Fig. 6.9) are compared with related data from five different simplified excited state ansatzes.

Four FX states of the 6P aggregate $|\bar{\Phi}_\alpha\rangle$ (with the FX index α, cf. Eq. 2.31 were selected for initial interface state ansatzes, according to $|\Psi(t=0)\rangle = |\bar{\Phi}_\alpha\rangle \otimes |\Psi_0\rangle$, with the ZnO cluster in the ground state $|\Psi_0\rangle$ (see Sec. 6.2.1). To ensures a "fair" comparisons with the laser–pulse induced kinetics, the four states $|\bar{\Phi}_\alpha\rangle$ were particularly chosen regarding energetic compatibility to the four photon energy $\hbar\omega_L$. These were: i) the $|\bar{\Phi}_1\rangle$ with energy of $\mathscr{E}_1 = 4.357$ eV (corresponding to $\hbar\omega_L = 4.35$ eV), ii) the $|\bar{\Phi}_3\rangle$ with energy of $\mathscr{E}_3 = 4.192$ eV (corresponding to $\hbar\omega_L = 4.2$ eV), iii) the $|\bar{\Phi}_8\rangle$ with energy of $\mathscr{E}_8 = 4.010$ eV (corresponding to $\hbar\omega_L = 4.0$ eV), and iv) the state $|\bar{\Phi}_{19}\rangle$ with energy of $\mathscr{E}_{19} = 3.900$ eV (corresponding to $\hbar\omega_L = 3.9$ eV). A fifth simulation run was

executed starting with the state $|\Psi(t=0)\rangle = |\mathrm{LX}_{m=1}\rangle = |\bar{\Phi}_1^e\rangle \otimes |\Psi_0\rangle$ (i.e., with an initial molecular 6P excitation directly attached to the ZnO cluster, cf. Eq. 6.2). In particular, the latter localized excitation is easily prepared and describes a very popular initial configuration in literature [84].

The Figs. 6.10a–d show the time–evolution of the populations $P_{\mathrm{X}}(t)$ and $P_{\mathrm{CS}}(t)$ for the single wave function kinetics, which follow from applying the four different $|\bar{\Phi}_\alpha\rangle$ with $\alpha \in \{1, 3, 8, 19\}$, respectively. In Fig. 6.10e, the fifth simulation run with the initially localized excitation $|\Psi(t=0)\rangle$ is given. In general, more structured curves result for all kinetics when comparing the data with the ones from direct laser–pulse simulations offered before in Fig. 6.8a–d. The prepared states, $|\Psi(0)\rangle$, may contain (energetically) rather different terms, because they are prepared as eigenstates (or molecular excitations) of the 6P aggregate. They expose a less smooth time–dependence than a wave packet, which is directly formed via laser–pulse excitation and contrarily contains only terms from a small energetic range.

The highest exciton level $\mathscr{E}_1$ is energetically equivalent with laser–pulse excitation at $\hbar\omega_L = 4.35$ eV. Both related kinetics are shown in the Figs. 6.8a and 6.10a, respectively. Interestingly, in both cases the $P_{\mathrm{CS}}(t)$ describes an oscillation of about 600 fs. The CS efficency can be compared again in terms of the ratio $P_{\mathrm{CS}}^{\max}/P_{\mathrm{X}}^{\max}$. It reaches a value of about 1/140 in the case of optical excitation and the value of about 1/80 with $|\Psi(t=0)\rangle = |\bar{\Phi}_1\rangle \otimes |\Psi_0\rangle$. With that, an overestimation of the CS process by a factor of 1.8 is detected for the initial FX.

However, this conclusion cannot be generalized straightly. In fact, better agreement appears between the simulations with $\hbar\omega_L = 4.2$ eV (see Fig. 6.8b) and the kinetics starting from $|\Psi(t=0)\rangle = |\bar{\Phi}_3\rangle \otimes |\Psi_0\rangle$ (shown in Fig. 6.10b). Also the results from $|\Psi(0)\rangle = |\mathrm{LX}_{m=1}\rangle$ (see Fig. 6.10e) shows rather well comparison with $\hbar\omega_L = 4.2$ eV – even though high frequent oscillations occur throughout the monitored time–span. In all three cases, the ratios $\eta_{\mathrm{CS}} = P_{\mathrm{CS}}^{\max}/P_{\mathrm{X}}^{\max}$ were found to be in very good agreement. After simulation time of 1000 fs, the η_{CS} is only slightly overestimated by factors of 1.3 and 1.2 when preparing the FX and localized excitation, respectively. Regarding the time–delay of the laser–induced excitation of about 200 fs with respect to the two excited state ansatzes, the latter two factors must be interpreted as a good agreement. The good matches are reasonable in both cases, because the laser–pulse of $\hbar\omega_L = 4.2$ eV itself induces a CS process which basically originates from a stable localization of molecular excitation right in front of the ZnO surface (see discussion in Sec. 6.5).

The latter conformity deteriorates critically when changing to $\hbar\omega_L = 4.0$ eV and in particular to $\hbar\omega_L = 3.9$ eV. With equivalent energies, the states $|\Psi(t=0)\rangle = |\bar{\Phi}_8\rangle \otimes |\Psi_0\rangle$ and $|\Psi(t=0)\rangle = |\bar{\Phi}_{19}\rangle \otimes |\Psi_0\rangle$ are prepared, respectively. Now, the focus is on lower regions of the FXs where the band becomes essentially denser. According to the discussion in Sec. 6.5, this leads to more sophisticated kinetics induced by laser–pulse excitations and clear destinctions to the prepared kinetics can be expected. The earlier kinetics with $\hbar\omega_L = 4.0$ eV and $\hbar\omega_L = 3.9$ eV gave ratios $P_{\mathrm{CS}}^{\max}/P_{\mathrm{X}}^{\max}$ of about 1/3 (see Figs. 6.8c) and 1/10 (see Figs. 6.8d), respectively. And indeed, essentially different values of about 1/8 and 1/220 were computed for the simulations with the ansatzes $|\Psi(t=0)\rangle = |\bar{\Phi}_8\rangle \otimes |\Psi_0\rangle$ and $|\Psi(t=0)\rangle = |\bar{\Phi}_{19}\rangle \otimes |\Psi_0\rangle$, respectively (see Figs. 6.10c and d). The latter means a remarkable underestimation of the CS process

Figure 6.10.: Time–evolution of the total 6P excited state (LX) and the total charge–separated (CS) state population. Comparison is drawn between kinetics which start from different initial excited state ansatzes $|\Psi(0)\rangle$ (i.e., without optical excitation; see pink colored formula). Panel a–e: $P_{\mathrm{X}}(t)$ (green solid lines, cf. Eq. 6.17) and $P_{\mathrm{CS}}(t)$ (blue dashed lines, cf. Eq. 6.18). Panel i–v: Related disorder averaged $\bar{P}_{\mathrm{X}}(t)$ (yellow solid lines, cf. Eq. 6.22) and $\bar{P}_{\mathrm{CS}}(t)$ (purple dashed lines, cf. Eq. 6.23). Introduced interface states $|\Psi(0)\rangle$ with FX of the 6P aggregate: 1st FX (i.e., $|\Psi(0)\rangle = |\bar{\Phi}_1\rangle \otimes |\Psi_0\rangle$) with energy 4.357 eV, 3rd FX ($|\bar{\Phi}_3\rangle \otimes |\Psi_0\rangle$) with energy of 4.192 eV, 8th FX ($|\bar{\Phi}_8\rangle \otimes |\Psi_0\rangle$) with energy of 4.01 eV and 19th FX ($|\bar{\Phi}_{19}\rangle \otimes |\Psi_0\rangle$) with energy of 3.90 eV. The fifth initial state ($|\bar{\Phi}_1^e\langle \otimes |\Psi_0\rangle$) describes the molecular excitation $6\mathrm{P}^*{}_{m=1}$ (i.e., $|\Psi(0)\rangle = |\mathrm{LX}_1\rangle$).

by more than one order of magnitude.

Together, the discussed results prove that kinetics with excited state ansatzes can be very inaccurate. Only under very certain conditions, artificially prepared coherent wave function dynamics aggree sufficiently well with the more involving dynamics based on direct laser–pulse treatment. In general, even stringer disagreement must be anticipated for even shorter pulse durations.

The inclusion of vibronic effects in the interface model would lead to dephasing and relaxation processes. In general, the latter can be expected to depress the coherent character of the above kinetics. These would then be less sensitive to particular wave packet formations and, in principle, the simulations with initial excited state ansatzes should perform better (although the interface model becomes even more complex with dissipative interaction). A final comparative study was executed in order to give a first impression on that. It concerns the disorder affected population kinetics, $\bar{P}_{\mathrm{X}}$ and $\bar{P}_{\mathrm{CS}}$, discussed in Sec. 6.6. The same Gaussian disorder and averaging procedures were applied on the kinetics starting from the excited states ansatzes. The averaged kinetics $\bar{P}_{\mathrm{X}}$ and $\bar{P}_{\mathrm{CS}}$ obtained with the five initial ansatzes are depicted in the Figs. 6.10i–v. They stand in comparison with the laser–pulse induced veraged kinetics shown in Fig. 6.8a–d. As suggested, better agreements are now observed for all types of initial ansatzes. The rapid oscillation are smoothed by means of the averaging and the kinetics become less sensitive to the exact energetic position of the initial state. Of course, the laser–pulse action still populates an energetically distinct wave packet of interface eigenstates. However, this effect influences less critically the averaged kinetics.

Especially when preparing the energetically upper initial states, i.e., applying either $|\Psi(t=0)\rangle = |\bar{\Phi}_1\rangle \otimes |\Psi_0\rangle$ or $|\Psi(t=0)\rangle = |\bar{\Phi}_3\rangle \otimes |\Psi_0\rangle$ (see Figs. 6.10i and ii) leads to very good agreement with the $\bar{P}_{\mathrm{X}}$ and $\bar{P}_{\mathrm{CS}}$ from laser excitations with $\hbar\omega_L = 4.35$ and $\hbar\omega_L = 4.2$ eV in Figs. 6.8a and b, respectively. Beyond the initial laser–pulse excitation phase of about 200 fs, both prepared kinetics show remarkable identical population dynamics. Respectively, the computed CS efficiencies η_{CS} from the ansatzes $|\bar{\Phi}_1\rangle$ and $|\bar{\Phi}_3\rangle$ coincide very well within 1 % and 5 % deviation from the reference values from laser–pulse treatment. Nevertheless, as above the comparison of laser–pulse and ansatz–based kinetics worsens in the cases of $|\Psi(t=0)\rangle = |\bar{\Phi}_8\rangle \otimes |\Psi_0\rangle$ and $|\Psi(t=0)\rangle = |\bar{\Phi}_{19}\rangle \otimes |\Psi_0\rangle$ (see Figs. 6.10iii and iv against Figs. 6.8c and d). The $\bar{P}_{\mathrm{X}}$ and $\bar{P}_{\mathrm{CS}}$ still show clear influence of the particular initial ansatzes – although the results are improved with respect to the coherent single wave function dynamics.

Finally, the $\bar{P}_{\mathrm{X}}$ and $\bar{P}_{\mathrm{CS}}$ from the fifth ansatz with the prominent molecular excitation $|\Psi(0)\rangle = |\mathrm{LX}_{m=1}\rangle$ are depicted in Fig. 6.10v. The smoothed averaged kinetics unveils a very rapid CS process within the first 20 fs. A likewise abrupt initial process was not observed before in $\bar{P}_{\mathrm{X}}$ (for any photon energy or FX ansatz). It clearly manifests a wrong impression on the initial fs–kinetics at the interface and pronounces a critical feature of that one very frequently applied localized excitation ansatz. Especially, this latter observed disagreement represents an important result of general relevance.

6.8. Summary and Concluding Remarks

Photoinduced charge separation (CS) kinetics across a *para*–sexiphenyl (6P)/ZnO hybrid interface are investigated. An atomistic interface system is modeled based on parametrization from different ab–initio methods and semi–empirical approaches. It takes into consideration an outstanding number of more than 125000 electronic interface states. First, the available charge transfer excitons are analyzed in detail by a separate calculation of the interface absorption coefficient. Its inspection allows unraveling the optically addressable states and to judge the subsequent wave packet formation. Then, coherent wave packet kinetics are present. They are achieved by solving the time–dependent Schrödinger equation including laser–pulse excitations of femtosecond duration.

As a main finding, it is demonstrated that excitations in various energetic regions generally result in very different femtosecond kinetics. In particular, the participation of hybridized charge transfer exciton, which can be directly addressed by laser–pulses, as well as the formation of CS states via decay of Frenkel exciton (FX) wave packets at the interface are uncovered. Likewise complex interplays between FXs, with different energies and oscillator strengthes, and a huge number of CS states must also be generally anticipated at other molecule/semiconductor interfaces. The most efficient CS process originates here from the formation of a stable FX which realizes prominent molecular excitations close to the interface and at the same time provides sufficient oscillator strength. It was found that electron migration away from the interface is possible. However, within all executed simulation scenarios the hole stayed rather close to the interface.

It was another key challenge to demonstrate that simulations on photoinduced CS kinetics at the hybrid interface should be more carefully considered concerning the optical excitation process. As testified, only its direct inclusion can guarantee that the correct interface states are addressed. This is clearly shown here in direct comparson with results from different initial excited state ansatzes. It is a general feature of all organic/inorganic interface that the inorganic part offers an enormous number of conduction band–like states. If those contribute in the wrong way, as it is the case under condition that an initial state is constructed by an expansion of pure FXs (or single molecular excitations) in the interface eigenstates, very misleading data concerning the CS must be anticipated.

Finally, it is discussed that additional accounting for energetic disorder is only of minor influence on the laser–pulse induced wave packet dynamics. However, the computations give message on partly better performance of initial ansatzes when ensemble averaged. Thereby, less critical disparity of the ensemble averaged data is found for ansatzes of the energetically upper FXs. In the lower band region, still very inaccurate data are obtained with the initial ansatzes.

Together with the simulations executed in Chap. 5, the presented discussion enlightens the fundamental aspects of the hybrid *para*–sexiphenyl/ZnO interface. The occuring optoelectronic processes are explained in a very detailed picture. In direct comparison, the mechanism of CS appears somewhat faster than the direct FX decay via excitation energy transfer from the 6P aggregate to the ZnO cluster.

7. Dissipative Hole Motion at the *para*–Sexiphenyl/ZnO Nano–Interface

Special emphasis is recently put on the investigations of charge separation kinetics at a diversity of organic/inorganic interface structures. Especially the process of free charge carrier generation is a hot topic. In this chapter, dissipative hole migration after a fast charge separation mechanism at the para–sexiphenyl (6P)/ZnO interface is studied. Parts of the following study were published in Refs. [140] and [205].

It is the intention to generally clarify whether the generated hole in the 6P aggregate can move away from an opponently created electron at the 6P surface. While the very initial interface kinetics are studied in Chap. 6, this process essentially takes place on the picosecond time–scale. The central issues is thereby the mutual Coulomb attraction between both charges. The presented simulations concentrate on the influence of dissipation on the moving hole. The opponent excess electron is immobilized at the surface of the ZnO slab. In fact, fast trapping of injected electrons is a typical finding at ZnO surfaces. Here, several simulations are prepared starting each from different characteristic electron and hole configurations.

The here employed interface model describes a huge film–like assembly of 2553 molecules standing upright on a macroscopic ZnO surface. A combination of different theories allows parameterizing an interface model which is both very realistic and extremely cheap. On one side, the intermolecular hole transfer integrals and the atomic partial charges for the molecular hole are determined on the DFT level. On the other side, atomic partial charges for the immobilized electron are introduced phenomenologically and the remaining neutral parts of the interface are taken into consideration via a polarizable continuum ansatz. The special formulation of the latter is the key point of the entire interface model. By its mean, the total interaction energy of the moving hole appears as a single electron–hole Coulomb term attributed with a constant screening factor.

The designed hole transfer system is then coupled to a bath of intramolecular vibrational modes. Non–Markovian open system dynamics are performed. The executed simulations are pioneering and incorporate an outstanding number of states. The own stochastic Schrödinger equation technique is demonstrated as a powerful instrument in application to systems of thousand states and more. Hole migration at room temperature are directly compared with related coherent wave packet motion of the hole at the interface. Their confrontation illustrates impressively the dominant character of dissipative effects when going beyond propagation times of 1 ps. The presented simulations provide further important insights into the 6P/ZnO interface considered as a photovoltaic material.

7.1. Background and Motivation

The development of organic/organic (i.e., bulk hetero junctions) and organic/inorganic hybrid materials for optoelectonics goes on in a continuous process of searching and understanding. Todays achievements are the result of yesterdays research and vice versa stimulate tomorrows research again. Especially the processes of charge separation (CS) up to free charge carrier generation find huge experimental interest concerning bulk hetero junctions [73, 97, 29] and extended molecular layer/semiconductor interfaces [1, 15, 14, 183] (for details, see also Sec. 6.1). Thereby, the two sub processes of i) charge transfer exciton formation, and ii) its dissociation into an electron and a hole (separated to both sides of the interface) are of central importance.

Besides measurements, meanwhile a huge number of computer simulations were performed on CS and the generation of free charge carriers in different types of bulk hetero junctions [81, 85, 206, 83, 84, 98, 207, 99, 192]. These works resulted from a diversity of methodologies and simulation techniques. The additional incorporation of the complex interaction with vibrational dynamics became possible, e.g., based on master equation approaches and rate models [81, 85, 206, 82, 99], by using multi–configuration time–dependent Hartree technique [83, 84, 98] or by nonadiabatic Ehrenfest dynamics [207]. Together these works pose the question about the best way of treating the underlying quantum dynamics in nanoscopic molecular/semiconductor interfaces. As discussed in Chap. 1, the mixing of organic and semiconductor components gives rise to challenging conceptual issues and the related computational approaches become highly demanding. Moreover, the number of relevant electronic states at such interfaces increases dramatically when turning to nanoscale structures and common ansatzes for vibronic quantum dynamics are generally very inefficient. Accordingly, most time–domain simulations to date concentrate on hybrid interfaces which can be approximately treated in terms of small periodic simulation cells and so approached with the method of ab–initio nonadiabatic molecular dynamics (see, e.g., Refs. [208, 34] and Chap. 1).

In order to describe dynamics including vibrational effects in finite and more expansive systems (with thousands of states), it needs for other techniques. Lately, Zhao et al. [49, 50, 51] suggested an alternative very promising approach based on a quantum state diffusion method. They described hot exciton relaxation [51] and charge carrier migration [49, 50] in a chain–like 1D molecular system of intermediate size. By that, it was demonstrated that with the quantum state diffusion method, in principle, dissipative quantum dynamics upon more than 100 states can be mastered. Motivated by these very promising findings, an own technique of the quantum state diffusion for large–scale application is specially developed in the framework of this thesis. Its basics and the implementation based on a non–Markovian stochastic Schrödinger equation (SSE) is explained in Chap. 4. Now, the power of the developed algorithm is demonstrated in direct application.

The present work joins the studies on the 6P/ZnO interface [68, 64] concerning excitation energy transfer (see Fig. 1.3a) and photo–induced CS kinetics (see Fig. 1.3b and c) discussed in Chaps. 5 and 6, respectively. As sketched in Fig. 1.3b and c, the CS process at the 6P/ZnO interface takes place in form of electron injection from excited 6P molecules across the interface into the ZnO substrate. It leaves behind a

hole charge in the 6P aggregate. This chapter is devoted to the subsequent long–term process of Coulomb–correlated electron and hole motion. Thereby, a very realistic type of 6P system architecture is employed. Directly inspired by recent TEM imagings [63, 68, 64, 65], it describes a monolayer of upright standing 6Ps which are assembled in a herringbone lattice (see also Fig. 1.2c), here consisting of a number of 2553 molecules.

In Chap. 6, an uniform model for simultaneous electron and hole motion at a 6P/ZnO interface is introduced. It is demonstrated that the total number of states (i.e., the product $N_e \times N_h$, where N_e and N_h are the numbers of possible electron and hole states, respectively) becomes truely vast when nanoscale systems are considered. This applies in particular in cases of semiconductor structure where usually N_e is already very large (see Sec. 6.2). In Chap. 6, the particular focus is on ultrafast coherent kinetics and many ten thousands of states can be handled. Now, picosecond dynamics are aspired and the inclusion of dissipative effects is the top priority. For this purpose, an uniform model is very inappropriate. Instead, the emphasis is put here directly on scenarios of ultrafast initial electron injections and subsequent electron immobilization at the ZnO interface. This type of "electron trapping" mechanism is a well–known phenomenon of ZnO substrates [34, 70]. (A likewise stable electron accumulation, e.g., is also monitored in Chap. 6 on the time–scale below 100 fs, cf. Fig. 6.7b). Here, it means a welcome computational advantage. Indeed, due to the immobilization, the electron plays not an active role on the picosecond time–scale, so it can be approximately incorporated by means of phenomenological initial state ansatzes. Only the much slower evolution of the hole (step 4 in Fig. 1.3b) has to be simulated.

In terms of Coulomb interaction, the hole feels attracted to the opponent electron. The latter is rendered phenomenologically by a static and somewhat delocalized 3d Gaussian distributed ($-1e$ totally charges) density. It is expected that this "underlying" potential energy surface characterizes basically the dissipative migration behavior of the hole within the 6P layer [84, 82, 73, 97, 207]. For computing site–dependent hole energies, atomic centered partial charges are introduced for the hole on a 6P molecule and for the electron charge density at the ZnO surface. While the former can be straightly obtained from standard DFT methods, the latter are part of the phenomenological electron ansatz. Besides the direct interaction energy between electron and hole, also the distinct interface surrounding of the two charge distributions must be modeled. Thereby, it is the intention to circumvent a single–particle treatment of the macroscopic ZnO substrate, which would be much too expansive (even based on a semi–empirical DFTB treatment as applied in Chaps. 5 and 6). Therefore, a polarizable continuum model is introduced at this place. It is specially developed as an essential part of this work. Accordingly, the concrete atomistic surrounding of the electron and hole is "smeared" to two dielectric half spaces extending to both sides of the interface. The atomistic picture of the hole and electron is kept while the entire surrounding can be condensed into a constant analytic screening factor. This combination of methodologies makes possible an extremely large–scale but still very realistic transfer model.

The hole transfer system is then simulated as an open quantum system coupled to a heat bath. Here, the 6P molecules are packed rather stiff in a herringbone structure and only intramolecular vibrational modes are incorporated in the bath model. The

simulations are started from different initial electron and hole positionings. In a first scenario, the electronic density is placed adjacent to the 6P molecule which initially hosts the hole. A second and third simulation run starts from rather remote electron and hole constellation with positions shifted along perpendicular directions, respectively. Such remote constellations would result when the fast electron trapping is accompanied with lateral movement.

The presented non–Markovian hole dynamics contains all 2553 molecules of the layer. They are of pioneering character and demonstrate the great efficiency of the own developed stochastic Schrödinger equation technique. So far, comparable simulations of picosecond dynamics with non–Markovian memory effects have been limited to systems of several ten states up to $N = 150$ (see, e.g., Refs. [51, 52]). Vice versa, simulations of likewise gigantic systems (and even larger) have been found in literature only in application of less comprehensive ansatzes. For instance in Ref. [54], Aspuru-Guzik et al. reported on exciton transfer in gigantic chromophore complexes based on the Kubo–Anderson model. In contrast to the present approach, this method can only account for classical Markovian type of system–bath interaction. Moreover, the very basic model of Haken, Strobl and Reinecker [195, 196] has been employed a lot (see, e.g., Refs. [197, 209, 54]). Even more limited, the latter only describes dephasing while dissipative effects are completely excluded. Alternative and very popular wave function based schemes are the Ehrenfest dynamics or the Monte–Carlo wave function approach. The former incorporates nuclear vibrations in terms of classical equations of motion. It was for instance applied in Ref. [55] to a supramolecular complex with 450 molecular states. The Monte–Carlo wave function method basically unravels dissipative Markovian kinetics of Lindblad–type and was used, e.g., in Ref. [53] for simulations with about 2600 states.

Thanks to the computationally cheap methodology, comprehensive insigths into the hole migration are obtained. Additionally, the corresponding purely coherent hole motion (i.e., wave packet motion obeying the ordinary Schrödinger equation) without decoherence and dissipation effects is computed. The loss of quantum character due to the dissipative action is then impressively exhibited by confronting the room temperature dynamics with the coherent dynamics. The close reference to experimental set–ups makes the discussed results very interesting and concrete statements related to earlier measurements on polymer/ZnO systems [72] are possible.

7.2. Overview on System and Study

An overview on the utilized 6P/ZnO interface achitecture is provided in Fig. 7.1. The 6P aggregation on flat ZnO surfaces is basically enlightened thanks to intensive TEM imaging and other experimental investigations during the last years [64, 68, 65]. In particular, it was uncovered that 6P molecules are subject to self–assembly when deposited on polished ZnO surfaces. With increasing molecular coverage on the (0001) ZnO sectional plane, e.g., initial flat–lying 6P arrange to such up–right standing kind of colonies depicted in Fig. 7.1b and d. Within the layer, the 6P arrange in so–called herringbone lattice structure (see Fig. 7.1c). In course of on–going aggregation, monolayered aggregates grow also to likewise 3d multilayer structures [65]. Nevertheless, the

Figure 7.1.: The *para*–sexiphenyl (6P)/ZnO interface system. Panel a: Chemical structure of the 6P molecule. Panel b: Top view on the 2553 upright standing 6P molecules aggregated to a circular monolayer with a radius of about 15 nm. Panel c: Regular herringbone lattice. Panel d: Side view on the layer.

initially created monolayer is the main concern of the present study.

The regularity of the 6P herringbone aggregation of the monolayer colonies is very similar to the one found in gas phase. Only minor distinctions owing to the contact to the ZnO substrate can be made out [64, 65, 71]. Therefore, the present layer is conveniently constructed by borrowing parameters from an unit cell which is actual defined for 6P crystal formation [210, 68, 64]. (The latter was determined via a geometry optimizations on using DFT and shows adequate agreement with experimental observations.) After construction, the 2d layer is finally placed on a wutzite ZnO(0001) surface under condition that van der Waals contact distance is satisfied (see Fig. 7.1d). The ZnO lattice is assumed to fill the entire half space opponent to the 6P aggregate. This describes typical macroscopic experimental system set–ups. To model the neutral charged ZnO substrate, a polarizable continuum ansatz is introduced in Sec. 7.3.4. Due to that, the lateral (in the $x - y$ plane) positioning of the film is irrelevant. The lattice structure of the ZnO is only employed for later describing the localization of the particular excess electron (see Sec. 7.3.4).

7.3. Modeling the Electronic Interface System

An open system dynamics approach represents the proper framework for simulating the dissipative hole motion. According to Sec. 3.3, then the electron–vibrational Hamilto-

nian of the interface system follows as, cf. Eq. 3.6,

$$\hat{H} = \hat{H}_{\mathrm{HT}} + \hat{H}_{\mathrm{B}} + \hat{H}_{\mathrm{HT\text{-}B}}. \tag{7.1}$$

The first term of $\hat{H}$ represents the Hamiltonain of the hole transfer system, $\hat{H}_{\mathrm{HT}}$. The second term in Eq. 7.1, $\hat{H}_{\mathrm{B}}$, symbolizes the Hamiltonian of the surrounding bath of nuclear vibrations and the third term, $\hat{H}_{\mathrm{HT\text{-}B}}$, collects the vibronic interaction of the latter with the hole transfer system. In Secs. 7.3.1 and 7.3.2, charge–separated interface states are constructed to describe the hole (in the 6P aggregate) in presence of an immobilized electron (in the ZnO slab). Based on these states, the $\hat{H}_{\mathrm{HT}}$ is specified (see Secs. 7.3.3–7.3.5). The Hamiltonians $\hat{H}_{\mathrm{B}}$ and $\hat{H}_{\mathrm{HT\text{-}B}}$ are considered in Sec. 7.4.

7.3.1. The immobilized excess electron

The energetic region close to the band edge is of substantial interest in experiment and theory whenever fast electron relaxation within the CB takes place by electron–phonon interaction processes. It is a characteristic feature of finite ZnO (wurtzite) structure that the energetically lowest CB states (which form the band edge) are spatially localized at the surface of the structure (see, e.g., Refs.[94, 34, 66]). Accordingly, in the present case a manifold of *surface states* must be expected at the interface region exposed to the 6P film. In a scenario of efficient electron–phonon coupling, the injected CB electron is barely able to penetrate the ZnO bulk zone. Instead, it relaxes swiftly and stays at the interface where it becomes immobilized immediately after its injection. Recent simulations [34] and related experimental investigations [94, 66] gave evidence on such *surface trapping* mechanisms at ZnO surfaces.

For this purpose, the state $|\Psi^{-}_{\mathrm{trap}}\rangle$ is introduced in Sec. 2.3.5 (see Eq. 2.53). It describes the charge distribution of an immobilized (or *trapped*) excess electron according to the state, cf. Eq. 2.53,

$$|\Psi^{-}_{\mathrm{trap}}\rangle = \sum_{a}^{N_{\mathrm{CB}}} C_a^{(\mathrm{trap})} |\Psi^{-}_{a}\rangle, \tag{7.2}$$

which expresses a superposition of all available anionic ZnO states $|\Psi^{-}_{a}\rangle$ (attributed with expansion coefficients $C_a^{(\mathrm{trap})}$). As explained in Sec. 2.2.3 (see Eq. 2.16), each $|\Psi^{-}_{a}\rangle$ represents an anionic cluster state where a single excess electron is "added" to the CB–like state $\bar{\psi}_a$ (with respect to the TB ground state configuration). By means of the coefficients in Eq. 7.2, therefore, a respective localized appearance of the immobilized excess electron within the CB can be straightly tailored.

7.3.2. The hole transfer states

Besides the electron trapping, also the modeling of the hole in the molecular aggregate is detailed described in Sec. 2.3.5. It assumes zero wave funtion overlap between the molecules and the molecules and the ZnO substrate (see also Sec. 6.2). According to the diabatization scheme introduced with Eq. 2.18, the interface states are then constructed as direct products of individual site states.

The interface states which represent a localized hole (LH) follow then in terms of the specially constructed charge–separated states, cf. Eq. 2.52,

$$|\mathrm{LH}_m\rangle = |\bar{\Phi}_m^+\rangle \times |\Psi_{\mathrm{trap}}^-\rangle = |\Phi_{\mathrm{cat}}^{(m)}\rangle \prod_{n\neq m}^{N^{6\mathrm{P}}} |\Phi_g^{(n)}\rangle \times |\Psi_{\mathrm{trap}}^-\rangle. \tag{7.3}$$

In abbreviated notation, $|\mathrm{LH}_m\rangle$ indicates the interface realizing a localized hole on the mth 6P site and the electron immobilized in the ZnO slab. Correspondingly, it contains the $|\Phi_{\mathrm{cat}}^{(m)}\rangle$ (giving the cationic state of the mth 6P) and the product of $N^{6\mathrm{P}}-1$ states $|\Phi_g^{(n)}\rangle$ with $n \neq m$ (of the other neutral 6Ps). Furthermore, the charged ZnO slab is represented by the state $|\Psi_{\mathrm{trap}}^-\rangle$ which realizes the *trapped* electron (see Eq. 7.2).

7.3.3. Hole transfer Hamiltonian

The coherent part of the hole dynamics obeys the hole transfer Hamiltonian, $\hat{H}_{\mathrm{HT}}$. In general, the latter is intensively discussed in Sec. 2.3.5. Utilizing the states Eq. 7.3, here the hole transfer Hamiltonian specifies to, cf. Eq. 2.51,

$$\hat{H}_{\mathrm{HT}} = \sum_{m}^{N^{6\mathrm{P}}} \mathscr{E}_m |\mathrm{LH}_m\rangle\langle \mathrm{LH}_m| + \sum_{m<n}^{N^{6\mathrm{P}}} \Big(\mathscr{V}_{mn}^{\mathrm{HT}} |\mathrm{LH}_m\rangle\langle \mathrm{LH}_n| + \mathrm{H.c.} \Big). \tag{7.4}$$

The diagonal element $\mathscr{E}_m$ gives the energy of the interface system when the hole is localized on the mth 6P molecule and the $\mathscr{V}_{mn}^{\mathrm{HT}}$ represents the different intermolecular hole transfer integrals. The latter let move the hole from the nth to the mth 6P (see Sec. 7.3.5). As typically, the interface ground state energy plus the single 6P (gas phase) ionization energy is shifted to zero (without changing the upcoming hole kinetics). Therefore, the $\mathscr{E}_m$ should be interpreted rather in terms of a site–specific hole energy (see Eq. 7.5). It only holds interaction terms of the hole with the surrounding 6Ps and the opponent $(-1e)$ charged ZnO slab.

7.3.4. Interaction energies in a polarizable continuum model

In Sec. 2.3.5, the general ansatz for electrostatic interaction energies in situation of CS is considered elaborately. In Chap. 6, it is utilized to introduce electrostatic interaction energy shifts and to simulate ultrafast CS processes at another 6P/ZnO system (see $\mathscr{E}_{ma}^{\mathrm{CS}}$ in Eq. 6.5).

By shifting constant energy terms to zero, for the present purpose, the electrostatic shift simplifies to, cf. Eqs. 2.47 and 2.54,

$$\mathscr{E}_m = \tag{7.5}$$
$$\int d^3\mathbf{x} d^3\mathbf{y} n_{\mathrm{h}}^{(m)}(\mathbf{x}) \frac{1}{|\mathbf{x}-\mathbf{y}|} \Big[\sum_{n\neq m}^{N^{6\mathrm{P}}} (n_g^{(n)}(\mathbf{y}) + \sum_{\mu} Z_\mu^{(m)} \delta(\mathbf{y} - \mathbf{R}_\mu^{(m)})) + \Omega(\mathbf{y}) + \rho_{\mathrm{e}}^{(\mathrm{trap})}(\mathbf{y}) \Big].$$

The charge densities of the hole on the mth 6P and the immobilized electron are conveniently introduced as $n_{\mathrm{h}}^{(m)}(\mathbf{x}) = n_{\mathrm{cat}}^{(m)}(\mathbf{x}) - n_g^{(m)}(\mathbf{x})$ and $\rho_{\mathrm{e}}^{(\mathrm{trap})}(\mathbf{y}) = \sum_a |C_a^{(\mathrm{trap})}|^2 \bar{\rho}_a(\mathbf{y})$

Figure 7.2.: Polarizable continuum model of hole and electron at the interface. Panel a: Side view on the interface profile. The light blue and red half space represents the dielectric continua related to the 6P aggregate and ZnO substrate, respectively. Red colored atomic centered partial charges related to the immobilized electron are indicated (dark hues indicate higher absolute values). Similarly, blue colored atomic charges of a hole localized on a certain 6P are added. Yellow colored atoms describe the each generated image charges. The arrows visualize the interactions, which are relevant in the image charge model (dashing) and the effectively resulting one (blue). Panel b: Potential energy well related to hole motion in the aggregate. Each tile represents an individual 6P site. Coloring (see scale) and vertical positioning gives the related site energies $\mathscr{E}_m^{\mathrm{PCM}}$ according to Eq. 7.6.

(see Eq. 7.2), respectively. According to Eq. 6.5, the $\bar{\rho}_a(\mathbf{x})$ gives again the charge density of the excess electron (in CB state $\bar{\psi}_a$). Together, the hole interacts with the surrounding 6Ps in ground state configuration (via density $n_g^{(n)}(\mathbf{x}) + \sum_\mu Z_\mu^{(m)} \delta(\mathbf{x} - \mathbf{R}_\mu^{(m)})$, see Eq. 2.47), the neutral ZnO in ground state configuration and the immobilized excess electron in the *trapped state* (via density $\Omega(\mathbf{y})$ plus the single–electron density $\rho_{\mathrm{e}}^{(\mathrm{trap})}(\mathbf{y})$, cf. Eq. 2.54).

In practice, the realization of Eq. 7.5 requires explicit electronic structure calculation of the ZnO part. Due to the size of the present ZnO slab, this describes an ultimate computational task which is beyond the scope of the thesis (even in application of the DFTB scheme). Instead, an approximate polarizable continuum model is specially developed for the 6P/ZnO interface in order to determine interaction energies $\mathscr{E}_m$. The model is computationally extremely cheap and introduces a truly macroscopic picture of the neutral interface structure. Only the particular hole and electron interaction is treated in atomistic resolution.

As indicated in Fig. 7.2a, two different dielectric half spaces are set up with a plane interface in between. They describe each the neutral 6P aggregate and ZnO substrate

and are attributed with the dielectric constants ϵ_{6P} and ϵ_{ZnO}, respectively.[1] Further, the continuous distribution of the hole on the mth 6P is substituted by a set of discretized partial charges according to $n_h^{(m)}(\mathbf{x}) \approx \sum_m \mathbb{Q}_h(\mathbf{R}_\mu^{(m)})\delta(\mathbf{x}-\mathbf{R}_\mu^{(m)})$. The latter are placed on the actual atomic positions $\mathbf{R}_\mu^{(m)}$, embedded in the aggregate–related dielectric half space (dark blue colored atoms in Fig. 7.2a). The $\mathbb{Q}_h$ for the 6P structure are straightly obtained from standard DFT routines (see Appendix G.1). In similar way, the charge density of the immobilized electron is replaced by another set of discretized partial charges, $\rho_e(\mathbf{x}) \approx \sum_j \mathbb{Q}_e(\mathbf{R}_j^{(ZnO)})\delta(\mathbf{x}-\mathbf{R}_j^{(ZnO)})$. They are centered in the opponent dielectric half space (pink colored atoms in Fig. 7.2a) on the atomic positions $\mathbf{R}_j^{(ZnO)}$ of the underlying ZnO(0001) lattice. It is the idea to avoid electronic structure calculations of the ZnO slab and to introduce the $\mathbb{Q}_e$ in a phenomenological way. For the sake of convenience, they are simply defined in terms of a discretized Gaussian distribution with standard deviations of $\sigma_x = \sigma_y = 10$ Å, and $\sigma_z = 5$ Å along the x, y and z axis, respectively. The level of brightness of the pink atoms in Fig. 7.2a gives an impression on the extent of the electron charge cloud. Its center is chosen centrally with respect to the circular 6P layer and placed 5 Å below the ZnO surface.

Now, the above interaction energies $\mathscr{E}_m$ (introduced in Eq. 7.5), are replaced by expressions $\mathscr{E}_m^{PCM}$ achieved from the sketched continuum model. For this purpose, here the principle of the *image charge effect* [211] was utilized. It was generalized and applied on the present situation of two entire sets of charges (for a detailed derivation, see Appendix C). The relevant interactions are indicated by the arrows in Fig. 7.2a. The set of physical hole charges (dark blue; in the 6P half space) interact with the set of physical electron charges (pink; in the ZnO half space), and with the set of image charges created by itself (yellow; also in the ZnO half space). For the total electrostatic energy, vice versa, terms of interaction between the set of physical electron charges (pink) and its image charges must be added (yellow; in the 6P half space). Each contribution is attributed with a characteristic screening factor (see Appendix C) and as the result, the $\mathscr{E}_m^{PCM}$ is found in terms of the remarkably simple expression

$$\mathscr{E}_m^{PCM} = \sum_\mu \sum_j \epsilon_{eff}^{-1} \frac{\mathbb{Q}_h(\mathbf{R}_\mu^{(m)})\mathbb{Q}_e(\mathbf{R}_j^{(ZnO)})}{|\mathbf{R}_\mu^{(m)} - \mathbf{R}_j^{(ZnO)}|}. \tag{7.6}$$

The interaction energy is condensed to a single hole and electron interaction term, where the presence of the dielectric surrounding leads to the appearance of the effective screening factor

$$\epsilon_{eff}^{-1} = \frac{\epsilon_{6P}/\epsilon_{ZnO} + \epsilon_{ZnO}/\epsilon_{6P}}{\epsilon_{6P} + \epsilon_{ZnO}}. \tag{7.7}$$

For practical realization, the values of $\epsilon_{6P} = 3.0$ and $\epsilon_{ZnO} = 8.5$ were utilized giving an effective dielectric constant of $\epsilon_{eff} = 3.61$. The computed values of $\mathscr{E}_m^{PCM}$ are rendered

[1] The model assumes both parts to extend uniformly upon the entire half space. While it seems an adequate assumption for the ZnO slab, it means a certain degree of approximation concerning the actual discoidal type of 6P aggregation. The model would be very realsitic, however, regarding a much larger multilayer design.

Figure 7.3.: Hole transfer in the *para*–sexiphenyl herringbone aggregate. The arrows exemplarily indicate the three different molecular nearest neighbor pairs with considerable intermolecular hole transfer couplings. Colorings and number labels are refered in the main text. The remaining (further remote) pair configurations are not relevant.

in Fig. 7.2b against the localization of the mth 6P in the layer with $N_{6P} = 2553$. As expected, it describes a 2d potential energy well. The hole localization with smalles potential energy is in the center of the disk (in closest distance to the immobilized electron). For further convenience, in practice this minimum energy value was shifted to zero. When localized at the outer edge of the 6P film, the hole carries the potential energy of about +0.14 eV.

7.3.5. Hole transfer integrals

The offdiagonal matrix elements of H_{HT} (see Eq. 7.4) describe the hole transfer integrals $\mathscr{V}_{mn}^{\mathrm{HT}}$. As discussed also in Sec. 6.2.3, charge transfer integrals decay exponentially with increasing intermolecular distance. The $\mathscr{V}_{mn}^{\mathrm{HT}}$ is therefore restricted to nearest neighbored 6Ps. This is a very typical assumption (see, e.g., Refs. [84, 212, 191, 52]). Due to the regularity of the herringbone lattice, hole transfer in the 2d monolayer can be essentially described by the three dimer configurations depicted in Fig. 7.3. In own earlier attempts published in Refs. [140, 205], first estimates of $\mathscr{V}_{mn}^{\mathrm{HT}}$ were obtained by employing the *energy splitting in dimer* technique [199] (see also Sec. 6.2.3 and the Appendix G.1). Using this simple method, a moderate coupling strength were estimated for dimer configuration 1 (pink colored arrow in Fig. 7.3) of about $|\mathscr{V}_{mn}^{\mathrm{HT}}| = 20$ meV. The dimer configuration 2 (blue colored arrow in Fig. 7.3), however, resulted in a much stronger transfer coupling of $|\mathscr{V}_{mn}^{\mathrm{HT}}| = 240$ meV. For the present work, both transfer integrals were computed anew on the DFT level with the state–of–the–art *projection methodology* of Andrienko et al. [213] and values of $\mathscr{V}_{mn}^{\mathrm{HT}} = -20$ meV for configuration 1 and -8.0 meV for configuration 2 were determined (for details, see Appendix G.1). For configuration 3, finally an even smaller value of about $\mathscr{V}_{mn}^{\mathrm{HT}} = -0.3$ meV was observed,

which demonstrates the critical dependence of $|\mathscr{V}_{mn}^{\mathrm{HT}}|$ on the intermolecular distance.

The essentially different value uncovered for configuration 2 (correcting the former estimate based on the *energy splitting in dimer* technique) is explained by means of the very asymmetrical orientation of the 6P pairs (see again blue arrow in Fig. 7.3). Due to that, the two electronic monomer structures polarize each other very asymetrically [200]. While the *projection method* particularly takes into account this effect [213], the *energy splitting in dimer* technique is well–known for its suffering from that [200].

7.4. The Vibronic Interaction Model

The hole transfer system is treated as an open system coupled to a nuclear vibrational bath (see Eq. 7.1). The bath is descibed by the Hamiltonian $\hat{H}_{\mathrm{B}}$ and the $\hat{H}_{\mathrm{HT\text{-}B}}$ describes the system–bath (or vibronic) interaction part. As moticated in Sec. 7.1, the present bath model incorporates exclusively intramolecular modes of the 6Ps. The harmonic oscillator ansatz for vibronic interaction models is already introduced as part of the general discussion in Sec. 3.3.3. Accordingly, the bath Hamiltonian can be written as, cf. Eq. 3.12,

$$\hat{H}_{\mathrm{B}} = \sum_{m,\xi} \hbar\omega_{m\xi} \hat{b}_{m\xi}^{\dagger} \hat{b}_{m\xi}. \tag{7.8}$$

Each 6P molecule m is characterized by an individual set of intramolecular vibrational frequencies $\omega_{m\xi}$ and standard harmonic oscillator ladder operators, $\hat{b}_{m\xi}$ and $\hat{b}_{m\xi}^{\dagger}$. Further, the model relies on the assumption that the frequencies $\omega_{m\xi}$ are uniform for the molecular ground and the cationic states.

By means of $\hat{H}_{\mathrm{HT\text{-}B}}$, the nuclear vibrations can modify the hole transfer behavior. Making use of the bilinear coupling model, it specifies to, cf. Eq. 3.13,

$$\hat{H}_{\mathrm{HT\text{-}B}} = \sum_{m,\xi} \mathscr{K}_{m\xi} (\hat{b}_{m\xi} + \hat{b}_{m\xi}^{\dagger}) \hat{L}_m. \tag{7.9}$$

The $\mathscr{K}_{m\xi} = \hbar\omega_{m\xi} g_{\xi}(m)$ gives the coupling strength of the hole to the vibrational mode ξ of the mth 6P. The projector operator related to transfer system appears as

$$\hat{L}_m = |\mathrm{LH}_m\rangle\langle\mathrm{LH}_m|. \tag{7.10}$$

As introduced in Sec. 3.3.4 (see Eq. 3.16), the vibronic interaction of each 6P molecule is finally characterized by a spectral density $J_m(\omega)$. The latter is equivalently for all 6Ps (i.e., it is $J_m(\omega) \equiv J(\omega)$), since here exclusively intramolecular modes are considered. By computing the frequencies and nuclear displacements of the 6P normal modes for the optimized 6P molecular structure, in principle, sophisticated spectral forms of $J(\omega)$ could be generated. However, the 6P behaves very different in vacuum (or solution) than in the much stiffer herringbone lattice. In fact, the twisting motions of the six phenyl rings with respect to each other show prominent anharmonic features. That is a well–known critical issue of the 6P which makes standard methods for frequency analysis based on linear displacements intricate[135, 63, 214]. (Different ansatzes were

tried here giving altogether highly questionable results.) Consequently, for the present purpose it shall suffice to introduce a functional expression for $J(\omega)$ instead. The super–Ohmic model is utilized according to Appendix E (see Eq. E.4). Besides the Debye–Drude model (see Sec. 4.5.1), this type is implemented most frequently in practice for studying charge migration processes in conjugated molecular aggregates [44, 215, 53]. For parametrization of $J(\omega)$ (see Eq. E.4), an inverse cut–off frequency of $\omega_c^{-1} = 50$ fs and a reorganization energy of $\lambda = 0.1$ eV were chosen as a physically plausible values.

7.5. Modeling the Dissipative Quantum Dynamics

As generally discussed in Sec. 3.1, coherent wave packet propagation is only under certain conditions an appropriate instrument to simulate realistic systems. In Chap. 6, e.g., coherent dynamics are employed to investigate the response of the 6P/ZnO interface system to an ultrafast laser–pulse on the femtosecond time–scale. In this work, however, the focus is put on hole kinetics in the intermediate regime. Features of coherence and at the same time energy dissipation and coherence dephasing play an important role (see Sec. 3.3). Accordingly, the hole transfer system must be studied in terms of an open system. In order to manage the desired large–scale transfer studies, priority is given to the stochastic Schrödinger equation (SSE) method. Its advantageous scaling behavior with increasing system size is generally introduced in Chap. 1 and further intensively debated in Chap. 4 (see Secs. 4.1, 4.4 and 4.6).

The SSE properly describes the behavior of the hole changing from ballistic (purely coherent) to diffusive (purely incoherent) type of motion. Here, it must be specified according to, cf. 4.58,

$$i\hbar\partial_t|\phi_z(t)\rangle = \Big(\hat{H}_{\mathrm{HT}} + \hat{\mathscr{F}}_z(t) + \hat{\mathscr{D}}(t;T=0)\Big)|\phi_z(t)\rangle, \tag{7.11}$$

including the parameterized hole transfer Hamiltonian, $\hat{H}_{\mathrm{HT}}$ (see Eq. 7.4). The quantum trajectory $|\phi_z(t)\rangle$ obeys a stochastic process introduced in terms of the stochastic force operator $\hat{\mathscr{F}}_z(t)$. (The z is treated as the index of stochastic force realizations and labels different solutions of Eq. 7.11.) The force decomposes into a number of $N_{6\mathrm{P}}$ independent molecular terms according to $\hat{\mathscr{F}}_z(t) = \sum_m \mathscr{F}_m(t;z)\hat{L}_m$. Each $\mathscr{F}_m(t;z)$ is accompanied by corresponding dissipative term $\hat{\mathscr{D}}_m(t)$. In Eq. 7.11, these enter via the action of the damping operator $\hat{\mathscr{D}}(t) = \sum_m \hat{\mathscr{D}}_m(t)$. (Details on the numerical integration of Eq. 7.11 are given in Appendix H.2.2.)

During the test simulations on the FMO complex in Sec. 4.5, the influences of $\hat{\mathscr{D}}(t)$ on the numerical performance of the linear SSE based on the approximate propagation scheme 4.66 is probed concerning the two proposed types of damping terms (see Eqs. 4.35 versus 4.41). Since no essential differences can be noted, the somewhat more convenient damping operator Eq. 4.41 is further utilized here. It follows as,

$$\hat{\mathscr{D}}(t;T=0) = \frac{2}{\hbar^2}\int_0^t d\tau J(\tau)\hat{L}_m\hat{L}_m(-\tau), \tag{7.12}$$

based on the Fourier transform of the spectral density $J(t)$ and the hole projectors $\hat{L}_m$

(introduced in Eq. 7.10).

In Sec. 4.5, furthermore the dependence of the numerical performance of the SSE on two different noise algorithms for $\mathfrak{F}_m(t;z)$ are inspected (see Eqs. 4.59 and 4.69). For the sake of clarity, they shall be distinguished further on as $\mathfrak{F}_m^{(1)}(t;z)$ and $\mathfrak{F}_m^{(2)}(t;z)$. The $\mathfrak{F}_m^{(1)}(t;z)$ reads, cf. Eq. 4.59,

$$\mathfrak{F}_m^{(1)}(t;z) = \sum_k^K \sqrt{\frac{\Delta\omega J(\omega_k)}{\pi}} \Big(\sqrt{[(1+n(\omega_k)]} W_{mk}^{(z_+)} e^{i\omega_k t} + \sqrt{n(\omega_k)} W_{mk}^{(z_-)} e^{-i\omega_k t} \Big), \quad (7.13)$$

based on $J(\omega)$ and the Bose–Einstein distribution $n(\omega)$. Both appear in Eq. 7.13 as parts of the reservoir correlation function $C^+(\omega_k)$ and $C^-(\omega_k)$ (see Eq. 4.37). The stochastic character of $\mathfrak{F}_m^{(1)}(t;z)$ arises from the two matrixes $W^{(z_+)}$ and $W^{(z_-)}$. Their matrix elements are independent complex–valued and Gaussian distributed random numbers (for convenient notation, the index z subdevided into z_+ and z_-, cf. Eq. 4.59).

The second algorithm, $\mathfrak{F}_m^{(2)}(t;z)$, is based on the expression Eq. 4.69. In the present case, it specifies to

$$\begin{aligned} \mathfrak{F}_m^{(2)}(t;z) = \sum_k^K \sqrt{\frac{\Delta\omega J(\omega_k)}{\pi}} \Big(& \sqrt{\coth(\frac{\hbar\omega_k}{2k_{\mathrm{B}}T}) + \sinh(\frac{\hbar\omega_k}{2k_{\mathrm{B}}T})^{-1}} \cos(\omega_k t + \zeta_{mk}) \\ & + i \sqrt{\coth(\frac{\hbar\omega_k}{2k_{\mathrm{B}}T}) - \sinh(\frac{\hbar\omega_k}{2k_{\mathrm{B}}T})^{-1}} \sin(\omega_k t + \zeta_{mk}) \Big). \end{aligned} \quad (7.14)$$

The $\{\zeta_{mk}\}_z$ represents a set of random numbers, which are now uniformly distributed over the interval $[0, 2\pi]$. In $\mathfrak{F}_m^{(2)}$, the Bose–Einstein distribution is defactorized and appears in form of the two temperature–dependent exponential fraction terms in Eq. 7.14. Numerical details on the random number generation are provided in Appendix H.2.2.

Once a set of $\mathcal{N}$ different solutions of Eq. 7.11 is computed, the reduced density operator is obtained according to Eq. 4.60, i.e., after performing the simple averaging process, $\hat{\rho}(t) = \sum_z |\phi_z(t)\rangle\langle\phi_z(t)|/\mathcal{N}$. Respective density matrix elements, e.g., the probability $P_m(t)$ to find the hole (at time t) localized on the mth 6P molecule are given by

$$P_m(t) = \frac{1}{\mathcal{N}} \sum_z \langle \mathrm{LH}_m|\phi_z(t)\rangle\langle\phi_z(t)|\mathrm{LH}_m\rangle. \quad (7.15)$$

The time–evolution of $P_m(t)$ is of particular interest in the upcoming studies. In the subsequent Sec. 7.6, the numerical validity of the linear SSE is validated for several 6P layers of increasing size. In Sec. 7.7, the 6P layer with 2553 6Ps is finally investigated.

7.6. Hole Motion in Small to Medium *para*–Sexiphenyl Aggregates

This section is dedicated to a discussion on hole motion in discoidal 6P clusters of different radii ranging from small to intermediate sizes. The studied 6P disks consist

of $N_{6P} = 7$, 19, 27, 35 and 59 molecules, respectively. Thereby, it is the intention to approve the workability of a linear SSE algorithm based on the approximate propagation scheme 4.66. As discussed throughout Secs. 4.4–4.6, its advantageous scaling of computational costs with increasing system size is darely paid with numerical difficulties which might lead to inaccurate results. In Sec. 4.6, a strategy is proposed which helps to properly quantify that error. It is particularily suited for the present scalable 6P layer.

7.6.1. Strategy

It is the idea to compute the hole kinetics of the five clusters (from $N_{6P} = 7$ to $N_{6P} = 59$) along three different lines. Two of them are simulated using the linear SSEs 7.11 with the scheme 4.66 (one with $\mathcal{F}_m^{(1)}(t;z)$ and the other with $\mathcal{F}_m^{(2)}(t;z)$). In the third run, the nonlinear SSE algorithm is applied which delivers numerically exact results (as discussed with Eq. 4.62). In comparison with data from the nonlinear algorithm, the former two linear approaches can be properly evaluated. If the quality of their results improves or does not decline (when increasing the aggregate size from $N_{6P} = 7$ to $N_{6P} = 59$), its workability can also be rendered to larger aggregates. In Sec. 7.7, the force generation which leads to better performance shall then be applied to the gigantic layer with $N_{6P} = 2553$.

7.6.2. Performance tests

All simulations are executed at room temperature. The hole is initially placed at the lower border of the aggregate (see blue spots in the sketched aggregates in Figs. 7.4 and 7.5). In this initial localization, the hole is each furthest from the excess electron localization.

Small aggregate

The discussion starts with the smallest cluster of $N_{6P} = 7$ (the radius of the cluster is about $r_{cl} = 6$ Å). In Figs. 7.4a-d, four different $P_m(t)$ are drawn versus time. The four related 6P sites are highlighted in the molecular sketch (see also the labeling). The green and blue colored kinetics in each panel result from the linear SSE based on $\mathcal{F}_m^{(1)}$ and $\mathcal{F}_m^{(2)}$, respectively. The pink colored curve provides the exact reference data computed by the nonlinear SSE. As shown, the kinetics resulting from both linear algorithms disagree clearly with the red reference curve. Closer inspection uncovers that the main disagreement owes to the initial period between 20 to 100 fs. As discussed in Sec. 4.4, in this period the hole kinetics are particularly subject to numerical renormalization errors. The declining oscillation features of all four $P_m(t)$ indicate dominant initial coherent wave packet motion. Later on, the latter becomes repressed by intensifying dissipative effects until 100 fs. In particular, $P_3(t)$ and $P_4(t)$ (see Figs. 7.4c and d, respectively) from both linear algorithms show too strong coherent features in comparison with the exact data (pink line). When confronting both linear SSEs with each other, one realizes finally that the one based on $\mathcal{F}_m^{(2)}$ performs clearly better.

Figure 7.4.: Dissipative hole motion in 6P layers. Panel a-d: Time–evolution of four prominent molecular hole populations $P_m(t)$ (see Eq. 7.15) for aggregate size of $N_{6P} = 7$ (see molecular labels in the sketch). The green and blue colored lines result each from employing the linear SSE algorithm with the force function $\mathscr{F}_m^{(1)}$ and $\mathscr{F}_m^{(2)}$, respectively. Pink lines give each the exact data from the nonlinear algorithm. Panel i-v: Similar hole population dynamics but related to the aggregate with $N_{6P} = 19$ as sketched.

Extending the aggregate size

To complete the performance test, the system size must now be increased stepwise. Therefore, hole kinetics are recorded for 6P disks of $N_{6P} = 19$ ($r_{cl} = 12$ Å), $N_{6P} = 27$ ($r_{cl} = 14$ Å), $N_{6P} = 35$ ($r_{cl} = 15$ Å) and $N_{6P} = 59$ ($r_{cl} = 2$ nm). The dynamics in the film of 19 molecules are illustrated in the lower half of Fig. 7.4. The Figs. 7.4i–v offer the evolution of $P_m(t)$ for five prominent 6Ps. The indicated molecular indexes are again refered to the sketch of the aggregate. In principle, the kinetics of the five $P_m(t)$ show rather similar behavior as obtained above for the disk with $N_{6P} = 7$. The hole is subject to dominant coherent motion within the initial period of 75 fs. In this phase, it distributes again over the entire cluster. After this initial phase, the dissipation becomes more dominant. In comparison of the three types of algorithms, the performance of the linear SSE based on $\mathscr{F}_m^{(2)}$ (blue lines) appears now clearly improved with respect to the case of $N_{6P} = 7$ presented in Figs. 7.4a-d. In fact, it shows very well agreement with the exact data from the nonlinear algorithm (pink line). In marked contrast to that, the computations using the force $\mathscr{F}_m^{(1)}$ (green line) are still rather inaccurate.

Concurrent observation were made from studying several characteristic population kinetics $P_m(t)$ within the layer with $N_{6P} = 27$. When increasing further the size of the aggregate up to $N_{6P} = 35$ and 59 molecules, the performance of the linear SSE algorithm based on $\mathscr{F}_m^{(2)}$ improves gradually. The most pronounced $P_m(t)$ for the layer with $N_{6P} = 59$ are shown in Fig. 7.5. As before, each panel depicts a different 6P population $P_m(t)$ according to the labels indicated in the attached illustration of the aggregate. The comparison of the utilized algorithms (again green, blue and pink colorings) give clear evidence on very good performance of the linear SSE based on $\mathscr{F}_m^{(2)}$ (blue colored lines). It delivers convincing results in agreement with the exact data (pink colored lines).

7.6.3. Summary and prognosis for large–scale aggregates

Preliminary studies on hole transfer are presented concerning a series of differently sized 6P layers ($N_{6P} = 7$, 19, 27, 35 and $N_{6P} = 59$). Particular focus lies on hole kinetics presented in Figs. 7.4 and 7.5. Thereby, the strategy developed in Chap. 4 is followed with the intention to identify a linear SSE algorithms (see Eq. 7.11) with good performance when based on the approximate propagation scheme 4.66. For all aggregate sizes, population kinetics resulting from two linear SSEs using two different force algorithms are compared with exact data from the nonlinear SSE 4.62. By gradually increasing the aggregate layer size, performance trends are clearly figured out.

In the first study (the smallest aggregate), the comparisons confirmed numerical difficulties of the linear algorithms. Both showed rather miserable workabilities. However, after that first impression, significant improvements of its performance are documented when the aggregate size is stepwise increased up to $N_{6P} = 59$. In particular, in application of the stochastic noise $\mathscr{F}_m^{(2)}$, the linear SSE algorithm is able to provide very convincing results for the intermediate sized aggregates. Very promising stepwise improvements are obtained. This strongly encourages the utilization of the linear SSE with $\mathscr{F}_m^{(2)}$ also in the ultimate aggregate with $N_{6P} = 2553$. In advance, its good per-

Figure 7.5.: Dissipative hole motion in 6P layers of $N_{6P} = 59$. Panel a-e: Time–evolution of five prominent molecular hole populations, $P_m(t)$, according to Eq. 7.15 (see molecular labels in the sketch of the aggregate). Corresponding to Fig. 7.4, comparison is each drawn between three different SSE algorithms (see legend).

formance can be prognosticated.

Remarks

A general answer on the question about the particular origin of the better numerical workability of the linear SSE based on $\mathscr{F}_m^{(2)}$ is given in Sec. 4.5.3. Besides, however, it could not be clarified completely why increasing system sizes improves the performance. A suggestive explanation could be as follows. By comparing the different kinetics in Figs. 7.4 and 7.5, one recognizes that the initial coherent character of the hole motion (see, e.g., the oscillation amplitude of the $P_m(t)$) decreases for an increasing system sizes. When extending the system, more and more vibrational modes introduce vibronic effects. A greater number of involved modes further leads to accelerated dissipation and coherence dephasing. Accordingly, the critical time interval of balanced coherent and dissipative processes foreshortens and the approximate propagation scheme 4.66 produces less numerical discrepancy.

7.7. Hole Motion in the Gigantic Aggregate

In Sec. 7.6.2, performance tests on the linear SSE 7.11 are executed. The algorithm based on the force $\mathscr{F}_m^{(2)}(t)$ (see Eq. 7.14) and damping $\hat{\mathscr{D}}(t;T=0)$ (see Eq. 7.12) shows gradually improved numerical performance when turning from small to medium sized aggregates. In what follows, that SSE algorithm is applied to the 6P layer with $N_{\mathrm{6P}} = 2553$. According to the former trend, now excellent performance can be anticipated.

The 6P aggregate is shown in Fig. 7.1. Its radius is about $r_{\mathrm{cl}} = 15$ nm. The interaction energy of the hole, $\mathscr{E}_m^{\mathrm{PCM}}$, renders the 2d potential energy well depicted in Fig. 7.2b. The well represent the hole energy with respect to its position in the layer. Each tile represents a single 6P molecule where the minimum energy (in the center) is shifted to zero.

In order to obtain a clear impression on the dissipative effects, also pure coherent hole dynamics shall be offered in direct confrontation. They were additionally computed by solving the ordinary time–dependent Schrödinger equation for the hole transfer system (i.e., Eq. 7.11 in absence of $\hat{\mathscr{F}}_z(t)$ and $\hat{\mathscr{D}}(t)$, cf. Sec. 3.2.1). As motivated in Sec. 7.1, three kinetics starting each from a different initial electron and hole configuration are investigated. To give an overview, the related initial electron–hole constellations are sketched in Fig. 7.6. Please remind that, in all three cases, the electron is placed centrally "beneath" the aggregate layers.

7.7.1. Close initial electron–hole configuration

For the beginning, the hole is placed in the center of the 6P layer (see Fig. 7.6a). This configuration represents a scenario of charge separation where the electron is trapped very fastly in direct vicinity to the created hole.

The temporal behavior of $P_m(t)$ is offered in Fig. 7.7. The hole population upon the layer is illustrated exemplarily for time steps of $t = 10$, 75, 250 and 1000 fs. The layer is visualized from the top view and each of the pixels represents an individual

Figure 7.6.: Dissipative hole motion in 6P layers of $N_{6P} = 2553$. Initial positioning of the hole with respect to the centrally configured electron charge distribution in the ZnO close to the surface (see again Fig. 7.2b). Panel a: Initial close electron–hole configuration (scenario 1). Panel b and c: Two marked remote configurations (scenario 2 and 3).

6P molecular site. The coloring gives the value of $P_m(t)$ according to the scales at the top of each panel. For direct comparison, the dissipative and coherent dynamics are illustrated opponent to each other in the left column (blue background coloring) and right column of panels (green background coloring), respectively (see indication in the upper right corner). Please note further that, for better illustration, the view on the blue colored "disks" (left column) are magnified. The green colored aggregates in Figs. 7.7i-iv represent the full aggregate and the dashed circles indicate the magnified areas visualized correspondingly in Figs. 7.7a-d. As expected, both types of dynamics resemble each other in the early time segment but differ increasingly with progress of time. The herringbone aggregation is characterized by two different values of the transfer coupling $\mathscr{V}^{\mathrm{HT}}$ (see Fig. 7.3). This explains the present observation that the hole apparently delocalizes preferentially along the x–axis of the film. Within the initial 75 fs (see Fig. 7.7b), it captures about 9 to 10 molecules along the x–axis (i.e., delocalized upon 5.5 nm), while in direction of the y–axis it delocalizes only over a distance of about 2 nm.

The coherent dynamics (green coloring) are characterized by continuous appearances of multiple interferences and superpositioning patterns. The typical features of wave packet motion are clearly visible (see Figs. 7.7iii and iv). In strict contrast, vibronic effects slow down such continuous delocalization across the layer. By means of energy dissipation, finally, the hole concentrates again in the center of the aggregate. The greatest delocalization area of the hole (due to initial dominance of wave packet motion) ranges to a radius of about 3 nm and is captured essentially within the first 1 ps (see Fig. 7.7d). Afterwards, the propagation slows down. The loss of coherence in the

Figure 7.7.: Spatio–temporal evolution of the hole population $P_m(t)$ (see Eq. 7.15) in the 6P layers of $N_{6P} = 2553$, starting from electron–hole configuration *scenario 1* (see Fig. 7.6a). Each pixel describes an individual 6P (aggregate from the top view, see Fig. 7.1b). Pixel coloring represents the population $P_m(t)$ (see color legends). Panels a-d: Four different time–steps (see pink time–line) of the dissipative kinetics at 300 K. Panel i-iv: Corresponding coherent kinetics from wave packet propagation. Green circles mark the zoomed area visualized in panels a-d (for details, see the main text).

system continuous steadily. Meanwhile, features of energy fluctuation and dissipation due to system–bath interaction become dominant. This process of thermal balancing of hole populations according to the potential energy well (presented in Fig. 7.2b) holds on throughout the total simulation time until 5 ps (not completely shown).

Now, the general question about whether the hole is able to move away from a trapped negative surface charge can already be answered. It is demonstrated that neither the hole transfer coupling is strong enough to "lift out" the hole of the Coulomb well nor the energy fluctuations at room temperature can "push the hole over the barrier". The hole separates not from a nearby trapped electron. Only under conditions that the electron additionally starts funneling rapidly into the ZnO bulk zone, the hole and electron can overcome their common attraction by initial ballistic motion away from each other. These findings agree very well with observations and conclusions which were made during earlier simulations on charge separation at a polymer/ZnO interface [34]. Here, a localized and tightly bound electron–hole pair is recreated within 5 ps after the related charge separation process took place.

7.7.2. Remote initial electron–hole configurations

Next, the two initial positions of the hole at the left hand side of the 6P layer (see Fig. 7.6b) and at its lower border (see Fig. 7.6c) are considered. Both constellations mimick again very quick charge separation. However, the electron trapping happens now further remote from the actual site of charge separation. For convenience, the electron trap is kept "beneath" the center of the aggregate and the initial hole localization is vice versa moved to the edge of the layer (each along the x and y–axis, respectively). Behind preparing such remote set–ups, it is the hope to uncover how long rather weakly bound charge–separated states survive or, in other words, on which time–scale the initial remote electron and hole appearance changes again to close constellation.

The data presented in Fig. 7.8 visualizes the kinetics of the hole population $P_m(t)$, where the initial positioning of the hole lies at the left hand side of the aggregate. The electron trap appears displaced about 15 nm along the x–axis (in the center of the layer). In the fashion of Fig. 7.7, the left and right column of panels illustrates the dissipative dynamics at room temperature and purely coherent kinetics, respectively. Please note that the four time–steps, chosen for illustration, cover now the range up to 5 ps (see also the time–line on the left hand side). Moreover, all illustrations (blue and green) represents the full aggregate layer now.

In the initial time–range (up to about $t = 500$ fs), the evolution of the hole at room temperature is characterized by fast wave packet motion along the x–axis (see Figs. 7.8a and b). Along the x–axis, nearest 6P neighbors are coupled rather efficiently, while delocalization in y–direction is hampered by the much weaker transfer integral. Inspection of the left column of panels further demonstrates that the hole dynamics from the ordinary Schrödinger equation appears more more pronounced. The ballistic wave packet motion drives the hole swiftly across the aggregate. Its delocalization is stronger and remains surprisingly unaffected by interaction with the electron (see Figs. 7.8i and ii). Scattering structures are visible only when it directly "overflows" the Coulomb well (see Fig. 7.8ii). This is in contrast to the stochastic simulations. In

Figure 7.8.: Spatio–temporal evolution of the hole in the 6P layers of $N_{6P} = 2553$, starting from the remote electron–hole configuration *scenario 2* (see Fig. 7.6b). Type of visualization corresponds to Fig. 7.7. Panels a-d: Dissipative relaxation of the hole at 300 K. Four different time–steps up to $t = 5$ ps (see pink time–line). Panel i-iv: Corresponding coherent wave packet dynamics (for details, see the main text).

fact, the comparison of both types of kinetics at later times unveils again clearly the influence of the vibrational bath. The initial phase of pronounced coherence and related ballistic motion lasts until about 500 fs. Then, dissipative effects and dephasing become clearly dominant. The continuously increasing diffusive character of the migration becomes apparent when comparing Figs. 7.8c with Figs. 7.8iii. A relaxation process drives the hole directively to the electron in the center of the aggregate. After about 5 ps simulation time, the hole is captured by the electron (see Fig. 7.8d). The pure wave packet motion cannot account for this effect and shows continuous processing of delocalization of population upon the entire aggregate (see Fig. 7.8iv). The "deepest" potential energy region is thereby somewhat omitted by the hole which owes to the larger off–resonances between the 6P site energy levels (see again Fig. 7.2).

Equivalent results are obtained when the hole starts migrating from the lower edge of the aggregate layer. In this third scenario, the electron trap is supposed to be shifted by about 15 nm along the y–axis with respect to the initial hole spot (see Fig. 7.6c). The corresponding kinetics of the hole population are depicted in Fig. 7.9. Efficient wave packet formation can be observed until about 500 fs. Thereby, the hole delocalizes again "preferentially" along the x–axis due to the non–isotropic transfer couplings (see Figs. 7.9a and b). Again, the system–bath coupling enable the hole to relax downwards in the potential well (see Figs. 7.9c and d). However, the steepest descent is now in the direction of the y–axis, which explains the much slower migration and thermalization compared to the foregoing scenario. Within the total simulation length of 5 ps, the hole is only partially moved back to the electron. This is nicely shown in Fig. 7.9d. Suggestively, the entire relaxation process takes place on a time–scale of about 50 ps. The kinetics from exclusive wave packet propagation are rather similar to the former case illustrated in Fig. 7.8i-iv. However, also the pure coherent motion of the hole is essentially slowed down by means of the much lower hole transfer integral along the y–axis. Here, in about 5 ps the opponent aggregate border is reached by the wave packet front of the hole (though a great share of the population still remains in the region close to the lower edge; see Fig. 7.9iv). Contrarily, in the former case of movement along the x–axis, the hole completely crosses the aggregate within less than 1 ps (see again Figs. 7.8ii and ii).

Together, very different time–scales of hole relaxation were found in dependence on the two remote electron and hole configurations. The distinct hole coupling strengthes between 6P nearest neighbors characterize critically the population dynamics. Hole migration along the y–axis of the aggregate is much slower than along the x–axis. It was demonstrated that the hole can follow the electron only slowly along the y–axis. This means that the weak hole transfer coupling along the y–axis has a stabilizing effect on separated electron–hole pairs. Accordingly, besides electron motion into the ZnO bulk zone, apparently also quick motion along the y–axis assists long–lasting electron and hole separations.

The study on the 6P/ZnO interface shall be completed with an impression on hole motion perpendicular to the interface, i.e., between the molecular layers shown in Fig. 1.2c. Therefore, the migration of the hole was finally also simulated in a 3d triple layer assembly of (3×500) 6P molecules. All the additionally required nearest 6P neighbor transfer integrals between the layers were determined. The latter transfer couplings

Figure 7.9.: Spatio–temporal evolution of the hole in the 6P layers of $N_{6P} = 2553$, starting from the remote electron–hole configuration *scenario 3* (see Fig. 7.6c). Type of visualization corresponds to Fig. 7.8, though other time–steps are drawn (for details, see the main text).

mediate the perpendicular evacuation of the hole from the ZnO surface. However, none of the relevant couplings exceeds 4 meV and indeed only very weak perpendicular motion of the hole was uncovered. Concretely, less than 2 % of the hole population moves from the first (direct adjacent to the ZnO) to the second (next attached) 6P layer within 5 ps. The total hole population in the third (next but one) layer was not worth mentioning.

7.8. Summary and Concluding Remarks

Studies on dissipative hole motion in a realistic layer of 2553 upright standing *para*–sexiphenyl (6P) molecules placed on a plane ZnO surface are presented. The 6P/ZnO hybrid interface is of general practical relevance and is also intensively analysed in Chaps. 5 and 6. Here, the hole migration is desired on the picosecond time–scale and the simulations are directly prepared with an immobilized electron charge localized in the ZnO surface region close to the 6P aggregate. Such electron and hole configurations may occur after ultrafast charge separation at the interface. Novel insights into the spatio–temporal evolution of the hole at the 6P/ZnO interface are obtained and important discussions are given about the time–scale in which fastly separated electron–hole pairs reapproach again.

The parametrization of the Hamiltonian of the gigantic interface presented a special challenge. The molecular hole charge distribution ($+1e$ totally charged) as well as the also required 6P–6P hole transfer couplings are determined based on DFT level. The electron, however, is introduced in a phenomenologic picture. It is mimicked by installing a distribution of partial charges in the ZnO slab ($-1e$ totally charged). This is imperative here in order to avoid a single–particle approach for the macroscopic ZnO substrate. The macroscopic surrounding of both localized particles (i.e., the remaining neutral interface structure) is involved in a specially developed polarizable continuum model. Thanks to it, the Coulomb–type electron–hole interaction can be computed both very accurate and extremely efficiently.

The hole transfer system is treated in contact with a room temperature bath. As the method of choice, the own developed stochastic Schrödinger equation (SSE) approach is employed. In preparation of the simulations of the gigantic 6P layer, the numerical workability of the SSE algorithms is confirmed. Thereby, the general strategy proposed in Chap. 4 is regarded and a series of differently sized 6P aggregates containing up to 59 molecules are studied in advance. For the first time, the SSE methodology is applied here to a system of 2553 states. This number is outstanding and appears as gigantic in comparison with existing studies on the same level of theory. In this light, the here discussed simulations are of pioneering character. They are only made possible by means of the remarkable efficiency of the own SSE ansatz. Despite the vast system size, it allows taking into account explicitly non–Markovian system–bath interaction and dissipative effects (e.g., leading to population relaxation). By that, the present dynamics are essentially more advanced than other wave function based methods (e.g., after Haken, Strobl and Reineker or the Monte Carlo wave packet propagation) as applied typically to likewise large–scale systems (see also Sec. 7.1).

The influence of dissipation and coherence dephasing is intensively discussed. There-

fore, the actual room temperature simulations are confronted with related dynamics from the ordinary Schrödinger equation (pure wave packet propagation). Simulations starting from three particular scenarios of initial electron and hole configuration are investigated. It is demonstrated that, in cases of close electron and hole configuration, the hole is unable to overcome the Coulomb barrier created by the immobilized electron at the ZnO surface. In particular, the very low hole charge mobility is an issue here. The energetic off–resonance of the hole states close to the electron exceeds the transfer coupling and the initial ballistic wave packet motion of the hole is too weak. Instead, the incorporation of relaxation processes moves the hole completely back to the site of the electron trap within about 1 ps. Under condition that the hole and electron are initially further remote, the kinetics clearly show initial phases of dominant wave packet motion and significant hole delocalization. Interestingly, rather long–lived separations of electron and hole can be achieved under certain conditions. With progress of time, however, again diffusive motion towards the electron becomes more and more noticeable due to the continuous acting of dephasing and dissipation.

Altogether, the provided time–domain simulations further improves the detailed understanding of the mechanism of charge separation at the 6P/ZnO. The bottom line is that efficient creation of free charge carriers can only be achieved under conditions that the hole as well as the electron maintain mobile and move away from the surface into more remote bulk regions. This is not clearly guaranteed concerning aggregates of upright–standing 6Ps on ZnO interfaces. As discussed, the created electrons are likely to remain at the surface region. Their appearance explains the generally weak yield of free charge carrier generation measured at different polymer/ZnO interface [72]. And as finally proved, furthermore also the created holes in the 6P aggregate cannot directly move away perpendicularly from the interface owing to very weak hole transfer couplings between two molecular layers of upright–standing 6Ps.

In order to enhance the free charge carrier creation, therefore, the focus should be rather on the flat–lying 6P assemblies on ZnO illustrated in Fig. 1.2d [65]. Other options are recently examined, like intermediate molecular films and special ZnO surface passivation techniques [14, 15, 183], but also different types of dopents (e.g., with Mg–atoms) are of interest [68, 72]. Especially the former two kinds of add–ons have a great development potential. Specific interlayer designs can be tailored to balance the Coulomb attraction across the interface or even to generate electric fields via static molecular dipoles which would act repulsively on the created electron and hole and so accelerating on the separation process.

8. Excitation Energy Transfer in a Tubular Dye Aggregate/CdSe Nanocrystal System

Tubular dye aggregates are considered as potential artificial light harvesting systems and have been very inspirational in the field of optoelectronics for the last two decades. Nowadays, especially excitation energy transfer phenomena in hybrid systems consisting of molecular aggregates and semiconductor nanocrystals are of high interest. This work discusses exciton relaxation kinetics within a realistic double–walled tubular dye aggregate and the successive excitation energy transfer to a closely placed CdSe nanocrystal. Some aspects of the latter were published in Ref. [186] while major parts of the discussion are based on very recent simulations and unpublished material.

In order to develop an exciton model of the tube, a 64 nm long tubular fragment consisting of 4140 dyes is constructed based on a nuclear structure taken from earlier molecular dynamics simulations. Further, a generalized Frenkel exciton ansatz is applied. It allows accounting properly for dispersion corrections. These are important here due to the double–walled structure of the aggregate.

Dissipative simulations of the exciton relaxation process are performed. Unidirectional translation of excitation energy from the outer to the inner wall is demonstrated in accordance with recent pump–probe experiments. Simulations starting from different exciton wave packets in the high–energy band region are executed. Thanks to the advantageous efficiency of the own stochastic Schrödinger equation technique, non–Markovian dissipative exciton dynamics across the entire tubular fragment are successfully performed. New findings are visualized in impressive molecular resolution.

For studying the excitation energy transfer to the nanocrystal, the Frenkel exciton model is merged with an exciton model of the nanocrystal. The Wannier–Mott exciton equation is solved and related excited states of the nanocrystal are obtained in terms of Coulomb correlated electron–hole pair states. Finally, a combined exciton Hamiltonian is created for the hybrid system. Vast numbers of excitonic energies and couplings are computed. The latter terms are responsible for the excitation energy transfer between the two bodies. Thereby, only very small values of the excitonic coupling of less than 1 meV are determined. The time–scale of the excitation energy transfer is quantified by computing transfer rates following Fermi's golden rule. Important observations on the transfer are made in dependence on the mutual positioning of nanocrystal and aggregate. In the last part, it is proved that the classical Förster model for energy transfer is insufficient here. By that, a very urgent debate also concerning other nanoscopic systems is instigated.

8.1. Background and Motivation

Hybrid organic/inorganic systems become more and more interesting. As generally introduced in Sec. 1, the intention of putting continuous effort into the field of hybrid nanosystems is to discover unique and not expectable electronic features which might give way to novel functional devices in many fields of optoelectronic nanotechnology. As discussed in Chap. 1, a plenty of experimental studies on hybrid materials were generally triggered for more than a decade by the hope to develop new models. Also theoretical works were moved on by the search for understanding the excitonic properties of hybrid systems. Supermolecular J–aggregates are one very promising class of organic components for the development of such new materials.

J–aggregates

Supramolecular J–aggregates are in the focus of experimental and theoretical studies for more than 80 years [101, 102]. In general, they are formed whenever (according to molecular aggregation) the transition dipole moments of neighbored molecules appear in "head–to–tail" alignment. The molecules, usually dye molecules (i.e., chromophores) of only a single type, conglomerate by means of self–assembly in aqueous solution. Typically, these regular aggregations lead to vast exciton delocalization, large oxcillator strengths and a superradiant sharp fluorescence band. This fluorescence peak is attributed with a very small Stokes shift but strongly red shifted with respect to the fluorescence of the non–aggregated dissolved dyes [103, 104]. Historically, this behavior was first discovered in 1936 for the so–called pseudoisocyanine dye [101, 216].

For the last 20 years, particular effort has been put into experimental and theoretical studies on J–aggregates of molecules belonging to the family of the (5,5',6,6'–tetrachlorobenzimidacarbo–)cyanine dyes [114, 115]. By chemical alternation of the chromophore side chains, their aggregation behavior can be enforced in a plenty of different ways [102]. It was soon uncovered that with the type of aggregation also the excitonic properties of the J–aggregates vary particularly [116]. This means that processing simple lab routines allows manufacturing a diversity of different aggregates with different excitonic properties. For instance, linear chain–like J–aggregates [217, 218, 106] as well as more complex 2d (plain [107, 110] and *tubular* [105, 120, 219, 108, 109]) or even 3d structures [113, 220] of nanoscale size were reported in literature, stable enough to last for a very long period of time.

By creating aggregates of different shape and size, systems are available which excitonic properties can be tuned appealingly and which can be easily fabricated [102]. Furthermore, it was elucidated already early that the relevant π–electron system of the individual cyanines are rather non–sensitive for the non–conjugated residuals and that essentially the different intermolecular excitonic couplings within the different aggregation type must be made responsible for the documented diversity of excitonic properties (see electronic structure computations, e.g., in Refs. [221] and [222]). This feature essentially simplifies theoretical models and has made cyanine aggregates to an interesting object for excitonic simulations (see, e.g., [119, 121, 107, 53, 122]).

Figure 8.1.: Self–assembly of C8S3 cyanine molecules (see also Fig. 2.1a) to a tubular dye aggregate (TDA) in aqueous solution. Measured absorption (green coloring) and fluorescence (red coloring) spectra of the dissolved C8S3 dyes (dashed lines) and the aggregated structure (full lines) are given in direct comparison. The J–aggregate effect as well as the two main bands of the TDA absorption spectra are indicated (for details, see the main text).

Tubular J–aggregates of C8S3 cyanine dyes

The type of tubular dye aggregate (TDA) which is part of the present study is illustrated in Fig. 8.1. Its structure shows great similarities to natural antenna complexes in photosynthetic complexes of bacteria and a variety of possible applications as artificial light harvesting systems have been reported [116]. As sketched in Fig. 8.1, these nanotubes are self–assembled in aqueous solution by the amphiphilic C8S3 cyanine dye. The latter belongs to the described family of molecules investigated very intensively (see, e.g., Refs. [219, 139, 8, 124, 125]).

In 2000, a series of pioneering studies of Berlepsch, Kirstein and Rabe et al. started [114, 223, 115, 116, 117]. In course of that, the fundamental spectroscopic properties of the TDAs were determined (see details below). It was estimated from diverse cryo–TEM imagings that the diameter of the TDAs amounts about 13 nm and their total wall thickness was uncovered as 4 nm [114, 223]. Impressively, the thread–like tubes reach lengths up to several microns and, once formed, they are attributed with remarkable stability. Then in 2004, Knoester and co–workers published a first general model of the aggregate internal structure proposing a double–walled construction. Each wall was thereby suggested to look like a rolled 2d brick work of the dyes molecules [118, 116]). In particular, the amphiphilic character of the C8S3 dyes is responsible for their arrangement to an inner and an outer wall, where the ionic backbones of the dyes are each exposed to the aqueous phase (see tubular illustration in Fig. 8.1 and details in Sec. 8.2). While there is common understanding on the double–walled architecture,

the precise intermolecular structure within the walls, however, is still subject of recent investigations and further on debated to date [224, 122]. For instance, in order to explain novel experimental findings the earlier brick work model was corrected later on in 2012 by suggesting a herringbone–like internal arrangement [224]. In 2015, then intensive molecular dynamics (MD) simulation were undertaken by Megow et al. [122]. In that work, again a brick work–like intermolecular architecture was suggested.

Excitonic properties of the tubular dye aggregate

The experimental steady–state spectra of the dissolved TDAs are drawn in Fig. 8.1 (filled green curve). In comparison with the also shown C8S3 monomer spectra (dashed green curve), the general J–aggregate effect can clearly be noticed. Thanks to the pioneering spectroscopic and theoretical works of Knoester et al. [118, 119], the excitonic processes in the TDA after laser–pulse excitation are widely understood to date – although investigations for further details and the run after discovering special excitonic features are still on [123, 124, 26, 125]. They demonstrated that the particular form of the measured main exciton bands can be straightly related to the double–walled structure of the TDA. Two main (low energetic) absorption peaks can be identified in the spectra given in Fig. 8.1 (indicated as band 1 and band 2). There "twofold" occurance echoes the fact that here, in principle, two (rolled up) J–aggregates are losely fused together. Thereby, the band 1 results mainly from Frenkel excitons residing on the inner cylinder wall and the band 2 (about 40 meV blueshifted) mainly from Frenkel excitons localized on the outer wall. Both bands are originated from excitons with transition dipole moments parallely aligned to the cylinder axis of the TDA. The focus of the present study lies on these two main bands.

Inclusion of dispersive interaction effects

The here utilized nuclear structure of the TDA is borrowed from the MD equilibration simulations executed by Megow et al. in 2015 [122]. Correspondingly, also the novel exciton model from the same authors is reapplied here in order to reproduce the two main J–band of the TDA. In contrast to the model of Knoester et al. [119], this model relies on a generalized Frenkel exciton Hamiltonian including dispersive interaction effects among the C8S3 dyes.

The standard Frenkel exciton description refers only to two states per molecule. By that, it strictly excludes intermolecular polarization effects and only electrostatic interactions contribute. In order to improve this minimal version of the Hamiltonian, the general idea of the configuration interaction ansatz can be worked into the exciton ansatz. For instance, concerning the CI scheme applied to the electronic structure of a certain molecule, different configurations with multiple excitations appear. These give rise to post–Hartree–Fock correlation effects. Here, the resulting corrections must be understood as van der Waals (dispersive) interactions of the ground (and first excited) electronic states of each C8S3 dye with its particularly surrounding. In fact, it was demonstrated in Ref. [122] that critically different dispersive corrections occur for C8S3 molecules residing on either the inner or the outer cylinder wall of the TDA. This effects is such strong that it dominates the shifts due to electrostatic couplings by a factor

Figure 8.2.: Exciton relaxation after high–energy optical excitation in the tubular dye aggregate. Panel a: Energy level scheme of the excitonic main band 1 to 2. The unidirectional excitation energy transfer (EET) between the bands is indicated. Panel b: Sketches of the related exciton migration from the outer to the inner wall (for details, see the main text).

of 50. The work in hand showcases another concrete application of this generalized exciton model.

Dissipative exciton kinetics in the gigantic aggregate

By utilizing a combination of steady–state absorption, pump–probe and time–resolved fluorescence measurements, it was uncovered in 2006 by van Loosdrecht, Knoester and co–workers that the appearing single fluourescence peak (filled red curve in Fig. 8.1) originates only from the "band 1 excitons" localized on the inner cylinder wall [119]. In order to understand the exciton dynamics behind that observation, the above described energetic distinction of excitons on the inner and the outer cylinder wall of the TDA is fundamental. In fact, due to efficient energy relaxation, after high–energy optical excitations unidirectional incoherent excitation energy transfer (EET) appears from the outer to the inner wall. Fig. 8.2 holds the related level scheme. The time–scale of the relaxation process was thereby announced to be smaller than the fluorescence time, which is of about 20 ps. Consequently, any radiative decay from excitons in the outer wall is quenched by the EET and only a single fluorescence peak appears from the bottom of the inner cylinder exciton band 1. Based on time–resolved fluorescence decay measurements and other experimental studies, it is meanwhile confirmed that coherently delocalized excitons on the outer wall are indeed transfered to the inner wall within few picoseconds [225, 219, 8, 139, 124, 125]. In 2014, an even faster relaxation time of 300 fs (population transfer from the outer to the inner tube) was published obtained from experimental quantum process tomography [124]. A time–scale of about 1 ps is in agreement with earlier results from 2d electronic spectroscopy studies [219, 139], which analysed the origin of the fast energy transfer from the vibronic point of view and concentrated thereby on a prominent intramolecular torsional mode of the C8S3 dye. Further evidence on the fast relaxation was given very recently using

ultrafast vibrational spectroscopy [125].

Motivated by the overwhelming amount of experimental works on exciton migration and energy relaxation, it is here the intention to clarify further details on that phenomenon using dissipative time–domain simulations. Therefore, a 64 nm long fragment of the TDA is constructed and its excitonic system is modeled as an open quantum system interacting with a bath of vibrational modes. Concerning the full number of 4140 dye molecules, the own stochastic Schrödinger equation methodology (developed in Chap. 4) is highly advantageous. The presented exciton kinetics are achieved at room temperature. They directly correspond to typical experimental conditions and are hence of great value. Moreover, the borrowed nuclear structure of the tube fragment was equilibrated at room temperature. This prepares a very realistic picture of static disorder in the TDA. Based on that, the offered dissipative exciton studies provide most realistic insights. Pioneering dissipative simulations are performed on unique scale and non–Markovian level of theory.

The tubular dye aggregate/nanocrystal hybrid system

Since 2007, films of planar J–aggregates and semiconductor nanostructures are functionalized together and analysed experimentally [111, 112, 13, 11, 26]. These works give message on the wide range of possible designs of hybrid J–aggregate/semiconductor systems applied in many scopes. Thereby, the trend to optoelectronic device fabrication is clearly noticable. For instance already in 2011, reports on the fabrication and performance of color–selective photodetectors based on hybid CdSe nanowires coated with J–aggregates were published [13].

By virtue of their interesting properties of light harvesting and energy funneling, it is anticipated that also TDAs can serve as auspicious resource for novel hybrid designs. Its tubular structure reminds of the light harvesting complexes in green sulfur bacteria. In nature, these chlorosomes enable bacteria to facilitate photosynthesis also in cases of very weak light irradiation. According to that, the TDAs garner widespread attention especially in the field of artificial photosynthesis [8, 26, 125]. Brush–like arrangements of TDAs could be functionalized together in order to efficiently collect photons. Stabilized rope–like bundles of several TDAs (twisted around each other) were indeed documented repeatedly (see, e.g., Refs. [116] and [126]). In assembly with semiconductor structures (e.g., polished flat surfaces, quantum dots (QDs) or dissolved nanocrystals), enhanced absorption cross sections in the visible spectral range can be achieved which further results in an improvement of the overall quantum yield. In 2015, TDAs decorated with QDs were manifactured and spectroscopically investigated by Rabe et al. [8]. First insights on very efficient EET from the QDs to the TDA were obtained. Significantly longer transfer times were measured for the respective backward process. Once harvested photon energy thus remains on the TDA up to nanoseconds and could be directively transmitted along the tube. Indeed, it was proven recently, that the TDAs show remarkable energy transmitting properties [113, 109]. Even at room temperature, excitons suggestively diffuse more than 1 μm along the tube (after focal laser–pulse excitation). The directive energy pathways and the tunable and efficient absorption even under low light conditions are particularly promising features concerning future applications as photodetectors and photovoltaic elements. In such

devices, the generation of electron–hole pair states and finally free charge carriers could be conceived, e.g., at a macroscopic semiconductor baseplate. Vice versa, such architecture would work in the fashion of a light emitter.

The second main part of the study is directly motivated by the spectroscopic measurements of the TDA/QD hybrid system by Rabe et al. [8]. It is the intention to further improve the, so far, very restricted theoretical understanding of the complex "backward" EET process starting from the TDA. After the formerly studied TDA–internal exciton relaxation process on the time–scale of few picoseconds in the TDA, this EET takes place on the nanosecond time–scale and must be considered to start from a thermal distribution of excitonic state population. Here, a comparable interface system is created for the theoretical investigation. In particular, a spherical CdSe nanocrystal (NC) of about 4.5 nm diameter is placed nearby the 64 nm long TDA fragment. Correspondingly, the exciton theories of both substructures must be merged together to an overall model for the TDA/NC system. Therefore, the formerly achieved excitonic energy levels of the TDA are introduced as possible energy donor states. Opponent to that, an atomistic TB model for the NC is employed. Based on that, Wannier–Mott excitons are computed in terms of Coulomb–correlated electron–hole pair states. The latter represent the possible EET acceptor states. As another key challenge of this work, thousands of excitonic couplings between both structures are computed in atomistic resolution making use of atomic partial transition charges. Their strength gives a direct answer on the question whether novel excitonic features due to the hybridization may be expected or not.

Applicability of Förster–type transfer mechanism

Until today, it is common standard to stress the ordinary Förster model of resonant EET also for theoretical descriptions of nanoscale hybrid systems. Originally, however, this theory was developed for simple non–atomistic modeling of EET between rather well–separated molecules [127]. Therefore, it is another intention of the present work to evaluate the applicability of the Förster model.

If the classical description due to Förster is valid, the EET rates display the famous $1/R^6$–dependence, where R denotes the donor–acceptor distance. The specific dependence is due to the fact that molecular electronic excitations are approximately represented using transition dipole moments. Although Förster's theory provides a simple tool for interpretation, systems considered nowadays are nanoscopic and particularly structured. They cannot be treated in fashion of well–separated molecular donor/acceptor pairs because the excitons usually appear delocalized upon vast areas equivalent to (or even larger than) the actual distance between the donor and acceptor structure. Then, the straight and uniform $1/R^6$–dependence of the Förster rate apparently undergoes drastic changes and the simple model of interacting transition point dipoles is no longer valid. For instance, by combining finite nanoparticles and infinite (macroscopic) structures of different dimensionalities, other dependencies on the inter–particle distance were declared some years ago by Govorov and co–workers [187, 131]. Here, a much more sophisticated atomistic model of the entire superstruction is applied. By virtue of that, the excitonic coupling takes into account the particular shape. It carries precise information on the nanoscopic TDA/NC structure. Based on the ex-

Figure 8.3.: Construction of the nuclear structure of the tubular dye aggregate (TDA). Panel a: View on the periodic molecular dynamics simulation box including the room temperature equilibrated TDA and the explicit water and methanol solvent molecules. Panel b: Construction of a 64 nm long fragment based on five periodic blocks (for details, see the main text).

citonic energies and couplings, transfer rates according to Fermi's golden rule are then computed. Concerning several spatial TDA/NC set–ups, the true distance dependence of the EET rate is finally explored and confronted with the $1/R^6$–dependence.

8.2. Equilibrated Structure of the Tubular Dye Aggregate

The internal molecular structure of the TDA was uncovered and precisely described in the work of Megow et al., who carried out extensive MD simulations at room temperature [122]. For the present purpose, an atomic structure is borrowed and further extended to a tubular fragment of 64 nm length. The equilibrated atomic structure is of enormous value here. It introduces structural disorder to the upcoming excitonic description in very realistic way and is much more sophisticated than the simple stochastic noise model applied earlier [118, 119].

The outtake of the simulation box with the equilibrated TDA structure is depicted in Fig. 8.3a. Besides the TDA (colored), it illustrates the number of 646926 explicit (water and methanol) solvent molecules. This TDA structure describes the starting point of all subsequent studies. Periodic boundary conditions were set up in order to mimick a tubular aggregate of infinite length without "open" endings. The entire aggregate

Figure 8.4.: The internal nuclear structure of the tubular dye aggregate (TDA). The TDA is described by six ribbons (panel a). Panel b shows that each ribbon consists of π–stacked C8S3 cyanine dyes. Together they describe the losely bound inner and outer cylinder wall (for details, see the main text).

consists of six ribbons which are wrapped helically around a common cylinder z–axis (see Fig. 8.4). The minimum extent of the box had to obey the helical periodicity and so conditioned a box length of 12.7 nm in direction of the z–axis. The dimensions in x and y direction were predefined by the radius of the tube. In order to ensure proper embedding, these box sizes measure about 17.2 nm. Further simulation details are provided in the Appendix G.2.

The periodicity of the nuclear structure (every 12.7 nm) along the tubular z–axis allows for properly extending it from only the single (actual simulated) fragment to in principle arbitrary length. In this work, the excitonic studies are carried out on a tube consisting of five such repetition blocks (see Fig. 8.3b). In total, this furtheron considered TDA structure includes a total number of $N_{\mathrm{dye}} = 4140$ C8S3 dye molecules and measures a gigantic length of 64 nm. Its internal molecular structure is illustrated in Fig. 8.4. Each of the six coiled ribbons are built up by two helixes (see Fig. 8.4a). Both are linked together and describe an outer and an inner helix (see Fig. 8.4b). The inner and outer cylinder is formed concerning all six ribbons together.

8.3. Generalized Frenkel Exciton Model for the Tubular Dye Aggregate

Apparently, the molecules in the inner wall of the tube experience a different environment compared to the dyes placed in the outer cylinders. According to Ref. [122], this is an important issue which demands for the generalized Frenkel exciton modeling introduced in Sec. 2.3.3. In fact, while dispersive correlation effects in isomorphic aggregates are identical for all molecules, here the particular inner and outer wall structuring

of the TDA leads to a crucial molecular dependence of this effects. In that respect, the generalized exciton model is more sophisticated than the typical Frenkel exciton model (see Sec. 2.3.2). It carefully takes into account dispersive correlation of each dye molecule and its surrounding. The influence of the dispersion is worked into the generalized Frenkel exciton Hamiltonian $\hat{H}_{\mathrm{FX}}^{(\mathrm{disp})}$ (see Eq. 2.33) by means of a perturbative treatment of a full configuration interaction approach. Energy corrections of the molecular excitation energies result with respect to the standard Frenkel exciton Hamiltonian $\hat{H}_{\mathrm{FX}}$ (see Eq. 2.22). Similarly, a correction prefactor of the excitonic coupling elements appeared and it follows

$$\hat{H}_{\mathrm{FX}}^{(\mathrm{disp})} = \sum_{m}^{N_{\mathrm{dye}}} \Big[E_{eg} + \Delta E_m^{(\mathrm{el})} + \Delta E_m^{(\mathrm{disp})}\Big] |\bar{\Phi}_m^e\rangle\langle\bar{\Phi}_m^e| + \Big(\sum_{m<n}^{N_{\mathrm{dye}}} \ell_{mn} \mathcal{J}_{mn} |\bar{\Phi}_m^e\rangle\langle\bar{\Phi}_n^e| + \mathrm{H.c.}\Big). \tag{8.1}$$

Here, the $|\bar{\Phi}_m^e\rangle$ describes the excited state of the complete TDA,

$$|\bar{\Phi}_m^e\rangle = |\Phi_e^{(m)}\rangle \otimes \prod_{n\neq m}^{N_{\mathrm{dye}}} |\Phi_g^{(n)}\rangle, \tag{8.2}$$

where the $|\Phi_g^{(m)}\rangle$ and $|\Phi_e^{(m)}\rangle$ indicate the molecular electronic S_0 ground and S_1 excited state of the mth C8S3 dye (see Secs. 2.1.3 and 2.1.4). Respectively, in $|\bar{\Phi}_m^e\rangle$ the mth dye is in the first excited state and the remaining $N_{\mathrm{dye}} - 1$ molecules are in ground state configuration (see Eq. 2.20). The direct product ansatz implies that zero wave function overlap among the dyes is assumed (see also Sec. 2.3.1). The E_{eg} in Eq. 8.1 describes the intramolecular excitation energy of the C8S3 cyanine. It was found as $E_{eg} = E_e^{\mathrm{dye}} - E_g^{\mathrm{dye}} = 2.64$ eV [122]. The second term, $\Delta E_m^{(\mathrm{el})}$, represent the correction of the former values due to intermolecular electrostatic Coulomb interaction and the third term, $\Delta E_m^{(\mathrm{disp})}$, gives the dispersive correlation interaction of each dye with its specific environment. Moreover, Eq. 8.1 includes the factor f_{mn} (for comparison, see again H_{FX} in Eq. 2.22). This factor approximates the influence of the polarizable surrounding of the mth and nth C8S3 dye and screens the excitonic coupling $\mathcal{J}_{mn}$.

8.3.1. Electrostatic shifts

The origin of the $\Delta E_m^{(\mathrm{el})}$ was explained in detail in Sec. 2.3.2 (see Eq. 2.28). It accounts for the Coulomb interaction of the permanent charge distributions of the mth dye (in S_1 excited state) and its environment (other dyes and solvents in electronic ground state). Here, it specifies to

$$\Delta E_m^{(\mathrm{el})} = \sum_{n\neq m}^{N_{\mathrm{dye}}} \Big(V_{mn}^{\mathrm{dye}}(e,g) - V_{mn}^{\mathrm{dye}}(g,g)\Big) + \sum_{k}^{N_{\mathrm{sol}}} \Big(V_{mk}^{\mathrm{sol}}(e,g) - V_{mk}^{\mathrm{sol}}(g,g)\Big). \tag{8.3}$$

By making use of the periodic boundary conditions, the summations properly consider each the number of $N_{\mathrm{dye}} - 1$ other dye molecules and all surrounding solvent molecules,

respectively. The $V_{mn}^{\mathrm{dye}}(a,g)$ represents the electrostatic interaction of the mth dye in ground ($a=g$) or excited state configuration ($a=e$) with the nth dye in the electronic ground state. Similarly, the term $V_{mk}^{\mathrm{sol}}(a,g)$ describes the electrostatic interaction energy between the mth dye (in state $a=g$ or $a=e$) and the kth solvent molecule in electronic ground state. In reference to Eq. 2.28 (with Eqs. 2.25 and 2.27), the terms $V_{mn}^{\mathrm{dye}}(e,g)$ and $V_{mk}^{\mathrm{sol}}(a,g)$ specify to

$$V_{mn}^{\mathrm{dye}}(a,g) = \int d\mathbf{x} \int d\mathbf{y} \frac{\left[n_a^{(m)}(\mathbf{x}) + e\sum_\mu Z_\mu^{(m)} \delta(\mathbf{x}-\mathbf{R}_\mu^{(m)})\right]\left[n_g^{(n)}(\mathbf{y}) + e\sum_\mu Z_\mu^{(n)} \delta(\mathbf{y}-\mathbf{R}_\mu^{(n)})\right]}{|\mathbf{x}-\mathbf{y}|} \tag{8.4}$$

and

$$V_{mk}^{\mathrm{sol}}(a,g) = \int d\mathbf{x} \int d\mathbf{y} \frac{\left[n_a^{(m)}(\mathbf{x}) + e\sum_\mu Z_\mu^{(m)} \delta(\mathbf{x}-\mathbf{R}_\mu^{(m)})\right]\left[\tilde{n}_g^{(k)}(\mathbf{y}) + e\sum_\mu \tilde{Z}_\mu^{(k)} \delta(\mathbf{y}-\tilde{\mathbf{R}}_\mu^{(k)})\right]}{|\mathbf{x}-\mathbf{y}|}, \tag{8.5}$$

respectively. The term $n_a^{(m)}(\mathbf{x}) + e\sum_\mu Z_\mu^{(m)} \delta(\mathbf{x}-\mathbf{R}_\mu^{(m)})$ is introduced as the molecular charge distribution of the mth dye (in state a) and added by the nuclear charges positioned at $\mathbf{R}_\mu^{(m)}$. Likewise, the term $\tilde{n}_g^{(k)}(\mathbf{x}) + e\sum_\mu \tilde{Z}_\mu^{(k)} \delta(\mathbf{y}-\tilde{\mathbf{R}}_\mu^{(k)})$ gives the total molecular charge distribution of the kth solvent molecule in its electronic ground state (with the μth nuclei charge $e\tilde{Z}_\mu^{(k)}$ of kth solvent at position $\tilde{\mathbf{R}}_\mu^{(k)}$). In practice, the density based Coulomb integrals in Eqs. 8.4 and 8.5 are further transformed to approximate sum expressions based on atomic centered partial charges. (Details on the computations are provided in Appendixes D and G.2.) The computed mean value of the electrostatic energy shifts, averaged with respect to all dyes in the inner cylinder wall amounts $\langle \Delta E_m^{(\mathrm{el})} \rangle_{\mathrm{in}} = 5.2$ meV. The mean value concerning molecule in the outer cylinder wall is $\langle \Delta E_m^{(\mathrm{el})} \rangle_{\mathrm{out}} = 5.9$ meV. Thereby, both data sets resemble very well Gaussian distributions with standard deviations of about 5.5 meV, i.e., a clear trend between $\Delta E_m^{(\mathrm{el})}$ in the inner and outer wall cannot be declared.

8.3.2. Dispersive correction shifts

The $\Delta E_m^{(\mathrm{disp})}$ in Eq. 8.2 specifies the dispersive energy shift. Its general form is discussed in Sec. 2.3.3 (see Eq. 2.33). The following implementation is directly related to the TDA and resembles the one presented in detail in Refs. [122] and [186]. The $\Delta E_m^{(\mathrm{disp})}$ generally reads

$$\Delta E_m^{(\mathrm{disp})} = \Delta E_{m,e}^{(\mathrm{disp})} - \Delta E_{m,g}^{(\mathrm{disp})}. \tag{8.6}$$

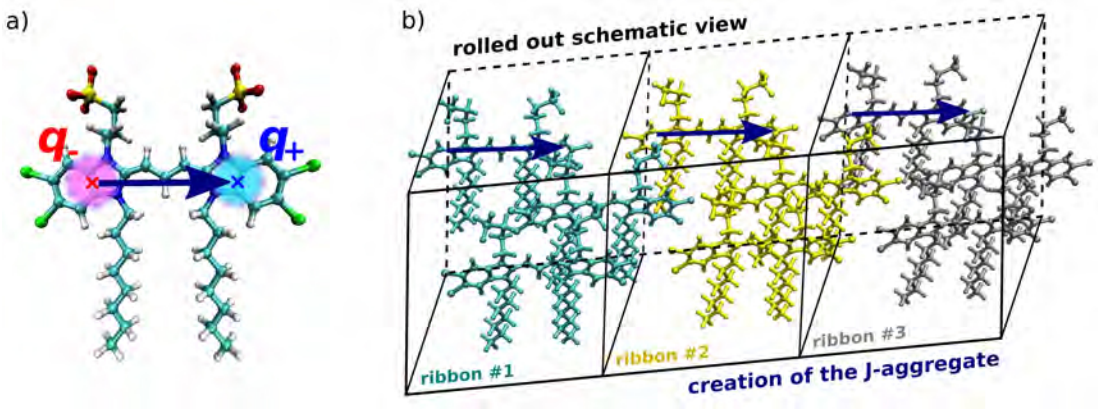

Figure 8.5.: The extended dipole model for the dispersive interaction between the C8S3 dyes. Panel a: Intramolecular positions of the extended transition dipole charges $q_-(a' \leftarrow a)$ and $q_+(a' \leftarrow a)$. The vector indicates an examplary extended transition dipole moment (for details, see the main text). Panel b: Sketch of the intermolecular structure within the walls of the TDA. Same colored dye molecules belong to the same ribbon (π–stacked winding). The orientation of the vectors signalize the (dominating) J–aggregate character created between the ribbons.

In the first step, it is assumed that the solvent molecules are here of negligible dispersive influence. The two absolute dispersion shifts follow then as, cf. Eq. 2.34,

$$\Delta E_{m,g}^{(\mathrm{disp})} = -\sum_{m' \neq m}^{N_{\mathrm{dye}}} \sum_{a,a'} \frac{|\mathcal{J}^{(m,m')}(a \leftarrow g, a' \leftarrow g)|^2}{E_a - E_g + E_{a'} - E_g} \tag{8.7}$$

and

$$\Delta E_{m,e}^{(\mathrm{disp})} = -\sum_{m' \neq m}^{N_{\mathrm{dye}}} \sum_{a,a'} \frac{|\mathcal{J}^{(m,m')}(a \leftarrow e, a' \leftarrow g)|^2}{E_a - E_e + E_{a'} - E_g}. \tag{8.8}$$

In the numerator, both latter expression contain a diversity of electronic transition coupling matrix elements (between the m'th and mth dye). The denominators are based on energy differences related to the respective excitation and de–excitation processes. Here, in principle all excited state energies E_a of the C8S3 dye (in vacuum) appear.

In the second step, the electronic coupling expressions in the numerator of Eqs. 8.7 and 8.8 are simplified to an interaction model based on *extended dipoles*. As illustrated in Fig. 8.5a, all C8S3 electronic transition charge densities (see Eq. 2.30) are thereby reduced to two localized *extended dipole charges*. In what follows, the latter shall be introduced as $q_+(a' \leftarrow a)$ and $q_-(a' \leftarrow a) = -q_+(a' \leftarrow a)$. The notation indicates that opposite signs are assumed. The absolute values of the charges differ in dependence on the particular state transition $a' \leftarrow a$. However, it is the basic idea that, independent on the index pair a and a', the $q_+(a' \leftarrow a)$ and $q_-(a' \leftarrow a)$ are localized

at the same positions in the C8S3 molecule, $\mathbf{R}_+^{(m)}$ and $\mathbf{R}_-^{(m)}$, respectively (as sketched in Fig. 8.5a). In general, the introduction of extended dipoles has a long tradition concerning the $S_0 \leftrightarrow S_1$ transition and the related excitonic couplings within molecular aggregates [118, 224, 123]. Here, the extended dipole model is applied to all higher excited state transitions. This must be clearly interpreted as a simplified and very specific ansatz which quality cannot be classified universally. Concerning the family of the present C8S3 cyanine dye, however, this model gives a reasonable approximation. In particular, similar dipole orientations were confirmed by extensive electronic structure computations of many higher excited state transitions of the dye (see Refs. [122] and [226] and references therein). In application, the electronic couplings in Eqs. 8.7 and 8.8 simplify to

$$\mathcal{J}^{(m,n)}(a' \leftarrow a, a_3 \leftarrow a_2) = q_+(a' \leftarrow a) q_+(a_3 \leftarrow a_2) w_{mn}. \tag{8.9}$$

The site dependence and spatial information is collected in the factor

$$w_{mn} = |\mathbf{R}_+^{(m)} - \mathbf{R}_+^{(n)}|^{-1} - |\mathbf{R}_+^{(m)} - \mathbf{R}_-^{(n)}|^{-1} - |\mathbf{R}_-^{(m)} - \mathbf{R}_+^{(n)}|^{-1} + |\mathbf{R}_-^{(m)} - \mathbf{R}_-^{(n)}|^{-1}. \tag{8.10}$$

Accordingly, the $\Delta E_m^{(\mathrm{disp})}$ separates into the simple product form

$$\Delta E_m^{(\mathrm{disp})} = -Q \cdot \mathcal{W}_m, \tag{8.11}$$

with the two factors

$$Q = \sum_{a>1} \sum_{a'>1} \Big[\frac{q_+(a \leftarrow e)^2}{E_a - E_e + E_{a'} - E_g} - \frac{q_+(a \leftarrow g)^2}{E_a - E_g + E_{a'} - E_g} \Big] q_+(a' \leftarrow g)^2, \tag{8.12}$$

and

$$\mathcal{W}_m = \sum_{n \neq m} w_{mn}^2. \tag{8.13}$$

The Q–factor in Eq. 8.12 is common for all C8S3 molecules. It describes an intramolecular quantity and depends not on the actual position of the dye. The latter dependences are collectively merged in the intermolecular variable $\mathcal{W}_m$. It holds all the spatial information about the mth dye and its specific surrounding in the TDA. While the $\Delta E_m^{(\mathrm{el})}$ (see Eq. 8.3) may be of different sign, the $\Delta E_m^{(\mathrm{disp})}$ appears exclusively with negative sign (as can be identified from Eqs. 8.7 and 8.8). In Ref. [122], a value of $Q = 7.61$ eVÅ^2 was estimated for the C8S3 dye. This Q–factor is reapplied here. In contrast to the Q–factor, the $\mathcal{W}_m$ is computed taking into consideration the present equilibrated TDA structure (see Eq. 8.13).

The expected difference of $\Delta E_m^{(\mathrm{disp})}$ for dyes in the inner and the outer TDA cylinder can be clearly confirmed. For the inner wall, a mean values of $\langle \Delta E_m^{(\mathrm{disp})} \rangle_{\mathrm{in}} = -463$ meV was computed, while the corresponding value for the outer wall amounts $\langle \Delta E_m^{(\mathrm{disp})} \rangle_{\mathrm{out}} = -413$ meV. Remarkably, both absolute values are about two orders of

magnitude larger than the above discussed electrostatic shifts (with $\langle \Delta E_m^{(\mathrm{el})} \rangle_{\mathrm{in}} = 5.2$ meV and $\langle \Delta E_m^{(\mathrm{el})} \rangle_{\mathrm{out}} = 5.9$ meV, cf. Sec. 8.3.1). Comparing the values of $|\langle \Delta E_m^{(\mathrm{disp})} \rangle_{\mathrm{in}} - \langle \Delta E_m^{(\mathrm{disp})} \rangle_{\mathrm{out}}| \approx 50$ meV and $|\langle \Delta E_m^{(\mathrm{el})} \rangle_{\mathrm{in}} - \langle \Delta E_m^{(\mathrm{el})} \rangle_{\mathrm{out}}| < 1$ meV demonstrates impressively the dominant influence of the polarization effects in the TDA.

8.3.3. Screened excitonic coupling

Besides the site–energy shifts, the dispersion leads to screening of the excitonic coupling $\mathcal{J}_{mn}$ [172, 227]. In approximation, therefore, the simple screening factor ℓ_{mn} is introduced in Eq. 8.1 with respect to the standard Frenkel exciton form (see Sec. 2.3.3). According to Eq. 2.29, the basic excitonic coupling elements follow as,

$$\mathcal{J}_{mn} = \int d\mathbf{x} \int d\mathbf{y} \frac{n_{eg}^{(m)}(\mathbf{x}) n_{ge}^{(n)}(\mathbf{y})}{|\mathbf{x} - \mathbf{y}|}, \tag{8.14}$$

with $n_{eg}^{(m)}(\mathbf{x})$ being the continuous molecular transition charge density related to the $S_0 \rightarrow S_1$ transition of the C8S3 cyanine. The $n_{eg}^{(m)}(\mathbf{x})$ is generally expressed in Sec. 2.3.2 (see Eq. 2.30). In practice, the matrix elements $\mathcal{J}_{mn}$ were computed based on the nuclear coordinates from the equilibrated TDA structure and atomic centered partial transition charges. The latter were approximately substituted for the transition densities (see Appendix D) and obtained as described in Appendix G.2.

According to Sec. 2.3.3, the screening factor can be approximated by a constant $\ell_{mn} \approx 1/\boldsymbol{n}^2$. The $\boldsymbol{n}$ is thereby the optical refractive index of the medium around the cyanines m and n. Constellations when both dyes are localized in the inner cylinder of the aggregate are attributed with a value of $\boldsymbol{n} = 1.89$ (i.e., $\ell_{mn} \approx 0.28$) [122]. Further, a value of $\boldsymbol{n} = 1.69$ (i.e., $\ell_{mn} \approx 0.35$) is utilized within the outer cylinder and the excitonic coupling between both cylinders is screened with $\boldsymbol{n} = 1.78$ (i.e., $\ell_{mn} \approx 0.32$) [122]. In all three cases the dispersion apparently means a noticeable reduction of the excitonic coupling.

8.4. Excitons of the Tubular Dye Aggregate

After computing all elements of the Hamiltonian in Eq. 8.1, the dispersion corrected Frenkel exciton states and energies are obtained by solving the eigenvalue problem, cf. Eq. 2.35,

$$\hat{H}_{\mathrm{FX}}^{(\mathrm{disp})} |\bar{\Phi}_\alpha^{(\mathrm{disp})}\rangle = \mathscr{E}_\alpha^{(\mathrm{disp})} |\bar{\Phi}_\alpha^{(\mathrm{disp})}\rangle. \tag{8.15}$$

The excitonic states $|\bar{\Phi}_\alpha^{(\mathrm{disp})}\rangle$ are thereby expressed using the basis of localized excited states introduced in Eq. 8.2, according to

$$|\bar{\Phi}_\alpha^{(\mathrm{disp})}\rangle = \sum_m^{N_{\mathrm{dye}}} \mathscr{C}_m(\alpha) |\bar{\Phi}_m^e\rangle, \tag{8.16}$$

Figure 8.6.: Generalized Frenkel excitons of the tubular dye aggregate. Panel a: Simulated absorption coefficient (main). Direct comparison with the measured spectra in Fig. 8.1 is given (inset). Panel b: Radial positions of the excitons are drawn against their energy (see Eq. 8.18). Each point represents one of 4140 excitons. Depicted energy range is given by the black region in panel a. The inset sketches the scale of the radius. Inner and outer tube regions are indicated. Pink colored arrows give the energetic and radial positions of the four excitons visualized in Fig. 8.7 (see also panel a).

where the expansion coefficients $\mathscr{C}_m(\alpha) = \langle \bar{\Phi}^e_m | \bar{\Phi}^{(\mathrm{disp})}_\alpha \rangle$ are utilized. Correspondingly, a number of $N_{\mathrm{dye}} = 4140$ excitonic energies $\mathscr{E}^{(\mathrm{disp})}_\alpha$ are found in terms of the eigenvalues.

8.4.1. Absorption line shape

The dark green filled curve of the main panel of Fig. 8.6a shows the absorption spectrum of the TDA, according to[1]

$$\mathscr{A}(\omega) \propto \omega \sum_{\alpha}^{N_{\mathrm{dye}}} |\mathbf{d}_\alpha|^2 \delta(\mathscr{E}^{(\mathrm{disp})}_\alpha - \hbar\omega). \tag{8.17}$$

The excitonic transition dipole moments are introduced as $\mathbf{d}_\alpha = \sum_m^{N_{\mathrm{dye}}} \mathscr{C}_m(\alpha) \mathbf{d}^{\mathrm{dye}}_m$, where the $\mathbf{d}^{\mathrm{dye}}_m$ represents the individual dipole moment of the $S_0 \rightarrow S_1$ transition of the mth C8S3 dye in the equilibrated TDA structure. They were computed using $\mathbf{d}^{\mathrm{dye}}_m = \sum_\mu \mathbf{R}^{(m)}_\mu q_{eg}(\mu)$ and based on the atomic partial transition charges $q_{eg}(\mu)$ and the positions $\mathbf{R}^{(m)}_\mu$ with atomic index μ (see Appendix G.2). For the absorption spectrum illustrated in Fig. 8.6a, the computed stick spectrum (see Eq. 8.17) was finally lifetime broadened by substituting a Lorentzian line functions with FWHM of 5 meV. As described in Sec. 8.2, the computed spectrum automatically includes effects of conformational disorder due to the formerly equilibrated nuclear structure of the TDA.

As shown in Fig. 8.6a, the excitons distribute across a region wider than 100 meV

[1] The convergence of the spectrum with respect to the length of the TDA was proved by means of additional computations. These were executed equivalently on shorter and longer aggregates of $N_{\mathrm{dye}} = 828$, 2484, 5769 and 7452 dyes.

and form two bands. These two main bands are indicated as band 1 and 2 in the measured absorption spectrum in Fig. 8.1 (for direct comparison of both spectra, see also the inset graphic of Fig. 8.6a). The excitonic coupling, which is rather strongly screened (see Sec. 8.3.3), cannot be solely responsible for the observed broad exciton distribution. Instead, the observed band width results here basically from the different excitation energies, $\Delta\mathscr{E}_m = \Delta E_m^{(\mathrm{el})} + \Delta E_m^{(\mathrm{disp})}$. And as discussed in Sec. 8.3.2, the distinct site–dependence of the dispersion correction $\Delta E_m^{(\mathrm{disp})}$ is mainly responsible for that. In particular, it was observed that, on average, the computed values of $\Delta E_m^{(\mathrm{disp})}$ related to dyes in the outer wall were essentially larger than those related to dyes in the inner wall. Therefore, it can be suspected that the energetically higher excitons are concentrated on the outer cylinder. This is in agreement with the earlier observations [118, 119]. Vice versa, the lower excitons are expected to reside on the inner cylinder of the TDA.

In order to analyse the exciton localization in this regard, the mean radii $\mathscr{r}_\alpha$ of the spatial delocalization of the αth exciton upon the TDA shall be introduced as

$$\mathscr{r}_\alpha = \frac{1}{N_{\mathrm{dye}}} \sum_m |\mathscr{C}_m(\alpha)|^2 \rho_m. \tag{8.18}$$

The radial distance of the mth dye with respect to the cylinder z–axis (see Figs. 8.2 and 8.4) is specified as $\rho_m = \sqrt{x_m^2 + y_m^2}$. In Fig. 8.6b, the computed values of $\mathscr{r}_\alpha$ are drawn against the excitonic energies $\mathscr{E}_\alpha^{(\mathrm{disp})}$. The trend shows clearly that excitons within the energetically higher absorption band appear in the outer wall of the TDA. Counterwise, the inner wall essentially hosts excitons of the energetically lower absorption peak.

8.4.2. Excitonic structures on the tubular dye aggregate

It follows a more detailed discussion on the localization of the excitons across the TDA cylinder walls. For this purpose, the site–dependent expansion coefficients $|\mathscr{C}_m(\alpha)|^2$ (see Eq. 8.16), shall now be directly plotted. In Fig. 8.7, four typical types of spatial structures of the excitons are rendered against the two essential cylinder coordinates (longitudinal z-axis and rotation angle φ). For better illustration, the cylinder form of the TDA is cut along the z–axis and rolled out (see sketch in Fig. 8.7e). The four overall structures of the expansion coefficients describe clearly different exciton localizations across the TDA. As indicated, the inner and outer wall is each represented by an individual map. The energies of the excitons in Figs. 8.7a–d are summarized in Tab. 8.4.2. For closer inspection, their positions in the lower band region (2.0512 eV), the upper band region (2.1972 eV) and in the middle band region (with 2.0912 eV and 2.1190 eV) are highlighted by the four arrows in the profile of Fig. 8.6a. The radial distribution of the four excitons can be taken from Fig. 8.6b (see again the pink arrows). Their participation numbers can be consulted by $\ell_\alpha = 1/\sum_m |\mathscr{C}_m(\alpha)|^4$. Independent on the actual spatial distribution, ℓ_α directly quantifies the localization character. A value of $\ell_\alpha = 1$ would measure a single molecule excitation, while $\ell_\alpha = 4140$ would indicate full delocalization. The computed values for the particular excitons shown in Fig. 8.7a–d are also given in Tab. 8.4.2.

Besides spot–like localized excitons (as sampled in the Figs. 8.7b and d), many ex-

Figure 8.7.: Spatial structure of the Frenkel excitons accross the tubular dye aggregate. Panel a–d: Structure maps of four examplarily chosen excitons. Further information are listed in Tab. 8.4.2 and indicated in Fig. 8.6 (pink arrows). The color code gives the exciton expansion coefficents ($|\mathscr{C}_m(\alpha)|^2$, cf. Eq. 8.16) versus molecular position along main cylinder z–axis and rotational angle φ. Figures on the left–hand and right–hand side give each the delocalization on the inner and outer cylinder wall, respectively. Panel e: Sketch of the preparation of the 2d maps.

Table 8.1.: Energies and participation numbers of the four excitons illustrated in Fig. 8.7.

Fig. 8.7	$\mathscr{E}_\alpha^{(\mathrm{disp})}$ [eV]	ℓ_α
a)	2.0512	79
b)	2.0912	376
c)	2.1190	177
d)	2.1972	53

citons are found with rather homogeneous distributions across the entire aggregate (see, e.g., the structures in Fig. 8.7c). Another prominent pattern is examplified with Fig. 8.7a. This scratch–like localization structure is the result of the windings of the six ribbons (see again Fig. 8.4). However, the direction of the "scratches" is perpendicular to the helical windings of the ribbons. Indeed, the strongest excitonic couplings were obtained between pairs of nearest neighbor molecules of two ribbons (see again Fig. 8.5b). Here, it is given evidence on that these "exciton strands" may extend across the complete TDA in terms of several circumvolutions. Reminding that energetic disorder is taken into account by means of the equilibrated nuclear structure, this is a remarkable finding. By scanning through all 4140 exciton localizations, it was noticed that the above types of patterns were uncovered in similarity on the inner as well as on the outer cylinders. Thereby, the localizations clearly turns from the inner to the outer cylinder when moving the excitonic energy from lower to higher energies in the band. This feature matches the trend figured out above more strictly with the mean exciton localization radius (see Eq. 8.18). Unfortunately, the complexity of the TDA system probibits a clear explanation on the appearances of the different exciton patterns. A systematic ordering of them with respect to the excitonic energy cannot be proposed.

In summary, the generalized exciton model leads to an absorption profile which agrees very well with spectroscopic measurements regarding positions as well as widths of the two main absorption bands. Also the relation between the energy and spatial localization of the excitons on the inner and outer wall, which was experimentally uncoverd by Pugžlys et al. [119], is here confirmed. In Ref. [118], this effect was proposed as the consequence of different excitonic couplings in the TDA. Here, it is proved instead that it is rather the effect of the distinct dispersion effects. The executed analysis on the radial exciton localization versus the excitonic energy brings with important insights in remarkable detail. These data are of significant value for understanding the TDA–internal exciton relaxation processes simulated in Sec. 8.5. Further, the extreme vast spread of the majority of the excitons (even at room temperature) is evidenced. As shown in Fig. 8.7, excitons are observed as delocalized upon hundreds of molecules and across several tens of nanometers alongside as well as around the TDA. The here obtained delocalization is essentially larger than the mean values which were typically documented so far (see, e.g., Refs. [118, 119, 8]). Very specific localization structures of the excitons are thereby enlightened.

8.5. Exciton Relaxation in the Tubular Dye Aggregate

As discussed in Sec. 8.1, exciton relaxation in the TDA were uncovered and reported in many different spectroscopic investigations. Now, this process shall be studied theoretically in terms of time–domain simulations of the reduced density operator. Thereby, the TDA excitonic system is considered as an open system in contact with a vibrational temperature bath characterized by the molecular vibrational modes of the C8S3 dyes (see Sec. 3.3). According to the general description given in Sec. 3.3.2, population relaxation of the Frenkel excitons can be anticipated accompanied by energy dissipation and coherence dephasing.

8.5.1. The vibronic interaction model

According to Eq. 3.6, the total system Hamiltonian shall be constructed as

$$\hat{H} = \hat{H}_{\mathrm{FX}}^{(\mathrm{disp})} + \hat{H}_{\text{FX-vib}} + \hat{H}_{\mathrm{vib}}. \tag{8.19}$$

The above generalized Frenkel Hamiltonian, $\hat{H}_{\mathrm{FX}}^{(\mathrm{disp})}$ (see Eq. 8.1), represents the transfer system and the vibrational bath Hamiltonian is introduced as $\hat{H}_{\mathrm{vib}}$ (for comparison, see also Eq. 7.4 in Chap. 7). The $\hat{H}_{\text{FX-vib}}$ collects all vibronic interaction terms between the excited states of the TDA and the bath.

The bath is modeled by making use of the harmonic oscillator model (see Sec. 3.3.3). According to Eq. 3.12, it is $\hat{H}_{\mathrm{vib}} = \sum_{m,\xi} \hbar\omega_{m\xi} \hat{b}_{m\xi}^{\dagger} \hat{b}_{m\xi}$, where the summation with respect to m and ξ runs over all $N_{\mathrm{dye}} = 4140$ dyes and all $N_{\mathrm{vib}} = 318$ intramolecular vibrational modes, respectively. Despite of the apparent strong delocalization of the Frenkel excitons, the neglection of intermolecular vibrations at this place is an adequate approximation because only very slow intermolecular conformational changes of the sterically hindered dyes are expected within the TDA (on timescales larger than several picoseconds). The appearance of static nuclear disorder is automatically modeled again thank to the equilibrated TDA nuclear structure.

Open system ansatzes are usually employed making use of the linear vibronic coupling model (see, e.g., Ref. [53]). Here, such ansatz is equivalent as well. In fact, for the family of the C8S3 cyanine molecules, the vibronic coupling strength is known to be only small with respect to the excitonic coupling in the related J–aggregates. Accordingly, the vibronic coupling Hamiltonian formulates, cf. Eq. 3.13,

$$\hat{H}_{\text{FX-vib}} = \sum_{m,\xi} \mathscr{K}_{m\xi} (\hat{b}_{m\xi} + \hat{b}_{m\xi}^{\dagger}) \hat{L}_m. \tag{8.20}$$

The projector operator $\hat{L}_m = |\bar{\Phi}_m^e\rangle\langle\bar{\Phi}_m^e|$ is based on the TDA state $|\bar{\Phi}_m^e\rangle$, which represents a molecular excitations localized on the mth dye (see Eq. 8.2). By taking the TDA ground state for reference, the vibronic interaction of the entire TDA in state $|\bar{\Phi}_m^e\rangle$ reduces to the interaction of the mth excited C8S3 dye. The particular coupling strength of vibrational mode ξ is represented by the $\mathscr{K}_{m\xi}$ in Eq. 8.20.

The influence of the vibronic coupling on the kinetics is prepared for a room temperature bath of $T = 300$ K. The quantum correlation function (introduced in Eq. 3.15)

is defined with the spectral density $J_m(\omega)$ (see Eq. 3.16). In literature, several analytical ansatzes of $J(\omega)$ can be found for cyanine–based aggregates and other biological systems [228, 53, 215]. Here, an Ohmic spectral density is utilized. Accordingly, it is $J(\omega) = \pi\hbar\lambda\frac{\omega}{\omega_c}e^{-\omega/\omega_c}$ (see Eq. E.4 in Appendix E). An adequate parametrization was found in Ref. [53]. There it was used for a planar J–aggregate of TDBC cyanines. The latter type of molecule is very similar to the C8S3. From that reference, values for reorganization energy and cut–off frequency are overtaken as $\lambda = 35$ cm^{-1} and $\omega_c = 150$ cm^{-1}, respectively.

8.5.2. The stochastic Schrödinger equation ansatz

The quantum state diffusion methodology based on a stochastic Schrödinger equation (SSE) is generally discussed in Chap. 4. Further, it is already applied in Chap. 7 to investigate dissipative hole motion within a layer of 2553 *para*–sexiphenyl molecules on a ZnO surface. By that study, the great performance of the own developed simulation technique is already demonstrated. The following dissipative study on the TDA includes the even larger number of 4140 dyes. Concerning an EET system, furthermore, the numerical costs cannot be lowered by simple restrictions of the intermolecular couplings to only nearest neighbor interaction (as in cases of charge transfer systems). On the present scale, the own developed SSE technique describes the most efficient instrument. Here, it enables to succeed the extreme computational challenge.

The simulation technique based on the cheap linear SSE is developed in Sec. 4.6. In order to determine the best performing stochastic algorithm, an initial procedure equivalently with the one executed in Sec. 7.6 must be employed. Therefore, the entire TDA structures was downscaled to several molecular tubular fragments of essentially smaller size. Then, exciton kinetics from the different linear SSE algorithms were compared with respective kinetics from the exact (but more expansive) nonlinear SSE (see Sec. 4.4.2). Successively, kinetics related to aggregate fragments of small up to medium size were compared. Again, the combination of the particular force generation function and damping operator given in Eqs. 4.69 and 4.41, respectively, delivered the most convincing results.

In application to the full TDA, therefore, the linear SSE algorithm is applied according to

$$i\hbar\frac{\partial}{\partial t}|\phi_z(t)\rangle = \Big(\hat{H}_{\mathrm{FX}}^{\mathrm{disp}} + \sum_m \mathscr{F}_m(t;z)\hat{L}_m + \hat{\mathscr{D}}(t)\Big)|\phi_z(t)\rangle, \tag{8.21}$$

with the fluctuative force algorithm, cf. Eq. 4.69,

$$\begin{aligned}\mathscr{F}_m(t;z) = \sum_k^K \sqrt{\frac{\Delta\omega J(\omega_k)}{\pi}}\Big(&\sqrt{\coth(\frac{\hbar\omega_k}{2k_{\mathrm{B}}T}) + \sinh(\frac{\hbar\omega_k}{2k_{\mathrm{B}}T})^{-1}}\cos(\omega_k t + \zeta_{mk}) \\ &+ i\sqrt{\coth(\frac{\hbar\omega_k}{2k_{\mathrm{B}}T}) - \sinh(\frac{\hbar\omega_k}{2k_{\mathrm{B}}T})^{-1}}\sin(\omega_k t + \zeta_{mk})\Big),\end{aligned} \tag{8.22}$$

and the dissipative damping operator expressed as, cf. Eq. 4.41,

$$\hat{\mathcal{D}}(t) = \frac{2}{\hbar^2} \int_0^t d\tau J(\tau) \hat{L}_m \hat{L}_m(-\tau). \tag{8.23}$$

The latter two expressions are based on the spectral density $J(\omega)$ (see Sec. 8.5.1) and its Fourier transform $J(t)$, respectively. Eq. 8.23 further depends on the local excited state projectors $\hat{L}_m$ (introduced in Eq. 8.20) and the force algorithm in Eq. 8.22 works with a set of random numbers $\{\zeta_{mk}\}_z$, which are uniformly distributed in $[0, 2\pi]$. The index z labels the differently prepared realizations of $\mathcal{F}_m(t; z)$ as well as the correspondingly achieved different system state trajectory $|\phi_z(t)\rangle$.

8.5.3. Kinetics of dissipation at room temperature

In order to uncover the TDA–internal exciton relaxation process, the evolution of the reduced density operator is computed in terms of the stochastic mean value, $\rho(t) = \sum_z |\phi_z(t)\rangle\langle\phi_z(t)|/\mathcal{N}$ (see Eq. 4.60). Here, a number of $\mathcal{N} = 1000$ trajectories were aquired to obtain converged data.

Firstly, the excitation energy in the TDA shall be discussed. Its time–dependence directly renders the dissipation in the system, i.e., the drain of energy from the electronic excitation to the vibrational bath. It is computed as the expectation value, cf. Eq. 3.11,

$$E_{\mathrm{S}}(t) = \sum_\alpha \mathscr{E}_\alpha^{(\mathrm{disp})} P_\alpha^{\mathrm{FX}}(t), \tag{8.24}$$

with energy $\mathscr{E}_\alpha^{(\mathrm{disp})}$ and population $P_\alpha^{\mathrm{FX}}(t)$ related to the excited state $|\bar{\Phi}_\alpha^{(\mathrm{disp})}\rangle$. The $\mathscr{E}_\alpha^{(\mathrm{disp})}$ are discussed in Sec. 8.4 (see Eq. 8.15) and the $P_\alpha^{\mathrm{FX}}(t)$ are straightly obtained as

$$P_\alpha^{\mathrm{FX}}(t) = \frac{1}{\mathcal{N}} \sum_z \langle \mathrm{FX}_\alpha | \phi_z(t) \rangle \langle \phi_z(t) | \mathrm{FX}_\alpha \rangle. \tag{8.25}$$

From the experimental point of view, the relaxation is directly measured by making use of optical pump–probe techniques (see, e.g., Refs. [119, 225, 219, 8, 139, 124, 125]). In order to mimick likewise laser–pulse excitations, here, two high–energy exciton wave packets are alternatively prepared, according to

$$P_\alpha^{\mathrm{FX}}(t=0) = \frac{1}{\sqrt{2\pi\sigma^2}} \exp\{ - \frac{(\mathscr{E}_\alpha^{(\mathrm{disp})} - \hbar\omega)^2}{2\sigma^2} \}. \tag{8.26}$$

Such initial pulse is spectrally focused at photon energy $\hbar\omega$ and induces a spectral Gaussian distribution with FWHM of 1 meV. The latter spectral broadening corresponds to a pulse–width of about 660 fs. (The prefactor in Eq. 8.26 accounts for the proper total exciton population of $\sum_\alpha P_\alpha^{\mathrm{FX}} = 1.0$.) Inspired by the measurements reported in Refs. [225, 219, 8, 139, 124, 125], a total simulation duration of 1000 fs was attempted right from the beginning.

The simulated $E_{\mathrm{S}}(t)$ in the TDA at 300 K is shown in Fig. 8.8a. For direct comparison, Fig. 8.8b provides a combined graphic of the absorption coefficient of the TDA

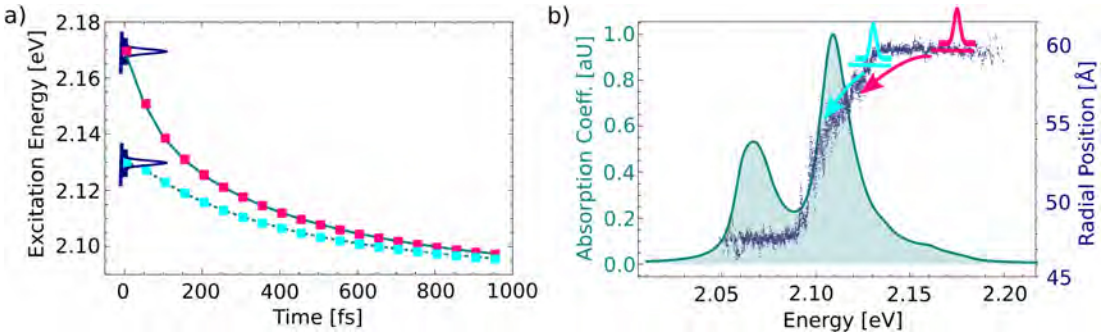

Figure 8.8.: Exciton relaxation within the tubular dye aggregate (TDA). Panel a: Time–evolution of excitation energy in the electronic system (see Eq. 8.24). The two data sets (pink and cyan color) result from two different initial exciton wave packets (see Eq. 8.26). Panel b: Migration of both exciton wave packets drawn against the TDA absorption spectrum (see Fig. 8.6a) as well as against the radial position in the TDA (see Fig. 8.6b).

excitons and their mean radial localization, $\bar{r}_\alpha$ (see again Figs. 8.6a and b, respectively). Two cases of different initially prepared population distribution around $\hbar\omega = 2.13$ eV and $\hbar\omega = 2.17$ eV are marked with the pink and cyan coloring, respectively. As illustrated, both lie in the energetically upper region of the absorption band. Starting from $E_S(t = 0) = \hbar\omega$, the excitation energy continuously decreases with progress of time. This procedure echos nicely the loss of excitation energy due to the vibronic coupling of each of the 4140 dye molecules. After the total simulation time of $t_s = 1000$ fs, a value of about $E_S(t_s) = 2.1$ eV is reached in both cases. This value lies 20 meV above the prescribed internal energy of the fully thermalized excitation ($E_S(\infty) = 2.08$ eV, according to detailed balance). However, it can be clearly recognized that the thermalization is still on. Following the trend, the presented simulation results allow characterizing the time–scale of the relaxation process to be roughly in the range of $\tau_{\text{rel}} < 3$ ps.

It was discussed initially (see Sec. 8.1) that, due to the dissipative kinetics, excitation energy is transfered from the outer wall to the inner wall of the TDA. This specific type of spatially unidirectional exciton migration can be resolved easily in the picture of molecular localized excitations, i.e., when concerning the population

$$P_m^{\text{LX}}(t) = \frac{1}{\mathcal{N}} \sum_z \langle \text{LX}_m | \phi_z(t) \rangle \langle \phi_z(t) | \text{LX}_m \rangle. \tag{8.27}$$

It describes the probability that the excitation is measured on the mth dye molecule. The Fig. 8.9a shows a histogram plot of the radial positions of the 4140 dyes within the TDA, $\rho_m^2 = x_m^2 + y_m^2$ (their positions with respect to the main cylinder axes z is not of interest). As illustrated, the dyes can be clearly distinguished and classified to belong either to the outer or the inner wall. The probability to find the excitation localized on the inner and outer cylinder, $P_{\text{in}}(t)$ and $P_{\text{out}}(t)$, is then computed by means of summing Eq. 8.27 with respect to all molecules m with $\rho_m < 54$ Å and $\rho_m \geq 54$ Å, respectively. The resulting evolutions of the computed $P_{\text{in}}(t)$ and $P_{\text{out}}(t)$ are depicted in Fig. 8.9b

Figure 8.9.: Migration of excitation energy from the outer to inner wall of the tubular dye aggregate (during exciton relaxation). Panel a: Histogram plot of radial positions of the 4140 dyes in the aggregate. Strict affiliation of the dyes to inner and outer wall can be set (see indication). Panel b: Time–evolution of the populations, $P_{\mathrm{in}}(t)$ and $P_{\mathrm{out}}(t)$, of molecular localized excited states summed up with respect to all dyes belonging to the inner (dashed lines) and outer wall (full lines), respectively. Simulation data and color code corresponds to Fig. 8.8.

by the dashed and full lines, respectively. The coloring distinguishes again between the two different utilized initial wave packet formations. For both cases, the results confirm clearly that at $t = 0$ almost the entire population is localized on the outer wall. In course of the relaxation process, then the excited state population is continuously transfered to molecular sites on the inner wall.

The $P_m^{\mathrm{LX}}(t)$ further contain information on the precise spatio–temporal evolution of the excitation on the cylinder walls. The illustrations in Fig. 8.10 impressively render the time–evolution of the spatial structure of a relaxing exciton wave packet upon the 4140 cyanine dyes (in the fashion of Fig. 8.7). The propagation of $P_m^{\mathrm{LX}}(t)$ is depicted exemplarily for six time steps (of $t = 0$, 50, 100, 250, 500 and 1000 fs) starting from the exciton wave packet with $\hbar\omega = 2.17$ eV. Surprisingly, the relaxation process is not accompanied with major lateral migration of the excitation. Instead, the structure of the prepared wave packet seems rather stable. With increasing time, its localization smears out on the outer wall. There the population deminishes while on the inner tubular wall a rather similar pattern appears with continuously increasing excited state populations.

In summary, the analysed time–domain simulations offer detailed insights on the spatio–temporal evolution of the excitation energy during the relaxation process. The data reports also directly on the interesting phenomenon of unidirectional exciton transition from the outer to the inner wall. For the first time, this important process is simulated directly and the TDA–internal exciton processes are documented up to 1 ps. Altogether, the simulated kinetics agree very well with the published experimental data of Refs. [225, 219, 8, 139, 124, 125]. It is proved that fast relaxation appears after optical excitation in the high–energy range. In particular, it is found that the exciton thermalization completes within 3 ps. This confirms further that the TDA–internal ex-

Figure 8.10.: Dissipative dynamics of the molecular excited state populations within the tubular dye aggregate. Simulation data corresponds to Figs. 8.8 and 8.9. Panel a–e: Delocalization of the excion wave packet upon the inner (bottom figure) and outer (upper figure) cylinder walls at five representative time–steps (see pink numbers indicated in the lower right corners and the overall time–line given below). Visualized color maps are prepared according to Fig. 8.7.

citon relaxation is much faster than the measured TDA fluorescence with about $\tau_{\mathrm{F}} \approx 20$ ps [118, 8]. In comparison to the present work, the focus of earlier time–domain simulations was exclusively on exciton relaxation within the inner cylinder wall. In these studies, the internal inter–wall translation of excitation energy remained completely unattended. Furthermore, the here executed simulations are substantially more sophisticated than earlier approaches which rely on simpler open system models (e.g., Pauli Master equation ansatzes [119]) and simple analytic model system [118, 119]. In this regard, the presented results supplement the existing theoretical works on the TDA system in many ways with novel insights.

In general, the here demonstrated open system studies are pioneering. The extent and quality of the here achieved dynamics are beyond any existing study on molecular structures of comparable scale (see, e.g., Refs. [161, 53, 54]). For the first time, non–Markovian dissipative dynamics are simulated in a system of more than 4000 molecules. This is made possible here only thanks to the own developed powerful SSE methodology.

8.6. Wannier–Mott Exciton Model for the Semiconductor Nanocrystal

The remaining of this chapter is devoted to the process of exciton translation from the TDA to a closely placed CdSe nanocrystal (NC). For this purpose, the excitonic system of the TDA (see Sec. 8.3) must be merged with an exciton model for the NC. The theoretical concept of Wannier–Mott excitons (WXs) are introduced in Sec. 2.2.2. In this section, it is applied on the NC. After defining the atomic structure of the NC, it follows the computation of the electronic ground state structure in a TB scheme (see Sec. 2.2.1). The related valence band and conduction band–like single–particle states offer an intuitive model of the WXs in terms of correlated electron–hole pair excitations. In Sec. 8.8, the WXs are finally employed as energy acceptor states for EET from the TDA to the NC.

8.6.1. Crystal structure and the electronic ground state

The spherical structure of the NC with a radius of about 4.5 nm is shown in Fig. 8.11a. It consists of a number of 819 Cd–atoms and 630 Se–atoms. The atoms are placed according to wurtzite structure with unit cell parametrization according to Ref. [80]. In general, atomic reorientations and other surface effects are conceivable. In CdSe NC, however, they are assumed to be of minor importance.

According to Sec. 2.2.1, the single–particle states of the NC follow as

$$|\psi_\lambda(\mathbf{r})\rangle = \sum_u \sum_l {}^u \sum_{\sigma=+,-} \mathscr{C}_{ul,\sigma}(\lambda)\chi_{ul}(\mathbf{r}-\mathbf{R}_u)|\zeta_\sigma\rangle, \tag{8.28}$$

with the atomic orbitals χ_{ul} (orbital type l of atom u) from the TB method. Here, the two spinor functions $|\zeta_+\rangle$ and $|\zeta_-\rangle$ are explicitely involved as the spin degree of freedom is not restricted. The spatial orbital and spin are collectively indicated by the index λ. By definition, the ψ_λ (with energies ϵ_λ) solve the TB eigenvalue problem

Figure 8.11.: Wannier–Mott excitons (WXs) of the CdSe nanocrystal (NC). Panel a:Crystal structure of the NC. Panel b: Energy level scheme of the lower part of the exciton band. The arrows indicate the five relevant bright excitons (two pairs of degenerate excitons and one single). Panel c: WX spectrum of the NC (purple color) against the Frenkel exciton spectrum of the tubular aggregate (green color, see also Fig. 8.6a). The gray lines indicate the energies of the WXs. The arrow marks the WX used for further analysis in Fig. 8.12b. Panel d: Contour plots of the transition densities and energies of the five relevant WXs (indicated in panel b).

Eq. 2.9 (inclusive spin–orbit coupling[2]). In practice, the $\mathscr{C}_{ul,\sigma}(\lambda)$ in Eq. 8.28 were determined by diagonalization of the spin–dependent TB Hamiltonian, $H_{ul\sigma,u'l'\sigma'}$ (see Eq. 2.9). The latter was created with respect to the present NC structure, where the required parameters (i.e., matrix elements of $H_{ul\sigma,u'l'\sigma'}$ and the overlap matrix $S_{ul,u'l'}$) were taken from Ref. [80]. (For further computational details, see Appendix G.4.)

According to the ϵ_λ, the ψ_λ are correspondingly assigned as either valence band (VB)–like or conduction band (CB)–like states. A number of N_{VB} occupied states ψ_λ (with energy ϵ_λ) and a number of N_{CB} unoccupied CB–like states $\bar{\psi}_{\bar{\lambda}}$ (with energy $\bar{\epsilon}_{\bar{\lambda}}$) are defined (see Sec. 2.2.1). Then, the total electronic ground state of the NC is formally deduced as

$$|\Psi_0\rangle = \prod_{\lambda=1}^{N_{\mathrm{VB}}} \hat{e}_\lambda^\dagger |\mathrm{vac}\rangle, \tag{8.29}$$

[2]By means of the spin–orbit coupling, the single–particle spin "quantum number" may generally take fractional values in the interval of $[-\frac{1}{2}, \frac{1}{2}]$. The spin–orbit coupling also prevents a proper factorization of the ψ_λ into a product of an orbital wavefunction and a spin function part.

making use of the operator $\hat{e}^{\dagger}_{\lambda}$ creating an electron with spinor state ψ_{λ}.

8.6.2. Correlated electron–hole pair states

Now, the occupied states ψ_{λ} and unoccupied states $\bar{\psi}_{\bar{\lambda}}$ are employed to design electron–hole pair excitations of the NC. As discussed in Sec. 2.2.2, these must be formulated prior to the computation of the aspired WXs. In principle, here a number of $N_{\mathrm{CB}} \times N_{\mathrm{VB}} = 49152096$ different electron–hole pair excitations can be considered. According to Eq. 2.11, these follow as

$$|\Psi^{\bar{\lambda}}_{\lambda}\rangle = \hat{e}^{\dagger}_{\bar{\lambda}}\hat{h}^{\dagger}_{\lambda}|\Psi_0\rangle, \tag{8.30}$$

based on $|\Psi_0\rangle$ (see Eq. 8.29) and without spin restriction. The $\hat{h}^{\dagger}_{\lambda}$ creates a hole in the VB. Counterwise, the $\hat{e}^{\dagger}_{\bar{\lambda}}$ creates an electron with state $\bar{\psi}_{\bar{\lambda}}$ (now in the CB). Likewise states $|\Psi^{\bar{\lambda}}_{\lambda}\rangle$ (with discrete spin–dependence) are formulated in Chap. 5. There, a band–like structure of energetically very dense lying $|\Psi^{\bar{\lambda}}_{\lambda}\rangle$ is observed, which motivates to directly approximate the $|\Psi^{\bar{\lambda}}_{\lambda}\rangle$ as an exciton. Here, however, this is not the case. In fact, preliminary studies showed that only very few energetically low–energy excitons are relevant for resonant EET from the TDA to the NC. For accurate energetic positioning of these few NC excitons, here, WXs are generated according to, cf. Eq. 2.12,

$$|\Psi_{\gamma}\rangle = \sum_{\lambda=1}^{N_{\mathrm{VB}}}\sum_{\bar{\lambda}=1}^{N_{\mathrm{CB}}} \mathfrak{C}_{\lambda\bar{\lambda}}(\gamma)|\Psi^{\bar{\lambda}}_{\lambda}\rangle. \tag{8.31}$$

The WXs, $|\Psi_{\gamma}\rangle$, obey the WX (eigenvalue) equation,

$$\hat{H}_{\mathrm{WX}}|\Psi_{\gamma}\rangle = \mathfrak{E}_{\gamma}|\Psi_{\gamma}\rangle, \tag{8.32}$$

as introduced in Sec. 2.3.2 (see Eq. 2.13). By that, direct Coulomb as well as exchange interaction between the created electron and hole is taken into account. In practice, the $|\Psi_{\gamma}\rangle$ were approached by determining the eigenstates of the Hamiltonian,

$$\hat{H}_{\mathrm{WX}} = \sum_{\bar{a}} \bar{\epsilon}_{\bar{a}}\hat{e}^{\dagger}_{\bar{a}}\hat{e}_{\bar{a}} + \sum_{a} \epsilon_a \hat{h}^{\dagger}_{a}\hat{h}_a + \sum_{a,b}\sum_{\bar{a},\bar{b}} \Big[- W_{\bar{a}a,b\bar{b}} + K_{\bar{a}a,b\bar{b}}\Big]\hat{e}^{\dagger}_{\bar{a}}\hat{h}^{\dagger}_{a}\hat{h}_b\hat{e}^{\dagger}_{b}. \tag{8.33}$$

Its eigenvalues $\mathfrak{E}_{\gamma}$ further represent the energies of the WXs Ψ_{γ}. In Eq. 8.33, the energies of the electrons and holes are contained as $\epsilon_{\bar{a}}$ and ϵ_a, respectively (see Eq. 2.13). Furthermore, the electron–hole pair coupling in Eq. 8.33 splits into the two parts of direct Coulomb interaction terms $W_{a\bar{a},\bar{b}b}$ (see Eq. 2.14) and exchange interaction terms $K_{a\bar{a},\bar{b}b}$ (see Eq. 2.15).

In view of the incredible number of possible WXs $N_{\mathrm{WX}} = N_{\mathrm{CB}} \times N_{\mathrm{VB}}$ which is presently $N_{\mathrm{WX}} \approx 50$ million, the WX equation cannot be solved straightly. In practice, therefore the basis set of $|\Psi^{\bar{\lambda}}_{\lambda}\rangle$ was truncated. As already announced above, here, only few Ψ_{γ} generated close to the band gap turned out to be relevant for later usage as EET acceptor states (see Sec. 8.7). In this concern, it is possible to take advantage of the

empirical observation of the higher the energy of a $|\Psi_{\bar{\lambda}}^{\bar{\lambda}}\rangle$ the lesser its contribution to a $|\Psi_\gamma\rangle$ at the lower band edge. A clear statement on that is vague, which is why Eq. 8.32 was solved in an iterative procedure where the number of participating VB and CB–like states were increased carefully until satisfactory convergence was achieved. The related computations of the NC were executed by D. Ziemann based on the former developed TB formalism and the excitonic modeling of CdSe NCs described in Ref. [80]. (For details on the computations of the different Coulomb matrix elements in Eq. 8.33 and its diagonalization procedure, see Appendix G.4.)

The computed WX energies $\mathfrak{E}_\gamma$ (defining the lower band edge) are presented in Fig. 8.11b. As typical, only few and rather isolated states are observed in the low–energy region. Moving upwards to energetically higher regions, the expected rapid increase of state density, i.e., realization of the band–like features, was found (not shown). The low–energy part of the NC exciton spectrum is also shown in Fig. 8.11c. There, the absorption lineshape (purple coloring) is confronted with the absorption band of the TDA (cyan coloring). It clearly demonstrates that only the lowest few levels are in energetic resonance with the Frenkel excitons (i.e., the EET donor states).

8.7. Resonant Energy Transfer from Aggregate to Nanocrystal

The excitonic structures of the TDA and the NC are topiced in Secs. 8.4 and 8.6, respectively. Now, the discussion turns to the phenomenon of EET from the TDA to the NC. Both (so far isolated) structures are therefore placed closely to each other. An impression of the system dimensionality is provided by the set–up in Fig. 8.12a. It exemplarily shows the NC placed centrally alongside the TDA (system z–axis) and in van der Waals contact to its surface.

The excitonic states of the combined TDA/NC system are introduced according to the general description in Sec. 2.3.4. Negligible wave function overlap of the organic and inorganic part is assumed and the excited electronic states of the interface system are expressed in terms of direct products. A basis set for expansion is created straightly and the interface excited states can be written as a linear combination of Frenkel exciton (FX)–like basis states,

$$|\mathrm{FX}_\alpha\rangle = |\bar{\Phi}_\alpha^{(\mathrm{disp})}\rangle \otimes |\Psi_0\rangle, \tag{8.34}$$

and WX–like basis states reading

$$|\mathrm{WX}_\gamma\rangle = |\bar{\Phi}_0\rangle \otimes |\Psi_\gamma\rangle. \tag{8.35}$$

The former FX–like state represent the TDA in FX state $|\bar{\Phi}_\alpha^{(\mathrm{disp})}\rangle$ (see Eq. 8.16), while the NC is in electronic ground state configuration $|\Psi_0\rangle$ (see Eq. 8.29). Counterwise, the latter WX–like state describes the TDA in ground state configuration $\bar{\Phi}_0$ (see Eq. 2.20) and the NC realizing the WX state Ψ_γ (see Eq. 8.31).

In Chap. 5, Frenkel–like excitons and electron–hole pair state are discussed for the *para*–sexiphenyl/ZnO system. Thereby, the electrostatic interaction between the organic and inorganic part turns out to be only of very weak influence on the excitonic

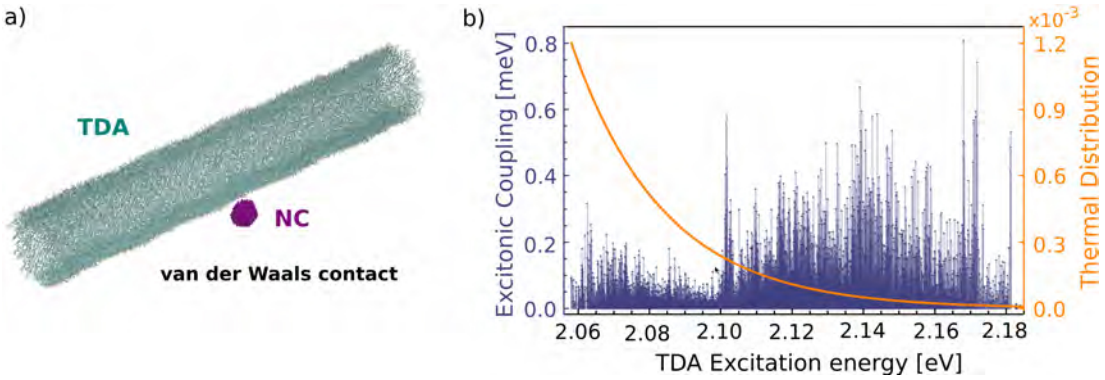

Figure 8.12.: Excitonic coupling between the tubular dye aggregate (TDA) and the nanocrystal (NC). Panel a: Installed system set–up (NC centrally and in van der Waals contact distance to the TDA). Panel b: Excitonic couplings (purple color) between first brightest Wannier–Mott exciton (indicated by the arrow in Fig. 8.11c) to all available Frenkel excitons drawn against their energy. Orange colored line shape gives the Boltzmann (thermal) distribution of the Frenkel excitons at 300 K.

structure of the interface. Here, it shall be directly argued in this sense and only the excitonic coupling between the two bodies is respected. Accordingly, the excitonic Hamiltonian of the TDA/NC system simplifies to

$$\hat{\mathscr{H}} = \hat{H}_{\mathrm{FX}}^{(\mathrm{disp})} + \hat{H}_{\mathrm{WX}} + \hat{\mathscr{J}}^{\mathrm{FX\text{-}WX}}. \tag{8.36}$$

The two exciton Hamiltonians, $\hat{H}_{\mathrm{FX}}^{(\mathrm{disp})}$ and $\hat{H}_{\mathrm{WX}}$, are introduced in Eqs. 8.1 and 8.33, respectively. The $\hat{\mathscr{J}}^{\mathrm{FX\text{-}WX}}$ represents the excitonic coupling between both types of possible excitons (see the expression below in Eq. 8.37). In particular, hybridized exciton states of partial FX and WX character may be formed. Whether these appear in the present case depends directly on the strength of $\hat{\mathscr{J}}^{\mathrm{FX\text{-}WX}}$ and is concerned in the subsequent section.

8.7.1. Excitonic coupling across the hybrid interface

In general, the strength of the excitonic coupling $\mathscr{J}^{\mathrm{F\hat{X}\text{-}WX}}$ depends critically on the spatial configuration of the TDA and the NC. Diverse experimental and theoretical investigations already put a lot of effort in this issue (see Sec. 8.1).

In Ref. [80], a theoretical study on the excitonic coupling between a single chromophore molecule and a likewise spherical CdSe NC is presented. Particular focus was thereby put on its dependence on the distance between the molecule and the NC surface. Here, the process of EET is not restricted to a single molecule, but the entire TDA is involved. This means that all 4140 C8S3 molecules participate in different way and a much more complex dependence of $\mathscr{J}^{\mathrm{F\hat{X}\text{-}WX}}$ on the mutual spatial configuration must be expected. In accordance, also significant variation with respect to the FX index α was anticipated right from the beginning. All the different matrix

elements, $\mathcal{J}_{\gamma\alpha}^{\text{FX-WX}} = \langle \text{WM}_\gamma | \hat{\mathcal{J}^{\text{FX-WX}}} | \text{FX}_\alpha \rangle$ (see Eq. 8.36), were computed individually. By inserting Eqs. 8.34 and 8.35, it follows

$$\mathcal{J}_{\gamma\alpha}^{\text{FX-WX}} = \langle \Phi_0 | \langle \Psi_\gamma | \sum_{i}^{N_{\text{el}}^{\text{TDA}}} \sum_{j}^{N_{\text{el}}^{\text{NC}}} \frac{e^2}{|\mathbf{r}_i - \mathbf{r}_j|} | \Psi_0 \rangle | \bar{\Phi}_\alpha^{(\text{disp})} \rangle. \tag{8.37}$$

As indicated, the $\mathbf{r}_i$ and $\mathbf{r}_j$ represent the coordinates of the number of $N_{\text{el}}^{\text{TDA}}$ electrons in the TDA and $N_{\text{el}}^{\text{NC}}$ electrons in the NC, respectively. The expression in Eq. 8.37 shows similarities to the more simple case of intermolecular excitonic coupling (see Eq. 2.29). However, here the $\mathcal{J}_{\gamma\alpha}^{\text{FX-WX}}$ couples the de–excitation of the αth FX and the excitation of the γth WX. This means that the $\mathcal{J}_{\gamma\alpha}^{\text{FX-WX}}$ must be constructed instead based on transition densities for the particular excitons.

Concerning the TDA, the transition density

$$\rho_\alpha^{\text{FX}}(\mathbf{x}) = \sum_{m}^{N_{\text{dye}}} \mathscr{C}_m^*(\alpha) n_{eg}^{(m)}(\mathbf{x}) \tag{8.38}$$

is required. It is based on the $S_0 \rightarrow S_1$ transition density $n_{eg}^{(m)}(\mathbf{x})$ of the mth C8S3 dye as introduced above in Sec. 8.3.3 (see Eq. 8.14). Via the complex conjugate of the expansion coefficients $\mathscr{C}_m^*(\alpha)$ (see Eq. 8.16), the molecular densities are rendered to the excitation of the αth FX. Similarly, the NC transition density

$$\rho_\gamma^{\text{WX}}(\mathbf{y}) = \sum_{\lambda}^{N_{\text{VB}}} \sum_{\bar{\lambda}}^{N_{\text{CB}}} \mathfrak{C}_{\lambda\bar{\lambda}}^*(\gamma) \rho_{\lambda\bar{\lambda}}^{(\text{e-h})}(\mathbf{y}) \tag{8.39}$$

is defined. It is based on the excitation of the γth WX in terms of the superposition of properly weighted electron–hole pair excitations (see Eq. 8.31). The latter transitions in the NC (i.e., $|\Psi_0\rangle \rightarrow |\Psi_\lambda^{\bar{\lambda}}\rangle$) are represented by the electron–hole transition densities,

$$\rho_{\lambda\bar{\lambda}}^{(\text{e-h})}(\mathbf{y}) = e \sum_{u,l} \sum_{u',l'} \chi_{u'l'}^*(\mathbf{y} - \mathbf{R}_{u'}) \chi_{ul}(\mathbf{y} - \mathbf{R}_u) \Big[\mathscr{C}_{u'l',+}^*(\lambda) \mathscr{C}_{ul,+}(\bar{\lambda}) + \mathscr{C}_{u'l',-}^*(\lambda) \mathscr{C}_{ul,-}(\bar{\lambda}) \Big], \tag{8.40}$$

which are itself based on the VB–like and CB–like single–particle states ψ_λ and $\bar{\psi}_{\bar{\lambda}}$ (see Eq. 8.28). In the description of the NC, electron spin is explicitly treated . Concerning Eq. 8.40, this results automatically in the proper total spin restriction.[3] The FXs in the TDA, on the other side, are exclusively constructed based on $S_0 \rightarrow S_1$ molecular transition, i.e., the singlet character of all FXs is strictly prescribed. Concerning Eq. 8.39, therefore the spin restriction is ensured by definition and its explicit consideration is unnecessary. By utilizing the expressions Eq. 8.38 and 8.39, the excitonic coupling (see

[3] The second term in the rectangular bracket of Eq. 8.40 demonstrates that the transition density becomes zero if the ψ_λ and $\bar{\psi}_{\bar{\lambda}}$ carry opponent spin quantum numbers. It can be proved straightly that, in these cases (and noting the possible rotation of the spin coordinate system), either $\mathscr{C}_{u'l',+}^*(\lambda) = 0$ and $\mathscr{C}_{ul,-}(\bar{\lambda}) = 0$ or vice versa $\mathscr{C}_{u'l',-}^*(\lambda) = 0$ and $\mathscr{C}_{ul,+}(\bar{\lambda}) = 0$.

Eq. 8.37) further transforms to

$$\mathcal{J}_{\gamma\alpha}^{\text{FX-WX}} = \int d^3\mathbf{x} \int d^3\mathbf{y} \frac{\left[\rho_\alpha^{\text{FX}}(\mathbf{x})\right]^* \rho_\gamma^{\text{WX}}(\mathbf{y})}{|\mathbf{x}-\mathbf{y}|}, \tag{8.41}$$

where the de–excitation of the FX is accounted for by the complex conjugation of $\rho_\alpha^{\text{FX}}(\mathbf{x})$. In order to compute the integral expression in Eq. 8.41, the transition densities $n_{eg}^{(m)}(\mathbf{x})$ and $n_{\lambda\bar{\lambda}}^{(\text{e–h})}(\mathbf{y})$ were approximated once more by making use of atomic centered partial transition charges (for details, see Appendixes D and G.4).

The first investigated TDA/NC arrangement is depicted in Fig. 8.12a. It describes the NC placed centrally alongside and in van der Waals contact to the TDA. Accordingly, Fig. 8.12b shows the computed excitonic couplings between the energetically lowest $|\text{WX}_{\gamma=1}\rangle$ and all 4140 FXs. The values are collectively drawn versus the energy $\mathscr{E}_\alpha^{(\text{disp})}$ of the related FXs. The energetic position of the particular $|\text{WX}_{\gamma=1}\rangle$ is indicated with the arrow in the spectrum of Fig. 8.11c (purple line). Although the NC is placed prominently to the TDA surface, the excitonic coupling terms take only values below 1 meV. In order to generalize this statement, also the coupling matrix elements related to energetically higher acceptor states $|\text{WX}_\gamma\rangle$ (with $1 < \gamma \leq 30$) were examined carefully. No larger excitonic couplings than the ones given in Fig. 8.12b were thereby found. Instead, the general trend of the higher WXs goes towards coupling values which are magnitudes smaller.

Even the highest peak values of the here computed excitonic couplings are smaller than the earlier documented values in Ref. [80]. Indeed, this is reasonable although the transition dipole moment of the pheophorbide–a molecule ($\mathbf{d}_m = 4.6$ D), which is coupled in Ref. [80] to a similar CdSe NC, amounts less than half of the present value of the C8S3 dye ($\mathbf{d}_m = 11.0$ D). The explanation for the here found smaller couplings lies in the delocalization of the FXs on the TDA. As discussed in Sec. 8.4.2, in the great majority of cases the FXs delocalize upon vast areas of the TDA. These areas appear huge with respect to the very particular attachment site of the NC (see Fig. 8.12a). And while the FXs are delocalized upon large zones, they efficiently couple only via very few dyes in direct vicinity of the NC. This effect considerably lowers their excitonic couplings.

Apparently, the EET process between TDA and NC takes place in the limit of weak excitonic coupling. In consequence, a transfer model based on incoherent rate expressions for resonant exciton transitions becomes adequate. In this context, one must also negate the noticeable formation of hybrid excitons at the interface which are especially attractive for novel photonic applications (see Sec. 1). Their appearance would require essentially higher values of $\mathcal{J}_{\gamma\alpha}^{\text{FX-WX}}$ (in the range of the intermolecular excitonic couplings $\mathcal{J}_{mn}$ between the C8S3 dyes).

8.7.2. Rates of excitation energy transfer

Only weak excitonic coupling matrix elements are reported in Sec. 8.7.1. Accordingly, the exciton translation from the TDA to the NC can be quantified based on a constant rate expressions of Fermi's golden rule. The corresponding formula is basically

enlightened in Sec. 3.2.2 (see Eq. 3.5). In application to the present situation, it reads

$$k_{\mathrm{TDA}\rightarrow\mathrm{NC}} = \frac{2}{\hbar}\sum_{\alpha}^{N_{\mathrm{FX}}}\sum_{\gamma}^{N_{\mathrm{WX}}} f(\mathscr{E}_{\alpha})|\mathscr{J}_{\gamma\alpha}^{\mathrm{FX\text{-}WX}}|^{2}\frac{\Gamma}{(\mathfrak{E}_{\gamma}-\mathscr{E}_{\alpha}^{(\mathrm{disp})})^{2}+\Gamma^{2}}. \tag{8.42}$$

The transfer starts from a thermal distribution of FX population using $f(E) = 1/Z \times \exp(-E/k_{\mathrm{B}}T)$. Its exponential decay is shown by the orange colored line in Fig. 8.12b for the installed temperature of 300 K (i.e., it is $k_{\mathrm{B}}T = 27$ meV). The original δ–function (see Eq. 3.4) is already adapted to homogeneous broadening and a Lorentzian function is substituted in Eq. 8.42. Concretely, a broadening of $\Gamma = 5$ meV is utilized as physically plausible value smaller than $k_{\mathrm{B}}T$. Accounting for inhomogeneous broadening was unnecessary at this place. As discussed in Sec. 8.2, disorder effects are already integrated by means of the basic equilibrated nuclear TDA structure. Further, only few WXs show the required energetic resonance with the band of FXs (see again Sec. 8.6.2 and Fig. 8.11c). In practice, the vast majority of higher WXs was disregarded from the summation in Eq. 8.42 and only the lowest previously determined WXs played a role for its computation.

The present rate model distinguishes from the ansatz employed beforehand in Chap. 5. There EET rates are computed for different transitions from a single donor state to a manifold of semiconductor states. Here, an initial thermalization process within the FX band of the TDA is assumed instead. This ansatz accords to the discussion in Sec. 8.5.3 which ascertains essentially faster internal FX relaxation and dephasing processes with τ_{rel} in the range of only few picoseconds. Contrarily, the EET is supposed to take place on a time–scale of at least one order of magnitude larger ($\tau_{\mathrm{rel}} \ll 1/k_{\mathrm{TDA}\rightarrow\mathrm{NC}}$). On that scale, exclusively incoherent population transfer proceeds in the absence of coherent wave packet migration.

Regarding the TDA/NC set–up depicted in Fig. 8.12a (NC in van der Waals contact), the EET rate of about $k_{\mathrm{TDA}\rightarrow\mathrm{NC}} = 4.2/\mathrm{ns}$ were computed. Being in the *inverse nanosecond* regime, this value truely confirms the above suspicion of $\tau_{\mathrm{rel}} \ll 1/k_{\mathrm{TDA}\rightarrow\mathrm{NC}}$. It gives message on exciton translation to the NC (even in the spatially attached configuration) which works essentially slower than the TDA–internal relaxation processes. Moreover, the related transfer–time in the nanosecond range generally confirms with the measured values of EET from the TDA to closely attached QDs reported by Rabe et al. [8].

8.7.3. Dependence on the system set–up

This last part of the EET study is devoted to the detailed understanding of the transfer rate $k_{\mathrm{TDA}\rightarrow\mathrm{NC}}$ in dependence on the TDA/NC system set–up. In Fig. 8.13, the $k_{\mathrm{TDA}\rightarrow\mathrm{NC}}$ is mapped under variation of the NC position along the system axes z and R. Thereby, the NC is translated without rotation upon a 2-D grid in the z-R–plane with respect to the TDA (see sketch on the left–hand side). By scanning upon this grid, rate values were computed for each of the grid points resulting in the pixel structure of the map surrounding the TDA (indicated in the lower left corner). The coloring of the pixels represents the computed rate values according to the given logarithmic scale.

Figure 8.13.: Rate for exciton transition from the tubular dye aggregate (TDA) to the nanocrystal (NC) according to Eq. 8.42. The color map in the main panel illustrates the dependence of the rate on the positioning of the NC. The NC is moved in the $z - R$–plane according to the sketch on the left–hand side. Please note the logathmic scale of the color map.

Apparently, the EET rate is rather independent on the longitudinal positioning of the NC alongside the TDA (in the range of about $|z| < 28$ nm). This approves the above statement, that (with respect to the z–axis) the FXs are rather equally distributed in the middle part of the TDA. The rate is also scanned when moving the NC around the "open" endings of the TDA. Placed right at the cylinder edge (the "rectangular corner" in Fig. 8.13), the EET rate decreases somewhat faster with increasing distance. This observation is physically plausible in view of of the smaller number of dye molecules exposed to the NC at the TDA edges and the argumentation given at the end of Sec. 8.7.1. Respective behavior is monitored for NC positions right in front of the "hollow" ending of the TDA.

The dependence of the $k_{\mathrm{TDA}\to\mathrm{NC}}$ on the TDA–NC distance deserves closer inspection. It is the intention of this study to evaluate the workability of the approximate Förster–type rate ansatz. In comparison with the present rate ansatz where the $\mathcal{J}_{\gamma\alpha}^{\text{FX-WX}}$ are deduced in atomic resolution, the Förster's ansatz is based on excitonic couplings from a point–dipole interaction model. Because of its simplicity, the latter (with its prominent $1/R^6$–dependence on the donor–acceptor distance R) is very commonly employed in literature (see, e.g., Refs. [111, 229, 8, 230, 11, 26]). Nevertheless, for the TDA/NC system the adequacy of the point–dipole interaction model is highly questionable. Although the TDA and the NC seems to be "well..seperated", their distance R would have to be much larger than the spatial exciton extention in order to properly establish a point–dipole ansatz. To prove this, the NC is placed again in the middle position ($z = 0$) with respect to the TDA (see lower left panel of Fig. 8.14). The $k_{\mathrm{TDA}\to\mathrm{NC}}$ was determined for increasing R values up to $R = 900$ nm (see Fig. 8.14a). In Fig. 8.14b, the *double logarithmic* plot of the calculated $k_{\mathrm{TDA}\to\mathrm{NC}}$ against the coordinate axis R is provided. The characteristic $\propto 1/R^x$–dependence can be determined straightly from a linear fit model (via the relation $\log(k_{\mathrm{TDA}\to\mathrm{NC}}) = -x\log(R) + a$). The nonlinear curve

Figure 8.14.: Rate for exciton transition from the tubular dye aggregate (TDA) to the nanocrystal (NC). Panel a: Rate dependence when the NC is moved perpendicular away from the TDA, according to the sketch in the lower left figure. Panel b: Double logarithmic plot of the data shown in panel a. Colored slope lines result from linear fitting routines in the three regions (same coloring). The fitted behaviors of the rate (with respect to distance R) are also indicated (for details, see the main text). Panel c: Dependence of the rate on the NC rotation around the axis ϕ (see again lower left panel).

in Fig. 8.14b approves directly the inadequacy of an uniform point–dipole approximation. Instead of a straight $1/R^6$–dependence, here at least three different regions must be distinguished with $R^{(\mathrm{I})} < 3$ nm, $3 < R^{(\mathrm{II})} < 40$ nm and $R^{(\mathrm{III})} > 40$ nm (see indications in Fig. 8.14b). Concretely, fit values of $x^{(\mathrm{I})} = 0.8$, $x^{(\mathrm{II})} = 3.3$ and $x^{(\mathrm{III})} = 5.7$ were obtained for the three zones. In close distance, the NC clearly "notices" the individual point charges dispersed upon of the opponent vast TDA. This perception of the atomistic structure explains the untypical dependency of $k_{\mathrm{TDA}\to\mathrm{NC}} \propto 1/R^{0.8}$ (region I). With increasing R this "impression" changes and the rate shows dependences of about $\propto 1/R^3$ (region II). In region III with $R > 40$ nm, the trend towards the prominent $1/R^6$–behavior becomes finally apparent.

In order to judge about the long distance asymptotic limit of the rate, here, the complete TDA length with about 64 nm must be taken into consideration. Indeed, all FXs localized on the entire TDA contribute to $k_{\mathrm{TDA}\to\mathrm{NC}}$. When the fitting procedure was repeated using only values of $R > 650$ nm, i.e., for distances at least ten times larger

than the TDA extension, a behavior of $k_{\mathrm{TDA}\rightarrow\mathrm{NC}}(R) \propto 1/R^{5.9}$ was uncovered. Only in this distance the Förster–type modeling of the EET seems adequate. In general, the point–dipole interaction model must be critically recaptured whenever cases of strongly delocalized excitons with diverse localization features are considered.

The characteristic distance behavior of EET between nanoparticles, nanowires and quantum wells were also studied in Refs. [187] and [131]. Based on an analytic macroscopic approach, the authors demonstrated that in their model, i) only the acceptor dimensionality is decisive for the specific R^{-x}–behavior of the EET rate in the long distance asymptotic limit and ii) indeed the typical behavior with $x = 6$ appears only in the case of a nanoparticle (i.e., a finite structured energy acceptor unit). The latter finding agrees very well with the asymptotic distance dependence computed here for a realistic system in atomistic resolution.

Additionally, the EET rate is probed against the rotational motion of the NC. In general, only minor variations of $k_{\mathrm{TDA}\rightarrow\mathrm{NC}}$ were uncoved while rotating the NC around the cylinder z–axis in fixed distance R. This is reasonable since the cylinder symmetry of the TDA is roughly rendered on its excitonic structure. The same observation was made when monitoring $k_{\mathrm{TDA}\rightarrow\mathrm{NC}}$ against the three internal axes of rotation of the NC. For instance, the values of $k_{\mathrm{TDA}\rightarrow\mathrm{NC}}$, scanned during rotation along the ϕ–axis, are illustrated in Fig. 8.14c. For the scan, the center of the NC was fixed at $z = 0$ and $R = 2$ nm (see again the sketch in the lower left of Fig. 8.14). As demonstrated, the computed rates show no essential sensitivity for the NC orientation. In view of the non–isotropic wurtzite structure of the NC, the minor dependence on its rotation (see periodic features in Fig. 8.14c) was actually unexpected. Instead, it seems that the nanoscale size and the rather spherical shape of the NC are more decisive here. This explanation is supported by shape of the relevant excitonic NC states. As shown in Fig. 8.11d, they describe states which are attributed with either "s–type" (rather spherical) or "p–type" transition densities. The latter appear threefold energetically bundled (almost degenerate) according to the typical p_x, p_y and p_z spatial orientations. The computed EET rates collect contributions from all these excitonic states and consequently show the rather unspecific dependence on the NC rotations.

Together the executed studies lead to the conclusion that only the perpendicular TDA–NC distance is of prior importance for the EET from the TDA to the NC. Only very small variation of the transfer rate is documented when rotating the NC with respect to the TDA longitudial axis or its own center of mass. Both findings are important insights as it is very cumbersome to control the rotational degrees of freedom under experimental conditions. Moreover, it is proved that, in the range of TDA–NC distances of $R < 40$ nm, the EET cannot be modeled in terms of Försters theory. Instead, critical overestimations of computed Förster rates must be anticipated. Proper workability of the latter is detected only in cases of distances larger than 650 nm. In general, this insight can be rendered to many modern hybrid systems which are constructed based on functional donor and acceptor components with excitonic delocalizations larger than their direct distance. In all these cases, the utilization of the Förster model ansatz should be thoroughly revisited.

8.8. Summary and Concluding Remarks

The focus of this chapter is put on a hybrid system describing a double–walled tubular dye aggregate (TDA) coupled to a CdSe nanocrystal (NC). In lab, the TDA is fabricated by self–assembly from C8S3 cyanine molecules in aqueous solution. Superstructions with about 13 nm diameter and length up to several μm were directly measured. Owing to their interesting excitonic properties, these TDAs are recently considered as very promising components especially for novel optoelectronic nanohybrid materials. The first concern of this study is the dissipative exciton migration within the TDA after its optical excitation. In the second main part of this study, the phenomenon of excitation energy transfer (EET) from the TDA to the NC is inspected. The latter means the translation of Frenkel excitons of the TDA to Wannier–Mott excitons of the NC.

In order to compute the excitons of the TDA, a 64 nm long tubular fragment is constructed based on a formerly equilibrated nuclear configuration. The here applied generalized excition approach is beyond the standard Frenkel model. Besides electrostatic effects, it takes into account corrections due to dispersion interactions of the dye molecules. It is shown that this type of correction is responsible for the appearance of the two main exciton bands, which can be straightly assigned to the outer and the inner cylinder wall of the TDA, respectively. An extensive study on the Frenkel excitons of the TDA is undertaken. Their spatial structuring across the cylinder walls is discussed in molecular detail. For the first time, a clear view on the localizations of the excitons on the inner and outer wall of the TDA is provided in dependence on their energy. Exciton delocalizations over hundreds of dye molecules are uncovered. This is surprising and appears vast concerning the equilibration of the nuclear structure. Several prominent types of exciton localizations are thereby observed. These particular findings have never been documented in literature beforehand.

Based on that, a pioneering open system study on the TDA–internal exciton relaxation at room temperature is presented. Therefore, an intramolecular vibrational bath is conceived and the own developed algorithm based on a stochastic Schrödinger equation is applied. In an unique way, it make possible to achieve the exciton relaxation kinetics upon the complete 64 nm long TDA structure. The enormous number of 4140 excited states are thereby included. The executed study demonstrates the power of the new simulation technique. On the present scale, it works much more efficiently than equivalent master equation approaches. In order to uncover the interesting relaxation processes, dissipative dynamics are computed starting from an exciton wave packet prepared in the high–energy region. Former time–domain simulations exclusively concentrated on relaxation processes within the inner wall and could not detect the supposed exciton migration from the outer to the inner wall. For the first time, this internal exciton translation is now directly simulated. Its spatio–temporal behavior is uncovered in molecular resolution. The relaxation process completes within less than 3 ps. This agrees with available spectroscopic data. Besides many novel insights on the TDA–internal excitonic structure and dynamics, the stochastic Schrödinger equation method is manifested as a highly potential instrument in application to large–scale open systems.

In the second main part of this work the TDA is accompanied by the NC. Coulomb–

correlated electron–hole pair excitations of the NC are computed based on a TB scheme and the Wannier–Mott exciton equation. After initial exciton relaxation within the TDA, excitation energy is further transfered from the TDA to the NC. This process was also in the focus of recent experimental investigations and measured to take place on the nanosecond time–scale. As the key quantity, the excitonic coupling between pairs of Frenkel and Wannier–Mott excitons is required. Here, all coupling terms are computed in full atomistic resolution. Concerning the gigantic size of the hybrid system, this describes a remarkable challenge and emphasizes the pioneering character of the entire study. Despite the significant computational effort, this ansatz is highly advantageous. On this basis, transfer rates accoring to Fermi's golden rule are formulated without utilizing the point–dipole approximation (used in the Förster model). Here, evidence is given that, even in van der Waals contact, the excitonic couplings stay below 1 meV and the total EET rate amounts $k_{\mathrm{TDA}\rightarrow\mathrm{NC}} \approx 4/\mathrm{ns}$ (i.e., it is $\tau_{\mathrm{EET}} \approx 250$ ps). The uncovered EET rates are moderate and confirm the roughly estimated transfer times based on earlier measurements.

Diverse architectures of hybrid systems based on TDAs are recently under experimental investigation. However, detailed theoretical insights on their excitonic properties in dependence on, e.g., the positioning and orientation of a close NC are still missing. In this regard, the rate of EET in the present TDA/NC system is finally inspected under variation of its geometry. Novel and important insights are discussed. Surprisingly, it was uncovered that the EET process is very robust against rotational motion of the NC as well as translation alongside the TDA. These are important informations, e.g., for specific device constructions which have also never been reported before.

In a final study, particular focus lies on the dependence of the rate on the vertical TDA–NC distance R. Here, it is clearly evidenced that the EET rate behaves neither according to the $1/R^6$–dependence, which is prescribed by the Förster theory, nor according to an uniform $1/R^x$–dependence (with constant x) at all. Instead, the dependence varies from $k_{\mathrm{TDA}\rightarrow\mathrm{NC}} \propto 1/R$ to $\propto 1/R^3$ in the range of $0 < R < 40$ nm. It is observed that the Förster dipole–interaction model possesses no validity here within distances of $R < 600$ nm. This is due to the nanoscopic extention of the TDA and the vast exciton delocalization. In general, modern hybrid nanosystems realize donor–acceptor distances which are much smaller than the exciton delocalization within the individual components. It must be expected that the Förster theory leads to overestimated EET strengths in all such systems. This finding is of exceptional relevance and declares the urgency for establishing more adapted transfer models.

9. Summary and Outlook

A broad section of modern physics and theoretical chemistry concentrates on electronic properties of composite nanostructures. Theoretical studies on that scale, on one side, critically depend on a nanostructured modeling of the system. On the other side, they require atomistic descriptions of the occurring quantum processes. This typically precludes fully ab–initio ansatzes. So, to meet both requirements, modern research yearns continuously for atomistic approaches and related computational schemes which are more and more efficient. In this thesis, new specific atomistic descriptions and efficient computational schemes are demonstrated. Particular focus lies here on hybrid interface systems consisting of molecular aggregates and semiconductor nanostructures. Well–established theoretical and computational ansatzes are therefore revisited and combined adequately regarding their respective performance goals. It is a key challenge of this work to introduce a new stochastic Schrödinger equation technique. It is particularly conceived for efficient simulation of non–Markovian dynamics of huge open quantum systems. The here accomplished simulation studies are impressive and pioneering concerning quality and scale. They witness major progress in the field of non–Markovian open system dynamics.

In the main part of this work, the developed models and methodologies are used to investigate mechanisms of photoinduced charge separation and excitation energy transfer processes in two realistic types of hybrid nano–systems of recent experimental interest [67, 72, 8, 26]. The hybrid system of *para*–sexiphenyl molecules aggregated on a flat ZnO surface is treated firstly. The second system describes a gigantic tubular aggregate of C8S3 cyanine dyes coupled to a closely positioned CdSe nanocrystal.

Quantum descriptions of such nanoscale systems are typically based on many thousands of vastly delocalized electronic states. That is particularly the case here and makes simplifying diabatic state ansatzes imperative. By means of that, the interface systems are each fragmented and their states are constructed as direct products of smaller substructure site states. The prize for this is paid with tremendous numbers of inter–site coupling terms, which are needed to fianlly describe the electronic Hamiltonians. Furthermore, many "standard" simulation methods are rather inefficient and suffer strongly with increasing number of states. In particular, the direct solution of the quantum master equation in order to obtain open quantum system dynamics is characterized with very unfavorable scaling features of the computational costs and should not be applied to large–scale systems. In order to overcome this limitation, here an own strategy based on the quantum state diffusion method is developed. More concretely, a stochastic Schrödinger equation is propagated which computational cost scales only linearly with the size of the system. Thanks to that great efficiency, non–Markovian dynamics in very realistic interface systems including several thousand states are successfully executed. An atomistic modeling allows investigating the interesting kinetics

in both huge quantum systems in remarkable resolution. By that, the present work completes the detailed understanding of the two particular interfaces in many ways, and so also the general comprehension of photoinduced charge separation kinetics and the excitation energy transfer is brought forward.

Spectroscopic investigations of *para*–sexiphenyl molecules on smoothed ZnO interfaces showed that, under irradiation of light, free charge carriers are generated to both sides of the interface [65, 68, 67]. So far, detailed theoretical insights on these processes are still missing. Here, time–domain simulations in atomistic resolution are performed. The direct energy transfer across the interface from the Frenkel excitons in the molecular part to electron–hole pair excitations in the ZnO are studied as well as the more involving process of Frenkel exciton migration to the interface region and subsequent decay into charge–separated states. The required transfer integrals for the electron injection from excited molecules into the ZnO substrate are modeled with an efficient and specially developed ansatz. Femtosecond simulations on the photoinduced coherent wave packet dynamics across the interface are presented. The detailed discussion notices also the formation of optically addressable charge–transfer excitons at the interface. In particular, the importance of the explicit laser–pulse simulation is demonstrated carefully. Here, alternatively prepared initial excited states are identified as highly potential sources of error. Since such initial conditions substituting an ultrafast laser–pulse are very commonly used in literature, the presented results are also generally of high relevance.

Efficient generation of free charge carriers is the decisive factor concerning a possible future photovoltaic device. For this purpose, basically the Coulomb–attraction between electron and hole must be overcome. Here, time–domain room temperature simulations in the picosecond–range are executed based on the own stochastic Schrödinger equation technique. Non–Markovian dissipative dynamics of a hole in a film of 2553 *para*–sexiphenyl molecules placed on a macroscopic ZnO slab become possible. The here applied interface set–ups are particularly motivated by recently observed scenarios of very fast electron trapping in opponent ZnO surface regions [66, 34, 70]. Remarkable characteristic features of the dynamics are illustratively explained. Specific differences with respect to pure coherent type of wave packet motion are emphasized in direct comparison. It is documented that, only under condition that the electron itself is swiftly evacuated from the interface into the ZnO bulk region, free charge carriers can be guaranteed on a long–term basis. In particular, the initial wave packet motion of the created hole is too "weak" in order to remove the hole from the trapped electron by means of ballistic motion. Based on the simulations, message is clearly given on basic problems of the *para*–sexiphenyl/ZnO interface concerning applications in photovoltaics. Altogether, the offered results bring forward the detailed understanding of the optoelectronic processes at the *para*–sexiphenyl/ZnO interface.

Also the second system is inspired by recent spectroscopic investigations [8, 26]. Accordingly, energy transfer from tubular dye aggregates to semiconductor nanocrystals is expected in the range of several hundred picoseconds. Besides, much faster exciton relaxation processes within the tubular aggregate were uncovered on the time–scale of

only few picoseconds [119, 139]. Here, a detailed theoretical description of both processes is presented. It starts with a 300 K equilibrated nuclear structure of a 64 nm long tubular aggregate. Based on that, a very sophisticated generalized Frenkel exciton Hamiltonian is constructed. It accounts for dispersive interactions of the individual C8S3 molecules. Here, dispersion play a critical role regarding the double–walled structure of the tubular aggregate [122]. By that, the present exciton model gives a much more realistic picture of the aggregate compared with preceding theoretical studies [118, 119].

Non–Markovian dynamics are executed to investigate the aggregate–internal exciton relaxation processes. The simulations are again based on the own stochastic Schrödinger equation technique. The complete tubular fragment involving the vast number of 4140 Frenkel excitons is simulated. From diverse experiments, it is further known that, during relaxation, energy is unidirectionally transfered from the outer to the inner cylinder wall of the tubular aggregate [118, 139, 125]. For the first time, this interesting process is now directly monitored in non–Markovian time–domain simulations. In agreement with the experiments, initially prepared high–energy exciton wave packets settle to thermal distribution within less than three picoseconds [139, 125]. The scale and level of the present simulations are pioneering and clearly beyond the simple models and master equation ansatzes of former studies [118, 119, 219].

Subsequently, energy transfer from the aggregate to the spherical CdSe nanocrystal is described. Therefore, the Frenkel exciton model is augmented by Wannier–Mott excitons of the nanocrystal. As a key challenge, huge numbers of excitonic coupling strengths are computed in atomicistic resolution. Even in van der Waals contact distance, these couplings stay below 1 meV. In turn, the generally expected hybrid excitons fail to appear. Then, rates for exciton transfer from the aggregate to the nanocrystal are computed based on Fermi's golden rule. Imposing insights into the transfer are gathered under variation of the spatial system set–up. Clear evidence is given that it is essentially the perpendicular distance between the two bodies which decides about the transfer strength. In agreement with measured data [8], the fastest transfer mechanism happens in the range of several hundred picoseconds. The positioning of the nanocrystal alongside the aggregate and its actual orientation are varied without considerable impact. Likewise detailed computations are documented here for the first time. They are highly relevant for future tubular aggregate/nanocystal system preparations. Finally, the substantial advantage of the here applied atomistic exciton model is emphasized against the more common Förster rate ansatz. In harsh contrast, the latter is based on a dipole–dipole interaction model. Due to the rather close distance between the two nanoscale components and the diverse forms of exciton delocalizations in the aggregate, this approximation becomes insufficient here and its application leads to extreme misinterpretations compared with the superior atomistic model. Only the latter can properly account for both the very different exciton localizations and the specific close arrangement of the tubular aggregate and the nanocrystal. This finding is generally valid for many systems in modern nanotechnology and of high significance.

Outlook

The here introduced atomistic models and computational schemes are combined for outstanding efficiency. Thanks to that, the sophisticated large–scale studies could be performed on conventional compute servers. This makes the entire approach interesting for many fields of recent research. Future investigations can profit a lot from this work.

In particular, the introduced stochastic Schrödinger equation technique represents a novel extremely promising instrument. It faces the increasing interest in time–domain simulations of larger and larger quantum systems and brings with highly advantageous computational scaling features. Its application is advisable whenever open system dynamics are aspired extending over more than several hundred states. While equivalent master equation ansatzes become more and more inefficient, on that scale the enormous potential of the stochastic Schrödinger equation starts working. Moreover, the here developed strategy is immensely versatile. As stated above, the here executed simulations represent a milestone in the field of dissipative dynamics. In turn, they are expected to have a great inspiring effect for diverse other applications in future. Just to give one concrete example, at this place, hybrid systems consisting of 2d transition metal chalcogenides and molecules shall be mentioned. These regular finite nanostructures lie in the particular focus of recent research and constitute ideal systems for future application.

Also further investigation of the dissipative charge separation kinetics at the *para*–sexiphenyl/ZnO interface would be interesting. In particular, an uniform dissipative model for the entire process of photoexcitation, exciton transition and charge separation would be desirable. In the present dissipative simulation, the electron treatment follows scenarios of ultrafast initial trapping. In a generalized model, however, the additional degree of freedom of the electron would mean a radical increase of the number of electronic states. Another task for the future could be the extension of the existing model by relaxation processes of the injected electron within the ZnO conduction band (i.e., for electron–phonon interaction). Unfortunately, the latter already means a formidable challenge concerning tiny finite ZnO clusters. In this regard, for the beginning the electron–phonon interaction of the electron could be modeled using representative phonon modes of the ZnO bulk system. Other future projects are motivated by the tubular aggregate/nanocystal system. For instance, Frenkel and Wannier–Mott excitons could be straightforwardly incorporated in a single time–dependent simulation study on exciton relaxation. The difficulty lies then in the two different characteristic time–scales of the exciton dynamics. Accordingly, a unified dissipative investigation would have to extend over several nanoseconds. For this purpose, it would be firstly required to recapture the stochastic force generation and to work out more adequate "on–the–fly" algorithms.

Appendices

A. Interface Charge Transfer Model

The introduction of the primary acceptor state of the electron after injection from an excited 6P into the ZnO lattice is only briefly introduced in Sec. 6.3. In this Appendix, further computational details are supplemented. The processing may be generalized to, in principle, any type of semiconductor surface layer exposed to any type of molecule.

A.1. Primary electron acceptor surface state

Lets consider the primary electron acceptor state $\bar{\phi}_{\mathrm{A}}$. In order to realize a certain spatial localization it is represented making use of the set of atomic orbital (AO) basis functions of the ZnO cluster (introduced in the TB scheme, cf. Sec. 2.2.1). The second key point of the approach concerns the partial occupation of these AOs. Occupied (or partially occupied) spin–orbitals cannot (or only partially) host the excess electron. Following the present frozen orbital treatment of the ZnO cluster (see Sec. 2.2.1) the injected electron exclusively populates CB–like states $\bar{\psi}_{\bar{\lambda}}$. In fact, it was recognized that the 4s and 4p–type Zn AOs of the cluster are only sparsely populated concerning its neutral ground state configuration. In other words, these AOs majorly contribute to the unoccupied CB–like states $\bar{\psi}_{\bar{\lambda}}$. At the interesting flat (or "top") surface of the ZnO cluster, especially the Zn $4\mathrm{p_x}$–type AOs were found to be unoccupied to great shares. Nevertheless, there were also observed small contributions of these AOs to the VB–like states. So, instead of being fully unoccupied, they are partially occupied. Therefore, it is the task to formulate a superposition state which is localized at the surface but at the same time completely unoccupied, i.e., free of any VB character.

For the beginning, a wave function superposition is considered consisting of a number of 25 $4\mathrm{p_x}$–type AOs. Thereby, each AO is localized on one of the 25 Zn atoms at the surface "beneath" the 6P molecule (see Fig. 6.2a in Sec. 6.3). The seven AOs, which are localized on the line of seven Zn atoms directly below the 6P (colored black in Fig. 6.2a), shall be populated in a pronounced manner with respect to the AOs localized somewhat more remote on the 18 surrounding Zn atoms. The latter render a belt of nearest neighbor atoms colored white in Fig. 6.2a. An initial superposition state is found with

$$|\bar{\phi}_{\mathrm{A}}\rangle = c_L \sum_{i=1}^{7} |\chi_i^L\rangle + c_B \sum_{k=1}^{18} |\chi_k^B\rangle, \tag{A.1}$$

where the χ_i^L represent the ith $4\mathrm{p_x}$–type AO in the distinguished line of Zn atom in the middle of the arrangement. In similarity, the χ_k^B give the remaining AOs residing on the surrounding belt. With the normalization condition $\langle\bar{\phi}_{\mathrm{A}}|\bar{\phi}_{\mathrm{A}}\rangle = 1$ and the overlap matrix S_{ij} of AOs, appropriate values for the expansion coefficients c_L and

c_B can be found. By assuming real–valued wave functions, one straightly finds $1 = c_L^2 \sum_{i,j\in L} S_{ij} + 2c_L c_B \sum_{i\in L}\sum_{k\in B} S_{ik} + c_B^2 \sum_{k,l\in B} S_{kl}$. It further leads straightly to

$$c_B = -\frac{\sum_i^7 \sum_k^{18} S_{ik}}{\sum_{k,l}^{18} S_{kl}} c_L + \left\{ \left[\frac{\sum_i^7 \sum_k^{18} S_{ik}}{\sum_{k,l}^{18} S_{kl}} c_L \right]^2 - \frac{\sum_{i,j}^7 S_{ij}}{\sum_{k,l}^{18} S_{kl}} c_L^2 + \frac{1}{\sum_{k,l}^{18} S_{kl}} \right\}^{\frac{1}{2}} . \tag{A.2}$$

With this an appropriately localized wave function superposition of AOs was formulated. Therefore, the pronounced occupation was defined with $c_L = 0.25$. Correspondingly, the relation in Eq. A.2 gave $c_B = 0.1703$. The particular value of c_L could also be defined differently (as long as the total occupation of the AOs is not overloaded by the excess electron). In the present case, each of the 25 Zn $4p_x$–type AOs was already occupied by about 14 % (with VB electrons).

In the second step, the $\bar{\phi}_\mathrm{A}$ must be expanded in the basis set of the cluster single–particle states,

$$|\bar{\phi}_\mathrm{A}\rangle = c_L \sum_i^L \Big[\sum_\lambda^{\mathrm{VB}} \tilde{\kappa}_\lambda(i)|\psi_\lambda\rangle + \sum_{\bar{\lambda}}^{\mathrm{CB}} \tilde{\kappa}_{\bar{\lambda}}(i)|\bar{\psi}_{\bar{\lambda}}\rangle \Big] + c_B \sum_k^B \Big[\sum_\lambda^{\mathrm{VB}} \tilde{\kappa}_\lambda(k)|\psi_\lambda\rangle + \sum_{\bar{\lambda}}^{\mathrm{CB}} \tilde{\kappa}_{\bar{\lambda}}(k)|\bar{\psi}_{\bar{\lambda}}\rangle \Big], \tag{A.3}$$

with the expansion coefficients $\tilde{\kappa}_{\bar{\lambda}}(i) = \langle\bar{\psi}_{\bar{\lambda}}|\chi_i\rangle$ and $\tilde{\kappa}_\lambda(i) = \langle\psi_\lambda|\chi_i\rangle$ related to the CB–like state $\bar{\psi}_{\bar{\lambda}}$ and the VB–like state ψ_λ, respectively. The expression Eq. A.3 gives the mathematically exact eigenstate representation. According to the physical meaning, however, it is now the trick to simply restrict the expansion to only CB–like states. Eliminated by the residual VB contribution, the new $\bar{\phi}_\mathrm{A}$ follows as

$$|\bar{\phi}_\mathrm{A}\rangle \approx c_L \sum_i^L \sum_{\bar{\lambda}}^{\mathrm{CB}} \tilde{\kappa}_{\bar{\lambda}}(i)|\bar{\psi}_{\bar{\lambda}}\rangle + c_B \sum_k^B \sum_{\bar{\lambda}}^{\mathrm{CB}} \tilde{\kappa}_{\bar{\lambda}}(k)|\bar{\psi}_{\bar{\lambda}}\rangle. \tag{A.4}$$

By the latter treatment, the $\bar{\phi}_\mathrm{A}$ is no longer normalized and the renormalized version $\phi_\mathrm{A} = \bar{\phi}_\mathrm{A}/|\bar{\phi}_\mathrm{A}|$ was introduced in a last step. The renormalized electron acceptor state reads

$$|\phi_\mathrm{A}\rangle = \sum_{\bar{\lambda}}^{\mathrm{CB}} \kappa_{\bar{\lambda}}|\bar{\psi}_{\bar{\lambda}}\rangle, \tag{A.5}$$

with the respective expansion coefficients

$$\kappa_{\bar{\lambda}} = \frac{1}{|\bar{\phi}_\mathrm{A}|}\Big[c_L \sum_i^L \tilde{\kappa}_{\bar{\lambda}}(i) + c_B \sum_k^B \tilde{\kappa}_{\bar{\lambda}}(k) \Big]. \tag{A.6}$$

The derived superposition ϕ_A fulfills the requirements of being normalized, being unoccupied and being appropriately localized on the surface beneath the 6P molecule.

A.2. Coupling of interface charge transfer

In Sec. 6.3.3 the electron injection processes into each CB–like state $\bar{\psi}_{\bar{\lambda}}$ is collectively characterized by a single coupling constant $\mathscr{V}^{\mathrm{CT}}$. This is possible as the parameter $\mathscr{V}^{\mathrm{CT}}$ shall be related to the injection of the electron into the constructed acceptor state ϕ_{A} (see Eq. A.5). With Eq. A.5, a clear relation between ϕ_{A} and all $\bar{\psi}_{\bar{\lambda}}$ is prepared. That relation can also be straightly applied to relate the charge transfer coupling to each $\bar{\psi}_{\bar{\lambda}}$. Accordingly, it follows

$$\mathscr{V}_{\bar{\lambda}}^{\mathrm{CT}} = \kappa_{\bar{\lambda}} \mathscr{V}^{\mathrm{CT}}, \tag{A.7}$$

with the CB–like state specific weights $\kappa_{\bar{\lambda}}$ (taken from Eq. A.6).

B. Generalized Frenkel Exciton Model

In order to develop an exciton model which takes into consideration intermolecular dispersive interaction effect, the standard Frenkel exciton model (see Sec. 2.3.2) can be generalized in the fashion of a full CI scheme. Its outcome is presented in Sec. 2.3.3. In what follows, the generalized Frenkel exciton Hamiltonian given in Eq. 2.35 is derived using a projection operator technique. It provides a very general ansatz to the theory and allows extending the exciton model to higher order corrections in a straight manner. In Chap. 8, the developed generalized exciton model with dispersive effects is applied to a gigantic tubular dye aggregate.

Without the restriction to only single molecular first excited states, now the electronic Hilbert space of an aggregate structure obeys the general completeness relation

$$\mathbf{1}_{\mathrm{el}} = \sum_{\vec{\pi}} |\Phi_{\vec{\pi}}\rangle\langle\Phi_{\vec{\pi}}| = \mathbf{P} + \mathbf{Q}. \tag{B.1}$$

The expression in the middle of Eq. B.1 is concerned first. The state $|\Phi_{\vec{\pi}}\rangle$ describes a possible aggregate state in terms of a direct product of the number of N_{mol} molecular (substructure) states with zero wave function overlap. The index vector $\vec{\pi}$ represents a vector of N_{mol} components π_m. The mth element of $\vec{\pi}$ holds the information about the mth molecular state (representing either ground, first or any higher excited state configuration). In Eq. B.1, the sum with respect to $\vec{\pi}$ is shorthand for N_{mol} individual summations over the elements π_m. The subspace of ground and singly excited aggregate states is of particular interest here. In Eq. B.1, the latter two are indicated by the zero vector $\vec{\pi} = \vec{0}$ (ground state), and the N_{mol} unity vectors, $\vec{\pi} = \vec{e}_m$ (first excited states). On the right–hand side of Eq. B.1, the unity operator is split up into two orthogonal projection operators, $\mathbf{P}$ and $\mathbf{Q}$. It is the idea to define $\mathbf{P}$ in such way that it spans the sub Hilbert space of aggregate ground and single first excited states, according to

$$\mathbf{P} = |\Phi_{\vec{0}}\rangle\langle\Phi_{\vec{0}}| + \sum_{m} |\Phi_{\vec{e}_m}\rangle\langle\Phi_{\vec{e}_m}|, \tag{B.2}$$

All higher excited state contributions are (perpendicular to $\mathbf{P}$ and) collected in the residual sub space $\mathbf{Q} = \mathbf{1}_{\mathrm{el}} - \mathbf{P}$.[1] By acting of $\mathbf{P}$ on an arbitrary composite state $|\Phi_{\vec{\pi}}\rangle$ its ground and single excited state character is probed.

At this place, it suffices to introduce an aggregate Hamiltonian $\hat{H}_{\mathrm{agg}}$ which obeys the stationary Schrödinger equation, $\hat{H}_{\mathrm{agg}}|\Psi\rangle = E|\Psi\rangle$, with an arbitrary composite state

[1] Originally this very convenient projector technique was introduced by Zwanzig and Mori for density matrix theory in Liouville space [231, 232]. It was their intention to describe few essential system degrees of freedom isolated from a much larger number of environmental degrees of freedom. In similarity, the individual nature of the higher excited states is irrelevant in the present application. Only their collective influence on the Frenkel excitons shall be of interest.

as $|\Psi\rangle = \sum_{\vec{\pi}} \mathscr{C}_{\vec{\pi}} |\Phi_{\vec{\pi}}\rangle$. It follows the perturbative expansion series of $\hat{H}_{\mathrm{agg}}$. Therefore, the arbitrary composite state $|\Psi\rangle$ is split up, according to

$$|\Psi\rangle = \mathscr{C}_{\vec{0}} |\Phi_{\vec{0}}\rangle + \sum_m \mathscr{C}_{\vec{e}_m} |\Phi_{\vec{e}_m}\rangle + \mathbf{Q}|\Psi\rangle, \tag{B.3}$$

by making use of $\mathbf{P}$ and $\mathbf{Q}$. By inserting Eq. B.3 into the general Schrödinger equation and projecting it on the bra state $\langle\Phi_{\vec{0}}|...$ provides

$$\left[\langle\Phi_{\vec{0}}|\hat{H}_{\mathrm{agg}}|\Phi_{\vec{0}}\rangle - E\right]\mathscr{C}_{\vec{0}} + \sum_m \langle\Phi_{\vec{0}}|\hat{H}_{\mathrm{agg}}|\Phi_{\vec{e}_m}\rangle \mathscr{C}_{\vec{e}_m} = -\sum_{\vec{\pi}} \langle\Phi_{\vec{0}}|\hat{H}_{\mathrm{agg}}\mathbf{Q}|\Phi_{\vec{\pi}}\rangle \mathscr{C}_{\vec{\pi}}, \tag{B.4}$$

while projection on $\langle\Phi_{\vec{e_m}}|...$ delivers

$$\sum_n \left[\langle\Phi_{\vec{e}_m}|\hat{H}_{\mathrm{agg}}|\Phi_{\vec{e}_n}\rangle - \delta_{mn}E\right]\mathscr{C}_{\vec{e}_n} + \langle\Phi_{\vec{e}_m}|\hat{H}_{\mathrm{agg}}|\Phi_{\vec{0}}\rangle \mathscr{C}_{\vec{0}} = -\sum_{\vec{\pi}} \langle\Phi_{\vec{e}_m}|\hat{H}_{\mathrm{agg}}\mathbf{Q}|\Phi_{\vec{\pi}}\rangle \mathscr{C}_{\vec{\pi}}. \tag{B.5}$$

Together, the coupled eigenvalue problem, specified with respect to subspace $\mathbf{P}$, is found. The right–hand sides of Eqs. B.4 and B.5 hold the coupling among the subspaces $\mathbf{P}$ and $\mathbf{Q}$. They generate the aspired dispersive interaction effects among the molecules. At this stage, the conventional Frenkel exciton level is identified in zero order approximation. In order to obtain the coupling effects of first order, likewise eigenvalue equations are constructed with respect to subspace $\mathbf{Q}$,

$$E\mathscr{C}_{\vec{\pi}'} = \langle\Phi_{\vec{\pi}'}|\mathbf{Q}\hat{H}_{\mathrm{agg}}|\Phi_{\vec{0}}\rangle \mathscr{C}_{\vec{0}} + \sum_n \langle\Phi_{\vec{\pi}'}|\mathbf{Q}\hat{H}_{\mathrm{agg}}|\Phi_{\vec{e}_m}\rangle \mathscr{C}_{\vec{e}_m} + \sum_{\vec{\pi}} \langle\Phi_{\vec{\pi}'}|\mathbf{Q}\hat{H}_{\mathrm{agg}}\mathbf{Q}|\Phi_{\vec{\pi}}\rangle \mathscr{C}_{\vec{\pi}}. \tag{B.6}$$

The last term on the right–hand side collectively represents all interactions between states within subspace $\mathbf{Q}$. Inserting Eq. B.6 iteratively into Eqs. B.4 and B.5, generates an expansion series with respect to the coupling among the states of subspace $\mathbf{P}$ and the ones of $\mathbf{Q}$. The focus is here on a first oreder treatment. Consequently, the interaction on the right–hand side of Eq. B.6 is reduced to its zero order expression. The zero order energies of the states in $\mathbf{Q}$ space can be defined as $E^{(0)}_{\vec{\pi}} = \langle\Phi_{\vec{\pi}}|\mathbf{Q}\hat{H}_{\mathrm{agg}}\mathbf{Q}|\Phi_{\vec{\pi}}\rangle$. It allows rewriting the truncated version of Eq. B.6 in the more appealing form

$$\mathscr{C}_{\vec{\pi}'} = \frac{\langle\Phi_{\vec{\pi}'}|\mathbf{Q}\hat{H}_{\mathrm{agg}}|\Phi_{\vec{0}}\rangle \mathscr{C}_{\vec{0}}}{E - E^{(0)}_{\vec{\pi}}} \mathscr{C}_{\vec{0}} + \frac{\sum_n \langle\Phi_{\vec{\pi}'}|\mathbf{Q}\hat{H}_{\mathrm{agg}}|\Phi_{\vec{e}_m}\rangle}{E - E^{(0)}_{\vec{\pi}}} \mathscr{C}_{\vec{e}_m}. \tag{B.7}$$

By inserting now Eq. B.7 into Eqs. B.4 and B.5 gives the closed set of equations

$$\Big\langle\Phi_{\vec{0}}\big|\big[\hat{H}_{\mathrm{agg}} + \Delta\hat{H}_{\mathrm{agg}}(E)\big]\big|\Phi_{\vec{0}}\big\rangle - E\Big]\mathscr{C}_{\vec{0}} + \sum_m \langle\Phi_{\vec{0}}\big|\big[\hat{H}_{\mathrm{agg}} + \Delta\hat{H}_{\mathrm{agg}}(E)\big]\big|\Phi_{\vec{e}_m}\rangle \mathscr{C}_{\vec{e}_m} = 0 \tag{B.8}$$

and

$$\sum_n \Big[\langle\Phi_{\vec{e}_m}|\big[\hat{H}_{\mathrm{agg}}+\Delta\hat{H}_{\mathrm{agg}}(E)\big]|\Phi_{\vec{e}_n}\rangle-\delta_{mn}E\Big]\mathscr{C}_{\vec{e}_n}+\langle\Phi_{\vec{e}_m}|\big[\hat{H}_{\mathrm{agg}}+\Delta\hat{H}_{\mathrm{agg}}(E)\big]|\Phi_{\vec{0}}\rangle\mathscr{C}_{\vec{0}}=0. \tag{B.9}$$

In both equations, the dispersive coupling to sub space **Q** is mediated by the operator

$$\Delta\hat{H}_{\mathrm{agg}}(E)=\sum_{\vec{\pi}}\frac{\mathbf{P}\hat{H}_{\mathrm{agg}}\mathbf{Q}|\Phi_{\vec{\pi}}\rangle\langle\Phi_{\vec{\pi}}|\mathbf{Q}\hat{H}_{\mathrm{agg}}\mathbf{P}}{E-E^{(0)}_{\vec{\pi}}}. \tag{B.10}$$

It simply adds to $\hat{H}_{\mathrm{agg}}$ and introduces corrections on the diagonal energy terms and the offdiagonal excitonic coupling matrix elements in Eqs. B.8 and B.9.

According to the standard Frenkel exciton model in Sec. 2.3.2, the present model further concentrates on the manifold of single excited state. Excitation and de–excitation processes are suppressed further on (see second brackets in Eqs. B.8 and B.9). Due to that, the Eqs. B.8 and B.9 decouple. Nevertheless, concerning the nonlinear dependence on the energy E, the equations cannot be solved straightly. In order to avoid this problematic, all intermolecular energy contributions are approximately removed from E in $\Delta\hat{H}_{\mathrm{agg}}(E)$ (see Eq. B.10). With regard to customary organic structures, indeed the remaining intramolecular energies should describe the main contribution to E.

After inserting Eq. B.10 into Eqs. B.8 and B.9, diverse coupling elements of the type $\langle\Phi_{\vec{0}}|\mathbf{P}\hat{H}_{\mathrm{agg}}\mathbf{Q}|\Phi_{\vec{\pi}}\rangle$ and $\langle\Phi_{\vec{e}_m}|\mathbf{P}\hat{H}_{\mathrm{agg}}\mathbf{Q}|\Phi_{\vec{\pi}}\rangle$ are formed. Thereby, a significant simplification is found in consequence of the initial assumptions of zero wave function overlap between the individual molecular states and the orthogonality of the different states belonging to one molecule. Because of that, the majority of the latter coupling terms vanish. In general, non–zero terms $\langle\Phi_{\vec{0}}|\mathbf{P}\hat{H}_{\mathrm{agg}}\mathbf{Q}|\Phi_{\vec{\pi}}\rangle$ can only be expected for $|\Phi_{\vec{\pi}}\rangle$ realizing excitations on at the most two molecules. So, the diagonal matrix elements of the ground state correction simplifies to

$$\langle\Phi_{\vec{0}}|\Delta\hat{H}_{\mathrm{agg}}|\Phi_{\vec{0}}\rangle=\sum_m^{N_{\mathrm{mol}}}\Big[\sum_{m'\neq m}^{N_{\mathrm{mol}}}\sum_{a,a'}\frac{|J_{mm'}(a\leftarrow g,a'\leftarrow g)|^2}{E^{(m)}_a-E^{(m)}_g+E^{(m')}_{a'}-E^{(m')}_g}\Big]=-\sum_m^{N_{\mathrm{mol}}}\Delta E^{(\mathrm{disp})}_{m,g}, \tag{B.11}$$

where the molecular indexes m and m' are introduced and the indexes a and a' refer to single molecular excited states (g indicates the molecular ground state). The $J_{mm'}(a\leftarrow g,a'\leftarrow g)$ in the nominator describes the intermolecular excitonic coupling between the excitation process from ground to the a'th excited state on molecule m' and the de–excitation from the ath excited to the ground state on molecule m (in the fashion of Eq. 2.29). Further, only the intramolecular excitation energies $E^{(m)}_g$ (for the ground state) and $E^{(m)}_{a'}$ (for the a'th excited state) of the mth molecule appear now in the denominator (see former approximation). The right–hand side of Eq. B.11 further defines the dispersion correction $\Delta E^{(\mathrm{disp})}_{m,g}$. It represents the share of the dispersive energy shift which is due to the influence of the aggregate surrounding on the mth molecule (in aggregate ground state configuration).

The matrix element $\langle\Phi_{\vec{e}_m}|\Delta\hat{H}_{\mathrm{agg}}|\Phi_{\vec{e}_m}\rangle$ related to the single first excited aggregate states can be simplified in similar way. Most conveniently it is formulated in direct reference to the former deduced total dispersive shift in the aggregate ground state configuration (see Eq. B.11), according to

$$\langle\Phi_{\vec{e}_m}|\Delta\hat{H}_{\mathrm{agg}}|\Phi_{\vec{e}_m}\rangle = \langle\Phi_{\vec{0}}|\Delta\hat{H}_{\mathrm{agg}}|\Phi_{\vec{0}}\rangle + \Delta E^{(\mathrm{disp})}_{m,g} - \Delta E^{(\mathrm{disp})}_{m,e}, \tag{B.12}$$

with the dispersion produced by the mth molecule in the first excited state

$$\Delta E^{(\mathrm{disp})}_{m,e} = -\sum_{m'\neq m}^{N_{\mathrm{mol}}}\sum_{a,a'}\frac{|J^{(m,m')}(a\leftarrow e, a'\leftarrow g)|^2}{E^{(m)}_a - E^{(m)}_e + E^{(m')}_{a'} - E^{(m')}_g}. \tag{B.13}$$

The impact of the dispersion on the excitonic couplings (i.e., the correction of $\mathcal{J}_{mn}$ in Eq. 2.22) shall be described in a different manner. Instead of formulating again a correction shift in terms of $\langle\Phi_{\vec{e}_m}|\Delta\hat{H}_{\mathrm{agg}}|\Phi_{\vec{e}_n}\rangle$, the dispersive influence on $\mathcal{J}_{mn}$, typically, is modeled directly in terms of a screening factor f_{mn} (as discussed in Sec. 2.3.3).

Finally, the two dispersive shifts (Eqs. B.11 and B.13) and the screening factor are introduced in the above excitonic equation B.9. When changing the aggregate state notation from the general form $|\Phi_{\vec{e}_m}\rangle$ into the more appealing form $|\bar{\Phi}^e_m\rangle$ (introduced in relation to the standard Frenkel exciton model in Sec. 2.3.2), it finally results the *generalized Frenkel exciton Hamiltonian*, cf. 2.33,

$$\hat{H}^{(\mathrm{disp})}_{\mathrm{FX}} = \sum_m^{N_{\mathrm{mol}}}\Big[\mathscr{H}_m + \Delta E^{(\mathrm{disp})}_{m,g} - \Delta E^{(\mathrm{disp})}_{m,e}\Big]|\bar{\Phi}^e_m\rangle\langle\bar{\Phi}^e_m| + \Big(\sum_{m<n}^{N_{\mathrm{mol}}} f_{mn}\mathcal{J}_{mn}|\bar{\Phi}^e_m\rangle\langle\bar{\Phi}^e_n| + \mathrm{H.c.}\Big). \tag{B.14}$$

C. Polarizable Continuum Model of the 6P/ZnO Interface

In this Appendix the dielectric model utilized in Sec. 7.3.4 is deduced. The interface under inspection is introduced in the main text. In Fig. 7.2, it is illustrated in terms of two infinite dielectric media describing an interface. The interface defines the $x-y$ plane. By that, an upper and lower half space with $z > 0$ and $z < 0$ is introduced. The half spaces are destinguished by the dielectric constants $\epsilon_{6\mathrm{P}}$ and ϵ_{ZnO}, respectively. The continuous charge densities of the hole and electron (represented by $\rho_{\mathrm{h}}(\mathbf{r})$ and $\rho_{\mathrm{el}}(\mathbf{r})$) shall be positioned in the upper and lower half space, respectively.

The total interaction energy of both charge densities at the interface is of interest. In general, it is defined as, cf. Ref. [211],

$$W_{\mathrm{tot}} = \frac{1}{2}\int d^3\mathbf{r}\Phi_{\mathrm{tot}}(\mathbf{r})\rho_{\mathrm{tot}}(\mathbf{r}), \tag{C.1}$$

based on the total electrostatic potential $\Phi_{\mathrm{tot}}(\mathbf{r})$ and the total charge density $\rho_{\mathrm{tot}}(\mathbf{r})$ of the interface architecture. The total potential subdevides into hole and electron contribution, i.e., $\Phi_{\mathrm{tot}}(\mathbf{r}) = \Phi_{\mathrm{h}}(\mathbf{r}) + \Phi_{\mathrm{el}}(\mathbf{r})$. Similarly, the total charge density at the interface sums up hole and electron terms, according to $\rho_{\mathrm{tot}}(\mathbf{r}) = \rho_{\mathrm{h}}(\mathbf{r}) + \rho_{\mathrm{el}}(\mathbf{r})$.

The Poisson equation [211] gives access to both potentials $\Phi_{\mathrm{h}}(\mathbf{r})$ and $\Phi_{\mathrm{el}}(\mathbf{r})$ for each subspace. For the upper half space it follows

$$\Phi_{\mathrm{h}}(\mathbf{r}; z > 0) = \frac{1}{\epsilon_{6\mathrm{P}}}\Big(\int d^3\mathbf{r}'\frac{\rho_{\mathrm{h}}(\mathbf{r}')}{|\mathbf{r}-\mathbf{r}'|} + \frac{\epsilon_{6\mathrm{P}}-\epsilon_{\mathrm{ZnO}}}{\epsilon_{6\mathrm{P}}+\epsilon_{\mathrm{ZnO}}}\int d^3\mathbf{r}'\frac{\tilde{\rho}_{\mathrm{h}}(\mathbf{r}')}{|\mathbf{r}-\mathbf{r}'|}\Big). \tag{C.2}$$

It collects two terms. The first one represents the presence of the "physical" hole charge density. The second term, however, appears as the image charge density, $\tilde{\rho}_{\mathrm{h}}(\mathbf{r}')$, of the physical hole which is induced due to the polarizable surrounding and appears in the opponent (lower) dielectric half space (mirrored at the interface; for details about the *image charge effect*, see also Ref. [211]). Similarly, the image charge density of the physical electron is of relevance. It can be introduced as $\tilde{\rho}_{\mathrm{el}}(\mathbf{r}')$. In the fashion of Eq. C.2, one straightly finds the other contributions to the total potential at the interface. They read,

$$\begin{aligned}
\Phi_{\mathrm{el}}(\mathbf{r}; z > 0) &= \frac{2\epsilon_{\mathrm{ZnO}}/\epsilon_{6\mathrm{P}}}{\epsilon_{6\mathrm{P}}+\epsilon_{\mathrm{ZnO}}}\int d^3\mathbf{r}'\frac{\rho_{\mathrm{el}}(\mathbf{r}')}{|\mathbf{r}-\mathbf{r}'|}, \\
\Phi_{\mathrm{h}}(\mathbf{r}; z < 0) &= \frac{2\epsilon_{6\mathrm{P}}/\epsilon_{\mathrm{ZnO}}}{\epsilon_{6\mathrm{P}}+\epsilon_{\mathrm{ZnO}}}\int d^3\mathbf{r}'\frac{\rho_{\mathrm{h}}(\mathbf{r}')}{|\mathbf{r}-\mathbf{r}'|}, \\
\Phi_{\mathrm{el}}(\mathbf{r}; z < 0) &= \frac{1}{\epsilon_{\mathrm{ZnO}}}\Big(\int d^3\mathbf{r}'\frac{\rho_{\mathrm{el}}(\mathbf{r}')}{|\mathbf{r}-\mathbf{r}'|} + \frac{\epsilon_{\mathrm{ZnO}}-\epsilon_{6\mathrm{P}}}{\epsilon_{6\mathrm{P}}+\epsilon_{\mathrm{ZnO}}}\int d^3\mathbf{r}'\frac{\tilde{\rho}_{\mathrm{el}}(\mathbf{r}')}{|\mathbf{r}-\mathbf{r}'|}\Big).
\end{aligned} \tag{C.3}$$

Based on the four parts of the total interface electrostatic potential, the interaction energy Eq. C.1 immediately follows according to

$$W_{\mathrm{tot}} = \frac{1}{2}\int_{z>0} d^3\mathbf{r}\Big(\Phi_{\mathrm{h}}(\mathbf{r}; z>0) + \Phi_{\mathrm{el}}(\mathbf{r}; z>0)\Big)\rho_{\mathrm{h}}(\mathbf{r}) + \frac{1}{2}\int_{z<0} d^3\mathbf{r}\Big(\Phi_{\mathrm{h}}(\mathbf{r}; z<0) + \Phi_{\mathrm{el}}(\mathbf{r}; z<0)\Big)\rho_{\mathrm{el}}(\mathbf{r}). \tag{C.4}$$

Inserting the particular expressions in Eqs. C.2 and C.3 further gives

$$W_{\mathrm{tot}} = \frac{1}{2}\frac{1}{\epsilon_{6\mathrm{P}}}\int d^3\mathbf{r}\int d^3\mathbf{r}'\Big(\frac{\rho_{\mathrm{h}}(\mathbf{r}')}{|\mathbf{r}-\mathbf{r}'|} + \frac{\epsilon_{6\mathrm{P}}-\epsilon_{\mathrm{ZnO}}}{\epsilon_{6\mathrm{P}}+\epsilon_{\mathrm{ZnO}}}\frac{\tilde{\rho}_{\mathrm{h}}(\mathbf{r}')}{|\mathbf{r}-\mathbf{r}'|} + \frac{2\epsilon_{\mathrm{ZnO}}}{\epsilon_{6\mathrm{P}}+\epsilon_{\mathrm{ZnO}}}\frac{\rho_{\mathrm{el}}(\mathbf{r}')}{|\mathbf{r}-\mathbf{r}'|}\Big)\rho_{\mathrm{h}}(\mathbf{r}) + \frac{1}{2}\frac{1}{\epsilon_{\mathrm{ZnO}}}\int d^3\mathbf{r}\int d^3\mathbf{r}'\Big(\frac{\rho_{\mathrm{el}}(\mathbf{r}')}{|\mathbf{r}-\mathbf{r}'|} + \frac{\epsilon_{\mathrm{ZnO}}-\epsilon_{6\mathrm{P}}}{\epsilon_{6\mathrm{P}}+\epsilon_{\mathrm{ZnO}}}\frac{\tilde{\rho}_{\mathrm{el}}(\mathbf{r}')}{|\mathbf{r}-\mathbf{r}'|} + \frac{2\epsilon_{6\mathrm{P}}}{\epsilon_{6\mathrm{P}}+\epsilon_{\mathrm{ZnO}}}\frac{\rho_{\mathrm{h}}(\mathbf{r}')}{|\mathbf{r}-\mathbf{r}'|}\Big)\rho_{\mathrm{el}}(\mathbf{r}). \tag{C.5}$$

Both first terms in the two brackets in Eq. C.5 are divergent and usually excluded in the framework of the image charge ansatz. Moreover, the interaction energy shall be determined in dependence on the hole position. In fact, the electron charge is immoblilized in Sec. 7.3.4, i.e., only terms which carry explicit dependence on the electron–hole distance have an effective influence on the hole transfer kinetics. The localization of the hole charge denstity in the 6P (monolayer) film changes only in the $x-y$ place. With respect to the z–axis, the hole density, however, is equivalent for each molecule. This means that the interaction of the physical hole charge density with its image charge density is independent on the particular positioning. Therefore, this interaction part can be suppressed. Moreover, the electron is immobilied by definition and clearly also the terms of interaction between the electron and its image can be dropped. Consequently, the relevant part of the interaction energy remains as a single terms,

$$W_{\mathrm{rel}} = \frac{\epsilon_{6\mathrm{P}}/\epsilon_{\mathrm{ZnO}} + \epsilon_{\mathrm{ZnO}}/\epsilon_{6\mathrm{P}}}{\epsilon_{6\mathrm{P}}+\epsilon_{\mathrm{ZnO}}}\int d^3\mathbf{r}\int d^3\mathbf{r}'\frac{\rho_{\mathrm{h}}(\mathbf{r}')\rho_{\mathrm{el}}(\mathbf{r}')}{|\mathbf{r}-\mathbf{r}'|}. \tag{C.6}$$

As supposed, the symmetry of the interface is apparently recaptured in W_{rel}. Finally, the $\rho_{\mathrm{h}}(\mathbf{r})$ and $\rho_{\mathrm{el}}(\mathbf{r})$ are represented by a number of N_{h} and N_{el} atomic centered partial hole and electron charges, respectively. They shall be positioned in the upper (lower) halfspace at coordinates $\mathbf{R}_\mu^{(m)}$ and $\mathbf{R}_i^{(\mathrm{ZnO})}$, respectively. This means it is $\rho_{\mathrm{h}}(\mathbf{r}) = \sum_\mu \mathbb{Q}_{\mathrm{h}}(\mathbf{R}_\mu^{(m)})\delta(\mathbf{R}_\mu^{(m)}-\mathbf{r})$ and $\rho_{\mathrm{el}}(\mathbf{r}) = \sum_i \mathbb{Q}_{\mathrm{e}}(\mathbf{R}_i^{(\mathrm{ZnO})})\delta(\mathbf{R}_i^{(\mathrm{ZnO})}-\mathbf{r})$, where the dependence on the molecular index m is introduced. It signalizes the corresponding hole localization in the film. Then, Eq. C.5 simplifies to

$$W_m = \frac{\epsilon_{6\mathrm{P}}/\epsilon_{\mathrm{ZnO}} + \epsilon_{\mathrm{ZnO}}/\epsilon_{6\mathrm{P}}}{\epsilon_{6\mathrm{P}}+\epsilon_{\mathrm{ZnO}}}\sum_{\mu}^{6\mathrm{P}_m}\sum_{i}^{\mathrm{ZnO}}\frac{\mathbb{Q}_{\mathrm{h}}(\mathbf{R}_\mu^{(m)})\mathbb{Q}_{\mathrm{e}}(\mathbf{R}_i^{(\mathrm{ZnO})})}{|\mathbf{R}_\mu^{(m)}-\mathbf{R}_i^{(\mathrm{ZnO})}|}, \tag{C.7}$$

which is utilized as Eq. 7.6 in Sec. 7.3.4.

D. Inter–Molecular Coulomb– and Excitonic Coupling

In this part, the approximate treatment of the integral terms of Coulomb–type interaction shall be discussed. Throughout this work, they appear as intermolecular electrostatic interaction energy shift, electrostatic interactions between semiconductor and molecules or in terms of the related excitonic couplings between either two molecules or a molecule and a semiconductor component.

The Hamiltonian of a composite system with $N_{\rm sub}$ substructures (either molecules or semiconductor components) is given in Eq. 2.17. At this place, the focus is on the Coulomb–type interaction term $\hat{V}_{s,s'}$ between the substructures with index s and s'. In the main part (see Chap. 2), the focus is solely on the electronic system. So the nucleus–nucleus interaction needs not to be considered at this place. The $\hat{V}_{s,s'}$ holds exclusively terms of electron contribution. Under condition that the direct product ansatz (introduced in Eq. 2.18) can be applied and that the substructures s and s' can realize the substructure states $|\Phi_a^{(s)}\rangle$ or $|\Phi_b^{(s)}\rangle$ and $|\Phi_{a'}^{(s')}\rangle$ or $|\Phi_{b'}^{(s')}\rangle$, the Coulomb–type interaction can be expressed as

$$V_{s,s'}(bb',aa') = \langle\Phi_b^{(s)}|\langle\Phi_{b'}^{(s')}|\hat{V}_{s,s'}|\Phi_a^{(s)}\rangle|\Phi_{a'}^{(s')}\rangle. \tag{D.1}$$

Terms of electrostatic interaction energy follow as diagonal elements without state transition, i.e., in terms of $V_{s,s'}(aa';aa')$. An excitonic coupling element appears whenever the Coulomb matrix element reflects a state transitions, commonly induced on both substructures, according to $V_{s,s'}(bb';aa')$ with $a \neq b$ and $a' \neq b'$. In this way, the coupling $\hat{V}_{ss'}$ mediates the electronic state transition: $|\Phi_a^{(s)}\rangle \rightarrow |\Phi_b^{(s)}\rangle$ concerning substructure s and the transition: $|\Phi_a^{(s)}\rangle \rightarrow |\Phi_{b'}^{(s')}\rangle$ in substructure s'. (The remaining scattering matrix elements with $a = b$ and $a' \neq b'$ (or vice versa) are not in the focus of this work.)

In order to introduce approximate forms of Eq. D.1 based on atomic centered partial (transition) charges, it is instructive to change to the coordinate representation, according to

$$V_{s,s'}(bb',aa') = \int dr_s \int dr_{s'} (\Phi_b^{(s)}(r_s)\Phi_{b'}^{(s')}(r_{s'}))^* \times \tag{D.2}$$
$$\sum_i \Big[\sum_j \frac{e^2}{|\mathbf{r}_i^{(s)} - \mathbf{r}_j^{(s')}|} + \sum_\mu \frac{e^2 Z_\mu^{(s')}}{|\mathbf{r}_i^{(s)} - \mathbf{R}_\mu^{(s')}|} + \sum_\mu \frac{e^2 Z_\mu^{(s)}}{|\mathbf{R}_\mu^{(s)} - \mathbf{r}_i^{(s')}|} \Big] \Phi_a^{(s)}(r_s)\Phi_{a'}^{(s')}(r_{s'}).$$

The rectanglular bracket includes the three types of Coulomb interactions. The integration is with respect to all electron coordinates. These are collected in r_s and $r_{s'}$ (with,

e.g., $r_s = \{\mathbf{r}_1^{(s)}, \mathbf{r}_2^{(s)}, ..., \mathbf{r}_{N_s}^{(s)}\}$). The first term represents the electron–electron interaction. Its summation runs over the electronic coordinates $\mathbf{r}_i^{(s)}$ and $\mathbf{r}_j^{(s')}$ of substructure s and s', respectively. The second and third term denotes the coupling between electrons and nuclei. Consequently, the summation with respect to the μth nuclear coordinate $\mathbf{R}_\mu^{(s)}$ as well as the μth atomic number $Z_\mu^{(s)}$ of substructure s is introduced. The Eq. D.2 can be simplified essentially taking into account the general many–electron antisymmetric character $\Phi(\mathbf{r}_1, \mathbf{r}_2, ...) = -\Phi(\mathbf{r}_2, \mathbf{r}_1, ...)$,

$$V_{s,s'}(bb';aa') = \int dr_s \int dr_{s'} (\Phi_b^{(s)}(r_s)\Phi_{b'}^{(s')}(r_{s'}))^* \times \tag{D.3}$$
$$\Big[\frac{e^2 N_s N_{s'}}{|\mathbf{r}_1^{(s)} - \mathbf{r}_1^{(s')}|} + \sum_\mu \big(\frac{e^2 N_s Z_\mu^{(s')}}{|\mathbf{r}_1^{(s)} - \mathbf{R}_\mu^{(s')}|} + \frac{e^2 N_{s'} Z_\mu^{(s)}}{|\mathbf{R}_\mu^{(s)} - \mathbf{r}_1^{(s')}|}\big)\Big] \Phi_a^{(s)}(r_s)\Phi_{a'}^{(s')}(r_{s'}).$$

The particular single–electron numbering within both substructures is arbitrary. Here, the labels $i = 1$ and $j = 1$ are kept. In a further step, the orthogonality of the substructure states (i.e., $\langle \Phi_b^{(s)} | \Phi_a^{(s)} \rangle = \delta_{ab}$) can be used to reexpress Eq. D.3,

$$\begin{aligned} V_{s,s'}(bb';aa') = &\int dr_s \int dr_{s'} (\Phi_b^{(s)}(r_s)\Phi_{b'}^{(s')}(r_{s'}))^* \frac{e^2 N_s N_{s'}}{|\mathbf{r}_1^{(s)} - \mathbf{r}_1^{(s')}|} \Phi_a^{(s)}(r_s)\Phi_{a'}^{(s')}(r_{s'}) \\ &+ \delta_{a'b'} \int dr_s \sum_\mu \Phi_b^{(s)}(r_s)^* \frac{e^2 N_s Z_\mu^{(s')}}{|\mathbf{r}_1^{(s)} - \mathbf{R}_\mu^{(s')}|} \Phi_a^{(s)}(r_s) \\ &+ \delta_{ab} \int dr_{s'} \sum_\mu \Phi_{b'}^{(s')}(r_{s'})^* \frac{e^2 N_{s'} Z_\mu^{(s)}}{|\mathbf{R}_\mu^{(s)} - \mathbf{r}_1^{(s')}|} \Phi_{a'}^{(s')}(r_{s'})\Big]. \end{aligned} \tag{D.4}$$

A more appealing form is found when the integrations with respect to the full number of electrons is transformed to an integration with respect to only the single relevant one. Therefore, the single–electron densities related to the substructure s are introduced,

$$n_{ba}^{(s)}(\mathbf{x}) = eN_s \int dr_s \Phi_b^{(s)}(r_s)^* \Phi_a^{(s)}(r_s) \delta(\mathbf{x} - \mathbf{r}_1^{(s)}). \tag{D.5}$$

Not to overload the notation, here it refers directly to the case of a molecular substructure s (see Eqs. 2.26 and 2.30). In case of $b = a$, Eq. D.5 indicates the charge density of the electronic system of substructure s in state a. However, if $b \neq a$, the Eq. D.5 is called the transition density of molecule s which describes the overlap of the electronic densities of state a and b. Making use of them, the coupling term in Eq. D.4 is recovered as

$$\begin{aligned} V_{s,s'}(bb';aa') = &\int d\mathbf{x} \int d\mathbf{y} \frac{n_{ba}^{(s)}(\mathbf{x}) n_{b'a'}^{(s')}(\mathbf{y})}{|\mathbf{x} - \mathbf{y}|} + \delta_{a'b'} \sum_\mu \int d\mathbf{x} \frac{n_{ba}^{(s)}(\mathbf{x}) \cdot eZ_\mu^{(s')}}{|\mathbf{x} - \mathbf{R}_\mu^{(s')}|} \\ &+ \delta_{ab} \sum_\mu \int d\mathbf{y} \frac{n_{b'a'}^{(s')}(\mathbf{y}) \cdot eZ_\mu^{(s)}}{|\mathbf{y} - \mathbf{R}_\mu^{(s)}|}\Big]. \end{aligned} \tag{D.6}$$

In a final step, the continuous charge densities $n_{ba}^{(s)}(\mathbf{x})$ are approximately replaced by a

set of partial charges $q_{ba}^{(s)}(\mathbf{R}_{\mu}^{(s)})$. Each charge is centered at one of the nuclear position $\mathbf{R}_{\mu}^{(s)}$ of substructure s and specific concerning the state indexes a and b. If $a = b$, electrostatic charges are identified. In the case of $a \neq b$, the charges represent the related transition on substructure s. The Appendix G holds detailed information about how these charges were deduced in the framework of this thesis (concerning molecules as well as semiconductor structures). The approximate form of the general Coulomb matrix element reads

$$V_{s,s'}(bb';aa') \approx \sum_{\mu,\nu} \Big(\frac{q_{ba}^{(s)}(\mathbf{R}_{\mu}^{(s)}) q_{b'a'}^{(s')}(\mathbf{R}_{\nu}^{(s')})}{|\mathbf{R}_{\mu}^{(s)} - \mathbf{R}_{\nu}^{(s')}|} + \delta_{a'b'} \frac{e q_{ba}^{(s)}(\mathbf{R}_{\mu}^{(s)}) Z_{\nu}^{(s')}}{|\mathbf{R}_{\mu}^{(s)} - \mathbf{R}_{\nu}^{(s')}|} + \delta_{ab} \frac{e Z_{\mu}^{(s)} q_{b'a'}^{(s')}(\mathbf{R}_{\nu}^{(s')})}{|\mathbf{R}_{\mu}^{(s)} - \mathbf{R}_{\nu}^{(s')}|} \Big). \tag{D.7}$$

The diagonal matrix elements of the Coulomb operator (i.e., in the case of $a = b$ and $a' = b'$), the Eq. D.7 approximates the sum of the electron–electron and electron–nuclei interaction given with Eqs. 2.25 and 2.27, respectively. The special case of excitonic interaction between two certain substructures follows as the offdiagonal elements (i.e., in case of $a \neq b$ and $a' \neq b'$), according to

$$V_{s,s'}(bb';aa') \approx \sum_{\mu,\nu} \frac{q_{ba}^{(s)}(\mathbf{R}_{\mu}^{(s)}) q_{b'a'}^{(s')}(\mathbf{R}_{\nu}^{(s')})}{|\mathbf{R}_{\mu}^{(s)} - \mathbf{R}_{\nu}^{(s')}|}, \tag{D.8}$$

where the action of the Kronecker–deltas have been taken into account. Specified to intermolecular excitonic coupling, Eq. D.8 approximates Eq. 2.29. Moreover, in Eqs. 5.15 and 8.41 is is formulated concerning the excitonic coupling between molecular and semiconductor structures. The expressions Eqs. D.7 and D.8 are a very computationally cheap instrument to compute both Coulomb–type interactions in atomistic resolution. This atomistic modeling is significantly more accurate than any alternativ model based on a multipole expansion ansatz.

E. Spectral Density and Correlation Function of Electron–Vibrational Interaction

Dynamics of open quantum systems are introduced in Sec. 3.3 and further discussed in Chap. 4 based on the mode specific electron–vibrational interaction according to the bilinear coupling model expressed in Sec. 3.3.3 (see Eq. 3.13). Thereby, the spectral density function and the correlation function of the system–bath interaction are introduced.

E.1. Spectral Density Function

The spectral density is defined by

$$J_m(\omega) = \pi \sum_{\xi} \left(\hbar\omega_\xi g_m(\xi)\right)^2 \delta(\omega - \omega_\xi). \tag{E.1}$$

The index m indicates its dependence on the respective electronic state. $J_m(\omega)$ represents the state–specific distribution of electron–vibrational interaction strength against the continuous vibrational frequency ω. With this it contains in compact manner the information of the frequencies of all molecular vibrational modes as well as the strength of their coupling to the electronic states. Under consideration that only intramolecular vibrational modes are involved, apparently identical molecules have equal spectral density functions and the molecular index m might be dropped. Further, Eq. E.1 is in direct relation to the reorganization energy, $\lambda_m = \sum_\xi \hbar\omega_\xi g_m(\xi)^2$, which can be found by integration, according to

$$\lambda_m(\omega) = \frac{1}{\pi} \int_0^\infty d\omega J_m(\omega)/\hbar\omega. \tag{E.2}$$

Please note finally that, by definition of Eq. E.1, the spectral density is restricted to positive frequencies (i.e., it is $J_m(\omega) = 0$ for all $\omega < 0$).

E.1.1. Empirical interaction models

In order to describe transfer processes in organic materials, the most popular empirical model of the spectral density in Eq. E.1 is the so–called *Debye–Drude model*. It is used for studying the FMO complex in Sec. 4.5.1 and follows as

$$J_m(\omega) = 2\hbar\lambda_m\gamma_m \frac{\omega}{\omega^2 + \gamma_m^2}. \tag{E.3}$$

It gives the spectral density as a shifted Lorentzian function parameterized by only the reorganization energy λ_m and a characteristic frequency γ_m. The latter must be interpreted as the inverse of the dominant vibrational relaxation time (specific for electronic state m). As above also Eq. E.3 is restricted to the positive frequency domain.

As a second also prominent modeling, the so–called *super–Ohmic spectral density* with exponential cutoff is employed in this work (see Chaps. 7 and 8). It is defined as

$$J_m(\omega) = \pi\hbar\lambda_m\Big(\frac{\omega}{\Omega_m}\Big)^2 e^{-\omega/\Omega_m}, \tag{E.4}$$

again with $J_m(\omega < 0) = 0$. The model parameter Ω_m reflects the characteristic frequency of the vibrational response. In application of both empirical models, particular knowledge on $\omega_{m\xi}$ and $g_m(\xi)$ is not needed. Finally it should be noted that the prefactors in Eqs. E.3 and E.4, are chosen carefully in order to preserve the above relation Eq. E.2.

Once the spectral density is known, the frequency–dependent correlation function and its corresponding time–dependent version can be achieved easily. Making use of Eq. E.1, the correlation function in the bilinear coupling model reads [44],

$$\begin{aligned} C_m(t-\tau) &= \frac{1}{\pi}\int_0^\infty d\omega J_m(\omega)\Big[\big(n(\omega)+1\big)e^{-i\omega(t-\tau)} + n(\omega)e^{i\omega(t-\tau)}\Big] \\ &= \frac{1}{\pi}\int_0^\infty d\omega J_m(\omega)\Big[\big(2n(\omega)+1\big)\cos(\omega(t-\tau)) - i\sin(\omega(t-\tau))\Big] \\ &= \frac{1}{\pi}\int_0^\infty d\omega J_m(\omega)\Big[\coth(\hbar\omega\beta/2)\cos(\omega(t-\tau)) - i\sin(\omega(t-\tau))\Big], \end{aligned} \tag{E.5}$$

with the Bose–Einstein distribution $n(\omega) = 1/(\exp\{\hbar\beta\omega\} - 1)$ and $\beta = 1/k_{\mathrm{B}}T$. The third line holds an appealing form which emphasizes the real and imaginary part of $C_m(t-\tau)$. It is utilized in Appendix F.4.

F. Proofs

In this final part of the Appendix, several mathematical proofs in relation to the discussion in the main part of this thesis are provided.

F.1. Equivalence of the Markovian SSE and the Lindblad QME

The equivalence of the quantum state diffusion methodology and the quantum master equation (QME) ansatz shall be demonstrated (see Sec. 4.1).

F.1.1. The linear SSE

The Markovian Lindblad form of dissipation (see Eq. 4.2) shall be derived starting from the Markovian Ito–Schrödinger equation, cf. Eq. 4.3,

$$\frac{d}{dt}|\psi(t)\rangle = \frac{1}{i\hbar}\hat{H}_{\mathrm{S}}|\psi(t)\rangle - \frac{1}{2\hbar^2}\sum_m \hat{L}_m^\dagger \hat{L}_m|\psi(t)\rangle + \frac{1}{i\hbar}\sum_m \hat{L}_m|\psi(t)\rangle\frac{dB_m}{dt}, \tag{F.1}$$

with the complex–valued white noise stochastic "Wiener process" $\frac{dB_m}{dt}$. To formulate a master equation according to Eq. 4.4, one has to consider further the projector $|\psi(t)\rangle\langle\psi(t)|$. It differential is found based on Eq. F.1 and reminding the rules of stochastic Ito calculus,

$$d|\psi(t)\rangle\langle\psi(t)| = \big[d|\psi(t)\rangle\big]\langle\psi(t)| + |\psi(t)\rangle\big[d\langle\psi(t)|\big] + \big[d|\psi(t)\rangle\big]\big[d\langle\psi(t)|\big]. \tag{F.2}$$

The third *Ito term* appears in addition to the standard algebraic product rule terms. (Please note that it is also possible to give the proof based on the analogue Stratonovich form of the stochastic equation F.1 with the identical result.) Now, making use of the Ito–Schrödinger equation, it follows

$$\begin{aligned} d\hat{\rho}(t) &= d\mathscr{M}\Big[|\psi(t)\rangle\langle\psi(t)|\Big] && \text{(F.3)}\\ &= \mathscr{M}\Big[\big[d|\psi(t)\rangle\big]\langle\psi(t)| + \text{H. c.}\Big] + \mathscr{M}\Big[\big[d|\psi(t)\rangle\big]\big[d\langle\psi(t)|\big]\Big] && \text{(F.4)}\\ &= \mathscr{M}\Big[\Big(\frac{1}{i\hbar}\hat{H}_{\mathrm{S}}dt - \frac{1}{2\hbar^2}\sum_m \hat{L}_m^\dagger\hat{L}_m dt + \frac{1}{i\hbar}\sum_m \hat{L}_m dB_m\Big)|\psi(t)\rangle\langle\psi(t)| + \text{H. c.}\Big] && \text{(F.5)}\\ &\quad + \mathscr{M}\Big[\big[d|\psi(t)\rangle\big]\big[d\langle\psi(t)|\big]\Big]. && \text{(F.6)} \end{aligned}$$

The noise–attributed term in the average vanishes due to its zero mean $\mathscr{M}[dB_m] = 0$. The other parts stay unaffected and one can directly identify the RDO, according to

$\hat{\rho}(t) = \mathscr{M}[|\psi(t)\rangle\langle\psi(t)|]$. The expression further simpifies,

$$d\hat{\rho}(t) = \frac{1}{i\hbar}\Big[\hat{H}_{\mathrm{S}}, \hat{\rho}(t)\Big]dt - \frac{1}{2\hbar^2}\sum_m \Big[\hat{L}_m^\dagger \hat{L}_m, \hat{\rho}(t)\Big]dt + \mathscr{M}\Big[\big[d|\psi(t)\rangle\big]\big[d\langle\psi(t)|\big]\Big]. \tag{F.7}$$

Finally, the last term shall be considered. The noise term appears either in linear or quadratic (correlation–type) form. All terms but the one proportional to $\mathscr{M}[dB_m dB_n^*]$ vanish. In fact, it is $\mathscr{M}[dB_m dB_n^*] = \delta_{mn}dt$ following Ito's rule for Wiener processes. Introducing into Eq. F.7 delivers a "sandwich term", which then completes the Lindblad form of the master equation, cf. Eq. 4.2,

$$\frac{d}{dt}\hat{\rho}(t) = \frac{1}{i\hbar}\Big[\hat{H}_{\mathrm{S}}, \hat{\rho}(t)\Big] - \frac{1}{2\hbar^2}\sum_m \Big[\hat{L}_m^\dagger \hat{L}_m, \hat{\rho}(t)\Big] + \frac{1}{\hbar^2}\sum_m \hat{L}_m \hat{\rho}(t) \hat{L}_m^\dagger. \tag{F.8}$$

F.1.2. The nonlinear SSE

The same proof can be given starting from the nonlinear Ito–Schrödinger equation 4.5 instead. According to Eq. F.2, one straightly finds

$$d\hat{\rho}(t) = \underbrace{\mathscr{M}\Big[\big[d|\bar{\psi}(t)\rangle\big]\langle\bar{\psi}(t)|\Big]}_{(1)} + \underbrace{\mathscr{M}\Big[|\bar{\psi}(t)\rangle\big[dt\langle\bar{\psi}(t)|\big]\Big]}_{(2)} + \underbrace{\mathscr{M}\Big[\big[d|\bar{\psi}(t)\rangle\big]\big[d\langle\bar{\psi}(t)|\big]\Big]}_{(3)}. \tag{F.9}$$

Introducing now the nonlinear form Eq. 4.5 delivers the indicated three terms. The first one gives

$$\begin{aligned}(1) &= \mathscr{M}\Big[\Big(\frac{1}{i\hbar}\hat{H}_{\mathrm{S}} + \frac{1}{i\hbar}\sum_m (\hat{L}_m - \langle\hat{L}_m\rangle)dB_m \\ &\qquad + \frac{1}{\hbar^2}\sum_m \big(\langle\hat{L}_m^\dagger\rangle\hat{L}_m - \frac{1}{2}\hat{L}_m^\dagger\hat{L}_m - \frac{1}{2}\langle\hat{L}_m^\dagger\rangle\langle\hat{L}_m\rangle\big)dt\Big)|\bar{\psi}(t)\rangle\langle\bar{\psi}(t)|\Big] \\ &= \frac{1}{i\hbar}\hat{H}_{\mathrm{S}}\hat{\rho}(t)dt + \frac{1}{\hbar^2}\sum_m \big(\langle\hat{L}_m^\dagger\rangle\hat{L}_m - \frac{1}{2}\hat{L}_m^\dagger\hat{L}_m - \frac{1}{2}\langle\hat{L}_m^\dagger\rangle\langle\hat{L}_m\rangle\big)\hat{\rho}(t)dt,\end{aligned} \tag{F.10}$$

where the zero mean of the Wiener process (i.e., $\mathscr{M}[dB_m] = 0$) is already taken into account (see Appendix F.1.1). Similarly, it follows the second term in Eq. F.9,

$$(2) = \frac{-1}{i\hbar}\hat{\rho}(t)\hat{H}_{\mathrm{S}}dt + \frac{1}{\hbar^2}\sum_m \hat{\rho}(t)\big(\langle\hat{L}_m\rangle\hat{L}_m^\dagger - \frac{1}{2}\hat{L}_m^\dagger\hat{L}_m - \frac{1}{2}\langle\hat{L}_m^\dagger\rangle\langle\hat{L}_m\rangle\big)dt, \tag{F.11}$$

and the third one (using $\mathscr{M}[dB_m dB_n^*] = \delta_{mn}dt$ [165, 141]),

$$\begin{aligned}(3) &= \mathscr{M}\Big[\frac{1}{\hbar^2}\sum_m (\hat{L}_m - \langle\hat{L}_m\rangle)|\bar{\psi}(t)\rangle\langle\bar{\psi}(t)|(\hat{L}_m^\dagger - \langle\hat{L}_m^\dagger\rangle)dt\Big] \\ &= \frac{1}{\hbar^2}\Big(\hat{L}_m\hat{\rho}(t)\hat{L}_m^\dagger - \hat{L}_m\hat{\rho}(t)\langle\hat{L}_m^\dagger\rangle - \langle\hat{L}_m\rangle\hat{\rho}(t)\hat{L}_m^\dagger + \langle\hat{L}_m^\dagger\rangle\langle\hat{L}_m\rangle\hat{\rho}(t)\Big)dt.\end{aligned} \tag{F.12}$$

Summation of the three terms delivers again the Lindblad master equation, cf. Eq. 4.2,

$$\frac{d}{dt}\hat{\rho}(t) = \frac{1}{i\hbar}\Big[\hat{H}_{\rm S}, \hat{\rho}(t)\Big] - \frac{1}{2\hbar^2}\sum_m \Big[\hat{L}_m^\dagger \hat{L}_m, \hat{\rho}(t)\Big] + \frac{1}{\hbar^2}\sum_m \hat{L}_m \hat{\rho}(t) \hat{L}_m^\dagger. \tag{F.13}$$

F.2. Norm–Conservation of the Nonlinear SSE

The norm conservation of the stochastic state vector is the fundamental feature of the nonlinear Schrödinger equations. In what follows, this feature shall be proved for the original Ito–Schrödinger equation 4.5. Similarly, it is straightly demonstrated for the non–Markovian stochastic Schrödinger equation discussed in Sec. 4.4.2 (see Eq. 4.62).

Possible variation of the norm of the state vector would be observed according to,

$$d\langle\bar{\psi}(t)|\bar{\psi}(t)\rangle = \underbrace{\langle\bar{\psi}(t)|\big[d|\bar{\psi}(t)\rangle\big]}_{(1)} + \underbrace{\big[d\langle\bar{\psi}(t)|\big]|\bar{\psi}(t)\rangle}_{(2)} + \underbrace{\big[d\langle\bar{\psi}(t)|\big]\,\big[|\bar{\psi}(t)\rangle\big]}_{(3)}, \tag{F.14}$$

where the third term again is the consequence of *Ito's calculus* [165, 141]. Making use of the nonlinear Markovian Ito–Schrödinger equation Eq. 4.5, one obtains

$$\begin{aligned}(1) =& \langle\bar{\psi}(t)|\Big[\frac{1}{i\hbar}\hat{H}_{\rm S} + \frac{1}{i\hbar}\sum_m (\hat{L}_m - \langle\hat{L}_m\rangle)dB_m \\ &+ \frac{1}{\hbar^2}\sum_m \big(\langle\hat{L}_m^\dagger\rangle\hat{L}_m - \frac{1}{2}\hat{L}_m^\dagger\hat{L}_m - \frac{1}{2}\langle\hat{L}_m^\dagger\rangle\langle\hat{L}_m\rangle\big)dt\Big)|\bar{\psi}(t)\rangle\Big]\end{aligned} \tag{F.15}$$

for the first term in Eq. F.14. Reminding the expectation value character of the $\langle\hat{L}_m\rangle = \langle\bar{\psi}(t)|\hat{L}_m|\bar{\psi}(t)\rangle$, it immediately simplifies to

$$(1) = \frac{1}{i\hbar}\langle\bar{\psi}(t)|\hat{H}_{\rm S}|\bar{\psi}(t)\rangle dt + \frac{1}{2\hbar^2}\sum_m \big(-\langle\hat{L}_m^\dagger\hat{L}_m\rangle + \langle\hat{L}_m^\dagger\rangle\langle\hat{L}_m\rangle\big)dt, \tag{F.16}$$

and so it is

$$(2) = \frac{-1}{i\hbar}\langle\bar{\psi}(t)|\hat{H}_{\rm S}|\bar{\psi}(t)\rangle dt + \frac{1}{2\hbar^2}\sum_m \big(-\langle\hat{L}_m^\dagger\hat{L}_m\rangle + \langle\hat{L}_m^\dagger\rangle\langle\hat{L}_m\rangle\big)dt. \tag{F.17}$$

The remaining third term in Eq. F.14 exactly balances the latter two. In particular, its only non–vanishing contribution transforms to

$$\begin{aligned}(3) =& \sum_{m,n}\langle\bar{\psi}(t)|\frac{-1}{i\hbar}(\hat{L}_n^\dagger - \langle\hat{L}_n^\dagger\rangle)dB_n^*\frac{1}{i\hbar}(\hat{L}_m - \langle\hat{L}_m\rangle)dB_m|\bar{\psi}(t)\rangle \\ =& \frac{1}{\hbar^2}\sum_m \big(\langle\hat{L}_m^\dagger\hat{L}_m\rangle - \langle\hat{L}_m^\dagger\rangle\langle\hat{L}_m\rangle\big)dt.\end{aligned} \tag{F.18}$$

Together, it results in $d\langle\bar{\psi}(t)|\bar{\psi}(t)\rangle = 0$, which gives evidence on the conservation of the norm during time–evolution according to Eq. 4.5.

The same proof can be more easily performed when using the *Stratonovich form* of Eq. 4.5 instead. According to the straight transformation rules [165, 141] one obtains

than, cf. Ref. [46],

$$d|\bar{\psi}(t)\rangle = \frac{1}{i\hbar}\hat{H}_{\mathrm{S}}|\bar{\psi}(t)\rangle dt + \frac{1}{i\hbar}\sum_m \big(\hat{L}_m - \langle\hat{L}_m\rangle\big)\big(dB_m + \langle\hat{L}_m^\dagger\rangle dt\big)|\bar{\psi}(t)\rangle \\ - \frac{1}{\hbar^2}\sum_m \big(\hat{L}_m^\dagger\hat{L}_m - \langle\hat{L}_m^\dagger\hat{L}_m\rangle\big)|\bar{\psi}(t)\rangle dt. \tag{F.19}$$

The latter Stratonovich stochastic differential equation obeys the standard algebraic rules and the norm derivative follows by standard product rule,

$$\begin{aligned} d\langle\bar{\psi}(t)|\bar{\psi}(t)\rangle =& \langle\bar{\psi}(t)|d|\bar{\psi}(t)\rangle + \text{H. c.} \\ =& \frac{1}{i\hbar}\sum_m \langle\bar{\psi}(t)|\big(\hat{L}_m - \langle\hat{L}_m\rangle\big)|\bar{\psi}(t)\rangle\big(dB_m + \langle\hat{L}_m^\dagger\rangle dt\big) \\ & - \frac{1}{\hbar^2}\sum_m \langle\bar{\psi}(t)|\big(\hat{L}_m^\dagger\hat{L}_m - \langle\hat{L}_m^\dagger\hat{L}_m\rangle\big)|\bar{\psi}(t)\rangle dt + \text{H. c.}, \end{aligned} \tag{F.20}$$

which directly gives $d\langle\bar{\psi}(t)|\bar{\psi}(t)\rangle = 0$ and so the same proof is delivered again.

Similarly, the conservation of the norm of the state vector $\bar{\phi}(t)$ during time–propagation according to the non–Markovian nonlinear stochastic Schrödinger equation 4.62 can be proved. By its derivation (see, e.g., Refs. [46, 156]), this equation is of Stratonovich type and so standard algebra can be straightly applied again in the fashion of Eq. F.19. Independent on the particular shape of the operator $\hat{O}(t)$, it follows

$$\begin{aligned} d_t\langle\bar{\phi}_z(t)|\bar{\phi}_z(t)\rangle =& \langle\bar{\phi}_z(t)|d_t|\bar{\phi}_z(t)\rangle + \text{H. c.} \\ =& \frac{1}{i\hbar}\langle\bar{\phi}_z(t)|\hat{H}_{\mathrm{S}}|\bar{\phi}_z(t)\rangle + \frac{1}{i\hbar}\sum_m \langle\bar{\phi}_z(t)|\big(\hat{L}_m - \langle\hat{L}_m\rangle\big)|\bar{\phi}_z(t)\rangle\xi_m(t;z) \\ & - \sum_m \langle\bar{\phi}_z(t)|\Big(\big(\hat{L}_m - \langle\hat{L}_m\rangle\big)\hat{O}(t) - \langle\big(\hat{L}_m - \langle\hat{L}_m\rangle\big)\hat{O}(t)\rangle\Big)|\bar{\phi}_z(t)\rangle + \text{H. c.}, \end{aligned} \tag{F.21}$$

which vanishes due to $\langle\hat{L}_m\rangle = \langle\bar{\phi}_z(t)|\hat{L}_m|\bar{\phi}_z(t)\rangle$. Again, the norm conservation is observed as $d_t\langle\bar{\phi}_z(t)|\bar{\phi}_z(t)\rangle = 0$.

F.3. Alternative Damping Operator

It shall be proved that the linear Schrödinger equation Eq. 4.32 can also be related to the version proposed in Refs. [160, 49, 50, 51], in particular concerning the appearance of the zero temperature damping term (see Eq. 4.41). To this end, the time–derivative in Eq. 4.18 must be reconsidered. One realize that the second order terms on the right–hand side contain the first order correction of the first order terms. Now, reminding the expansion executed beforehand to find Eq. 4.18, one immediately finds the correction according to,

$$|\psi_{\alpha\beta}^{(1)}(t)\rangle = |\psi_{\alpha\beta}(0)\rangle + \frac{1}{i\hbar}\sum_{m,\xi}\int_0^t d\tau[\hat{A}_{m\xi}(\tau) + \theta_{m\xi}\hat{B}_{m\xi}(\tau)^*]|\psi_{\alpha\beta}(0)\rangle. \tag{F.22}$$

After inserting that correction, the second order equation can be rewritten as

$$\frac{\partial}{\partial t}|\psi_{\alpha\beta}(t)\rangle = \frac{1}{i\hbar}\sum_{m,\xi}\left[\hat{A}_{m\xi}(t)+\theta_{m\xi}\hat{B}_{m\xi}(t)^*\right]|\psi^{(1)}_{\alpha\beta}(t)\rangle + \frac{1}{(i\hbar)^2}\int_0^t d\tau\sum_{m,\xi}\mathcal{K}^2_{m\xi}\hat{L}_m(t)\hat{L}_m(\tau)e^{-i\omega_{m\xi}(t-\tau)}|\psi_{\alpha\beta}(0)\rangle\ . \tag{F.23}$$

The second order term independent on α and β still appears here because it is the result from the non–commutativity of the derivative operator $\hat{D}_{m\xi}(t)$ (see Eq. 4.15) with the operator $\hat{A}_{m\xi}(t)$ (see Eq. 4.14) within the expansion series. Next, one notices that, in contrast to the formulation Eq. 4.18, all occurring terms in Eq. F.23 are already of second order in the coupling strength (not only the damping term).

Then the argumentation, which leads from Eq. 4.18 to Eq. 4.32, is similarly reapplied. In Sec. 4.2.4, thereby a strict second order treatment with the focus on the final RDO level is employed. Based on Eq. F.23, it is now possible to strictly follow the second order treatment already on the wave function level. After making use again of the possible simplification in Sec. 4.2.2 and the transformational steps concerning the Gaussian averages demonstrated in Sec. 4.2.3, one finally finds the alternative equation of motion

$$i\hbar\frac{\partial}{\partial t}|\phi_{\alpha\beta}(t)\rangle = \big(\hat{H}_{\rm S}+\hat{\mathscr{F}}(t;\alpha,\beta)-i\hbar\hat{\mathscr{D}}_{T=0}(t)\big)|\phi_{\alpha\beta}(t)\rangle, \tag{F.24}$$

with the identical force term Eq. 4.34, but the zero temperature damping term Eq. 4.41.

F.4. Alternative Force Function

In Sec. 4.5.3, the alternative noise algorithm $\mathscr{F}^{(2)}(t)$ (see Eq. 4.69) is phenomenologically introduced as an expression to generate a stochastic force which is equivalent to the one described in Eq. 4.59. Equivalence means here identical stochastic moments. The $\mathscr{F}^{(2)}(t)$ therefore shall obey the relations $\bar{\mathscr{M}}_z[\mathscr{F}^{(2)}_m(t)]=0$ and $\bar{\mathscr{M}}_z[\mathscr{F}^{(2)}_m(t)^*\mathscr{F}^{(2)}_n(t')]=\delta_{mn}C_m(t-t')$, with $\bar{\mathscr{M}}_z[...]$ being the mean operation with respect to the stochastic element in $\mathscr{F}^{(2)}(t)$ and $C_m(t)$ being the time–domain correlation function (see, e.g., Eq. E.5).

The theory of stochastic noise gives the very general expression of a complex–valued force (e.g., arising from a thermal bath) [165]:

$$F(t;\{\phi_k\}) = \sum_{k=1}^{N}\Big(A(\omega_k)\cos(\omega_k t+\phi_k)+iB(\omega_k)\sin(\omega_k t+\phi_k)\Big). \tag{F.25}$$

It describes a Fourier representation of a noise–like process attributed with random phases ϕ_k and frequency steps $\omega_k = k\Delta\omega$ or equaly $\omega_k = k\frac{2\pi}{T}$. The time variable t is defined for the interval $[0,T]$. The real–valued amplitudes $A(\omega_k)$ and $B(\omega_k)$ are thereby not random and it can be generally proved that it is $\bar{\mathscr{M}}_z[F(t)]=0$. Therefore, the mean value operation is considered as $\bar{\mathscr{M}}_z[F(t)] = (2\pi)^{-1}\int_0^{2\pi}d\phi_k F(t;\{\phi_k\})$.

It remains to adapt the amplitudes $A(\omega_k)$ and $B(\omega_k)$ under condition that the it is $\bar{\mathscr{M}}_z[F(t)^*F(t')] = C(t-t')$. The starting point is described by the relation

$$\bar{\mathscr{M}}_z[F(t;\{\phi_k\})^*F(t';\{\phi_{k'}\})] = (2\pi)^{-2}\int_0^{2\pi}\int_0^{2\pi} d\phi_k d\phi_{k'} F(t;\{\phi_k\})^*F(t';\{\phi_{k'}\}). \quad \text{(F.26)}$$

Inserting the general force expression Eq. F.25 and making use of several trigonometric integral relations concerning the occuring products of sine and cosine terms, the latter correlation expression translates to

$$\bar{\mathscr{M}}_z[F(t)^*F(t')] = \sum_{k=1}^{N}\frac{1}{2}\Big(A(\omega_k)^2\cos(\omega_k t) - 2iA(\omega_k)B(\omega_k)\sin(\omega_k t) + B(\omega_k)^2\cos(\omega_k t)\Big). \quad \text{(F.27)}$$

To bring the discrete sum in line with the integral expression of $C(t)$ given in Eq. E.5, it is considered in the limit $N, T \to \infty$,

$$\bar{\mathscr{M}}_z[F(t)^*F(t')] = \int_0^{\infty}\frac{d\omega}{2\Delta\omega}\Big[\big(A(\omega)^2 + B(\omega)^2\big)\cos(\omega t) - 2iA(\omega)B(\omega)\sin(\omega t)\Big]. \quad \text{(F.28)}$$

The $C(t)$ in Eq. E.5 is based on the harmonic oscillator modes of the bath, while Eq. F.28 arises by the statistics of the stochastic noise. Respective comparison allows finding the prefactors $A(\omega)$ and $B(\omega)$ and deriving an analytical expression of $F(t)$. Therefore, the $C(t)$ in Eq. E.5 shall be rewritten by introducing the spectral density $J(\omega) = \pi\sum_\xi \mathscr{K}_\xi^2\delta(\omega-\omega_\xi)$ (see Eq. E.1), with $\omega \geq 0$ and $\mathscr{K}_\xi = \hbar\omega_\xi g_m(\xi)$. Based on that, the Eq. F.28 can be adapted to agree with $C(t)$ in Eq. E.5. Concerning the real part of Eq. F.28 and Eq. E.5, one finds the condition of $A(\omega)^2 + B(\omega)^2 = \frac{2\Delta\omega}{\pi}J(\omega)\coth(\hbar\omega\beta/2)$. By comparing the imaginary part of both expression, it follows $A(\omega)B(\omega) = \frac{\Delta\omega}{\pi}J(\omega)$. Together, it is

$$\big(A(\omega) + B(\omega)\big)^2 = \frac{\Delta\omega}{\pi}J(\omega)\big(2\coth(\hbar\omega\beta/2) + 2\big). \quad \text{(F.29)}$$

To solve this, the ansatz $A(\omega)^2 = a^2(\coth(\hbar\omega\beta/2)+b)$ and $B(\omega)^2 = a^2(\coth(\hbar\omega\beta/2)-b)$ seems adequate. Insertion into Eq. F.29 gives

$$\big(A(\omega) + B(\omega)\big)^2 = a^2\Big(\coth(\hbar\omega\beta/2) + 2\sqrt{\coth(\hbar\omega\beta/2)^2 - X^2}\Big). \quad \text{(F.30)}$$

It immediately shows that it is $a = \Delta\omega J(\omega)/\pi$. The last square root term in Eq. F.30 must become 1 (see Eq. F.29). Therefore, the trigonometric relation $\coth(x)^2 - \sinh(x)^{-2} = 1$ is helpful. One identifies $b = \sinh(\hbar\omega\beta/2)^{-1}$ and so the amplitudes become

$$A(\omega) = \sqrt{\frac{\Delta\omega}{\pi}J(\omega)}\sqrt{\coth(\hbar\omega\beta/2) + \sinh(\hbar\omega\beta/2)^{-1}} \quad \text{(F.31)}$$

$$B(\omega) = \sqrt{\frac{\Delta\omega}{\pi}J(\omega)}\sqrt{\coth(\hbar\omega\beta/2) - \sinh(\hbar\omega\beta/2)^{-1}}. \quad \text{(F.32)}$$

The force expression Eq. F.25 specifies finally to

$$F(t) = \sum_{k=1}^{N} \sqrt{\frac{\Delta\omega}{\pi} J(\omega_k)} \Big(\sqrt{\coth(\hbar\omega_k\beta/2) + \sinh(\hbar\omega_k\beta/2)^{-1}}\, \cos(\omega_k t + \phi_k) \tag{F.33}$$

$$+ i \sqrt{\coth(\hbar\omega_k\beta/2) - \sinh(\hbar\omega_k\beta/2)^{-1}}\, \sin(\omega_k t + \phi_k) \Big). \tag{F.34}$$

For the latter obtained force is is $\bar{\mathscr{M}}_z[F(t)^* F(t')] = C(t-t')$. Its generalization to the molecular site specific force terms $\mathscr{F}_m^{(2)}(t)$ with $\bar{\mathscr{M}}_z[\mathscr{F}_m^{(2)}(t)^* \mathscr{F}_n^{(2)}(t')] = \delta_{mn} C_m(t-t')$ is trivial. By that, the equivalence of Eqs. 4.69 and 4.59 is demonstrated.

Please note further that the complex–valued "quantum noise" in Eq. F.33 becomes real–valued "classical noise" when taking the limit $\lim_{T\to\infty} F(t)$. In the same way, one recognizes that it is always $B(\omega) < A(\omega)$. This means that it is generally $\mathrm{Im}[\mathscr{F}_m^{(2)}(t)] < \mathrm{Re}[\mathscr{F}_m^{(2)}(t)]$. In particular, concerning small frequencies, i.e., slowly varying bath vibrational motions, it becomes $B(\omega) \ll A(\omega)$, which (in dependence on $J(\omega)$) can significantly reduces the imaginary part of the slowly oscillating amplitudes in $\mathscr{F}_m^{(2)}(t)$. The absence of these makes $\mathscr{F}_m^{(2)}(t)$ to a beneficial force algorithm when simulating the stochastic Schrödinger equation 4.58 based on the propagation scheme 4.66 (see also the discussion in Sec. 4.5.3).

G. Electronic Structure Computations

In this chapter, detailed information on the electronic structure methods employed in Chaps. 5 to 8 are provided. The computations related to the *para*–sexiphenyl molecule, the C8S3 cyanine dye, the ZnO cluster and the spherical CdSe nanocrystal are documented.

G.1. *para*-Sexiphenyl

Diverse electronic charge densities of the 6P are required in the studies on excitation energy transfer, hole transfer and photoinduced charge separation (see Chaps. 5, 6 and 7, respectively). The molecular singlet ground state, the first singlet excited state and the cationic state must be concerned. Energies, atomic charges and couplings were computed based on a combination of (TD)DFT and CIS approaches. For this end, own software codes extending the GAUSSIAN suite [233] were developed as an essential part of this thesis.

G.1.1. Molecular energies

The geometry of the *para*-sexiphenyl is presented in Fig. 2.1a. The molecular excitation energy, $E_{eg} = E_e^{6P} - E_g^{6P}$, introduced in Chap. 5 (see Eq. 5.5) represents the difference of the S_1 excited state energy and the S_0 ground state energy of a single 6P. In this work, the value of $E_{eg} = 4.02$ eV was used for the 6P molecule. This gas–phase value was determined based on 6P measurements in DCM solution [234] (which gave the value of 3.88 eV) by incorporating a gas–to–solvent shift of -0.14 eV. The latter shift was computed on the TDDFT level of B3LYP/cc–pVTZ [235, 236] and by making use of a related polarizable continuum model. This level of DFT setting is specially suited for molecules with extended π–conjugated systems and known to deliver reasonable results. Later on, the value of $E_{eg} = 4.02$ eV was confirmed by an INDO/CIS computation based on the parametrization of Ref. [133] and a 6P ground state geometry optimized on the B3LYP/SVP level [235, 237]. The INDO/CIS approach was chosen since the TDDFT method notoriously lacks on accuracy concerning excitation energies and in this particular combination the INDO/CIS method is known to deliver precise excitation energies [238, 135].

Further, the 6P molecular ionization energy, $E_{\mathrm{I}}^{6P} = E_+^{6P} - E_g^{6P}$, must be computed. In Chap. 6 (see Eq. 6.5), it is defined as the energy difference between the 6P cationic and neutral ground state. The definition takes into account intramolecular relaxation processes. In this fashion, it is superior to an ansatzes based on Koopman's theorem (i.e., when using instead only the LUMO energy of the neutral ground state computation). A value of $E_{\mathrm{I}}^{6P} = 6.83$ eV was obtained again on the B3LYP/cc–pVTZ level including

nuclear geometry optimization. This value lies within 10 % deviation of available 6P solid state data [239, 240].

G.1.2. Atomic centered partial (transition) charges

In Chaps. 5, 6 and 7, the different energies of the isolated 6P molecules are corrected by electrostatic shifts due to the interaction with their particular surroundings (i.e., the other 6P molecules and the ZnO cluster). Throughout this thesis, the respective Coulomb integrals are strictly treated introducing an atom–atom interaction model (see discussion in Secs. 5.3.1, 6.2.2 and 7.3.4). For that purpose, atomic centered partial charges, $q_a^{(m)}(\mu)$ (with $a \in \{g,\ e,\ \mathrm{cat}\}$), are introduced related to the position $\mathbf{R}_\mu$ of atom μ in molecule m. They replace the related types of 6P molecular densities $n_a^{(m)}(\mathbf{r})$ (defined here without the nuclei, cf. Eq. 2.26). In similarity, atomic centered partial transition charges $q_{eg}^{(m)}(\mu)$ were introduced to substitute the transition density $n_{eg}^{(m)}(\mathbf{r})$ (see Eq. 2.30), which describes the transition from the 6P molecular S_0 ground to S_1 first excited state. The latter are essential to deduce the excitonic coupling terms of the 6P (see, e.g., Sec. 5.3.1) or its response to an optical excitation (see Sec. 6.2.4).

The sets of charges specific for the S_0 ground, S_1 excited and $+1e$ cationic state were computed utilizing the CHELPG electrostatic fitting procedure [241] available in the Gaussian09 electronic structure kit. This method generates atomic charges using a space grid fitting procedure of their electrostatic potential to the one of the continuous density. By that, the CHELPG provides very physical and accurate atomic charges in case of medium sized organic structures [241]. The corresponding electronic structures and geometry optimizations were executed again on B3LYP/cc–pVTZ level of (TD)DFT. A likewise approach concerning the molecular $S_0 \leftrightarrow S_1$ transition density was not available, which is why related 6P molecular transition charges were determined utilizing the popular population analysis based on natural transition orbitals [242]. In subsequence, the deduced 6P transition charges were rescaled to the exact transition density based dipole moment of $|\mathbf{D}_{eg}| = 12.7$ D, which was determined parallely.

G.1.3. Transfer integrals for intermolecular hole hopping

Firstly, the vertical π–stacking of 6P molecules studied in Chap. 5 shall be concerned. The hole hopping transfer integral, $\mathscr{V}_{mn}^{\mathrm{HT}} = \delta_{m,n\pm1}\mathscr{V}^{\mathrm{HT}}$, is introduced as part of the charge separation Hamiltonian in Eq. 6.4 and further discussed in Sec. 6.2.3. In order to estimate the hopping constant $\mathscr{V}^{\mathrm{HT}}$, focus was put on a 6P dimer configuration. Both 6Ps realized flat geometry. Their intermolecular distance was chosen according to the set–up given in Sec. 6.2. The monomer and dimer electronic ground states were computed based on DFT making use of the long–range corrected cam–B3LYP functional [243] in combination with the correlation consistent cc–pVTZ basis set [236]. By comparing the computations of the 6P dimer with the 6P monomer, a level splitting $\Delta\epsilon$ of the monomer HOMO energies was figured out. In a simple picture, this splitting value gives a typcial measure for the hole transfer that appears among the 6P HOMOs (*energy splitting in dimer* technique). Concretely, the relation $\mathscr{V}^{\mathrm{HT}} = \Delta\epsilon/2$ was applied. Thanks to the symmetric arrangement of the 6P molecules in the dimer, this

simple relation gives reasonable results here (see also the discussion given in Sec. 7.3.5).

It follows the description of the computation of the transfer integrals required in Chap. 7. As illustrated in Fig. 7.3, the lattice structure of the 6P herringbone aggregate simplifies the transfer model. Reminding the usual nearest neighbor coupling, only three transfer integrals must be determined. However, the related dimer constellations do not obey the mutual symmetry demanded for properly utilizing the former mentioned *energy splitting in dimer* technique (see Sec. 7.3.5). In the present case, the latter could only give vague estimations of the couplings [200]. Therefore, the *projection method* was applied instead [213]. Again the electronic structures of the 6P monomer and the three 6P dimer configurations were computed (again on the formerly mentioned cam–B3LYP/cc–pVTZ level of DFT). Furthermore, the sophisticated counterpoise technique was applied. For the *projection method*, three electronic structures are required concerning each dimer configuration: the monomer A, the monomer B and the dimer AB [213]. Though the computations become more costly using the counterpoise technique, by its mean the basis set superposition error is avoided. It is highly recommended and supposed to give essentially more accurate results especially considering very close DA set–ups [213]. The hole transfer integral obtained with the *projection method* must be further adapted to the transfer model introduced with the hole transfer Hamiltonian in Eq. 7.4. The latter is expanded using an orthonormal state ansatz. The straightly computed $\mathscr{V}^{\mathrm{HT}}$, however, gives the transfer integral with regard to the (in general) overlapping D and A states. The Löwdin symmetrical orthogonalization [244, 132, 245] is usually applied to adapt this value to the orthogonal state model (see also Sec. G.3),

$$\mathscr{V}^{\mathrm{HT}} \rightarrow \frac{\mathscr{V}^{\mathrm{HT}} - (E_A + E_D)S_{AD}/2}{1 - S_{AD}^2}. \tag{G.1}$$

The E_D and E_A denote the energies of the computed HOMOs of the 6P donor and acceptor structure. The S_{AD} gives the appearing wave function overlap between both orbitals according to the dimer configuration.

G.2. C8S3 Cyanine Dye

G.2.1. Monomer

The geometry of the 5,5',6,6'-tetrachlorobenzimidacarbo-cyanine (C8S3) molecule is illustrated in Fig. 2.1b. It is employed in Chap. 8 when studying the tubular dye aggregate. The electrostatic interactions between the C8S3 dyes as well as the intermolecular excitonic couplings were determined based on atomic centered partial (transition) charges (see Eq. 8.4 and 8.14). These were borrowed from earlier studies [122]. The related electronic structure caluclations of the C8S3 including geometry optimizations were thereby executed by J. Megow. The geometry optimization of the C8S3 dye was accomplished on the DFT level with the cam–B3LYP [243] and Ahlrichs' triple zeta valence TZVP atomic orbital basis set [246] for all atoms. With the same functional and basis set, the molecular excitation energy (see E_{eg} in Eq. 8.1) was determined using TDDFT. The atomic centered centered partial charges (for the electronic S_0 ground

and S_1 first excited state) as well as the atomic transition charges (representing the $S_0 \leftrightarrow S_1$ transition) of all heavy atoms (C,N,S,O) were approximately introduced based on the CHELPG method [241] (see also Appendix G.1).

G.2.2. Molecular Dynamics Simulations of the tubular dye aggregate

As described in Sec. 8.2, in total 828 C8S3 molecules were utilized to construct the tubular aggregate structure which was then simulated in the periodic box shown in Fig. 8.3a. The extensive Molecular Dynamics simulations were earlier performed by J. Megow in the framework of the studies presented in Ref. [122]. For the studies discussed in Chap. 8, a snap shot of the simulation cell with an equilibrated aggregate structure was borrowed.

The basic simulation box contained a number of 81672 water and 10746 methanol solvent molecules. These were distributed properly in the insight and outside of the aggregate (see top view on the simulation box in Fig. 8.3). The latter molecule numbers accord to the experimental solution mixture of both parts (9:1). In total, the simulation box contained about 350000 atoms. The dimension of the periodic cell approximately amounts $12.7 \times 17.2 \times 17.2$ nm^3. Furthermore, the molecular dynamics followed lab conditions via simulation under constant pressure and temperature (NPT ensemble with 1 atm and 300 K, respectively). The simulations were carried out by using the NAMD software [247] in application of the AMBER force field [248] with the GAFF parameter set [249] for short–range interactions. The remaining intermolecular Coulomb interactions were computed with the particle mesh Ewald method [250] based on atomic centered partial charges of the nuclear optimized ground state configurations of the C8S3 dye (as described above) and the water and methanol solvent molecule (as described in Ref. [122] and references within). The nuclear geometry applied in Chap. 8 was achieved after the simulation time of 3 ns, where time–steps of 0.5 fs were carried out. In course of the simulations, the molecular blueprint (visualized in Fig. 8.3a) was equilibrated to a stable 300 K configuration. This was in agreement with the cryo–TEM observations (see Sec. 8.1). The stability of the TDA was confirmed by monitoring the simulations up to 12 ns without noticing significant changes of the configuration [122]. For the present purpose, that basic simulation box was finally extended to five fold length along the main cylinder axis (see Fig. 8.3b). By that, a 64 nm long tubular dye aggregate including 4140 dyes was constructed.

G.3. ZnO Cluster

In this part of the Appendix, computational details to reproduce the electronic structure of the ZnO cluster are provided. In two very similar shapes the ZnO cluster is part of the studies discussed in Chaps. 5 and 6. Basic information on the crystal structure are given first. Subsequently, details on the electronic structure methods are offered. Based on these, the two sets of valance band (VB)–like and conduction band (CB)–like states can be determined. Finally, the approximate introduction of atomic centered partial charges is explained. The latter allow computing very efficiently and in atomistic resolution the electrostatic interaction as well as the excitonic coupling of the ZnO

cluster, e.g., with a neighbored molecular aggregate.

G.3.1. Nuclear geometry

Both hemispherical ZnO clusters introduced in Chaps. 5 and 6 are based on the same wurtzite lattice structure parameterization given in Ref. [137]. The hemispherical shape was obtained placing the particular (0001) crystal face in the $x-y$–plane. The wurtzite lattice is then periodically built up in direction of $\pm x$, $\pm y$ and $-z$. The hemisherical shape is finally obtained by reducing the generated 3d–structure to atomic positions $\mathbf{R}$ under condition that $\mathbf{R} \leq d/2$ is realized, where d is the aspired diameter of the cluster. The hemispherical ZnO cluster applied in Chap. 5 was designed in that way that only O atoms terminate the curved surface of the cluster (see argumentation in Sec. 5.1). In Chap. 6, no such specific termination condition was obeyed. In both studies, nevertheless, the flat "top" surfaces are of main relevance (see Secs. 5.1 and 6.1). Independent on the particular surface termination, the strict cutting results in so–called dangling bonds around the clusters. In particular concerning finite ZnO structures, these non–saturated bonds must be passivated in some way. Therefore, pseudo–H atoms were added to the cluster surfaces according to an established technique [251] (equivalently for Chaps. 5 and 6). In detail, the H atoms of the passivation layer were placed all around the clusters. Concerning the Zn-H and O-H bonding angles, the set–up of the H atoms complies with the precribed ZnO wurtzite lattice structure. However, the interatomic distances were alternated to 1.0 Å and 1.14 Å in the case of the O-H and Zn-H bond, respectively. The latter two values were chosen in such a way that the ZnO nano structure deviates as little as possible from the bulk structure. In total, the clusters used in Chaps. 5 and 6 contained the number of 3903 and 3783 atoms, respectively.

G.3.2. Single–particle states

The electronic states and energies of the vast ZnO clusters with by far more than one thousand states are computed based on a tight–binding (TB) scheme [252]. It delivered the electronic single–particle (TB) states and energies related to the neutral ground state of the cluster. Concerning partial charging features which are specific on ZnO surfaces, the density functional based tight–binding (DFTB) methodology was supposed to provide essentially more accurate results than the traditional empirical TB ansatz. A brief introduction of both is given in Sec. 2.2.1. The particular numerics were performed by D. Ziemann (see Refs. [80, 253]) based on the open–source DFTB+ software package [136] with the parameterization of Ref. [137]. The two–center approximation and an optimized minimal basis of atomic orbitals (AO's) were used. The Zn, O and H atoms were thereby described by 9 AO's, 4 AO's and 1 AO, respectively (with the H atoms of the surface passivation, see above).

Finally, the number of N_{VB} VB–like states ψ_b and the number of N_{CB} CB–like states $\bar{\psi}_a$ were deduced according to the energetic ordering of the obtained single–particle states. Concerning Chap. 5, the latter were represented using 18256 AO's leading to the numbers of $N_{\mathrm{VB}} = 12253$ and $N_{\mathrm{CB}} = 6003$. The cluster used in Chap. 6 (with

the other termination technique) resulted in 20035 AO's and it was $N_{\mathrm{VB}} = 13750$ and $N_{\mathrm{CB}} = 6285$.

G.3.3. Atomic partial charges of VB–like and CB–like electron states

Atomic centered partial charges and transition charges are determined in relation to each VB and CB–like state. They describe the electronic single–particle densities and transition densities between two such single–particle states. For this purpose, an own software package were developed.

The notation of: $\chi_i^{(\mu)}$, for the ith AO of the μth atom; ψ_λ, for the λth VB–like state; and $\bar{\psi}_{\bar{\lambda}}$, for the $\bar{\lambda}$th single electron CB–like state is employed (see Sec. 2.2.1). The excess electron charge distribution $\bar{\rho}_{\bar{\lambda}}(\mathbf{r})$ is defined in terms of the CB–like state $\bar{\psi}_{\bar{\lambda}}$ (without the nuclear background as well as the other electrons in the VB). It is introduced in Secs. 2.3.4 and 2.3.5 (see, e.g., Eq. 2.46), but also applied to formulate the electrostatic interaction energy shifts in Sec. 6.2.2 (see, e.g., Eqs. 6.5) and Sec. 7.3.4 (see, e.g., Eqs. 7.5). In practice, the Coulomb–type integrals based on the density $\bar{\rho}_{\bar{\lambda}}(\mathbf{r})$ are translated to expressions based on atomic charges $\bar{q}_{\bar{\lambda}}(\mu)$ (see Appendix D). In approximation it follows

$$\bar{\rho}_{\bar{\lambda}}(\mathbf{r}) = -e|\bar{\psi}_{\bar{\lambda}}(\mathbf{r})|^2 \approx \sum_{\mu}^{\text{atoms}} \bar{q}_{\bar{\lambda}}(\mu)\delta(\mathbf{r} - \mathbf{R}_\mu), \tag{G.2}$$

where the electronic charges $\bar{q}_{\bar{\lambda}}(\mu)$ are placed at the atomic positions of the cluster $\mathbf{R}_\mu$. Historically, one could directly calculate Mulliken charges according to, cf. Ref. [132],

$$\bar{q}_{\bar{\lambda}}(\mu) = -e\sum_{i}^{(\mu)}\sum_{\nu}\sum_{j}^{(\nu)}\langle\bar{\psi}_{\bar{\lambda}}|\chi_i^{(\mu)}\rangle\langle\chi_j^{(\nu)}|\bar{\psi}_{\bar{\lambda}}\rangle S_{\mu i,\nu j}. \tag{G.3}$$

These charges would already give a possible discretized charge distribution of state $\bar{\psi}_{\bar{\lambda}}$. The overlap matrix $S_{\mu i,\nu j}$ takes into consideration the non–orthogonality of the AOs $\chi_i^{(\mu)}$ and cares for the normalization condition of the electronic cluster states in the AO basis set. Although the Mulliken charges in Eq. G.3 sum up to the proper values of -1, there might occur unphysical charges owing to the overlap matrix. In fact, certain charges of positiv sign were obtained in the above single–electron charge distributions. For this reason, the Löwdin symmetrical orthogonalization [244, 245, 132] is applied to achieve an orthogonal AO basis set $\zeta_i^{(\mu)}$, according to

$$|\zeta_i^{(\mu)}\rangle = \sum_{\nu}\sum_{j}\left[S^{-1/2}\right]_{\mu i,\nu j}|\chi_j^{(\nu)}\rangle. \tag{G.4}$$

Based on this orthonormal basis set, the Löwdin population analysis delivers more "physically plausible" charges related to the CB–like states,

$$\bar{q}_{\bar{\lambda}}(\mu) = -e\sum_{i}^{(\mu)}\langle\bar{\psi}_{\bar{\lambda}}|\zeta_i^{(\mu)}\rangle\langle\zeta_i^{(\mu)}|\bar{\psi}_{\bar{\lambda}}\rangle. \tag{G.5}$$

They are directly utilized for the practical realization of the interaction energy shifts in Sec. 6.2.2 (see, e.g., Eqs. 6.5). Please note that, for the sake of convenience, the former notation of Eq. G.3 is kept in Eq. G.5. In similarity, electronic charges are found representing the VB–like states,

$$q_\lambda(\mu) = -e \sum_i^{(\mu)} \langle \psi_\lambda | \zeta_i^{(\mu)} \rangle \langle \zeta_i^{(\mu)} | \psi_\lambda \rangle. \tag{G.6}$$

The latter charges $q_\lambda(\mu)$ contribute indirectly as part of the neutral ground state charges of the cluster (see below).

G.3.4. Atomic partial charges of the neutral ground state

The neutral ground state charge density $\Omega(\mathbf{r})$ is introduced in Secs. 2.3.4 and 2.3.5 (e.g., in Eqs. 2.41, 2.49 and 2.54) as the sum of the nuclear charges eZ_μ at atomic positions $\mathbf{R}_\mu$ and the collective density emerging from the occupied VB–like states ψ_λ. In practice, also the $\Omega(\mathbf{r})$ was translated to an expression based on atomic centered partial charges Ω_μ^g,

$$\Omega(\mathbf{r}) \approx \sum_\mu^{\text{atoms}} [eZ_\mu + \sum_\lambda q_\lambda(\mu)] \delta(\mathbf{r} - \mathbf{R}_\mu). \tag{G.7}$$

The utilized charges $q_\lambda(\mu)$ (of the VB–like states ψ_λ) are already introduced in Eq. G.6. Finally, the atomic centered partial charges

$$\Omega_\mu^g = eZ_\mu + \sum_\lambda q_\lambda(\mu) \tag{G.8}$$

are defined which represent the total ground state of the ZnO cluster and sum up to zero.

G.3.5. Atomic partial (transition) charges of the electron–hole pair states

Furthermore, electron–hole pair excitations of the ZnO cluster are required in Chap. 5. In approximation, they describe the excited states of the cluster. Their electrostatic charge density is directly found in terms of the above single–particle picture. In fact, each electron–hole pair excitation formulates the electronic structure of the cluster where a single VB–electron is lifted up into the CB. With respect to the neutral ground state of the cluster, the charge density of an electron–hole pair hence appears as the sum of the negatively charged density of a certain CB–like state (occupied by the excited electron) and the positively charged density of the generated hole in a certain VB–like state. Making use of the above introduced approximate picture, the latter can be directly identified by the atomic centered partial charges $q_{\bar{\lambda}}^{\mathrm{e}}(\mu) = \bar{q}_{\bar{\lambda}}(\mu)$ and $q_\lambda^{\mathrm{h}}(\mu) = -q_\lambda(\mu)$, respectively. The electron and hole electrostatics simply add up as performed in Sec. 5.3.2 (see Eq. 5.11).

Besides the electrostatic interaction of the electron–hole pairs, also their excitonic

transition density is of relevance in Chap. 5 (see Eq. 5.15). In the case of an uncorrelated electron–hole pair, only two single–particle states contribute to the transition density, according to

$$\rho^{(\text{e-h})}_{\lambda\bar{\lambda}}(\mathbf{r}) = -e\psi_{\lambda}(\mathbf{r})\bar{\psi}_{\bar{\lambda}}(\mathbf{r})^{*} \approx \sum_{\mu}^{\text{atoms}} q^{(\text{e-h})}_{\lambda\bar{\lambda}}(\mu)\delta(\mathbf{r}-\mathbf{R}_{\mu}). \tag{G.9}$$

In contrast to the above single–particle densities, the transition density gives zero by integration with respect to $\mathbf{r}$. However, its approximate reduction to related atomic centered partial transition charges works similarily as demonstrated on the right–hand side of Eq. G.2. By expanding the single–particle states in the mid of Eq. G.9 again in the orthonormalized AO basis set (and following the Löwdin population analysis), one straightly finds an analytic expression for the transition charges,

$$q^{(\text{e-h})}_{\lambda\bar{\lambda}}(\mu) = -e\sum_{i}^{(\mu)}\langle\psi_{a}|\zeta_{i}^{(\mu)}\rangle\langle\zeta_{i}^{(\mu)}|\psi_{b}\rangle \tag{G.10}$$

It is based on the same expansion coefficients already needed for the computation of the electrostatic charges (see Eqs. G.5 and G.6).

G.4. Spherical CdSe Nanocrystal

In Chap. 8, excitation energy transfer from a tubular dye aggregate to a CdSe nanocrystal (NC) is discussed. Finally, Fermi Golden Rule–like transfer rate are developed. For this end, the energies and transition densities of the Wannier–Mott excitons of the NC were needed. These are introduced and discussed throughout Sec. 8.6. The particular data on the NC excitons was greatly delivered by D. Ziemann (see also Ref. [80]).

The description of the NC starts with a spherical crystal structure constructed with a radii of 2.5 nm. Concretely, this resulted in a number of 819 Cd and 630 Se atoms. In general, the approach to the NC is similar with the ansatz followed concerning the ZnO cluster (see Appendix G.3). Surface relaxation effect due to lattice tension, however, were not relevant concerning the CdSe NC and an additional passivation technique was not necessary. Further the empirical TB ansatz sufficed here. The number of occupied states ψ_{λ} amounted $N_{\text{VB}} = 9072$. Further, a number of $N_{\text{CB}} = 5418$ unoccupied CB–like states $\bar{\psi}_{\bar{\lambda}}$ were determined. Therefore, a minimum basis set (sp3s*) was utilized to prepare Cd and Se AOs. This basis set approach delivered accurate results for CdSe structures already before [80]. Further, a TB parameterization specially suited for CdSe NC including spin–orbit coupling was applied [254, 255, 256, 257]. The TB problem, i.e., the diagonalization of the TB Hamiltonian (see Eq. 2.9) was succeeded based on an iterative eigenvalue solver adapted to sparse matrix systems provided in the Intel Math Kernel Library.

In Refs. [254, 255, 256, 257], also general information on the methodology to describe singly excited states of a NC (especially of CdSe composition) can be found. In order to determine the Wannier–Mott excitons (correlated electron–hole pairs) of the NC, these works combine a tight–binding description of the individual electron and hole

states with a subsequent consideration of the Coulomb–attraction in a CI methodology. This stepwise approach is also introduced in the framework of the Secs. 2.2.1 and 2.2.2 and applied in Sec. 8.6. Finally, the Wannier–Mott exciton equation 8.32 with the Wannier–Mott exciton Hamiltonian (see Eq. 8.33) must be solved to obtain the expansion coefficient $\mathfrak{C}_{\lambda\bar{\lambda}}(\gamma)$. The latter give message on the shape of the excitons $|\Psi_\gamma\rangle$ (see Eq. 8.31) based on all possible electron–hole pair configurations $|\Psi_\lambda^{\bar{\lambda}}\rangle$ (see Eq. 8.30). Their proper superpositing relies on the determination of the electron–hole pair coupling in the exciton Hamiltonian (see Eq. 8.33), i.e., on both the direct Coulomb interaction and the exchange interaction terms. The latter two types of terms are generally introduced in Eqs. 2.14 and 2.15, respectively. In practice, these integral terms were computed in approximate manner by substituting again related atomic centered partial (transition) charges, according to

$$W_{eh,e'h'} \approx \sum_{\mu,\nu} \frac{q_{ee'}(\mu) q_{hh'}(\nu)^*}{|\mathbf{R}_\mu - \mathbf{R}_\nu|}, \qquad \text{and} \qquad K_{eh,e'h'} \approx \sum_{\mu,\nu} \frac{q_{eh}^{(\text{e-h})}(\mu) \big(q_{e'h'}^{(\text{e-h})}(\nu)\big)^*}{|\mathbf{R}_\mu - \mathbf{R}_\nu|}. \quad \text{(G.11)}$$

Therefore, different atomic centered partial (transition) charges were required related to the nuclear structure of the NC. The μth atom is positioned at position $\mathbf{R}_\mu$. In $W_{eh,e'h'}$, electrostatic charges (with $-e\sum_{\bar{s}} \bar{\psi}_e(\mathbf{x},\bar{s})^* \bar{\psi}_{e'}(\mathbf{x},\bar{s}) \approx \sum_\mu q_{ee'}(\mu)\delta(\mathbf{x}-\mathbf{R}_\mu)$ and $-e\sum_s \psi_h(\mathbf{y},s)^* \psi_{h'}(\mathbf{y},s) \approx \sum_\mu q_{hh'}(\mu)\delta(\mathbf{y}-\mathbf{R}_\mu)$) of the electron and hole appear with $q_{ee'}(\mu)$ and $q_{hh'}(\mu)$ under condition that $e = e'$ and $h = h'$, respectively. In the remaining cases, the charges represent the transition densities between the states $\bar{\psi}_e$ and $\bar{\psi}_{e'}$ (i.e., within the CB) and between the states ψ_h and $\psi_{h'}$ (i.e., within the VB). In contrary to that, in the exchange term $K_{eh,e'h'}$, exclusively transition charges related to electron–hole pair excitation and de–excitation appear, i.e., processes between the VB and CB (with $-e\sum_{\bar{s}} \bar{\psi}_e(\mathbf{x},\bar{s})^* \psi_h(\mathbf{x},\bar{s}) \approx \sum_\mu q_{eh}^{(\text{e-h})}(\mu)\delta(\mathbf{x}-\mathbf{R}_\mu)$). These latter type of charges are furthermore applied in order to finally compute the excitonic coupling terms between the molecular aggregate and the NC in Sec. 8.7.1 (see Eq. 8.41 with Eqs. 8.39 and 8.40). The concrete expressions of all these charges confirm with the forms introduced above in Secs. G.3.3 and G.3.5.

The Wannier–Mott exciton equation describes a mathematical eigenvalue problem. Its dimensionality was by far too large to be directly solved. Therefore, the Hamiltonian in Eq. 8.33 is diagonalized concerning a reduced state space of electron–hole pair excitations. Starting from both band edges, more and more combinations of hole states (VB–like) and electron states (CB–like) were successively activated until the eigensystem in the interesting very low–energy region showed adequate convergence. Finally, the energetically lowest 30 WXs were determined by taking into consideration the energetically lowest 40 electron and highest 200 hole states. For the diagonalizations, the LAPACK matrix algebra software package was utilized.

H. Further Computational Details

H.1. Excited States of the *para*–Sexiphenyl/ZnO Interface

In Sec. 6.4, the full system eigenstates (FSEs) of the *para*–sexiphenyl/ZnO interface are aspired to clarify the response of the interface to a weak optical excitation. For this purpose, it is generally required to diagonalize the interface system Hamiltonian $\hat{H}(t=0)$ given in Eq. 6.4. However, the related Hamiltonian matrix is here of the dimensionality 120081x120081 and diagonalization means a computational obstacle. Instead the relevant interface eigenstates were here determined in an approximate manner by reducing the basis set to expand the interface Hamiltonian in the first place. In particular, this concerns the number of charge–separated (CS) states $|\mathrm{CS}_{ma}\rangle$ (see Eq. 6.3).

In the localized state picture, exclusively the 20 6P exited states $|\mathrm{LX}_m\rangle$ interact with the optical field while the $|\mathrm{CS}_{ma}\rangle$ are only involved by means of the interface coupling $\mathscr{V}_a^{\mathrm{CT}}$. Accordingly, it is: the weaker the $\mathscr{V}_a^{\mathrm{CT}}$ the smaller the contribution of the $|\mathrm{CS}_{ma}\rangle$ with $m = 1$ to the interesting bright FSEs which appear noticable in the interface absorption spectrum. The contribution of the other $|\mathrm{CS}_{ma}\rangle$ with $m \in \{2, ..., 20\}$ is even smaller. This latter issue is directly exploited in Sec. 6.4. Namely, in order to facilitate the diagonalization, the rule of $|\mathscr{V}_a^{\mathrm{CT}}| > 1$ meV was established. All elements in the Hamilton matrix related to the states $|\mathrm{CS}_{ma}\rangle$ with $m \in \{1, ..., 20\}$ which do not fulfill this condition were ignored. Afterwards, the diagonalization procedure was performed taking into consideration only the remaining (i.e., most relevant) matrix elements. With this limit it was possible to reduce the total number of 6285 CB–like states to only the substantial amount of 1689 states. The introduced truncation limit is illustrated in Fig. 6.2 by the pink coloring. Concerning finally the number of the generated system eigenstates this corresponds to a reduction from 125720 original states (excluding the interface ground state) to 33800 essential states. In practice, the reduced eigenvalue problem was then solved using a sparse matrix algorithm from the LAPACK software package.

H.2. Time–Domain Simulations

The time–domain simulation discussed in this work were performed using different numerical propagation techniques. They were implemented in a software packages which was specially developed in the framework of this thesis.

H.2.1. Coherent wave packet propagation

In the case of coherent wave packet motion, the time–evolution of the system state is prescribed by the ordinary (time–dependent) Schrödinger equation 3.1. The *Cheby-*

shev polynom expansion method is one very efficient method to solve the ordinary Schrödinger under condition that the system Hamiltonian is time–independent. Basically, it uses a polynom expansion series to approximate the time–evolution operator according to Eq. 3.2. The simulated state trajectory is obtained in a successive manner. The larger the time increments are chosen the more terms are required in the expansion series to obtain converged results. The Chebyshev method is well–known for its high accuracy and applied to the studies on excitation energy transfer presented in Chap. 5. Time–steps between 0.1 fs and 50 fs could be utilized in dependence on the exciton transfer kinetics. The number of polynoms were adapted dynamically to properly achieve convergence. In the study on ultrafast photoinduced charge separation kinetics discussed in Chap. 6, the interface Hamiltonian is explicitly time–dependent (see Eq. 6.6). The very common RK4 method is applied. It describes one of the most standard explicit iterative methods to directly propagate an intial value problem, here the time–dependent Schrödinger equation. As such it can take into consideration the explicit time–dependence of the Hamiltonian. Concerning the latter, the very rapidly oscillating terms mimicking the laser–pulse action (see again Eq. 6.6) were smoothed by making use of the *rotating wave approximation* [146]. This was without a noticable effect on the resulting kinetics, however, the size of the time–steps could be chosen decisively larger (here between 0.02 and 0.2 fs). Please note finally that the full number of 125721 interface states were contained in the dynamics.

H.2.2. Integration of the stochastic Schrödinger equations

When a system is conditioned by a surrounding bath, the time–evolution of its state obeys the stochastic Schrödinger equation (SSE). The dissipative hole and exciton kinetics presented in Chaps. 7 and 8 are based on solving the latter. For this purpose, again the iterative RK4 method is applied. This is generally possible here due to the fact that the force is implemented in terms of a continuous functional form – though very fluctuative. The propagation of the linear SSE 4.58 required the renormalization scheme sketched in Eq. 4.66. The nonlinear SSE 4.62 conserves the vector norm of the state. It could be integrated straightly based on the RK4. For efficent computation of the force algorithm given in Eq. 4.59 (based on the noise terms on the right–hand side of Eqs. 4.56 and 4.57) the FFTW software libary was employed. All random numbers were produced based on the (most commonly used) Linear Congruential Generator algorithm, where the polar method was further used to obtain complex–valued Gaussian random numbers [258]. The FFTW was also applied to determine the Fourier transform of the spectral density and the correlation function required in the damping terms Eqs. 4.35 and 4.41, respectively.

Bibliography

[1] V. M. Agranovich, Yu. N. Gartstein, and M. Litinskaya. Hybrid resonant organic-inorganic nanostructures for optoelectronic applications. *Chemical Reviews*, 111: 5179–5214, 2011.

[2] Brian E. Hardin, Henry J. Snaith, and Michael D. McGehee. The renaissance of dye-sensitized solar cells. *Nat. Photonics*, 6:162–169, 2012.

[3] Yana Vaynzof, Artem A. Bakulin, Simon Gélinas, and Richard H. Friend. Direct observation of photoinduced bound charge-pair states at an organic-inorganic semiconductor interface. *Phys. Rev. Lett.*, 108:246605, 2012.

[4] Kenny F. Chou and Allison M. Dennis. Förster resonance energy transfer between quantum dot donors and quantum dot acceptors. *Sensors*, 15(6):13288–13325, 2015.

[5] Sophia Buhbut, Stella Itzhakov, Elad Tauber, Menny Shalom, Idan Hod, Thomas Geiger, Yuval Garini, Dan Oron, and Arie Zaban. Built-in quantum dot antennas in dye-sensitized solar cells. *ACS Nano*, 4(3):1293–1298, 2010.

[6] Hyunbong Choi, Pralay K. Santra, and Prashant V. Kamat. Synchronized energy and electron transfer processes in covalently linked cdse-squaraine dye-tio$_2$ light harvesting assembly. *ACS Nano*, 6:5718–5726, 2012.

[7] Zhihua Xu, Feng Gao, Elena A. Makarova, Ahmed A. Heikal, and Victor N. Nemykin. Energy transfer from colloidal quantum dots to near-infrared-absorbing tetraazaporphyrins for enhanced light harvesting. *The Journal of Physical Chemistry C*, 119(18):9754–9761, 2015.

[8] Yan Qiao, Frank Polzer, Holm Kirmse, Egon Steeg, Sergei Kühn, Sebastian Friede, Stefan Kirstein, and Jürgen P. Rabe. Nanotubular j-aggregates and quantum dots coupled for efficient resonance excitation energy transfer. *ACS Nano*, 9 (2):1552–1560, 2015.

[9] Antonio Alvaro Ranha Neves, Andrea Camposeo, Roberto Cingolani, and Dario Pisignano. Interaction scheme and temperature behavior of energy transfer in a light-emitting inorganic-organic composite system. *Advanced Functional Materials*, 18(5):751–757, 2008.

[10] R. Schlesinger, F. Bianchi, S. Blumstengel, C. Christodoulou, R. Ovsyannikov, B. Kobin, K. Moudgil, S. Barlow, S. Hecht, S. R. Marder, F. Henneberger, and N. Koch. Efficient light emission from inorganic and organic semiconductor hybrid structures by energy-level tuning. *Nat. Commun*, 6(6754), 2015.

[11] Chen Wang and Emily A. Weiss. Accelerating fret between near-infrared emitting quantum dots using a molecular j-aggregate as an exciton bridge. *Nano Letters*, 17(9):5666–5671, 2017.

[12] K. Becker, J. M. Lupton, J. Müller, A. L. Rogach, D. V. Talapin, H. Weller, and J. Feldmann. Electrical control of förster energy transfer. *Nature Materials*, 5: 777–781, 2006.

[13] Brian J. Walker, August Dorn, Vladimir Bulović, and Moungi G. Bawendi. Color-selective photocurrent enhancement in coupled j-aggregate/nanowires formed in solution. *Nano Letters*, 11(7):2655–2659, 2011.

[14] Andrii Kovalchuk, David A. Egger, Tarek Abu-Husein, Egbert Zojer, Andreas Terfort, and Ryan C. Chiechi. Dipole-induced asymmetric conduction in tunneling junctions comprising self-assembled monolayers. *RSC Adv.*, 6:69479–69483, 2016.

[15] Fortunato Piersimoni, Raphael Schlesinger, Johannes Benduhn, Donato Spoltore, Sina Reiter, Ilja Lange, Norbert Koch, Koen Vandewal, and Dieter Neher. Charge transfer absorption and emission at zno/organic interfaces. *The Journal of Physical Chemistry Letters*, 6(3):500–504, 2015.

[16] Moungi Bawendi Seth Coe, Wing-Keung Woo and Vladimir Bulović. Electroluminescence from single monolayers of nanocrystals in molecular organic devices. *Nature*, 420:800 – 803, 2002.

[17] Seth Coe-Sullivan, Wing-Keung Woo, Jonathan S. Steckel, Moungi Bawendi, and Vladimir Bulović. Tuning the performance of hybrid organic/inorganic quantum dot light-emitting devices. *Organic Electronics*, 4(2):123 – 130, 2003.

[18] Rakhi Grover, Ritu Srivastava, Gayatri Chauhan, M. N. Kamalasanan, and D. S. Mehta. White electroluminescence from hybrid organic inorganic LEDs based on thermally evaporated nanocrystals. *EPL (Europhysics Letters)*, 99(1):17003, 2012.

[19] G. G. Paschos, N. Somaschi, S. I. Tsintzos, D. Coles, J. L. Bricks, Z. Hatzopoulos, D. G. Lidzey, P. G. Lagoudakis, and P. G. Savvidis. Hybrid organic-inorganic polariton laser. *Sci. Rep*, 7(11377), 2017.

[20] Rahul Jayaprakash, Kyriacos Georgiou, Harriet Coulthard, Alexis Askitopoulos, Sai K. Rajendran, David M. Coles, Andrew J. Musser, Jenny Clark, Ifor D. W. Samuel, Graham A. Turnbull, Pavlos G. Lagoudakis, and David G. Lidzey. A hybrid organic-inorganic polariton led. *Light Sci. Appl*, 8(81), 2019.

[21] Elisabeth Holder, Nir Tessler, and Andrey L. Rogach. Hybrid nanocomposite materials with organic and inorganic components for opto-electronic devices. *J. Mater. Chem.*, 18:1064–1078, 2008.

[22] Burak Guzelturk, Pedro Ludwig Hernandez Martinez, Qing Zhang, Qihua Xiong, Handong Sun, Xiao Wei Sun, Alexander O. Govorov, and Hilmi Volkan Demir. Excitonics of semiconductor quantum dots and wires for lighting and displays. *Laser & Photonics Reviews*, 8(1):73–93, 2014.

[23] Alexey V. Akimov, Amanda J. Neukirch, and Oleg V. Prezhdo. Theoretical insights into photoinduced charge transfer and catalysis at oxide interfaces. *Chemical Reviews*, 113(6):4496–4565, 2013.

[24] S Blumstengel, S Sadofev, and F Henneberger. Electronic coupling of optical excitations in organic/inorganic semiconductor hybrid structures. *New Journal of Physics*, 10:065010, 2008.

[25] Dae Mann Kim. *Introductory Quantum Mechanics for Semiconductor Nanotechnology*. Wiley-VCH, Berlin, 1st edition, 2010. ISBN 978-3527409754.

[26] Francesca S. Freyria, José M. Cordero, Justin R. Caram, Sandra Doria, Amro Dodin, Yue Chen, Adam P. Willard, and Moungi G. Bawendi. Near-infrared quantum dot emission enhanced by stabilized self-assembled j-aggregate antennas. *Nano Letters*, 17(12):7665–7674, 2017.

[27] Carles Curutchet and Benedetta Mennucci. Quantum chemical studies of light harvesting. *Chemical Reviews*, 117(2):294–343, 2017.

[28] Aman Kumar Agrawal, Prabhat Kumar Sahu, Sudipta Seth, and Moloy Sarkar. Electrostatically driven förster resonance energy transfer between a fluorescent metal nanoparticle and j-aggregate in an inorganic-organic nanohybrid material. *The Journal of Physical Chemistry C*, 123(6):3836–3847, 2019.

[29] Oksana Ostroverkhova. Organic optoelectronic materials: Mechanisms and applications. *Chemical Reviews*, 116(22):13279–13412, 2016.

[30] Lars Dworak, Victor V. Matylitsky, Ting Ren, Thomas Basché, and Josef Wachtveitl. Acceptor concentration dependence of förster resonance energy transfer dynamics in dye-quantum dot complexes. *The Journal of Physical Chemistry C*, 118(8):4396–4402, 2014.

[31] Zheng Hua, Qinfeng Xu, Xiangnan Huang, Chunfeng Zhang, Xiaoyong Wang, and Min Xiao. Energy transfer from a single semiconductor nanocrystal to dye molecules. *ACS Nano*, 8(7):7060–7066, 2014.

[32] Walter R. Duncan, William M. Stier, and Oleg V. Prezhdo. Ab initio nonadiabatic molecular dynamics of the ultrafast electron injection across the alizarin-tio$_2$ interface. *Journal of the American Chemical Society*, 127(21):7941–7951, 2005.

[33] Oleg V. Prezhdo, Walter R. Duncan, and Victor V. Prezhdo. Dynamics of the photoexcited electron at the chromophore-semiconductor interface. *Accounts of Chemical Research*, 41(2):339–348, 2008.

[34] G. Wu, X. Zhang, and G. Lu. Charge separation and exciton dynamics at polymer/zno interface from first-principle simulations. *J. Phys. Chem. Lett.*, 5:2649, 2014.

[35] Eike Verdenhalven, Andreas Knorr, Marten Richter, Bjoern Bieniek, and Patrick Rinke. Theory of optical excitations in dipole-coupled hybrid molecule-semiconductor layers: Coupling of a molecular resonance to semiconductor continuum states. *Phys. Rev. B*, 89:235314, 2014.

[36] M P Ljungberg, O Vänskä, P Koval, S W Koch, M Kira, and D Sánchez-Portal. Charge-transfer states and optical transitions at the pentacene-tio$_2$ interface. *New Journal of Physics*, 19(3):033019, 2017.

[37] Run Long, Oleg V. Prezhdo, and Weihai Fang. Nonadiabatic charge dynamics in novel solar cell materials. *Wiley Interdisciplinary Reviews: Computational Molecular Science*, 7(3):e1305, 2017.

[38] Judith F. Specht, Eike Verdenhalven, Björn Bieniek, Patrick Rinke, Andreas Knorr, and Marten Richter. Theory of excitation transfer between two-dimensional semiconductor and molecular layers. *Phys. Rev. Applied*, 9:044025, 2018.

[39] L Susan Blackford, Antoine Petitet, Roldan Pozo, Karin Remington, R Clint Whaley, James Demmel, Jack Dongarra, Iain Duff, Sven Hammarling, Greg Henry, et al. An updated set of basic linear algebra subprograms (blas). *ACM Transactions on Mathematical Software*, 28(2):135–151, 2002.

[40] E. Anderson, Z. Bai, J. Dongarra, A. Greenbaum, A. McKenney, J. Du Croz, S. Hammarling, J. Demmel, C. Bischof, and D. Sorensen. Lapack: A portable linear algebra library for high-performance computers. In *Proceedings of the 1990 ACM/IEEE Conference on Supercomputing*, Supercomputing '90, pages 2–11, 1990. ISBN 0-89791-412-0.

[41] C Leforestier, R.H Bisseling, C Cerjan, M.D Feit, R Friesner, A Guldberg, A Hammerich, G Jolicard, W Karrlein, H.-D Meyer, N Lipkin, O Roncero, and R Kosloff. A comparison of different propagation schemes for the time dependent schrödinger equation. *Journal of Computational Physics*, 94(1):59 – 80, 1991.

[42] Toshiaki Iitaka. Solving the time-dependent schrödinger equation numerically. *Phys. Rev. E*, 49:4684–4690, 1994.

[43] Katharina Kormann, Sverker Holmgren, and Hans O. Karlsson. Accurate time propagation for the schrödinger equation with an explicitly time-dependent hamiltonian. *The Journal of Chemical Physics*, 128(18):184101, 2008.

[44] V. May and O. Kühn. *Charge and Energy Transfer Dynamics in Molecular Systems*. Wiley-VCH, 3rd edition, 2011. ISBN 978-3527407323.

[45] H.-P. Breuer and F. Petruccione. *The Theory of Open Quantum Systems*. Oxford University Press, 2nd edition, 2007. ISBN 978-0199213900.

[46] P. Garbaczewski and R. Olkiewicz. *Dynamics of Dissipation.* Lecture Notes in Physics, 1st edition, 2002. ISBN 978-3540441113.

[47] L. Diósi and W. T. Strunz. The non-markovian stochastic schrödinger equation for open systems. *Phys. Lett. A*, 235:569, 1997.

[48] L. Diósi, N. Gisin, and W. T. Strunz. Non-markovian quantum state diffusion. *Phys. Rev. A*, 58:1699, 1998.

[49] X. Zhong and Y. Zhao. Non-markovian stochastic schrödinger equation at finite temperatures for charge carrier dynamics in organic crystals. *J. Chem. Phys.*, 138:014111, 2013.

[50] X. Zhong, Y. Zhao, and J. Cao. Coherent quantum transport in disordered systems: Ii. temperature dependence of carrier diffusion coefficients from the time-dependent wavepacket diffusion method. *New J. Phys.*, 16:045009, 2014.

[51] Y. Ke, Y. Liu, and Y. Zhao. Visualization of hot exciton energy relaxation from coherent to diffusive regimes in conjugated polymers: A theoretical analysis. *J. Phys. Chem. Lett.*, 6:1741, 2015.

[52] T. Fujita, S. Atahan-Evrenk, N. P. D. Sawaya, and A. Aspuru-Guzik. Coherent dynamics of mixed frenkel and charge-transfer excitons in dinaphtho[2,3-b:2'3'-f]thieno[3,2-b]-thiophene thin films: the importance of hole localization. *J. Phys. Chem. Lett.*, 7:1374, 2016.

[53] Stéphanie Valleau, Semion K. Saikin, Man-Hong Yung, and Alán Aspuru-Guzik. Exciton transport in thin-film cyanine dye j-aggregates. *The Journal of Chemical Physics*, 137(3):034109, 2012.

[54] Nicolas P. D. Sawaya, Joonsuk Huh, Takatoshi Fujita, Semion K. Saikin, and Alán Aspuru-Guzik. Fast delocalization leads to robust long-range excitonic transfer in a large quantum chlorosome model. *Nano Letters*, 15(3):1722–1729, 2015.

[55] Juan Aragó and Alessandro Troisi. Regimes of exciton transport in molecular crystals in the presence of dynamic disorder. *Advanced Functional Materials*, 26 (14):2316–2325, 2016.

[56] T. Yao. Zinc oxide. In K.H. Jürgen Buschow, Robert W. Cahn, Merton C. Flemings, Bernhard Ilschner, Edward J. Kramer, Subhash Mahajan, and Patrick Veyssiére, editors, *Encyclopedia of Materials: Science and Technology*, pages 9883 – 9887. 2001.

[57] Agnieszka Kolodziejczak-Radzimska and Teofil Jesionowski. Zinc oxide–from synthesis to application: A review. *Materials*, 7(4):2833–2881, 2014.

[58] Jing Yu Lao, Jian Guo Wen, and Zhi Feng Ren. Hierarchical zno nanostructures. *Nano Letters*, 2(11):1287–1291, 2002.

[59] Zhong Lin Wang. Nanostructures of zinc oxide. *Materials Today*, 7(6):26 – 33, 2004.

[60] Vaseem Mohammad, Ahmad Umar, and Yoon-Bong Hahn. *ZnO Nanoparticles: Growth, Properties, and Applications*, volume 5, pages 1–36. 2010.

[61] A.B. Djurišić, A.M.C. Ng, and X.Y. Chen. Zno nanostructures for optoelectronics: Material properties and device applications. *Progress in Quantum Electronics*, 34(4):191 – 259, 2010.

[62] Oliver T. Hofmann and Patrick Rinke. Band bending engineering at organic/inorganic interfaces using organic self-assembled monolayers. *Advanced Electronic Materials*, 3, 6 2017.

[63] E. Zojer, N. Koch, P. Puschnig, F. Meghdadi, A. Niko, R. Resel, C. Ambrosch-Draxl, M. Knupfer, J. Fink, J. L. Brédas, and G. Leising. Structure, morphology, and optical properties of highly ordered films of para-sexiphenyl. *Phys. Rev. B: Condens. Matter Mater. Phys.*, 61:16538, 2000.

[64] R. Resel. Crystallographic studies on hexaphenyl thin films - a review. *Thin Solid Films*, 433:1, 2003.

[65] M. Sparenberg, A. Zykov, P. Beyer, L. Pithan, C. Weber, Y. Garmshausen, F. Carlá, S. Hecht, S. Blumstengel, F. Henneberger, and S. Kowarik. Controlling the growth mode of para-sexiphenyl (6p) on zno by partial fluorination. *Phys. Chem. Chem. Phys.*, 16:26084, 2014.

[66] J.-C. Deinert, D. Wegkamp, M. Meyer, C. Richter, M. Wolf, and J. Stähler. Ultrafast exciton formation at the zno(10-10) surface. *Phys. Rev. Lett.*, 113: 057602, 2014.

[67] S. Friede, S. Kuehn, S. Sadofev, S. Blumstengel, F. Henneberger, and Th. Elsaesser. Nanoscale transport of surface excitons at the interface between zno and a molecular layer. *Phys. Rev. B: Condens. Matter Mater. Phys.*, 91:121415, 2015.

[68] S. Blumstengel, H. Glowatzki, S. Sadofev, N. Koch, S. Kowarik, J. P. Rabe, and F. Henneberger. Band-offset engineering in organic/inorganic semiconductor hybrid structures. *Phys. Chem. Chem. Phys.*, 12:11642, 2010.

[69] Oliver T. Hofmann, Jan-Christoph Deinert, Yong Xu, Patrick Rinke, Julia Stähler, Martin Wolf, and Matthias Scheffler. Large work function reduction by adsorption of a molecule with a negative electron affinity: Pyridine on zno($10\bar{1}0$). *The Journal of Chemical Physics*, 139(17):174701, 2013.

[70] Julia Stähler and Patrick Rinke. Global and local aspects of the surface potential landscape for energy level alignment at organic-zno interfaces. *Chemical Physics*, 485-486:149 – 165, 2017.

[71] Karol Palczynski, Georg Heimel, Jan Heyda, and Joachim Dzubiella. Growth and characterization of molecular crystals of para-sexiphenyl by all-atom computer simulations. *Crystal Growth & Design*, 14(8):3791–3799, 2014.

[72] Moritz Eyer, Johannes Frisch, Sergey Sadofev, Norbert Koch, Emil J. W. List-Kratochvil, and Sylke Blumstengel. Role of hybrid charge transfer states in the charge generation at znmgo/p3ht heterojunctions. *The Journal of Physical Chemistry C*, 121(40):21955–21961, 2017.

[73] X.-Y. Zhu, Q. Yang, and M. Muntwiler. Charge transfer excitons at organic semiconductor surfaces and interfaces. *Acc. Chem. Res.*, 42:1779, 2009.

[74] Rachel D. Harris, Stephanie Bettis Homan, Mohamad Kodaimati, Chen He, Alexander B. Nepomnyashchii, Nathaniel K. Swenson, Shichen Lian, Raul Calzada, and Emily A. Weiss. Electronic processes within quantum dot-molecule complexes. *Chemical Reviews*, 116(21):12865–12919, 2016.

[75] D. Basko, G.C. La Rocca, F. Bassani, and V.M. Agranovich. Förster energy transfer from a semiconductor quantum well to an organic material overlayer. *The European Physical Journal B - Condensed Matter and Complex Systems*, 8: 353–362, 1999.

[76] Dmitri S. Kilin, Kiril Tsemekhman, Oleg V. Prezhdo, Eduard I. Zenkevich, and Christian von Borczyskowski. Ab initio study of exciton transfer dynamics from a core-shell semiconductor quantum dot to a porphyrin-sensitizer. *Journal of Photochemistry and Photobiology A: Chemistry*, 190:342 – 351, 2007.

[77] Hiroyuki Tamura, Jean-Maurice Mallet, Martin Oheim, and Irene Burghardt. Ab initio study of excitation energy transfer between quantum dots and dye molecules. *The Journal of Physical Chemistry C*, 113(18):7548–7552, 2009.

[78] V. Agranovich, R. Atanasov, and F. Bassani. Hybrid interface excitons in organic-inorganic quantum wells. *Solid State Communications*, 92(4):295 – 301, 1994.

[79] V M Agranovich, D M Basko, G C La Rocca, and F Bassani. Excitons and optical nonlinearities in hybrid organic-inorganic nanostructures. *Journal of Physics: Condensed Matter*, 10(42):9369–9400, 1998.

[80] D. Ziemann and V. May. Distant and shape dependent excitation energy transfer in nanohybrid systems: Computations on a pheophorbide-a cdse nanocrystals complex. *The Journal of Physical Chemistry Letters*, 5:1203, 2014.

[81] D. Caruso and A. Troisi. Long range exciton dissociation in organic solar cells. *Proc. Natl. Acad. Sci. U. S. A.*, 109:13498, 2012.

[82] H. Vazquez and A. Troisi. Calculation of rates of exciton dissociation into hot charge transfer states in model organic photovoltaic interfaces. *Phys. Rev. B: Condens. Matter Mater. Phys.*, 88:205304, 2013.

[83] H. Tamura, R. Martinazzo, M. Ruckenbauer, and I. Burghardt. Quantum dynamics of ultrafast charge transfer at an oligophene-fulleren heterojunction. *J. Chem. Phys.*, 137:22A540, 2012.

[84] H. Tamura and I. Burghardt. Ultrafast charge separation in organic photovoltaics enhanced by charge delocalization and vibronically hot exciton dissociation. *J. Am. Chem. Soc.*, 135:16364, 2013.

[85] A. Troisi. How quasi-free holes and electrons are generated in organic photovoltaic interfaces. *Faraday Discuss.*, 163:377, 2013.

[86] Stavros Athanasopoulos, Steffen Tscheuschner, Heinz Bässler, and Anna Köhler. Efficient charge separation of cold charge-transfer states in organic solar cells through incoherent hopping. *The Journal of Physical Chemistry Letters*, 8(9): 2093–2098, 2017.

[87] Veljko Janković and Nenad Vukmirović. Combination of charge delocalization and disorder enables efficient charge separation at photoexcited organic bilayers. *The Journal of Physical Chemistry C*, 122(19):10343–10359, 2018.

[88] Sarah Maria Falke, Carlo Andrea Rozzi, Daniele Brida, Margherita Maiuri, Michele Amato, Ephraim Sommer, Antonietta De Sio, Angel Rubio, Giulio Cerullo, Elisa Molinari, and Christoph Lienau. Coherent ultrafast charge transfer in an organic photovoltaic blend. *Science*, 344(6187):1001–1005, 2014.

[89] Guangjun Nan, Xu Zhang, and Gang Lu. The lowest-energy charge-transfer state and its role in charge separation in organic photovoltaics. *Phys. Chem. Chem. Phys.*, 18:17546–17556, 2016.

[90] William Stier and Oleg V. Prezhdo. Nonadiabatic molecular dynamics simulation of light-induced electron transfer from an anchored molecular electron donor to a semiconductor acceptor. *The Journal of Physical Chemistry B*, 106(33):8047–8054, 2002.

[91] Run Long, Niall J. English, and Oleg V. Prezhdo. Photo-induced charge separation across the graphene-tio$_2$ interface is faster than energy losses: A time-domain ab initio analysis. *Journal of the American Chemical Society*, 134(34): 14238–14248, 2012.

[92] Zi Li, Xu Zhang, and Gang Lu. Dipole-assisted charge separation in organic–inorganic hybrid photovoltaic heterojunctions: Insight from first-principles simulations. *The Journal of Physical Chemistry C*, 116(18):9845–9851, 2012.

[93] P. R. Berger and M. Kim. Polymer solar cells: P3ht:pcbm and beyond. *Journal of Renewable and Sustainable Energy*, 10(1):013508, 2018.

[94] William A. Tisdale, Matthias Muntwiler, David J. Norris, Eray S. Aydil, and X.-Y. Zhu. Electron dynamics at the zno $(10\bar{1}0)$ surface. *The Journal of Physical Chemistry C*, 112(37):14682–14692, 2008.

[95] Daniel R. Jones and Alessandro Troisi. A method to rapidly predict the charge injection rate in dye sensitized solar cells. *Phys. Chem. Chem. Phys.*, 12:4625–4634, 2010.

[96] Natalia Martsinovich and Alessandro Troisi. High-throughput computational screening of chromophores for dye-sensitized solar cells. *The Journal of Physical Chemistry C*, 115(23):11781–11792, 2011.

[97] T. M. Clarke and J. R. Durrant. Charge photogeneration in organic solar cells. *Chem. Rev.*, 110:6736, 2010.

[98] M. Huix-Rotllant, H. Tamura, and I. Burghardt. Concurrent effects of delocalization and internal conversion tune charge separation at regioregular polyphene-fulleren heterojunction. *J. Phys. Chem. Lett.*, 6:1702, 2015.

[99] S. L. Smith and A. W. Chin. Phonon-assisted ultrafast charge separation in the pcbm band structure. *Phys. Rev. B: Condens. Matter Mater. Phys.*, 91:201302, 2015.

[100] Myeong H. Lee, Juan Aragó, and Alessandro Troisi. Charge dynamics in organic photovoltaic materials: Interplay between quantum diffusion and quantum relaxation. *The Journal of Physical Chemistry C*, 119(27):14989–14998, 2015.

[101] Edwin E. Jelley. Spectral absorption and fluorescence of dyes in the molecular state. *Nature*, 138:1009–1010, 1936.

[102] Frank Würthner, Theo E. Kaiser, and Chantu R. Saha-Möller. J-aggregates: From serendipitous discovery to supramolecular engineering of functional dye materials. *Angewandte Chemie International Edition*, 50(15):3376–3410, 2011.

[103] Julia L Bricks, Yuri L Slominskii, Ihor D Panas, and Alexander P Demchenko. Fluorescent j-aggregates of cyanine dyes: basic research and applications review. *Methods and Applications in Fluorescence*, 6(1):1–31, 2017.

[104] Tobias Brixner, Richard Hildner, Jürgen Köhler, Christoph Lambert, and Frank Würthner. Exciton transport in molecular aggregates - from natural antennas to synthetic chromophore systems. *Advanced Energy Materials*, 7(16):1–33, 2017.

[105] S. S. Lampoura, C. Spitz, S. Dähne, J. Knoester, and K. Duppen. The optical dynamics of excitons in cylindrical j-aggregates. *The Journal of Physical Chemistry B*, 106(12):3103–3111, 2002.

[106] T. Virgili, L. Lüer, G. Cerullo, G. Lanzani, S. Stagira, D. Coles, A. J. H. M. Meijer, and D. G. Lidzey. Role of intramolecular dynamics on intermolecular coupling in cyanine dye. *Phys. Rev. B*, 81:125317, 2010.

[107] Dylan H. Arias, Katherine W. Stone, Sebastiaan M. Vlaming, Brian J. Walker, Moungi G. Bawendi, Robert J. Silbey, Vladimir Bulović, and Keith A. Nelson. Thermally-limited exciton delocalization in superradiant molecular aggregates. *The Journal of Physical Chemistry B*, 117(16):4553–4559, 2013.

[108] Hans v. Berlepsch and Christoph Böttcher. Supramolecular structure of ttbc j-aggregates in solution and on surface. *Langmuir*, 29(16):4948–4958, 2013.

[109] Justin R. Caram, Sandra Doria, Dörthe M. Eisele, Francesca S. Freyria, Timothy S. Sinclair, Patrick Rebentrost, Seth Lloyd, and Moungi G. Bawendi. Room-temperature micron-scale exciton migration in a stabilized emissive molecular aggregate. *Nano Letters*, 16(11):6808–6815, 2016.

[110] Che-Hsuan Cheng, Zidong Li, Aaditya Hambarde, and Parag B. Deotare. Efficient energy transfer across organic-2d inorganic heterointerfaces. *ACS Applied Materials & Interfaces*, 10(45):39336–39342, 2018.

[111] Qiang Zhang, Tolga Atay, Jonathan R. Tischler, M. Scott Bradley, Vladimir Bulović, and A. V. Nurmikko. Highly efficient resonant coupling of optical excitations in hybrid organic/inorganic semiconductor nanostructures. *Nature Nanotechnology*, 2:555–559, 2007.

[112] Brian J. Walker, Vladimir Bulović, and Moungi G. Bawendi. Quantum dot/j-aggregate blended films for light harvesting and energy transfer. *Nano Letters*, 10:3995–3999, 2010.

[113] Katie A. Clark, Emma L. Krueger, and David A. Vanden Bout. Temperature-dependent exciton properties of two cylindrical j-aggregates. *The Journal of Physical Chemistry C*, 118(42):24325–24334, 2014.

[114] H. von Berlepsch, C. Böttcher, A. Ouart, C. Burger, S. Dähne, and S. Kirstein. Supramolecular structures of j-aggregates of carbocyanine dyes in solution. *The Journal of Physical Chemistry B*, 104(22):5255–5262, 2000.

[115] Hans von Berlepsch, Stefan Kirstein, and Christoph Böttcher. Supramolecular structure of j-aggregates of a sulfonate substituted amphiphilic carbocyanine dye in solution: Methanol-induced ribbon-to-tubule transformation. *The Journal of Physical Chemistry B*, 108(48):18725–18733, 2004.

[116] Stefan Kirstein and Siegfried Daehne. J-aggregates of amphiphilic cyanine dyes: Self-organization of artificial light harvesting complexes. *International Journal of Photoenergy*, 2006(20363):1–21, 2006.

[117] Jennifer L. Lyon, Dörthe M. Eisele, Stefan Kirstein, Jürgen P. Rabe, David A. Vanden Bout, and Keith J. Stevenson. Spectroelectrochemical investigation of double-walled tubular j-aggregates of amphiphilic cyanine dyes. *The Journal of Physical Chemistry C*, 112(4):1260–1268, 2008.

[118] Cătălin Didraga, Audrius Pugžlys, P. Ralph Hania, Hans von Berlepsch, Koos Duppen, and Jasper Knoester. Structure, spectroscopy, and microscopic model of tubular carbocyanine dye aggregates. *The Journal of Physical Chemistry B*, 108(39):14976–14985, 2004.

[119] A. Pugžlys, R. Augulis, P. H. M. van Loosdrecht, C. Didraga, V. A. Malyshev, and J. Knoester. Temperature-dependent relaxation of excitons in tubular molecular aggregates: Fluorescence decay and stokes shift. *The Journal of Physical Chemistry B*, 110(41):20268–20276, 2006.

[120] Dörthe M. Eisele, Jasper Knoester, Stefan Kirstein, Jürgen P. Rabe, and David A. Vanden Bout. Uniform exciton fluorescence from individual molecular nanotubes immobilized on solid substrates. *Nature Nanotechnology*, 4:658–663, 2009.

[121] S. M. Vlaming, E. A. Bloemsma, M. Linggarsari Nietiadi, and J. Knoester. Disorder-induced exciton localization and violation of optical selection rules in supramolecular nanotubes. *The Journal of Chemical Physics*, 134(11):114507, 2011.

[122] Jörg Megow, Merle I. S. Röhr, Marcel Schmidt am Busch, Thomas Renger, Roland Mitrić, Stefan Kirstein, Jürgen P. Rabe, and Volkhard May. Site-dependence of van der waals interaction explains exciton spectra of double-walled tubular j-aggregates. *Phys. Chem. Chem. Phys.*, 17:6741–6747, 2015.

[123] Katie A. Clark, Craig W. Cone, and David A. Vanden Bout. Quantifying the polarization of exciton transitions in double-walled nanotubular j-aggregates. *The Journal of Physical Chemistry C*, 117(50):26473–26481, 2013.

[124] Joel Yuen-Zhou, Dylan H. Arias, Dorthe M. Eisele, Colby P. Steiner, Jacob J. Krich, Moungi G. Bawendi, Keith A. Nelson, and Alán Aspuru-Guzik. Coherent exciton dynamics in supramolecular light-harvesting nanotubes revealed by ultrafast quantum process tomography. *ACS Nano*, 8(6):5527–5534, 2014.

[125] Raj Pandya, Richard Y. S. Chen, Alexandre Cheminal, Tudor Thomas, Arya Thampi, Arelo Tanoh, Johannes Richter, Ravichandran Shivanna, Felix Deschler, Christoph Schnedermann, and Akshay Rao. Observation of vibronic-coupling-mediated energy transfer in light-harvesting nanotubes stabilized in a solid-state matrix. *The Journal of Physical Chemistry Letters*, 9(18):5604–5611, 2018.

[126] Katie A. Clark, Emma L. Krueger, and David A. Vanden Bout. Direct measurement of energy migration in supramolecular carbocyanine dye nanotubes. *The Journal of Physical Chemistry Letters*, 5(13):2274–2282, 2014.

[127] Th. Förster. Zwischenmolekulare energiewanderung und fluoreszenz. *Annalen der Physik*, 437(1-2):55–75, 1948.

[128] G. Itskos, G. Heliotis, P. G. Lagoudakis, J. Lupton, N. P. Barradas, E. Alves, S. Pereira, I. M. Watson, M. D. Dawson, J. Feldmann, R. Murray, and D. D. C. Bradley. Efficient dipole-dipole coupling of mott-wannier and frenkel excitons in (ga,in)n quantum well/polyfluorene semiconductor heterostructures. *Phys. Rev. B*, 76:035344, 2007.

[129] Arun Gopi, Sivasankaran Lingamoorthy, Suraj Soman, Karuvath Yoosaf, Reethu Haridas, and Suresh Das. Modulating fret in organic-inorganic nanohybrids for

light harvesting applications. *The Journal of Physical Chemistry C*, 120(46): 26569–26578, 2016.

[130] Carles Curutchet, Alberto Franceschetti, Alex Zunger, and Gregory D. Scholes. Examining förster energy transfer for semiconductor nanocrystalline quantum dot donors and acceptors. *The Journal of Physical Chemistry C*, 112(35):13336–13341, 2008.

[131] Pedro Ludwig Hernández-Martínez, Alexander O. Govorov, and Hilmi Volkan Demir. Förster-type nonradiative energy transfer for assemblies of arrayed nanostructures: Confinement dimension vs stacking dimension. *The Journal of Physical Chemistry C*, 118(9):4951–4958, 2014.

[132] A. Szabo and N. S. Ostlund. *Modern Quantum Chemistry: Introduction to Advanced Electronic Structure Theory.* Dover Publications Inc., 1st edition, 1996. ISBN 978-0486691862.

[133] Michael C. Zerner. *Semiempirical Molecular Orbital Methods*, pages 313–365. John Wiley & Sons, Ltd, 2007. ISBN 978-0470125793.

[134] F. Bechstedt. *Many-Body Approach to Electronic Excitations: Concepts and Applications.* Springer, 1st edition, 2015. ISBN 978-3662445921.

[135] E. Zojer, J. Cornil, G. Leising, and J. L. Brédas. Theoretical investigation of the geometric and optical properties of neutral and charged oligophenylenes. *Phys. Rev. B*, 59:7957–7968, 1999.

[136] B. Aradi, B. Hourahine, and Th. Frauenheim. Dftb+, a sparse matrix-based implementation of the dftb method. *The Journal of Physical Chemistry A*, 111 (26):5678–5684, 2007.

[137] Matti Hellström, Kjell Jorner, Maria Bryngelsson, Stefan E. Huber, Jolla Kullgren, Thomas Frauenheim, and Peter Broqvist. An scc-dftb repulsive potential for various zno polymorphs and the zno-water system. *The Journal of Physical Chemistry C*, 117(33):17004–17015, 2013.

[138] J. M. Zhang and Y. Liu. Fermi's golden rule: its derivation and breakdown by an ideal model. *European Journal of Physics*, 37(6):065406, 2016.

[139] Franz Milota, Valentyn I. Prokhorenko, Tomas Mancal, Hans von Berlepsch, Oliver Bixner, Harald F. Kauffmann, and Jürgen Hauer. Vibronic and vibrational coherences in two-dimensional electronic spectra of supramolecular j-aggregates. *The Journal of Physical Chemistry A*, 117(29):6007–6014, 2013.

[140] Thomas Plehn and Volkhard May. Charge and energy migration in molecular clusters: A stochastic schrödinger equation approach. *The Journal of Chemical Physics*, 146(3):034107, 2017.

[141] N. G. Van Kampen. *Stochastic Processes in Physics and Chemistry.* North-Holland Personal Library, 3rd edition, 2007. ISBN 978-0444529657.

[142] G. Lindblad. On the generators of quantum dynamical semigroups. *Comm. Math. Phys.*, 48:119–130, 1976.

[143] R. Alicki and M. Fannes. Wave-function approach to dissipative processes in quantum optics. *Lett. Math. Phys.*, 11:259–262, 1986.

[144] R. Alicki and M. Fannes. Wave-function approach to dissipative processes in quantum optics. *Commun. Math. Phys.*, 108:353–361, 1987.

[145] Klaus Mølmer, Yvan Castin, and Jean Dalibard. Monte carlo wave-function method in quantum optics. *J. Opt. Soc. Am. B*, 10:524–538, 1993.

[146] M. O. Scully and M. S. Zubairy. *Quantum Optics*. Cambridge University Press, 1st edition, 1997. ISBN 978-0521434584.

[147] Carmichael H. *An Open Systems Approach to Quantum Optics*. Springer, 1st edition, 1993. ISBN 978-3540566342.

[148] Jean Dalibard, Yvan Castin, and Klaus Mølmer. Wave-function approach to dissipative processes in quantum optics. *Phys. Rev. Lett.*, 68:580–583, 1992.

[149] N. Gisin and I. C. Percival. The quantum-state diffusion model applied to open systems. *Journal of Physics A: Mathematical and General*, 25:5677–5691, nov 1992.

[150] N Gisin and I C Percival. Quantum state diffusion, localization and quantum dispersion entropy. *Journal of Physics A: Mathematical and General*, 26:2233–2243, 1993.

[151] N Gisin and I C Percival. The quantum state diffusion picture of physical processes. *Journal of Physics A: Mathematical and General*, 26:2245–2260, 1993.

[152] P. Gaspard and M. Nagaoka. Non-markovian stochastic schrödinger equation. *J. Chem. Phys.*, 111:5676, 1999.

[153] W. T. Strunz, L. Diósi, and N. Gisin. Open system dynamics with non-markovian quantum trajectories. *Phys. Rev. Lett.*, 82:1801, 1999.

[154] T. Yu, L. Diósi, N. Gisin, and W. T. Strunz. Non-markovian quantum-state diffusion: Perturbation approach. *Phys. Rev. A*, 60:91, 1999.

[155] Strunz W. T. The brownian motion stochastic schrödinger equation. *Chem. Phys.*, 268:237, 2001.

[156] J. Gambetta and H. W. Wiseman. Non-markovian stochastic schrödinger equations: Generalization to real-valued noise using quantum-measurement theory. *Phys. Rev. A*, 66:012108, 2002.

[157] Yu T. Non-markovian quantum trajectories versus master equations: Finite-temperature heat bath. *Phys. Rev. A*, 69:062107, 2004.

[158] I. de Vega, D. Alonso, P. Gaspard, and W. T. Strunz. Non-markovian stochatsic schrödinger equations in different temperature regimes: A study of the spin-boson model. *J. Chem. Phys.*, 122:124106, 2005.

[159] I. de Vega, D. Alonso, and P. Gaspard. Two-level system immersed in a photonic band-gap material: A non-markovian stochastic schrödinger-equation approach. *Phys. Rev. A*, 71:023812, 2005.

[160] X. Zhong and Y. Zhao. Charge carrier dynamics in phonon-induced fluctuation systems from time-dependent wavepacket diffusion approach. *J. Chem. Phys.*, 135:134110, 2011.

[161] Takatoshi Fujita, Jennifer C. Brookes, Semion K. Saikin, and Alán Aspuru-Guzik. Memory-assisted exciton diffusion in the chlorosome light-harvesting antenna of green sulfur bacteria. *The Journal of Physical Chemistry Letters*, 3(17):2357–2361, 2012.

[162] D. Suess, A. Eisfeld, and W. T. Strunz. Hierarchy of stochastic pure states for open quantum system dynamics. *Phys. Rev. Lett.*, 113:150403, 2014.

[163] David P. Landau and Kurt Binder. *A guide to Monte Carlo simulations in statistical physics*. Cambridge University Press, 1st edition, 2014. ISBN 978-1107074026.

[164] G. E. P. Box and Mervin E. Muller. A note on the generation of random normal deviates. *Ann. Math. Statist.*, 29:610–611, 1958.

[165] P. E. Kloeden, E. Platen, and H. Schurz. *Numerical Solution of SDE Through Computer Experiments*. Springer, 3rd edition, 2002. ISBN 978-3540570745.

[166] Crispin Gardiner. *Stochastic Methods*. Springer-Verlag Berlin Heidelberg, 4th edition, 2009. ISBN 978-642089626.

[167] A. Barchielli and M. Gregoratti. *Quantum Trajectories and Measurements in Continuous Time: The Diffusive Case*. Lecture Notes in Physics 782, 1st edition, 2011. ISBN 978-3642242489.

[168] Jan Roden, Alexander Eisfeld, Wolfgang Wolff, and Walter T. Strunz. Influence of complex exciton-phonon coupling on optical absorption and energy transfer of quantum aggregates. *Phys. Rev. Lett.*, 103:058301, 2009.

[169] R. E. Fenna and B. W. Matthews. Chlorophyll arrangement in a bacteriochlorophyll protein from chlorobium limicola. *Nature*, 258:573–577, 1975.

[170] A. Ishizaki and G. R. Fleming. Unified treatment of quantum and incoherent hopping dynamics in electronic energy transfer: Reduced hierarchy equation approach. *J. Chem. Phys.*, 130:234111, 2009.

[171] Julia Adolphs and Thomas Renger. How proteins trigger excitation energy transfer in the fmo complex of green sulfur bacteria. *Biophysical Journal*, 91(8):2778 – 2797, 2006.

[172] Julian Adolphs, Frank Müh, Mohamed El-Amine Madjet, and Thomas Renger. Calculation of pigment transition energies in the fmo protein. *Photosynthesis Research*, 95(2):197, 2007.

[173] G. Ritschel, J. Roden, W. T. Strunz, and A. Eisfeld. An efficient method to calculate excitation energy transfer in light-harvesting systems: Application to the fenna-matthews-olson complex. *New J. Phys.*, 1613:113034, 2011.

[174] P. Nalbach, D. Braun, and M. Thorwart. Exciton transfer dynamics and quantumness of energy transfer in the fenna-matthews-olson complex. *Phys. Rev. E*, 84:041926, 2011.

[175] A. Ishizaki and G. R. Fleming. Theoretical examination of quantum coherence in a photosynthetic system at physiological temperature. *Proc. Natl. Acad. Sci. U. S. A.*, 106:17255, 2009.

[176] A. Ishizaki and G. R. Fleming. On the adequacy of the redfield equation and related approaches to the study of quantum dynamics in electronic energy transfer. *J. Chem. Phys.*, 130:234110, 2009.

[177] Christoph Kreisbeck. Quantum transport through complex networks - from light-harvesting proteins to semiconductor devices, November 2012. URL `https://epub.uni-regensburg.de/26532/`.

[178] Yu-Chen Wang, Yaling Ke, and Yi Zhao. The hierarchical and perturbative forms of stochastic schrödinger equations and their applications to carrier dynamics in organic materials. *Wiley Interdisciplinary Reviews: Computational Molecular Science*, 9(1), 2019.

[179] Thomas Plehn, Dirk Ziemann, and Volkhard May. Simulations of frenkel to wannier-mott exciton transitions in a nanohybrid system. *The Journal of Physical Chemistry C*, 122(49):27925–27934, 2018.

[180] S. Blumstengel, S. Sadofev, C. Xu, J. Puls, and F. Henneberger. Converting wannier into frenkel excitons in an inorganic/organic hybrid semiconductor nanostructure. *Phys. Rev. Lett.*, 97:237401, 2006.

[181] S. Blumstengel, S. Sadofev, C. Xu, J. Puls, R. L. Johnson, H. Glowatzki, N. Koch, and F. Henneberger. Electronic coupling in organic-inorganic semiconductor hybrid structures with type-ii energy level alignment. *Phys. Rev. B*, 77:085323, 2008.

[182] Hiroyuki Tamura, Jean-Maurice Mallet, Martin Oheim, and Irene Burghardt. Ab initio study of excitation energy transfer between quantum dots and dye molecules. *The Journal of Physical Chemistry C*, 113(18):7548–7552, 2009.

[183] Laura Foglia, Lea Bogner, Martin Wolf, and Julia Stähler. Localization-dependent charge separation efficiency at an organic/inorganic hybrid interface. *Chemical Physics Letters*, 646:25 – 30, 2016.

[184] F. Della Sala, S. Blumstengel, and F. Henneberger. Electrostatic-field-driven alignment of organic oligomers on zno surfaces. *Phys. Rev. Lett.*, 107:146401, 2011.

[185] Na Sai, Kevin Leung, and James R. Chelikowsky. Hybrid density functional study of oligothiophene/zno interface for photovoltaics. *Phys. Rev. B*, 83:121309, 2011.

[186] Thomas Plehn, Dirk Ziemann, Jörg Megow, and Volkhard May. Frenkel to wannier-mott exciton transition: Calculation of fret rates for a tubular dye aggregate coupled to a cdse nanocrystal. *The Journal of Physical Chemistry B*, 119 (24):7467–7472, 2015.

[187] Pedro Ludwig Hernández-Martínez, Alexander O. Govorov, and Hilmi Volkan Demir. Generalized theory of förster-type nonradiative energy transfer in nanostructures with mixed dimensionality. *The Journal of Physical Chemistry C*, 117 (19):10203–10212, 2013.

[188] Thomas Plehn, Dirk Ziemann, and Volkhard May. Atomistic simulations of charge separation at a nanohybrid interface: Relevance of photoinduced initial state preparation. *The Journal of Physical Chemistry Letters*, 9(1):209–215, 2018.

[189] Thomas Plehn, Dirk Ziemann, and Volkhard May. Charge separation at an organic/inorganic nano-hybrid interface: atomistic simulations of a para-sexiphenyl zno system. *Phys. Chem. Chem. Phys.*, 20:26870–26884, 2018.

[190] Brian O'Regan and Michael Grätzel. A low-cost, high-efficiency solar cell based on dye-sensitized colloidal tio_2 films. *Nature*, 353:737–740, 1991.

[191] Anna Köhler and Heinz Bässler. *Electronic Processes in Organic Semiconductors - An Introduction*. Wiley-VCH, Berlin, 1st edition, 2010. ISBN 978-3527332922.

[192] C. Poelking and D. Andrienko. Design rules for organic donor-acceptor heterojunctions: Pathway for charge splitting and detrapping. *J. Am. Chem. Soc.*, 137: 6320, 2015.

[193] V. Jankovic and N. Vukmirovic. Origin of space-separated charges in photoexcited organic heterojunctions on ultrafast time scale. *Phys. Rev. B: Condens. Matter Mater. Phys.*, 95:075308, 2017.

[194] Alexandra Carvalho, Natalia Martsinovich, Ricardo Vieira, and Alessandro Troisi. Charge injection rates in hybrid nanosilicon-polythiophene bulk heterojunction solar cells. *The Journal of Physical Chemistry C*, 117(1):110–115, 2013.

[195] H. Haken and P. Reineker. The coupled coherent and incoherent motion of excitons and its influence on the line shape of optical absorption. *Zeitschrift für Physik*, 249:253–268, 1972.

[196] H. Haken and G. Strobl. An exactly solvable model for coherent and incoherent exciton motion. *Zeitschrift für Physik A Hadrons and nuclei*, 262:135–148, 1973.

[197] Ilya Rips. Stochastic models for exciton transport: The haken-strobl model. *Phys. Rev. E*, 47:67–79, 1993.

[198] Jean-Luc Brédas, David Beljonne, Veaceslav Coropceanu, and Jérôme Cornil. Charge-transfer and energy-transfer processes in π-conjugated oligomers and polymers: A molecular picture. *Chemical Reviews*, 104:4971–5004, 2004.

[199] Notker Rösch and Alexander A. Voityuk. *Quantum Chemical Calculation of Donor–Acceptor Coupling for Charge Transfer in DNA*, pages 37–72. Springer Berlin Heidelberg, Berlin, Heidelberg, 2004.

[200] Edward F. Valeev, Veaceslav Coropceanu, Demetrio A. da Silva Filho, Seyhan Salman, and Jean-Luc Brédas. Effect of electronic polarization on charge-transport parameters in molecular organic semiconductors. *Journal of the American Chemical Society*, 128(30):9882–9886, 2006.

[201] S. Verma and H. N. Ghosh. Exciton energy and charge transfer in porphyrin aggregate/semiconductor (tio_2) composites. *J. Phys. Chem. Lett.*, 3:1877, 2012.

[202] M. J. Lundqvist, M. Nilsing, S. Lunell, B. Åkermark, and P. Persson. Spacer and anchor effects on the electronic coupling in ruthenium-bis-terpyridine dye-sensitized tio_2 nanocrystals studied by dft. *J. Phys. Chem. B*, 110:20513, 2006.

[203] H. Tamura, I. Burghardt, and M. Tsukada. Exciton dissociation at thiophene/fullerene interfaces: The electronic structures and quantum dynamics. *J. Phys. Chem. C*, 115:10205, 2011.

[204] M. D. Newton. Quantum chemical probes of electron-transfer kinetics: The nature of donor-acceptor interactions. *Chem. Rev.*, 91:767, 1991.

[205] Thomas Plehn and Volkhard May. Charge migration kinetics at a nanoscale zno/molecule interface structure: A stochastic schrödinger equation approach. *Chemical Physics*, 515:187 – 192, 2018.

[206] E. Maggio and A. Troisi. Theory of the charge recombination reaction at the semiconductor-adsorbate interface in the presence of defects. *J. Chem. Phys. C*, 117:24196, 2013.

[207] Z. Sun and S. Stafstroem. Dynamics of charge separation at an organic donor-acceptor interface. *Phys. Rev. B*, 90:115420, 2014.

[208] A. V. Akimov, A. J. Neukirch, and O. V. Prezhdo. Theoretical insights into photoinduced charge transfer and catalysis at oxide interfaces. *Chem. Rev.*, 113: 4496, 2013.

[209] T. Meier, Y. Zhao, V. Chernyak, and S. Mukamel. Polarons, localization, and excitonic coherence in superradiance of biological antenna complexes. *The Journal of Chemical Physics*, 107(10):3876–3893, 1997.

[210] Kenneth N. Baker, Albert V. Fratini, Timothy Resch, Howard C. Knachel, W.W. Adams, E.P. Socci, and B.L. Farmer. Crystal structures, phase transitions and energy calculations of poly(p-phenylene) oligomers. *Polymer*, 34(8):1571 – 1587, 1993.

[211] L. D. Landau, E. M. Lifshitz, and L. P. Pitaevskii. *Electrodynamics of Continuous Media*. Butterworth-Heinemann, 2nd edition, 1984. ISBN 978-0750626347.

[212] R. P. Fornari and A. Troisi. Theory of charge hopping along a disordered polymer chain. *Phys. Chem. Chem. Phys.*, 16:9997, 2014.

[213] Björn Baumeier, James Kirkpatrick, and Denis Andrienko. Density-functional based determination of intermolecular charge transfer properties for large-scale morphologies. *Phys. Chem. Chem. Phys.*, 12:11103–11113, 2010.

[214] Georg Heimel, Maria Daghofer, Johannes Gierschner, Emil J. W. List, Andrew C. Grimsdale, Klaus Müllen, David Beljonne, Jean-Luc Brédas, and Egbert Zojer. Breakdown of the mirror image symmetry in the optical absorption/emission spectra of oligo(para-phenylene)s. *The Journal of Chemical Physics*, 122(5): 054501, 2005.

[215] V. Coropceanu, J. Cornil, D. A. da Silva Filho, Y. Olivier, R. Silbey, and Brédas J.-L. Charge transport in organic semiconductors. *Chem. Rev.*, 107:926, 2007.

[216] G. Scheibe, A. Mareis, and H. Ecker. Über reversible polymerisation als ursache neuartiger absorptionsbanden (iii). *Naturwissenschaften*, 25:474–475, 1937.

[217] Johannes Moll, Siegfried Daehne, James R. Durrant, and Douwe A. Wiersma. Optical dynamics of excitons in j aggregates of a carbocyanine dye. *The Journal of Chemical Physics*, 102(16):6362–6370, 1995.

[218] Kaoru Ohta, Mino Yang, and Graham R. Fleming. Ultrafast exciton dynamics of j-aggregates in room temperature solution studied by third-order nonlinear optical spectroscopy and numerical simulation based on exciton theory. *The Journal of Chemical Physics*, 115(16):7609–7621, 2001.

[219] Jaroslaw Sperling, Alexandra Nemeth, Jürgen Hauer, Darius Abramavicius, Shaul Mukamel, Harald F. Kauffmann, and Franz Milota. Excitons and disorder in molecular nanotubes: A 2d electronic spectroscopy study and first comparison to a microscopic model. *The Journal of Physical Chemistry A*, 114(32):8179–8189, 2010.

[220] Samuel Rhodes, Wenlang Liang, Ekaterina Shteinberg, and Jiyu Fang. Formation of spherulitic j-aggregates from the coassembly of lithocholic acid and cyanine dye. *The Journal of Physical Chemistry Letters*, 8(18):4504–4509, 2017.

[221] David M. Coles, Anthony J. H. M. Meijer, Wing C. Tsoi, Martin D. B. Charlton, Ji-Seon Kim, and David G. Lidzey. A characterization of the raman modes in a j-aggregate-forming dye: A comparison between theory and experiment. *The Journal of Physical Chemistry A*, 114(44):11920–11927, 2010.

[222] Metin Aydin, Özge Dede, and Daniel L. Akins. Density functional theory and raman spectroscopy applied to structure and vibrational mode analysis of 1,1',3,3'-tetraethyl-5,5',6,6'-tetrachloro-benzimidazolocarbocyanine iodide and its aggregate. *The Journal of Chemical Physics*, 134(6):064325, 2011.

[223] H. von Berlepsch, C. Böttcher, A. Ouart, M. Regenbrecht, S. Akari, U. Keiderling, H. Schnablegger, S. Dähne, and S. Kirstein. Surfactant-induced changes of morphology of j-aggregates: Superhelix-to-tubule transformation. *Langmuir*, 16 (14):5908–5916, 2000.

[224] Dörthe M. Eisele, C. W. Cone, E. A. Bloemsma, S. M. Vlaming, C. G. F. van der Kwaak, R. J. Silbley, M. G. Bawendi, J. Knoester, J. P. Rabe, and D. A. Vanden Bout. Utilizing redox-chemistry to elucidate the nature of exciton transitions in supramolecular dye nanotubes. *Nature Chemistry*, 4:655–6662, 2012.

[225] R. Augulis, A. Pugžlys, and P. H. M. van Loosdrecht. Exciton dynamics in molecular aggregates. *physica status solidi c*, 3(10):3400–3403, 2006.

[226] Christian Friedl, Thomas Renger, Hans v. Berlepsch, Kai Ludwig, Marcel Schmidt am Busch, and Jörg Megow. Structure prediction of self-assembled dye aggregates from cryogenic transmission electron microscopy, molecular mechanics, and theory of optical spectra. *The Journal of Physical Chemistry C*, 120(34): 19416–19433, 2016.

[227] Jörg Megow, Thomas Renger, and Volkhard May. Mixed quantum-classical description of excitation energy transfer in supramolecular complexes: Screening of the excitonic coupling. *ChemPhysChem*, 15(3):478–485, 2014.

[228] Doran I. G. Bennett, Pavel Malý, Christoph Kreisbeck, Rienk van Grondelle, and Alán Aspuru-Guzik. Mechanistic regimes of vibronic transport in a heterodimer and the design principle of incoherent vibronic transport in phycobiliproteins. *The Journal of Physical Chemistry Letters*, 9(10):2665–2670, 2018.

[229] Jonathan E. Halpert, Jonathan R. Tischler, Gautham Nair, Brian J. Walker, Wenhao Liu, Vladimir Bulović, and Moungi G. Bawendi. Electrostatic formation of quantum dot/j-aggregate fret pairs in solution. *The Journal of Physical Chemistry C*, 113(23):9986–9992, 2009.

[230] Chen Wang and Emily A. Weiss. Sub-nanosecond resonance energy transfer in the near-infrared within self-assembled conjugates of pbs quantum dots and cyanine dye j-aggregates. *Journal of the American Chemical Society*, 138(30):9557–9564, 2016.

[231] Robert Zwanzig. Memory effects in irreversible thermodynamics. *Phys. Rev.*, 124:983–992, 1961.

[232] Hazime Mori. Transport, Collective Motion, and Brownian Motion*). *Progress of Theoretical Physics*, 33(3):423–455, 1965.

[233] M. J. Frisch, G. W. Trucks, H. B. Schlegel, G. E. Scuseria, M. A. Robb, J. R. Cheeseman, G. Scalmani, V. Barone, G. A. Petersson, H. Nakatsuji, X. Li, M. Caricato, A. V. Marenich, J. Bloino, B. G. Janesko, R. Gomperts, B. Mennucci, H. P. Hratchian, J. V. Ortiz, A. F. Izmaylov, J. L. Sonnenberg, D. Williams-Young, F. Ding, F. Lipparini, F. Egidi, J. Goings, B. Peng, A. Petrone, T. Henderson, D. Ranasinghe, V. G. Zakrzewski, J. Gao, N. Rega, G. Zheng, W. Liang, M. Hada, M. Ehara, K. Toyota, R. Fukuda, J. Hasegawa, M. Ishida, T. Nakajima, Y. Honda, O. Kitao, H. Nakai, T. Vreven, K. Throssell, J. A. Montgomery, Jr., J. E. Peralta, F. Ogliaro, M. J. Bearpark, J. J. Heyd, E. N. Brothers, K. N. Kudin, V. N. Staroverov, T. A. Keith, R. Kobayashi, J. Normand, K. Raghavachari, A. P. Rendell, J. C. Burant, S. S. Iyengar, J. Tomasi, M. Cossi, J. M. Millam, M. Klene, C. Adamo, R. Cammi, J. W. Ochterski, R. L. Martin, K. Morokuma, O. Farkas, J. B. Foresman, and D. J. Fox. Gaussian 16 Revision B.01, 2016. Gaussian Inc. Wallingford CT.

[234] Björn Kobin, Lutz Grubert, Sylke Blumstengel, Fritz Henneberger, and Stefan Hecht. Vacuum-processable ladder-type oligophenylenes for organic-inorganic hybrid structures: synthesis, optical and electrochemical properties upon increasing planarization as well as thin film growth. *J. Mater. Chem.*, 22:4383–4390, 2012.

[235] Axel D. Becke. Density-functional thermochemistry. iii. the role of exact exchange. *The Journal of Chemical Physics*, 98(7):5648–5652, 1993.

[236] Thom H. Dunning. Gaussian basis sets for use in correlated molecular calculations. i. the atoms boron through neon and hydrogen. *The Journal of Chemical Physics*, 90(2):1007–1023, 1989.

[237] Ansgar Schäfer, Hans Horn, and Reinhart Ahlrichs. Fully optimized contracted gaussian basis sets for atoms li to kr. *The Journal of Chemical Physics*, 97(4): 2571–2577, 1992.

[238] Vladimír Lukeš, Adélia Justina Aguiar Aquino, Hans Lischka, and Harald-Friedrich Kauffmann. Dependence of optical properties of oligo-para-phenylenes on torsional modes and chain length. *The Journal of Physical Chemistry B*, 111 (28):7954–7962, 2007.

[239] Shinjiro Matsuoka, Hiroyuki Fujii, Taisuke Yamada, Chyongjin Pac, Akito Ishida, Setsuo Takamuku, Mitsuhiro Kusaba, Nobuaki Nakashima, and Shozo and Yanagida. Photocatalysis of oligo(p-phenylenes): photoreductive production of hydrogen and ethanol in aqueous triethylamine. *The Journal of Physical Chemistry*, 95(15):5802–5808, 1991.

[240] Naoki Sato, Kazuhiko Seki, and Hiroo Inokuchi. Polarization energies of organic solids determined by ultraviolet photoelectron spectroscopy. *J. Chem. Soc., Faraday Trans. 2*, 77:1621–1633, 1981.

[241] Curt M. Breneman and Kenneth B. Wiberg. Determining atom-centered monopoles from molecular electrostatic potentials. the need for high sampling

density in formamide conformational analysis. *Journal of Computational Chemistry*, 11(3):361–373, 1990.

[242] Richard L. Martin. Natural transition orbitals. *The Journal of Chemical Physics*, 118(11):4775–4777, 2003.

[243] Takeshi Yanai, David P Tew, and Nicholas C Handy. A new hybrid exchange-correlation functional using the coulomb-attenuating method (cam-b3lyp). *Chemical Physics Letters*, 393(1):51 – 57, 2004.

[244] Per-Olov Löwdin. On the non-orthogonality problem connected with the use of atomic wave functions in the theory of molecules and crystals. *The Journal of Chemical Physics*, 18(3):365–375, 1950.

[245] George Bruhn, Ernest R. Davidson, Istvan Mayer, and Aurora E. Clark. Löwdin population analysis with and without rotational invariance. *International Journal of Quantum Chemistry*, 106(9):2065–2072, 2006.

[246] Florian Weigend and Reinhart Ahlrichs. Balanced basis sets of split valence, triple zeta valence and quadruple zeta valence quality for h to rn: Design and assessment of accuracy. *Phys. Chem. Chem. Phys.*, 7:3297–3305, 2005.

[247] James C. Phillips et al. Scalable molecular dynamics with NAMD. *J. Comput. Chem.*, 26:1781–1802, 2005.

[248] D. A. Case. *AMBER 8*. University of California, San Francisco, CA, 2004.

[249] J. Wang, R.M. Wolf, J.W. Caldwell, P.A. Kollman, and D.A. Case. *J. Comput. Chem.*, 25(9):1157–1174, 2004.

[250] Tom Darden, Darrin York, and Lee Pedersen. Particle mesh ewald: An n·log(n) method for ewald sums in large systems. *The Journal of Chemical Physics*, 98 (12):10089–10092, 1993.

[251] H.-X. Deng, S.-S. Li, J. Li, and S.-H. Wei. Effect of hydrogen passivation on the electronic structure of ionic semiconductor nanostructures. *Phys. Rev. B: Condens. Matter Mater. Phys.*, 85:195328, 2012.

[252] M. Elstner, D. Porezag, G. Jungnickel, J. Elsner, M. Haugk, T. Frauenheim, S. Suhai, and G. Seifert. Self-consistent-charge density-functional tight-binding method for simulations of complex materials properties. *Phys. Rev. B: Condens. Matter Mater. Phys.*, 58:7260, 1998.

[253] D. Ziemann and V. May. Exciton formation and quenching in an au/cds core/shell nano-structure. *J. Phys. Chem. Lett.*, 6:4054, 2015.

[254] S. Schulz, S. Schumacher, and G. Czycholl. Tight-binding model for semiconductor quantum dots with a wurtzite crystal structure: From one-particle properties to coulomb correlations and optical spectra. *Phys. Rev. B*, 73:245327, 2006.

[255] N. Baer, S. Schulz, P. Gartner, S. Schumacher, G. Czycholl, and F. Jahnke. Influence of symmetry and coulomb correlation effects on the optical properties of nitride quantum dots. *Phys. Rev. B*, 76:075310, 2007.

[256] M. Korkusinski, M. Zielinski, and P. Hawrylak. Multiexciton complexes in inas self-assembled quantum dots. *Journal of Applied Physics*, 105(12):122406, 2009.

[257] Marek Korkusinski, Oleksandr Voznyy, and Pawel Hawrylak. Fine structure and size dependence of exciton and biexciton optical spectra in cdse nanocrystals. *Phys. Rev. B*, 82:245304, 2010.

[258] G. Marsaglia and T. A. Bray. A convenient method for generating normal variables. *SIAM Review*, 6(3):260–264, 1964.

Danksagung

Während ich in den letzten Jahren an dieser Thesis arbeitete, wurde ich von vielen Menschen unterstützt. An dieser Stelle möchte ich Ihnen dafür danken.

Zuerst und ganz besonders, möchte ich meinen Dank an *Dr. Volkhard May* zum Ausdruck bringen. Durch ihn wurde es mir möglich, zu den in dieser Doktorarbeit niedergeschriebenen Ergebnissen zu kommen. Seiner unterstützenden, ratwissenden und ermutigenden Rolle als Doktorvater habe ich sehr viel zu verdanken. Ich lernte sehr seine fokussierte Führung schätzen, weil sie mir genug Freiraum ließ, meine eigenen Überlegungen zu verwirklichen. Ich genoss die vielen interessanten und inspirierenden fachlichen Unterhaltungen in kleiner Runde. Auch an den regelmäßigen formlosen privaten Runden außerhalb des Instituts hatte ich große Freude. Darüber hinaus möchte ich mich für die Ermöglichung der Teilnahme an internationalen Konferenzen und wissenschaftlichen Aufenthalten bedanken.

Prof. Irene Burghardt unterstützte mich dabei viele Aspekte meiner Arbeit aus der Sichtweise der theoretischen Chemie zu betrachten. Ihr ist es auch zu verdanken, dass ich mehrere quantenchemische Rechenmethoden während eines wissenschaftlichen Aufenthaltes am *Institut für Physikalische und Theoretische Chemie der Goethe Universität Frankfurt* kennenlernte.

Des Weiteren, möchte ich meinem Kollegen *Dirk Ziemann* für die regen Diskussionen und die Ausführung der elektronischen Strukturrechnungen zum ZnO Cluster und CdSe Nanokristall danken. Mein Dank gilt weiterhin *Dr. Jörg Megow*. Dieser unterstützte mich sehr in der frühen Phase meiner Forschungsarbeit mit wertvollen Hinweise und Erklärungen. Zusätzlich bedanke ich mich für die Bereitstellung der von mir verwendeten Kernstruktur des tubulären Farbstoffaggregates.

Ich bin sehr dankbar für die Finanzierung des *Sonderforschungsbereiches 951 – HIOS*. An dieser Stelle möchte ich auch die noch mitwirkenden Mitarbeiter im Umfeld des Sonderforschunsbereiches wertschätzen. Die vielen interessanten Veranstaltungen bereicherten mein Denken. So sind meine Studien zum tubulären Farbstoffaggregat maßgeblich von den spektroskopischen Messungen von *Prof. Jürgen Rabe* und *Dr. Stefan Kirstein* inspiriert. An dieser Stelle danke ich auch *Katherine Herman* für die bereitgestellten Steady–State Spektren.

Ein großes Dankeschön soll an *Prof. Beate Röder* gehen. Ihr freundlicher, aber auch immer persönlicher Umgang half mir in vielen Momenten. Im Allgemeinen danke ich der *AG Photobiophysik* für die unkomplizierte Zusammenarbeit.

Nicht geringer möchte ich mich bei meiner Freundin, meiner Familie und allen Freunden bedanken, die mich außerhalb der Universität mit viel Verständnis, vor allem zum Ende meiner Promotion, ganz enscheidend unterstützten. Dies trug ebenfalls wesentlich zum Erfolg dieser Thesis bei.

Selbstständigkeitserklärung

Ich erkläre, dass ich die Dissertation selbständig und nur unter Verwendung der von mir gemäß § 7 Abs. 3 der Promotionsordnung der Mathematisch-Naturwissenschaftlichen Fakultät, veröffentlicht im Amtlichen Mitteilungsblatt der Humboldt-Universität zu Berlin Nr. 42/2018 am 11.07.2018 angegebenen Hilfsmittel angefertigt habe.

Berlin, den 13.10.2019 Thomas Plehn